UNIVERSIDADE DE SANTIAGO DE COMPOSTELA

FACULTAD DE FÍSICA

Departamento de Física de Partículas

Fragment Distributions of Transfer- and Fusion-Induced Fission from ^{238}U+^{12}C Reactions Measured Through Inverse Kinematics

Diego Ramos Doval

Septiembre de 2016

USC
UNIVERSIDADE
DE SANTIAGO
DE COMPOSTELA

UNIVERSIDADE DE SANTIAGO DE COMPOSTELA

FACULTAD DE FÍSICA

Departamento de Física de Partículas

Fragment Distributions of Transfer- and Fusion-Induced Fission from ^{238}U+^{12}C Reactions Measured Through Inverse Kinematics

Memoria presentada por:
Diego Ramos Doval
como disertación para optar al
Grado de Doctor
en Ciencias Físicas
Septiembre de 2016

USC
UNIVERSIDADE
DE SANTIAGO
DE COMPOSTELA

UNIVERSIDADE DE SANTIAGO DE COMPOSTELA

Manuel Caamaño Fresco, Investigador Ramón y Cajal del Departamento de Física de Partículas de la Universidad de Santiago de Compostela; **Fanny Farget**, Investigadora CR1 del CNRS en GANIL, Francia; y **José Benlliure Anaya** (tutor), Catedrático de Física Atómica, Molecular y Nuclear de la Universidad de Santiago de Compostela,

CERTIFICAN:

que la memoria titulada **Fragment Distributions of Transfer- and Fusion-Induced Fission from ^{238}U + ^{12}C Reactions Measured Through Inverse Kinematics** ha sido realizada bajo su dirección por **Diego Ramos Doval** en el **Departamento de Física de Partículas de esta Universidad**, y constituye el **Trabajo de Tesis** que presenta para optar al **Grado de Doctor en Ciencias Físicas.**

Santiago de Compostela, a 5 de Septiembre de 2016

Fdo. Manuel Caamaño Fresco

Fdo. Fanny Farget

Fdo. José Benlliure Anaya

Fdo. Diego Ramos Doval

USC
UNIVERSIDADE
DE SANTIAGO
DE COMPOSTELA

Contents

List of Figures

List of Tables

Introduction

Soon after its discovery in 1939, nuclear fission was understood as a long and complex process involving extreme deformations, nuclear structure, and heat flows that decide the characteristics of the emerging fission-fragments distributions. Nevertheless, despite almost 80 years of intense research, fission is still far from being fully understood, and the theoretical and experimental knowledge is not yet complete.

Nuclear fission at low excitation energy is one of the nuclear phenomena where both the macroscopic and microscopic aspects of the nuclear matter are involved: the deformation that the fissioning system reaches at the scission point corresponds to a collective movement of the nucleons, while the produced fragment distributions are strongly affected by the shell structure of their energy levels.

The large amount of experimental data on the fragment distributions reveals the fission of actinides as an asymmetric process that produces one heavy fragment with a mean mass number rather constant of $A \sim 140$, independently on the fissioning system, and a light-fragment mass that complements the total mass of the fissioning system. Models that take into account nuclear structure assign the heavy fragment stabilization to gaps of energy to the spherical shell $N = 82$ and to the deformed shell $N \sim 88$. However, experimental information on the sharing of both protons and neutrons between the nascent fragments was not accessible until recently.

Historically, the analysis of experimental fission observables suffered from two main drawbacks: they are seldom obtained in the same experiment and the measurement of the atomic number is either absent or scarce. The use of inverse kinematics for studying fission, pioneered by Schmidt et al. at GSI, opens a possibility to solve these problems. Contrary to direct

kinematics, where a light beam is accelerated and impinges on a heavy target, in inverse kinematics is the heavy nucleus the one accelerated. In this way, the fission fragments acquire higher velocities and facilitate the measurement of their atomic charge. In the first experimental application of this technique, Schmidt et al. measured an almost constant mean value of the charge of the heavy fragment in more than 20 different fissioning systems, suggesting that protons also play an important role in the fission process.

Currently, two complementary experimental campaigns take profit from the use of inverse kinematics and the capabilities of magnetic spectrometers to measure simultaneously the mass and the atomic charge of fission fragments: SOFIA at GSI, which measures electromagnetic-induced fission of neutron-deficient systems; and the fission campaign in VAMOS/GANIL, where systems around ^{238}U are studied through transfer- and fusion-induced fission.

This thesis is part of the fission campaign in VAMOS/GANIL, where the transfer reactions permit, in addition, to investigate the evolution of the fission observables as a function of the excitation energy of the fissioning system.

Apart from the study of the fission process, this process presents the possibility of producing neutron-rich nuclei, which are a current topic of research on nuclear physics, studying, for instance, the evolution of the shell structure in nuclei far from the stability. The fission of the nuclei presented in this work produces neutron-rich fragments from $Z = 30$ to $Z = 70$ that open the possibility of such investigations.

In addition to basic research, the present study is also relevant for energy and industrial applications. 4th-generation reactors are designed to produce energy using fuels other than ^{235}U and to incinerate radioactive waste based on a continuos fission burning above the barrier, induced by fast-neutron capture. Experimental data of fission yields of minor actinides, in a range of excitation energies comparable with fast neutrons, are required for the construction of such reactors, improving the safety and efficiency with accurate models and evaluations.

Chapter 1

Motivations

This chapter presents a general description of nuclear fission showing the basics of widely used models, from the liquid drop model to the GEF code, as well as recent experimental approaches and techniques that provide new experimental information. Some unresolved points in the fission description are also discussed.

1.1 The Discovery of Nuclear Fission

Soon after the discovery of the neutron by Chadwick in 1932 [1], many efforts were put in the production of transuranic elements, bombarding uranium with neutrons in order to populate heavier elements through successive β disintegrations following the neutron capture. In 1934, Fermi suggested that he had discovered the element Z=93 [2], claiming that the observation did not correspond to any element from uranium to lead. However, the fact that many different radioactive species were produced from the natural uranium bombarded with neutrons raised many doubts about the interpretation of the results in terms of transuranic elements. Contrary to the Fermi interpretation, in 1939, Hahn and Strassman univocally identified barium and lanthanum as products of the neutron-capture uranium [3].

In 1939, Meitner and Frisch coined the term "fission" and were the first to suggest a theoretical explanation to the process on the basis of the nu-

clear liquid drop model [4]. They treated the stability of the nuclei in terms of surface tension, which they estimated to be zero for $Z \sim 100$. Since uranium had only a slightly smaller charge, they argued that the uranium nucleus may divide itself into two nuclei of equal size after receiving excitation energy from the captured neutron binding energy. Meitner and Frisch predicted a total kinetic energy of 200 MeV due to the repulsion of the two nuclei, calculated from nuclear radius and charge, which was quickly confirmed experimentally by Frisch in 1939 [5]. Only few months later, Bohr and Wheeler developed a detailed and extensive theoretical description of the fission process based on the liquid drop model [6], where they introduce the fissility concept as a measurement of the stability of the liquid drop against deformation.

Since then many experimental information came out and a variety of models were developed, either using fully microscopic approaches, or combining micro- and macroscopic views, as well as phenomenological codes relying on experimental data.

1.2 General Description of Fission

Nuclear fission is a complex reaction where a highly-deformed heavy nucleus splits into two fragments with intermediate masses as a consequence of the large-scale collective motion of the nucleons inside the fissioning system. In the fission process, a strong rearrangement of the nucleons occurs from the initial configuration of the fissioning nucleus up to the formation of both fragments.

The outcome of a single fission decay depends on the initial conditions of the fissioning nucleus in terms of excitation energy, fissility, deformation and angular momentum; and, due to the stochastic nature of the process, also on the path followed by the fissioning system on a potential that defines the deformation and the mass asymmetry of the pre-formed fragments. In order to relate the initial conditions with the products of the reaction, the features of the fragment distributions are studied.

In the case of induced fission, part of the excess of energy introduced in the system due to the primary reaction is transformed in a collective motion of the nucleons that increases the deformation of the nucleus. During the deformation process, there is a competition between the surface tension and Coulomb repulsion of the pre-fragments, increased by the deformation of the system.

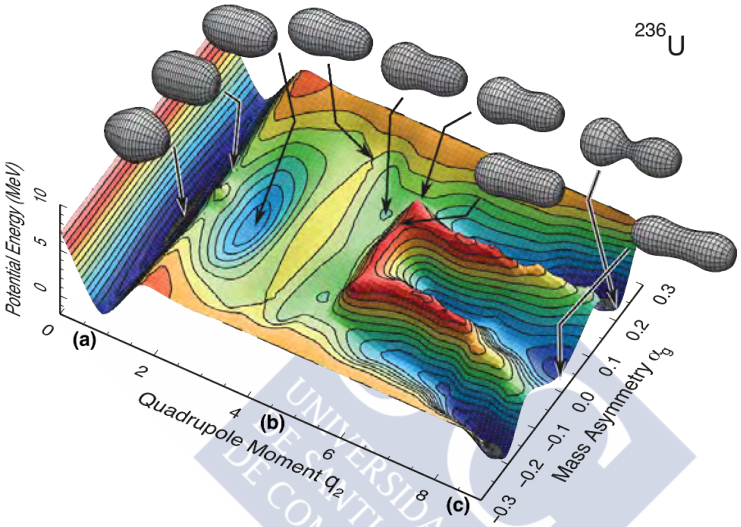

Figure 1.1: Potential energy surface of ^{236}U as a function of the quadrupole momentum and mass asymmetry calculated in a macroscopic-microscopic approach [7], presented in Sec. 1.2.2. Shapes of the nucleus at different points are also presented

An example of the potential energy landscape of the fission process for ^{236}U is shown in Fig. 1.1. The data was calculated with a macroscopic-microscopic model in [7]. The potential energy is presented as a function of the quadrupole momentum (q_2), which defines the deformation, and the mass asymmetry (α_g). A minimum of excitation energy is required to promote the compound nucleus from the ground state (a), to the saddle point (b), where the Coulomb repulsion dominates above the surface tension and the fissioning system deforms until the scission point (c), where both fragments are completely separated and emitted back to back with a

high kinetic energy. Points (a), (b), and (c) in the figure are referred only to the path with $\alpha_g = 0$. The shape of the system at different positions is also presented.

The excitation energy of the pre-fragments along the process can be separated into two components:

$$E_x = E_x^{coll} + E_x^{single} \ . \tag{1.1}$$

E_x^{coll} is the collective excitation energy, which is the energy acquired in collective degrees of freedom, such as deformation or rotations. E_x^{single} corresponds to single particle excitation energy. The main sources of E_x^{single} are the initial energy that the fissioning system possesses above the fission barrier, B_f, and the energy dissipated in the coupling of collective and intrinsic degrees of freedom, E_{diss}:

$$E_x^{single} = (E_x - B_f) + E_{diss} \ . \tag{1.2}$$

E_x^{single} is shared between the pre-fragments according their level density, which favors heat flows towards the heavy fragment, while the partition of E_x^{coll} depends strongly on structure effects within the fragments.

Since its discovery, different theoretical approaches have been developed in order to describe the fission process. Some of these approaches are discussed in the following.

1.2.1 Liquid Drop Model

The liquid drop model (LDM) treats the nuclear matter as an incompressible liquid composed of nucleons that are bound through the strong interaction. This model assumes a homogeneous nuclear density and considering the ground-state nucleus as an sphere of radius $r = r_0 A^{1/3}$, where A is the mass number and $r_0 = 1.15$ fm is a constant that corresponds

to the classic radius of a nucleon. The first detailed LDM, performed by Bohr and Wheeler [6], is presented in this section.

Under the previous assumptions, Weizsäcker [8] developed in 1935 a semi-empirical formula to calculate the binding energy ($B(Z,A)$) of ground-state nuclei:

$$B(Z,A) = a_v A - a_s A^{2/3} - a_c \frac{Z(Z-1)}{A^{1/3}} - a_a \frac{(A-2Z)^2}{A} - \delta(A). \quad (1.3)$$

The strong interaction is treated here as a volume force, $a_v A$, proportional to the mass of the nucleus. The surface contribution, $a_s A^{2/3}$, takes into account that nucleons in the surface of the nucleus interact with less neighbors, reducing the binding energy. The Coulomb term, $a_c \frac{Z(Z-1)}{A^{1/3}}$, reduces also the binding energy due to the Coulomb repulsion between protons inside the nucleus. The asymmetry component, $a_a \frac{(A-2Z)^2}{A}$, accounts for the quantum effect of the Pauli exclusion principle, which says that an excess of neutrons in the nucleus populate higher energy levels, increasing the total energy of the nucleus and diminishing its binding energy. Finally, the pairing term, $\delta(A)$, defined as:

$$\delta(A) = \begin{cases} a_p A^{-3/4}\,, & \text{even-Z, even-N} \\ 0\,, & \text{odd-A} \\ -a_p A^{-3/4}\,, & \text{odd-Z, odd-N} \end{cases} \quad (1.4)$$

takes into account the excess of energy required to break pairs of protons and neutrons that present large overlap in their wave functions.

The values of the constants are adjusted to the experimental mass measurements, and result in $a_v = 15.5$ MeV, $a_s = 16.8$ MeV, $a_c = 0.72$ MeV, $a_a = 23$ MeV, and $a_p = 34$ MeV.

The extension of this description to the case of deformed nuclei was perfomed by Bohr and Wheeler [6]. The deformation renders the radius of the nuclear surface dependent on the polar and azimuthal angle, θ and ϕ. This radius, $R(\theta,\phi)$, may be parametrized following a multipolar series:

$$R(\theta,\phi) = R_0 \left[1 + \sum_{n,\mu} \alpha_{n\mu} Y_{n\mu}(\theta,\phi) \right] , \quad (1.5)$$

where R_0 is the radius of the spherical nucleus, $Y_{n\mu}(\theta, \phi)$ are the spherical harmonics, and the parameters $\alpha_{n\mu}$ represent the weight of the different types of deformation.

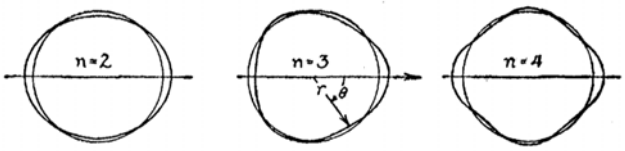

Figure 1.2: Scheme of the principal deformations involved in the fission process, as described in [6]: quadrupole (n=2), octupole (n=3), and hexadecapole (n=4). $\mu = 0$ is assumed due to the rotational symmetry along the fission axis.

Figure 1.2 presents the principal deformations involved in the fission process according the description in [6], attending to the multipolar order: n=2 corresponds to a quadrupole deformation, which is the elongation along one symmetry axis; n=3 corresponds to an octupole deformation, which produces an asymmetry left-right; and n=4 corresponds to a hexadecapole deformation, a high order deformation that occurs when both pre-fragments are connected through a neck.

Lower order deformation are not taken into account since they do not affect to the fission process, and n=3 is neither considered since the Bohr and Wheeler model only predicts symmetric fission. In addition $\mu = 0$, because the fission deformation is assumed to have rotational symmetry around the axis connecting both fragments.

The binding energy of the deformed nucleus within the liquid drop model differs from the spherical one only on the surface and Coulomb terms, both depending on the radius. Since the quadrupole deformation dominates along the fission process, the surface and Coulomb terms of a nucleus with deformation ϵ may be written, as a first approximation, as

an expansion of the spherical terms on the quadrupole deformation α_{20}:

$$\begin{aligned} E_s(\epsilon) &= E_s(0)\left(1+\frac{2}{5}\alpha_{20}^2\right) , \\ E_c(\epsilon) &= E_c(0)\left(1-\frac{1}{5}\alpha_{20}^2\right) , \end{aligned} \tag{1.6}$$

where $E_s(0)$ and $E_c(0)$ correspond to the surface and Coulomb terms of the binding energy for the spherical nucleus.

Bohr and Wheeler defined the first potential surface by using the deformation energy, E_{def}, which corresponds to the binding energy difference between deformed and spherical nucleus:

$$E_{def} = B(\epsilon) - B(0) = \frac{a_{20}}{5}\left(2E_s(0) - E_c(0)\right). \tag{1.7}$$

A fission barrier appears from the previous calculation at low deformation, where the binding energy is higher than that of the spherical shape. However, at higher deformation, there is an inversion that favors energetically the nuclear fission. The inversion point is called *saddle point*, and corresponds to the deformation of the nucleus that reaches unstable equilibrium.

Figure 1.3 presents the potential energy calculated by Bohr and Wheeler as a function of the quadrupole deformation and secondary degrees of freedom (hexadecapole deformation, in this case), where the fission trajectory, indicated with x, follows the path of lowest potential. The *saddle point* correspond to the place where equipotential lines cross.

This approach permits to define the *Fissility parameter*, which accounts for the stability of the nucleus. The fission barrier exists when $2E_s(0) > E_c(0)$ (see Eq. 1.7), hence, the *Fissility parameter*, defined as

$$x = \frac{E_c(0)}{2E_s(0)} \overset{\propto}{\sim} \frac{Z^2}{50A}, \tag{1.8}$$

indicates large fission barriers when $x >> 1$ and an unbound nucleus when $x < 1$.

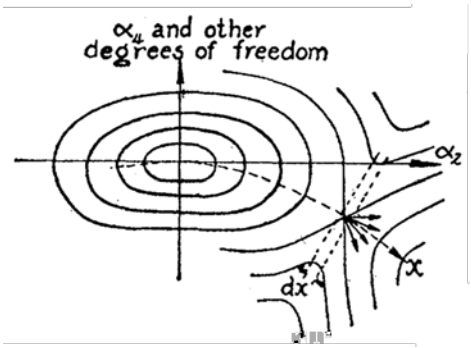

Figure 1.3: Potential energy as a function of the quadrupole and hexadecapole deformations, extracted from [6]. The dashed line indicates the trajectory followed by the system. The *saddle point*, indicated with dx, corresponds to the point where the two equipotential lines cross.

This early model provides good predictions in terms of fission barriers, as it was observed as soon as measurements were available. The basis of the liquid-drop approach is still present, with several improvements and upgrades, in current models based on a macroscopic contribution. The weakness of the model relies in the fact that, in order to reproduce the measured fragment distributions, ad-hoc corrections need to be applied.

1.2.2 Microscopic-Macroscopic Approach. Strutinsky Model.

The large discrepancies between the fragment distributions predicted by the Liquid-Drop model and the ones experimentally measured lie on the effect of the shell structure of the nuclei, which is not handled by a macroscopic approach such as the liquid-drop model.

The quantum nature of nucleons under a central potential defines energy levels where they are located inside the nucleus. The level scheme of nucleons inside the nucleus is described by the shell model, which considers protons and neutrons independently, moving in a central potential, with

energy and wave function described by the Schödinger equation. Some nuclear configurations with certain number of protons and neutrons, called *magic numbers*, were observed to be more stable than others [9]. In nuclei with these numbers, the levels above the valence nucleons present larger gaps that make the promotion of nucleons to higher levels more energy-consuming. The shell model and the the appearance of magic numbers were extended to deformed nuclei by Nilsson [10] in 1955, who investigated the evolution of the single particle energy as a function of the deformation.

Later, Strutinsky [11] developed a new model in 1967, where the level scheme of Nilsson is used to calculate the shell-model correction to the liquid-drop energy of the nucleus as a function of the occupation number and deformation. This combination of microscopic and macroscopic approaches was applied to describe more accurately asymmetric fission.

In this model, the binding energy, W, is defined as the sum of the binding energy obtained through the the LDM, $\widetilde{W}$, and the energy difference between a distribution of nucleon states described by Nilsson and a smooth distribution of states described by the LDM, δU, summed over the number of protons and neutrons:

$$\begin{aligned} W =& \widetilde{W} + \sum_{Z,N} \delta U \ , \\ \delta U =& U - \widetilde{U} \ , \end{aligned} \tag{1.9}$$

where U is the sum of the individual energies in the shell-model potential:

$$U = \sum_{\nu} e_\nu 2 n_\nu \ , \tag{1.10}$$

being e_ν the nucleon levels in the average potential and n_v the occupation numbers. $\widetilde{U}$ is the sum over all occupied energy states in the LDM smooth distribution:

$$\widetilde{U} = 2 \int_{-\infty}^{\tilde{\lambda}} e \tilde{g}(e) \mathrm{d}e \ , \tag{1.11}$$

being $\tilde{g}(e)$ the LDM level density and $\tilde{\lambda}$ the corresponding Fermi level.

$\tilde{g}(e)$ is defined by Strutinsky as a gaussian of width γ:

$$\tilde{g}(e) = \frac{1}{\gamma\sqrt{\pi}} \sum_{\nu} e^{-\frac{1}{\gamma^2}(E-E_\nu)^2} \ . \tag{1.12}$$

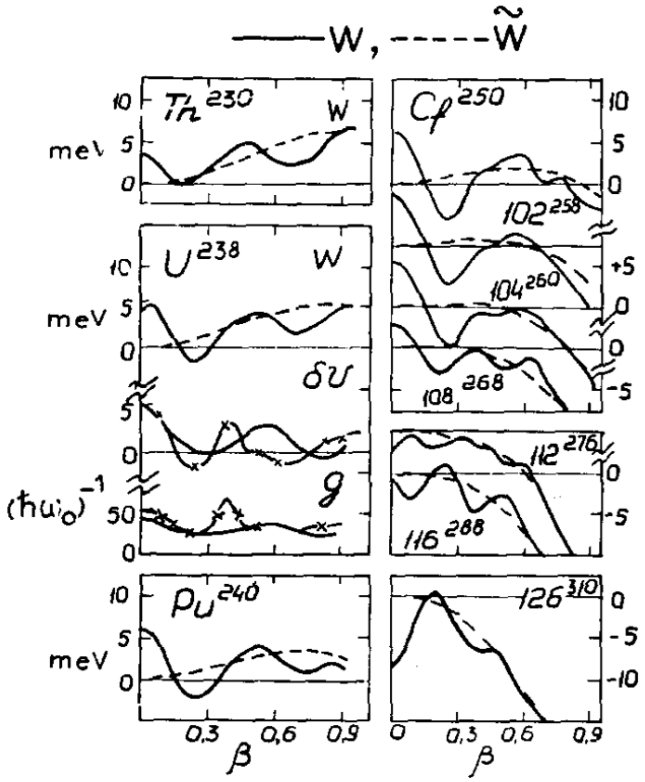

Figure 1.4: Binding energy of heavy nuclei calculated through the Strutinsky model (W), compared to LMD ($\widetilde{W}$), as a function of the deformation parameter (β). For ^{238}U, the calculated shell correction (δU) and the Fermi shell level densities (g) are shown separately for protons (solid line) and for neutrons (crosses). Picture extracted from [11].

Some results of these calculations are presented in Fig. 1.4 in terms of the binding energy W as a function of the deformation parameter β,

which is related to the radius along the symmetry axis as $R = R_0(1 + \frac{2}{3}\beta)$. For comparison, the LDM binding energy $\widetilde{W}$ is included, represented with dashed lines. The calculated shell correction δU and the Fermi shell level densities g of ^{238}U are shown separately for protons (solid line) and for neutrons (crosses).

In the nuclei addressed in Fig. 1.4, these calculations predict ground states few MeV lower than the LDM spherical ones and with deformed shapes, in agreement with experimental measurements. The fission thresholds of deformed transuranic nuclei are estimated larger than the LDM ones, rendering these nuclei relatively stable to fission. A second and even third fission barrier appears naturally, allowing the existence of fission isomers.

Contrary to the approximation included in the LDM of Bohr and Wheeler, where only quadrupole and hexadecapole deformations were considered, the Strutinsky model permits the evolution of the potential energy with the octupole deformation, introducing the description of asymmetric fission. Figure 1.5 presents the potential energy of ^{240}Pu, calculated under this approach including both macroscopic and microscopic contributions (solid line) and with only the macroscopic contribution (dashed line): the upper picture shows the potential as a function of the quadrupole ("symmetric") deformation, α_{20}, where a second barrier is predicted in the micro-macro approach; the lower picture shows the potential in the second barrier as a function of the octupole ("asymmetric") deformation, α_{30}, where the minimum of potential is clearly shifted from zero, predicting the asymmetric fission.

1.2.3 Scission-Point Model

The Scission-Point model, developed by Wilkins et al. [13] in 1976, consists in a static model based on the assumption of statistical equilibrium among collective degrees of freedom at the scission point. The distribution of fission fragments is determined near the scission-point from the relative potential energies of the complementary nascent fragments pairs, neglect-

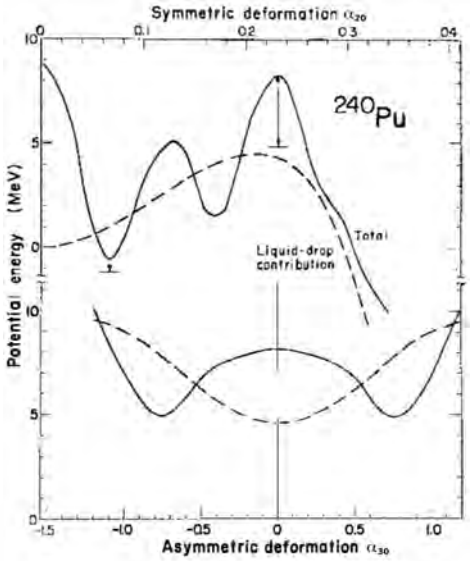

Figure 1.5: Energy potential of ^{240}Pu, calculated with a microscopic-macroscopic model that includes the Strutinsky approach as a function of the quadrupole deformation (upper) and as a function of the octupole deformation in the second barrier (lower). The solid line takes into account both macroscopic and microscopic contributions and the dashed line includes only the macroscopic component. Picture extracted from [12].

ing the evolution of the fissioning system along the deformation potential prior to the scission point. Geometrically, the fragment pairs are treated as nearly touching, coaxial spheroids with a tip separation d and deformations β_1 and β_2, defined in terms of the semi-major R and semi-minor r axes of a prolate spheroid, $R = R_0(1 + \frac{2}{3}\beta)$ and $r = R_0(1 - \frac{1}{3}\beta)$.

The total potential energy at scission, V, is treated as the sum of the contributions of both fragments separately, with a collective component described through the liquid drop model, V_{LDM}, and single-particle terms introduced as shell, S, and pairing, P, corrections. Coulomb V_C and nuclear V_N potential terms are also included in order to account for the

interaction between the two coaxial spheroids:

$$\begin{aligned} V(N_1, Z_1, \beta_1, N_2, Z_2, \beta_2, \tau, d) = V_{LDM}(N_1, Z_1, \beta_1) + V_{LDM}(N_2, Z_2, \beta_2) \\ + S(N_1, \beta_1, \tau) + S(Z_1, \beta_1, \tau) + S(N_2, \beta_1, \tau) + S(Z_2, \beta_1, \tau) \\ + P(N_1, \beta_1, \tau) + P(Z_1, \beta_1, \tau) + P(N_2, \beta_1, \tau) + P(Z_2, \beta_1, \tau) \\ + V_C(N_1, Z_1, \beta_1, N_2, Z_2, \beta_2, d) + V_N(N_1, Z_1, \beta_1, N_2, Z_2, \beta_2, d) \ . \end{aligned} \tag{1.13}$$

The shell correction S is calculated based on the Strutinsky method (see Sec. 1.2.2), and it takes into account the deformation and the intrinsic temperature that determines the population of the single-particle levels. Figure 1.6 presents the shell correction as a function of the deformation for both protons and neutrons, separately. The red regions represent the strongest shell corrections, containing values lower than -4 MeV. At small deformation we can observe the spherical magic numbers 50 and 82, while at higher deformation ($\beta \sim 0.6$) deformed closed shells appear in $N \sim 66, 88$.

The pairing correction P accounts for the pairing energy of the nucleons inside the nucleus, calculated in this model from the BCS (Bardeen, Cooper, and Schrieffer) standard formalism [14].

The Coulomb interaction V_C is calculated as the Coulomb repulsion of two spheroids of charge $Z_1 e$ and $Z_2 e$:

$$V_C = \frac{Z_1 Z_2 e^2 F}{D} \ , \tag{1.14}$$

where the factor $F \in [1.0, 1.1]$ accounts for the difference between the Coulomb interaction of two uniformly charged spheroids and that of two point charges separated by a distance D.

Finally, the term V_N describes the nuclear interaction between both fragments at the scission point. Wilkins et al. use the interaction proposed by Krappe and Nix [15] with a fixed tip distance $d = 1.4$ fm, in order to limit the nuclear-interaction strength to the order of the binding energy of one nucleon.

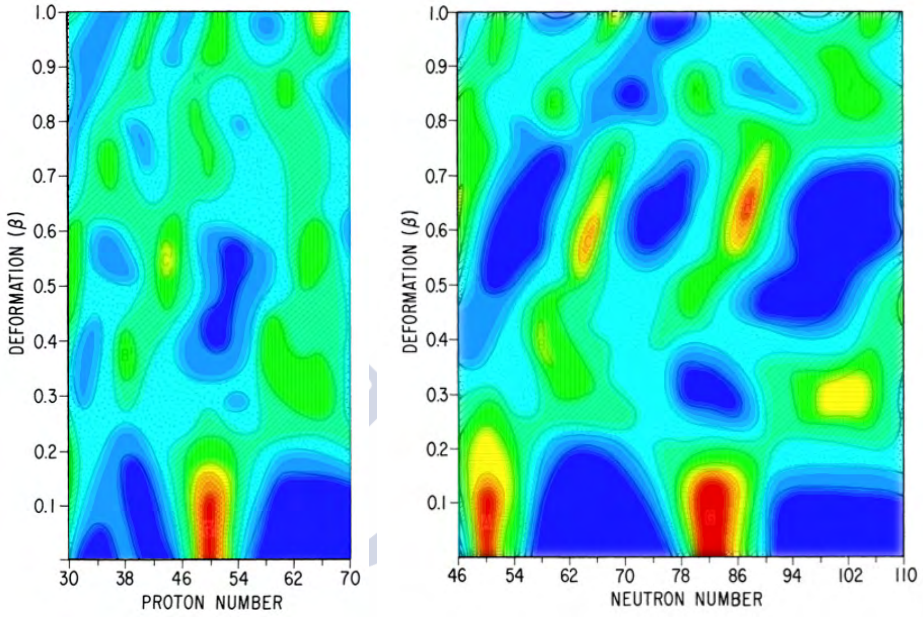

Figure 1.6: Shell corrections of the nascent fission-fragment potential as a function of the deformation parameter β, for protons and neutrons, separately, calculated with the scission-point model. Regions of strong shell effects are indicated in red. Pictures from [13].

This approach implies a state of quasiequilibrium for the system near the scission point with the condition of intermediate coupling between the collective and single-particle levels populated as the system moves along the collective degrees of freedom toward scission. This situation is described by introducing a collective temperature, $T_{coll} = 1$ MeV, that accounts for the statistical quasiequilibrium of the collective degrees of freedom, and a value of the effective intrinsic temperature, $\tau = 0.75$ MeV, that accounts for an intermediate coupling.

The quasiequilibrium among collective degrees of freedom is fundamental for the calculation of the relative probabilities of formation of comple-

mentary fission fragments pairs, given by:

$$\Phi(N, Z, \tau, d) = \int_{\beta_1=0}^{\beta_{max}} \int_{\beta_2=0}^{\beta_{max}} e^{\frac{-V(N,Z,\beta,\tau,d)}{T_{coll}}} \mathrm{d}\beta_1 \mathrm{d}\beta_2 \ , \tag{1.15}$$

where β_{max} is fixed to 1.0 in the case of Wilkins et al. [13].

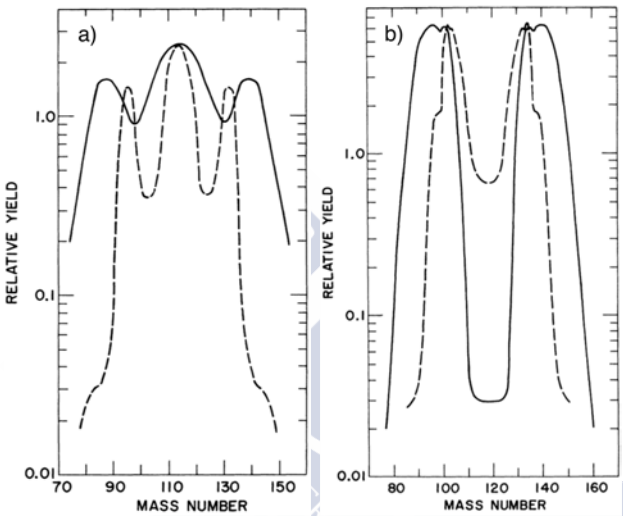

Figure 1.7: Mass yields of ^{227}Ra (a) and ^{236}U (b) calculated under the scission-point model formulated in [13] (dashed line), compared to experimental data (solid line) from ^{226}Ra(p, f) ($E_p = 13$ MeV), and ^{235}U(n_{th}, f). Pictures from [13].

Figure 1.7 presents the mass distribution of ^{227}Ra (a) and ^{236}U (b). The calculated data from the scission-point model of [13] are presented with dashed lines while experimental data, from ^{226}Ra(p, f) [16] with $E_p = 13$ MeV, and from ^{235}U(n_{th}, f) [17], are indicated with solid lines. This early version of the scission-point model reproduces the main features of the mass distributions, predicting two and three humped shapes. However, the model is not able to reproduce the position and width of the distributions, either because this model does not account for the dissipation effects from the saddle to the scission point, or due to a wrong assignment of the fixed parameters d, τ or T_{coll}.

1.2.4 Fission Channels and Random Neck Rupture

In 1990, Brosa, Grossmann, and Müller [18] developed a new model in order to describe the features of measured observables of fission, such as the fragment distribution, the total kinetic energy, and the neutron evaporation, based on two complementary steps: the *fission channels*, present in the potential energy surface; and the *random neck rupture*, happening at scission.

In this model, the potential energy surface is calculated under the Strutinsky's approach (See Sec. 1.2.2). Brosa et al. do not calculate the full potential landscape as a function of the deformation parameters; they define, instead, several *distinguished points* where the process finds bifurcations in the potential. Each bifurcation corresponds to one fission channel, which confers fixed characteristics to the system at the scission. Five channels are described by Brosa et al.:

- *Super-long channel:* it is a symmetric channel that corresponds to the symmetric valley of the potential energy surface. It is characterized by a large deformation in both fragments, which produces a wider fragments distribution with low total kinetic energy and high neutron evaporation.

- *Super-short channel:* it is also a symmetric channel, only observed in nuclei heavier than ^{252}Cf. It is characterized by two quasi-spherical fragments about the same mass, and it produces narrow mass distributions with high total kinetic energy and negligible neutron evaporation.

- *Standard I channel:* it is an asymmetric channel, governed by the double magic nucleus ^{132}Sn, centered around $A \sim 135$ and $Z \sim 52$ in actinides. It is characterized by an almost spherical heavy fragment and a deformed light fragment. The neutron evaporation is higher in the light than in the heavy fragment due to the excess of energy stored in deformation. It presents a compact configuration at scission that produces a high total kinetic energy.

- *Standard II channel:* it is another asymmetric channel, centered around $A \sim 140$ and $Z \sim 54$ in actinides. It is characterized by a deformed heavy fragment and a spherical light fragment, with a configuration less compact than the *Standard I* at scission, leading lower total kinetic energy and larger total neutron evaporation.

- *Super-asymmetric channel:* it is a third asymmetric channel, rarely present, with a highly asymmetric mass distribution.

Figure 1.8 represents the scission configuration of the channels, *Super short* (a), *Super long* (b), *Standard I* (c), and *Super asymmetric* (d). The mass distribution that corresponds to each channel is presented with dots and the neutron evaporation with solid lines.

The potential energy surface calculation in terms of fission channels is not sufficient to describe the final fragment observables; to do this, the connection between the scission point and the formation of the fission fragments is needed. The *random neck rupture* provides the link between both the scission configuration and the nascent fragments.

Brosa et al. describe both pre-fragments at scission as two spheroids connected through a hyperbolic flat neck, with a general shape function. Figure 1.9 illustrates this scission configuration: the upper part refers the pre-scission situation, when both pre-fragments are connected through an neck; the lower part refers the post-scission situation, when both spheroid fragments are separated, with major (a_i) and minor (b_i) axis.

Under this configuration, Brosa et al. describe the scission split as the break of the system at a random position along the neck. The larger the neck, the higher the number of possible different snaps, and hence, the wider the distribution of fragments.

This model provides an average mass number in agreement with the measured asymmetry, and the predicted variances are no longer too small when compared to experimental measurements. Both improvements come from considering the properties of the fissioning configuration, and not only the fragments themselves, since magic numbers in fragments suggest

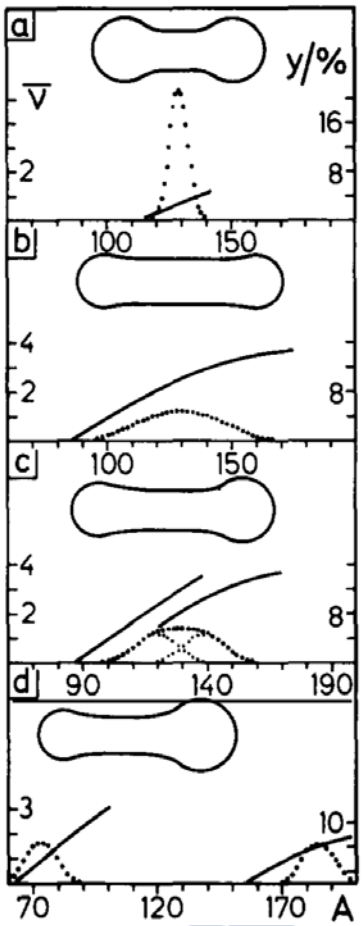

Figure 1.8: Schematic draw of the scission configuration of the *Super short* (a), *Super long* (b), *Standard I* (c), and *Super asymmetric* (d) channels. The mass distribution (dots) and the neutron evaporation (solid line) of each channel are also presented. Picture from [18].

$A = 132$ while $A = 140$ is observed. This value is achieved by adding the excess of nucleons in the neck to the already $A = 132$ heavy pre-fragment once the system splits.

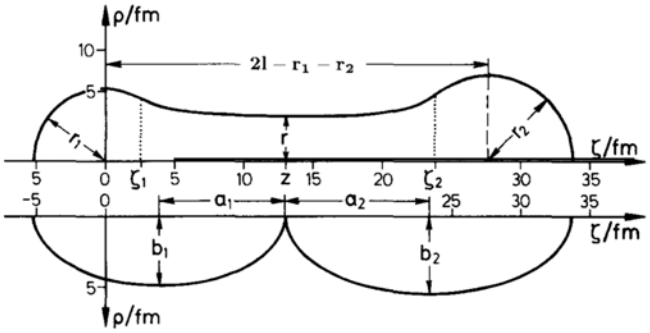

Figure 1.9: View of the scission configuration under the description of Brosa et al. [18]. The upper part represents the pre-scission situation, where both pre-fragments are connected through a neck. The lower part presents the post-scission situation, when both fragments split.

1.2.5 Semi-empirical GEF code (GEneral description of Fission observables)

The GEF code [19] is a complete tool for the description of the fission observables, developed by K.-H. Schmidt and B. Jurado in the last decade. The GEF code consists in a semi-empirical description that make use of many theoretical ideas of mostly rather general character, avoiding microscopic calculations, where several parameters are adjusted to fit experimental information. In this way, empirical information is used for developing a global description of the fission process, while the theoretical frame assures that the model is able to provide predictions of the fission observables for a wide range of fissioning systems.

The GEF code describes the potential energy surface based on the separability principle, which allows to describe the fission process as two separated steps: one consists in the deformation of the compound nucleus, governed by the macroscopic potential; and a second step, where the shells on the fission path that produce the complex structure of the fission channels start to play a role at a given deformation, primarily independent of

the fissioning system, but essentially given by fragment shells.

This description also accounts for dynamical effects between the saddle and the scission point introducing an "effective" potential energy surface. This effective potential energy, empirically adjusted, takes into account the impact of dissipative and inertial forces in the distribution of specific observables, which induce memory on the fission trajectory with a characteristic time, prior the scission point, during which the potential energy surface affects the final observable distribution. This stochastic process produces a broadening of the observables distributions that are used to adjust the value of the effective potential energy.

The thermodynamic approach of the fission process performed by GEF translates into a entropy-driven energy-sorting mechanism [20]. Below 20 MeV of excitation energy, the pairing correlation leads to an effective number of degrees of freedom of the nucleus that increases proportionally to the excitation energy. This makes that its temperature, defined as the average excitation energy per degree of freedom, remains constant. Experiments on nuclear level densities [21] have shown that modeling the temperature of nuclei as a function of the nuclear mass fit to the data on nuclear level density at low E_x:

$$T \propto A^{-2/3}, \tag{1.16}$$

with a level density very well described by the constant-temperature formula:

$$\rho(E_x) \propto e^{E_x/T}, \tag{1.17}$$

Concerning the nascent fragments at scission, assuming thermal equilibrium among their intrinsic degrees of freedom, the level density of each fragment is described by the previous formula with an specific temperature for each one. As a consequence, there is no solution for the sharing of E_x with $T_1 = T_2$. Instead, as long as some excitation energy remains in the fragment with higher temperature (light fragment), its excitation energy is transferred to the fragment with lower temperature (heavy fragment). In this situation, the entropy of the system is a linear function of the energy

partition, which is maximum if the available excitation energy is concentrated on the nucleus with lower temperature. Hence, this flow of E_x from the hot fragment to the cold one can be seen as a way for the entire system to maximize the number of occupied states or its entropy.

This superfluid behavior is joint with the Fermi-gas behavior at higher E_x, where the total E_x is shared by the fragments in proportion to their masses:

$$\frac{E_{x1}}{E_{x2}} = \frac{A_1}{A_2} \tag{1.18}$$

Only microscopic approaches are able to relate the adjusted parameters in macroscopic models with properties of the nuclear force. Nevertheless, the semi-empirical GEF code permits to calculate fission observables without specific adjustments to measured data of individual systems. This approach provides a consistent description of all available experimental observables over a wide range of fissioning systems, which is relevant for examining the consistency of experimental results and for evaluating nuclear data. The accuracy of this code in terms of fission fragment distributions motivates the comparison performed in this work between the experimental data and the GEF code predictions.

1.3 Inverse Kinematics. A New Experimental Technique for Fission Studies

Historically, the experimental investigation of fission was focused on neutron-induced fission, in which an intensive flux of neutrons is sent to a stable heavy target where the fission process takes place. The use of this technique was also motivated by the direct application in reactors, where neutron-induced fission activates the chain reaction. However, neutron-induced fission experiments are restricted to the use of long-lived nuclei as targets. This limits the number of fissioning systems that can be investigated to few stable and long-half-life nuclei and, many times, with high production costs.

With the arrival of intense heavier beams, the fission process was studied with transfer and fusion reactions, which overcomes some of the limitations of the neutron-induced fission. Nevertheless, direct kinematics, where the light nucleus is accelerated and sent to a heavy target producing a recoil fissioning system, suffers from some limitations when measuring the fission fragments distributions. The low velocity of the fragments prevents a full identification: only the complete mass distribution of the fragments is measured, while the nuclear charge, whenever possible, is limited to the light fragment due to the appearance of charge states fluctuations at low energy that disturb the conventional energy-loss measurements.

This limitation can be overcome with the use of inverse kinematics, introduced in fission research by K.-H. Schmidt et al. [22] in 1994. This technique consists in accelerating the heavy nuclei and sending it to a light target; in this way, the fission process occurs in flight. This technique permits to reduce the experimental limitations associated with low-energy fragments: the Lorentz boost of the fissioning system also affects the fission fragments, which are emitted with much higher velocity, compared to direct kinematics, allowing the direct measurement of their nuclear charge with a classical dE-E telescope. Another advantage of inverse kinematics is that no long-lived heavy nuclei are needed to build the target. Exotic nuclei might be accelerated and sent to a stable light target permitting the fission study of exotic fissioning systems. A third advantage is that the forward fragments emission produced by the Lorentz boost allows a large acceptance in the fissioning system reference frame with reduced angular coverage in the laboratory.

Nowadays, two collaborations profit from the inverse kinematics technique to perform fission investigations: The SOFIA collaboration at GSI (Germany) [23] and the VAMOS fission campaign at GANIL (France) [24].

The SOFIA campaign focuses on electromagnetic-induced fission. The experiment uses a primary beam of ^{238}U that is accelerated up to 1 GeV/u and sent to a beryllium target to produce a secondary cocktail beam through fragmentation reactions. The actinides of this secondary beam are selected and identified in the FRS (*FRagment Separator*). At the final

focal plane, these nuclei, with energies around 730 MeV/u, are Coulomb excited in lead and uranium targets, and decay through fission with a certain probability. Both fission fragments are identified, event by event, in nuclear charge and in mass by using a double ionization chamber (*Twin-MUSIC*) and a large acceptance dipole magnet (*ALADIN*), measuring, at the same time, their velocities with a dedicated setup.

The VAMOS/GANIL fission campaign uses a beam of ^{238}U at 6 MeV/u sent to a ^{12}C target, where the beam nuclei are excited by inelastic, transfer, and fusion reactions, producing fissioning systems from ^{238}U up to ^{250}Cf. The transfer reaction is reconstructed in a silicon telescope that provides a direct measurement of the excitation energy produced. One of the fragments from the subsequent fission decay is identified, event by event, in mass and nuclear charge, as well as in velocity, with the VAMOS spectrometer and a dedicated setup at its focal plane. The low energy beam permits the limited angular and Time-of-Flight resolution to be sufficient for the reconstructing at the fissioning system reference. This work presents new experimental results concerning fission fragments yields, neutron excess, total neutron evaporation, even-odd staggering of the fragment nuclear charge, and their evolution with the excitation energy obtained in the last campaign of this collaboration.

1.4 Importance of Fission Observables

In both the theoretical interpretation and the application framework many questions related to the fission process remain open: the role of nuclear structure and shell effects, the sharing of the excitation energy between the fission fragments, the prediction capability of theoretical models, the demand of more accurate measurements, etc. These might be addressed with experimental information that combines, at the same time, accurate measurements and correlations between observables. Some key points are presented in the following.

1.4.1 Theoretical Unresolved Points

As mentioned in Section 1.2.3, the asymmetric behavior of the fragments distribution at low excitation energy has been understood as the effect of the spherical shell $N = 82$ and the deformed shell $N \sim 88$. However, since the experimental information of the nuclear charge of full fragment distribution is accessible, this description can be revisited. The experimental observation of the stabilization of the nuclear charge of the heavy fragment around $Z \sim 54$ [25] indicates that shell structure in protons might also play a role. Simultaneous measurements of both isotopic and isobaric yields are an important source of information to understand the effect of neutrons and protons shells on the process.

The sharing of the excitation energy between both fragments in the fission process is another open question. Recent measurements and models indicate that, at very low excitation energy, the pre-fragments remain in a statistical equilibrium with constant temperature at scission that produces a flux of excitation energy from the light to the heavy fragment, while, at higher excitation energy, a Fermi gas behavior is assumed (see Sec. 1.2.5). The limit between both regimes and their validity remain, so far, unsettled. Experimental information about the evolution with the excitation energy of the sharing of nucleons at scission and the neutron evaporation might clarify the picture.

In general, many theoretical approaches have been developed during the last decades intending to reproduce specific and isolated fission observables. Simultaneous measurements and their correlations might help to constrain theoretical models in order to reproduce the fission process in a general way, ensuring its predictive capability.

1.4.2 Fission Applications

Nowadays, nuclear reactors use ^{235}U as fuel due to its high fission probability at any neutron energy. However, the reserves of ^{235}U are limited and

new reactors based on other types of fuel are required. Two new types of nuclear reactors are being considered: subcritical reactors, where the fissile material has a fission barrier that prevents the neutron-induced fission at very low energy, ensuring a safety operation; and fast reactors, where the distribution of neutrons that reaches energies of few MeV might be used to incinerate radioactive waste, simultaneously to the energy production. In both cases, an accurate knowledge of the fission cross sections and fission yields is mandatory in order to optimize their development and operation.

Another important application of the fission process is the production of radioactive beams. Since the number of neutrons per nuclear charge in actinides is higher than in lighter nuclei to compensate the Coulomb repulsion, the fission of actinides will produce neutron-rich nuclei as fission products. The fission of actinides with a very asymmetric fragments distribution permits to produce neutron-rich light nuclei, from $Z \sim 30$ to $Z \sim 43$, as well as, heavier nuclei, from $Z \sim 49$ to $Z \sim 60$; while the fission of highly excited actinides produces intermediate neutron-rich nuclei that might complement the previous. An accurate knowledge of the fission yields would permit the estimation of the production rate of specific nuclei.

A third application involves the r-process in the stellar nucleosynthesis. Three processes are understood to be responsible of the production of elements heavier than Fe: the proton capture (rp-process), slow neutron capture (s-process), and rapid neutron capture (r-process). Each process populates different regions of the nuclear chart and occurs in different stellar scenarios. In stars with a high neutron density, the r-process, which consists in fast successive neutron captures and consecutive β^- decays, explains the production of elements heavier than Bi. However, in this region, the fission process dominates the β^- decay and, hence, the stellar abundances are affected by the fission process, not only in the region of heavy elements, but also in the region of the fission products. More accurate experimental data, such as fission cross sections and fission yields are necessary to improve the stellar nucleosynthesis models.

USC
UNIVERSIDADE
DE SANTIAGO
DE COMPOSTELA

Chapter 2

Experimental Setup

This chapter describes the experimental setup designed for fission measurements via transfer reactions in inverse kinematics of this work. It begins with a general view of the GANIL facilities, including the production and acceleration of the $^{238}U^{+31}$ beam used in this experiment. It continues with a discussion on the experimental setup and its capabilities for nuclear fission investigations. Later, a detailed description of the detectors that identify the transfer reaction, and the VAMOS spectrometer setup that identifies the fission fragments is presented. Finally, the electronic scheme, including the acquisition trigger logic, is discussed.

2.1 The GANIL facility

GANIL (Grand Accélérateur National d'Ions Lourds) is one of the largest laboratories in the world dedicated to scientistic research with ion beams. This large european facility has led to numerous discoveries since 1983 to the present day in different fields, from radiotherapy to the physics of the atom, from condensed matter to astrophysics. This scientific production is particularly remarkable in the field of nuclear physics and exotic nuclei [26], thanks to the production and acceleration of stable and radioactive beams at GANIL.

Stable nuclei are produced with an Electron Cyclotron Resonance (ECR) ion source and accelerated in the Compact Cyclotrons (C01 or C02) at

around 0.5 MeV/u. Then, they are sent to two coupled Separated-Sector Cyclotrons (CSS1 and CSS2) where they are further accelerated, reaching average energies of 24 MeV/u and 96 MeV/u respectively.

Figure 2.1 shows a schematic view of the GANIL facilities, where the different acceleration stages appear on the left side of the picture, including both Compact Cyclotrons (C01 and C02) and both Separated-Sector Cyclotrons (CSS1 and CSS2); the experimental areas are placed on the right side.

Radioactive beams are produced in two different ways depending on the required energy: at intermediate energies, they are produced by the In-Flight Separation technique [27], whereas low-energy radioactive beams are obtained by using the Isotope Separation On Line (ISOL) technique [28].

In the In-Flight Separation method, a thin production target is impinged by the stable beam that comes from CSS2 cyclotron. Radioactive nuclei are produced by fragmentation reactions and leave the target around forward angles and velocities similar to those of the projectile. These products are selected in flight in the $LISE$-spectrometer [29] by means of their magnetic rigidity and sent to the experimental area.

The ISOL technique requires the SPIRAL facility [30]. In this case, the radioactive products are extracted from a thick production target with the Electron Cyclotron Resonance Ion Source (ECRIS) Nanogan III. The heavy atoms extracted from the source are ionized inside a plasma created by a radio frequency field, and remain confined until they are extracted by applying a voltage between the ion source and the extraction electrode. These low-energy radioactive nuclei are selected by a relatively low resolution separator; later they are injected into the compact cyclotron CIME where they achieve an energy ranging from 1.7 MeV/u to 25 MeV/u. Finally, the beam is sent to the α-spectrometer, composed of two dipole magnets and one degrader that select the desired nuclear species in magnetic rigidity and nuclear charge, plus quadrupole magnets for beam focusing. From there, the beam is sent to the experimental areas.

The stable $^{238}U^{+31}$ beam used in this experiment is produced in the ECR ion source by the sputtering technique, which consists in accelerating positive ions of oxygen or neon toward a negatively biased metallic sample of uranium. After striking it, uranium atoms are evaporated into a plasma and ionized. Then, they are driven to the Compact Cyclotron C01 and the Separated-Sector Cyclotron CSS1 where they are accelerated up to 6.14 MeV/u. The beam is directly sent from the CSS1 to the α-spectrometer, where its emittance and energy spread are controlled, and then to the experimental area. The final beam intensity with this configuration is $3 \cdot 10^{10}$ pps. Nevertheless, the intensity in this experiment was reduced to 10^9 pps to avoid radiation damage on the detectors.

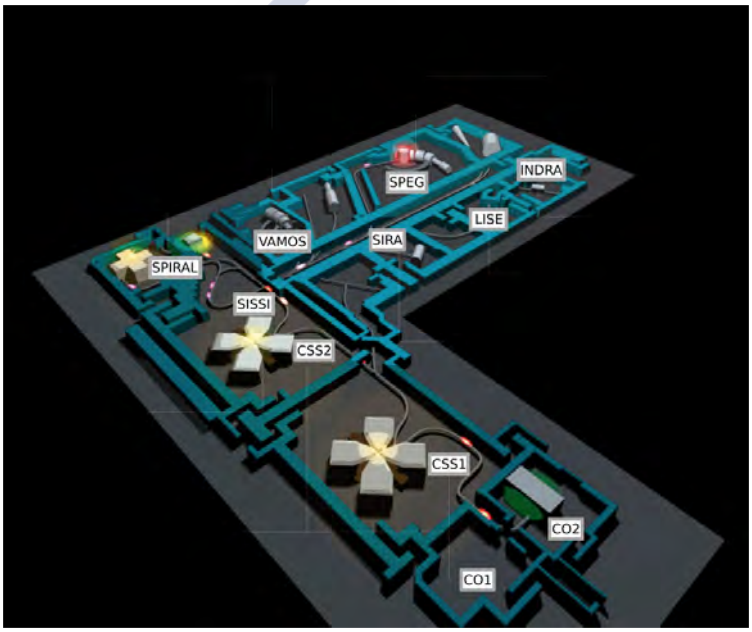

Figure 2.1: Schematic view of the GANIL facility. The left side corresponds to the acceleration area. In front of if, on the right side, the experimental areas are depicted.

2.2 The Experiment

A beam of ^{238}U at 6.14 MeV/u is sent to the cave G1, where the VAMOS spectrometer is placed, and impinges on a ^{12}C target of 100 μg/cm^2. The energy loss in the target, assuming that the reaction occurs in the middle of the target, is 6.29 MeV, therefore the average energy of the ^{238}U nuclei when the reaction takes place is 6.11 MeV/u. This energy, which corresponds to 69.80 MeV in the center of mass, is an 8.2% above the S-wave coulomb barrier between ^{238}U and ^{12}C. In such configuration, fusion and transfer reactions, as well as elastic and inelastic scattering, take place. Other channels, such as break-up reactions, are strongly suppressed. Once the reaction occurs, the beam-like product may decay by a fission process whenever the excitation energy allows it.

Due to the inverse kinematics, both fission fragments are emitted to forward angles within a cone of 25 deg in this case, whereas the target-like recoil from transfer or inelastic reactions is more likely emitted at higher angles. This recoil is detected by a double sided silicon detector (SPIDER) located downstream after the target, described in Section 2.3.2. Both fragments pass through the central hole of the SPIDER detector and one of them triggers the Start detector, providing a time reference (see Section 2.3.1). This fragment, emitted within the acceptance of VAMOS, is deflected by a magnetic field when moving into the VAMOS spectrometer before being detected at the focal plane setup. The nominal flight path between the target and the focal plane of VAMOS is 7.6 m, varying in $\pm$0.35 m depending on the magnetic rigidity and the emission angle of the fragment. The fusion and transfer reactions introduce excitation energy into the system that promotes the compound nucleus and/or the recoil to excited states that may decay by gamma emission. The fission fragments acquire excitation energy during the fission process that may also be released through gamma emission. These gamma rays can be measured by any of the 6 germanium detectors (EXOGAM) surrounding the target at backward angles (Section 2.3.3). Each of the above-mentioned detectors are reviewed in the following section and they are shown in Fig. 2.2 within the full experimental setup.

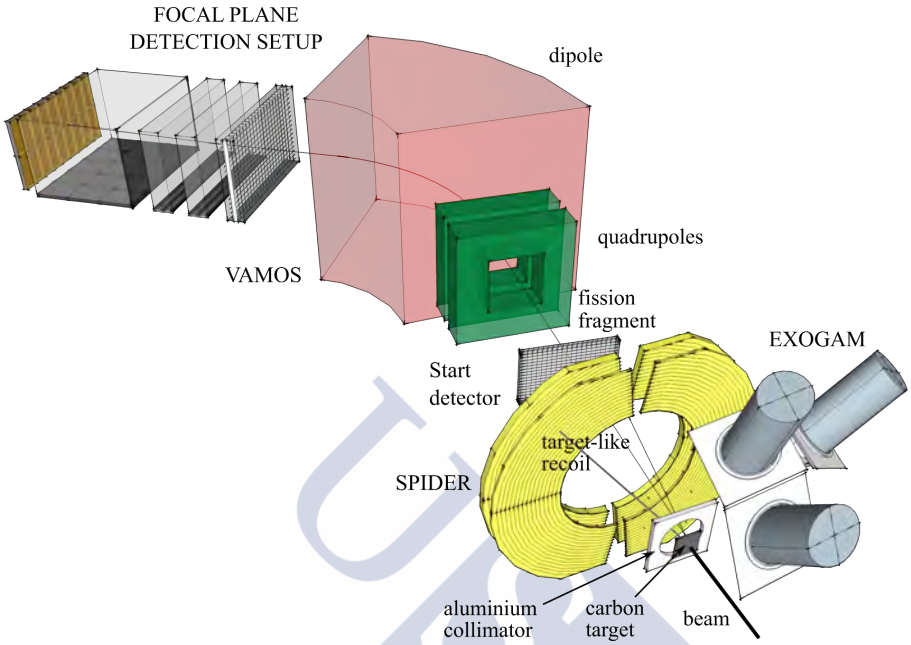

Figure 2.2: Experimental setup scheme. The thick black line on the right side represents the beam that impinges on the target. A transfer reaction is shown followed by a fission decay where the three thin lines represents the target-like recoil and the two fission fragments. The recoil is stopped in the SPIDER detector while one of the fission fragments triggers the Start detector and goes through the VAMOS spectrometer, where it is measured with the focal-plane detection setup. The EXOGAM detector, for γ-rays measurements, is also shown surrounding the target (for clarity, only three EXOGAM detectors are shown).

2.3 Target Position Detection

The experimental setup located at the target region, before the VAMOS spectrometer, includes three different types of detectors: the Start detector is a multi-wire parallel-plate avalanche counter designed for time measurements; the SPIDER detector is a telescope with two annular, double-sided, stripped silicon detectors for light particles measurement and identifica-

tion; the EXOGAM detector is composed of germanium detectors for γ-ray measurements. A detailed description of these detectors is presented in this section.

2.3.1 Start Detector

The Start detector is a multi-wire parallel-plate avalanche counter placed 170 mm downstream behind the target. This detector is composed of three planes of wires; the central one has vertical wires polarized at -500 V while both external planes comprise grounded horizontal wires. The gap between each plane is of 2.4 mm and the active area is of 60 x 60 mm^2. The detector is filled with 5.5 mbar of isobutane gas (iC_4H_{10}). This gas is widely used in gaseous detectors because of its high rate of energy loss per unit of gas pressure, allowing a low pressure operation and thin windows. The gas is isolated from the vacuum of the beam line by two aluminized Mylar windows of 0.9 μm thickness.

When a fragment passes through the detector, it ionizes the gas, releasing electrons that are accelerated by the electric field between the wire planes and the anodes, producing an avalanche; the corresponding ions are collected on the central cathode. The output signal is read from the central wire plane, providing a time reference. The resolution of this measurement reaches 500 ps, improving a factor 2 with respect to the previous experiment, which used the cyclotron frequency as time reference.

2.3.2 SPIDER Detector

The SPIDER (Silicon Particle Identification DEtector Ring) detector provides the energy, the trajectory, and the isotopic identification of the target-like recoil.

SPIDER [31] is a ΔE-E telescope comprising two annular, double-sided stripped silicon detectors with 70 μm and 1042 μm of thickness, separated

4 mm. The front side of each detector is segmented into 16 rings of 1.5 mm pitch. The back side is segmented into 16 radial sectors, each covering an angular range of 22.5 deg. Each detector has a central hole of 48 mm diameter that allow the non-interception of the fission fragments. SPIDER is located 41.5 mm behind the target and covers polar angles between 30 deg and 47 deg. The geometry of this detector is shown in Figure 2.3.

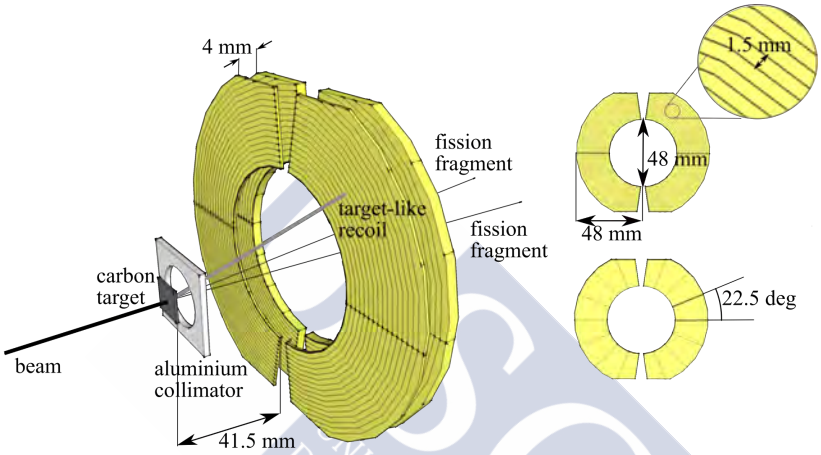

Figure 2.3: Schematic layout of the SPIDER detector. The incoming beam and outgoing products are drawn with lines. The target-like recoil is stopped in the detector and both fission fragments pass through the central hole. The carbon target and the aluminium collimator are also shown.

SPIDER measures the energy loss (ΔE) and the residual energy (E_{res}) of the target-like recoils that punch through the first detector and they are fully stopped in the second one. These two variables provide the isotopic identification of the target-like nuclei. The annular segmentation of the telescope provides a measurement of both polar and azimuthal angle with an uncertainty below 1 deg for the polar angle and $\sim$ 22 deg for the azimuthal angle. In order to avoid the degradation of the measurement with the temperature, a cooling system was used in SPIDER, based on the circulation of liquid silicone at -35 °C that keeps the temperature stable at -1 °C.

An aluminium collimator with a radius of 4 mm was placed 3.5 mm behind the target to avoid that the beam halo impinges on SPIDER. Both the SPIDER and the Start detector, as well as the target and the collimator, are located inside a vacuum chamber that rotates with the spectrometer around the target position.

The interaction of a fast high-Z particle with matter produces δ-electrons that contribute to the noise of the measurements destroying the resolution. In this case, the reaction chamber is surrounded by a magnetic field of 750 G to deflect the δ-electrons created in the interaction of the beam with the target.

2.3.3 EXOGAM Detector

The purpose of EXOGAM, a modular array of germanium detectors [32], in this experiment is to investigate nuclear excitations in transfer reactions by measuring γ-rays emitted by the target-like recoil, and to provide a cross-check of the fission-fragment identification.

The target region is surrounded by six clovers of EXOGAM. Each clover comprises 4 germanium crystal detectors and each crystal is further divided into four different segments, as it is shown in Fig. 2.4. These detectors measure γ-rays with high intrinsic efficiency and high energy resolution.

In this experiment, the EXOGAM crystals are polarized up to 3 kV. They were placed at backward angles, between 120 deg and 150 deg, with a distance respect to the target of 140.5 mm, 160 mm, and 158.1 mm, depending on the orientation.

An efficiency of 22% relative to the absolute efficiency of a 76 x 76 mm^2 NaI detector, and an energy resolution lower than 1.9 keV as full width half maximum for the 1.3 MeV photopeak were measured using a ^{60}Co source placed 250 mm far from the detector [33].

When a γ-ray interacts with the germanium crystal either by photo-

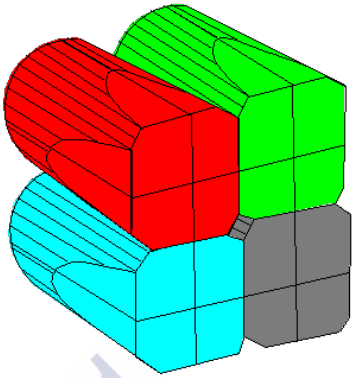

Figure 2.4: Clover of the EXOGAM detector, compound of four independent germanium crystals. Each crystal is segmented into four sections that provide individual signals.

electric effect, multiple Compton effect, or by pair production, it delivers hole-electron pairs as secondary particles. They travel through the detector under the effect of an electric field, creating an electric signal. If the γ-ray is completely absorbed in the detector, this signal is proportional to the energy of the γ-ray as long as all the secondary particles remain inside the detector volume.

Twenty different signals come out of each clover: four of these signals correspond to the central contact of each crystal and they carry a very high energy resolution and timing information. The remaining sixteen signals correspond to outer contacts that indicate the segment where the γ-ray interaction occurs. This segmentation is required to correct the Doppler broadening produced by emission from moving nuclei, and thus to maintain a good energy resolution.

Low temperature is another requirement for an optimal performance of a germanium detector: due to the small bandgap (0.7 eV), a large thermally-induced leakage current would appear when operating at room-temperature, degrading the energy resolution. For this reason, the EXOGAM detector is provided with a cooling system in which a reservoir of liquid nitrogen is kept in thermal contact with the detector.

2.4 VAMOS spectrometer

The VAMOS spectrometer deflects ions attending to their momentum and charge, which provides a well-resolved mass, charge state, and atomic number identification thanks to its detection setup. VAMOS is a large solid-angle, ray-tracing magnetic spectrometer that comprises one magnetic dipole, two magnetic quadrupoles, and one Wien filter (not used) [34, 35, 36, 37, 38]. The aim of the dipole is the ions deflection itself, providing a relationship between the deflection radius and the momentum and charge of the ions. The role of the quadrupoles is focusing the trajectory of the ions. The first quadrupole focuses in y-axis, perpendicular to the plane of dispersion, and the second quadrupole focuses in x-axis, the dispersive axis.

2.4.1 Operational Description

In a magnetic spectrometer, charged particles are deflected under the effect of the magnetic field B of the dipole. The radius of curvature ρ characterizes the deflection of the trajectory. This radius is defined by the equilibrium between two forces: the Lorentz force and the centrifugal force. The definition of *magnetic rigidity* $B\rho$ reflects such equilibrium:

$$B\rho = 3.105 \frac{A}{q} \beta\gamma \propto \frac{p}{q} , \tag{2.1}$$

where β is the velocity in units of light speed, γ is the Lorentz factor, $\gamma = \left(1 - \beta^2\right)^{-1/2}$, A and q are the mass number and the charge state of the fragment, respectively; the proportionality factor 3.105 enables to express $B\rho$ in [Tm] units. The *magnetic rigidity* is then a characteristic of each fragment that relates its momentum and charge state.

In a similar way, the nominal value $B\rho_0$ of the spectrometer can be defined as the *magnetic rigidity* of a particle that is deviated along a reference path, or the central trajectory, once the magnetic field of the spectrometer is fixed. Ions with a magnetic rigidity equal to the nominal value of the

spectrometer describe a central trajectory, while ions with higher $B\rho$ move in more open trajectories and ions with lower $B\rho$, in closer trajectories. The position of the ions after passing through the VAMOS magnetic setup is, therefore, directly related with its $B\rho$. A reconstruction method based on the ion optics of the spectrometer and $B\rho_0$ makes it possible to obtain the $B\rho$ of each ion, event by event, through the measurement of its position and angles at the VAMOS detection plane [36, 39]. A detailed description of the reconstruction method is presented in Section 2.4.3.

The masses of the fission fragments in this work range from A$\sim$80 up to A$\sim$160. The use of a spectrometer allows to achieve sufficient resolution in order to discriminate in mass. In a standard calculation of mass (A) based on the kinetic energy (E) and velocity (v) measurements, the resolution in mass is limited by the resolution in the energy and in the time-of-flight measurements:

$$A \simeq \frac{2E}{v^2} \quad \leftrightarrow \quad \left(\frac{\Delta A}{A}\right)^2 \simeq \left(\frac{\Delta E}{E}\right)^2 + \left(2\frac{\Delta t}{t}\right)^2 \quad \rightarrow \quad \frac{\Delta A}{A} > \frac{\Delta E}{E} \; . \tag{2.2}$$

Concerning the resolution of the energy measurement, this is typically around 0.5-1% in a silicon detector [40] and $\sim$1% in an ionization chamber [41]. These numbers result in $\Delta A/A > 1\%$, limiting the separation between masses to fragments with A$<$100.

By using a spectrometer, the mass resolution is now limited by the time-of-flight and $B\rho$ resolution

$$\left(\frac{\Delta A}{A}\right)^2 \simeq \left(\frac{\Delta B\rho}{B\rho}\right)^2 + \left(\frac{\Delta t}{t}\right)^2 \; . \tag{2.3}$$

The $B\rho$ of fragments is reconstructed based on the position measurement, therefore the $B\rho$ resolution is determined by the resolution in the position measurement and the dispersion of momentum of the spectrometer. The dispersion is a magnitude that quantifies the deviation of a charged particle traveling through a magnetic field ($\delta x/\delta B\rho$). A larger momentum dispersion permits a higher $B\rho$ resolution with a fix position

resolution. The average momentum dispersion in VAMOS was observed to be 1.8 cm/% in the focal plane [36], which places an ion with 1% of difference in $B\rho$ with respect to $B\rho_0$, 1.8 cm away from the center at the focal plane.

In this case, taking into account the time of flight resolution of 500 ps, the position resolution of 270 μm (x) and 350 μm (y) [42] and a dispersion of 1.8 cm/%, it is achieved a mass resolution of 0.3%, which means $\Delta A/A \approx 1/300$. Masses are now well resolved in the range of interest, being the time-of-flight measurement the main limitation in mass resolution.

The angular acceptance of VAMOS is ±100 mrad in the dispersive plane and ±160 mrad in the perpendicular plane [39]. The momentum acceptance is ± 30%. Figure 2.5 presents the solid angle of VAMOS as a function of the relative magnetic rigidity.

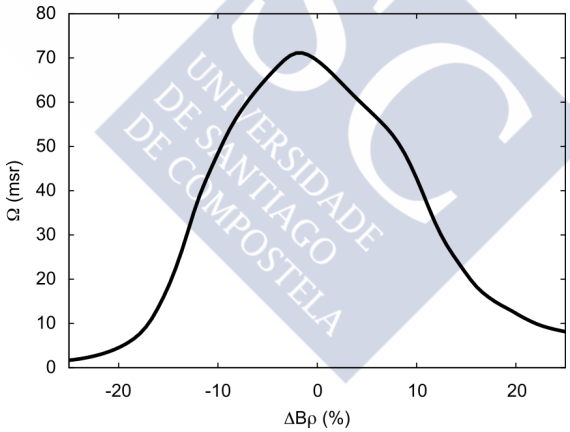

Figure 2.5: Solid angle of VAMOS in [msr] units, as a function of the relative magnetic rigidity, $\Delta B\rho = (B\rho - B\rho_0)/B\rho_0$, in percentage [42].

In this experiment, the spectrometer was used with four different settings in order to increase the acceptance both in $B\rho$ and in angle (see Fig. 2.6). These include two orientations with respect to the beam axis and three nominal values of the magnetic rigidity. Their characteristics are summarized in Table 2.1.

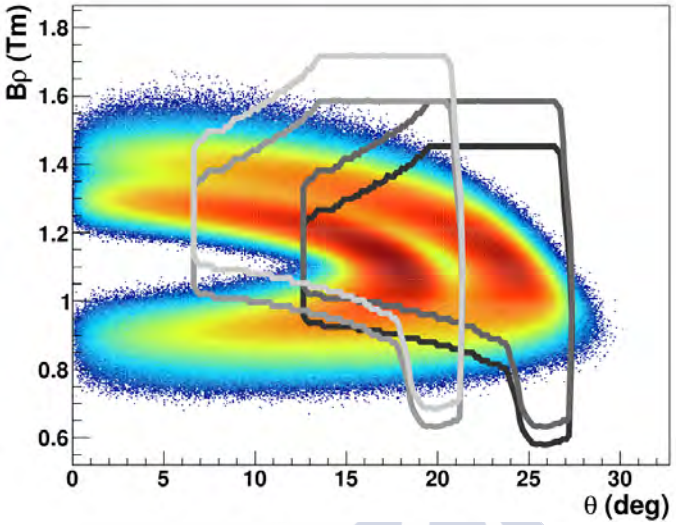

Figure 2.6: Coverage of the VAMOS settings in the $(B\rho, \theta)$ phase space of fission fragments, simulated under the experimental conditions.

Settings of VAMOS		
Setting	**VAMOS angle**	**Bρ_0**
1	20 deg	1.1 Tm
2	20 deg	1.2 Tm
3	14 deg	1.2 Tm
4	14 deg	1.3 Tm

Table 2.1: Summary of the different combinations of orientation of VAMOS with respect to the beam axis and the nominal values of magnetic rigidity used in this experiment.

The selection of the settings was done in order to maximize the acceptance of VAMOS in $B\rho$ and angle in the region of the maximum fission fragments production. Figure 2.6 presents the simulated phase-space of asymmetric-fission fragments in $(B\rho, \theta)$ of a fissioning system that satisfies the conditions of this experiment. The limits of acceptance of the four settings are depicted on top. The combination of the four settings cov-

ers a large range of the phase space of the fragments with certain overlap between them.

2.4.2 Detection system

The detection system at the focal plane of VAMOS allows a complete identification in terms of atomic number, mass, and charge state of fission fragments. The identification procedure is explained in Chapter 4. A description of each detector is detailed in the following.

The central trajectory through the spectrometer defines the z-axis downstream. The focal plane position is defined in this axis at 7600 mm far from the target. The vertical axis, perpendicular to z is tagged as y-axis, and the remaining orthogonal one corresponds to the x-axis.

The experimental setup at the VAMOS focal plane has an active area of 1000 x 150 mm^2. This system is compounded of several detectors that provide different observables of the fission fragments: One multi-wire parallel-plate avalanche counter measures the time of flight of the fragments; two drift chambers, separated by 119.5 mm, measure both positions x and y, and both angles θ and ϕ; one ionization chamber measures the energy loss; and finally, an array of 20x2 silicon detectors measures the remaining energy of the fragments stopped in it. The distance along the z-axis between the objects of the detection system and the target are displayed in Table 2.2.

2.4.2.1 Multi-Wire Parallel-Plate Avalanche Counter

The multi-wire parallel-plate avalanche counter (MWPPAC) measures the time of flight of the fragments between the target and the VAMOS focal plane. This detector is based on the same detection mechanism as the Start detector [42]. It is a large area detector (1000 x150 mm^2) composed of a central cathode with vertical wires and two anodes with horizontal wires.

Distances at the focal plane of VAMOS		
Object		**Distance (mm)**
Mylar Window (0.9 μm)		7610
MultiWire Chamber		7645
Drift Chamber I	Row 1	7810
	Row 2	7850
Drift Chamber II	Row 1	7929
	Row 2	7968
Mylar Window (2.5 μm)		8074
Ionization Chamber	Row 1	8134
	Row 2	8254
	Row 3	8374
Si Wall		8441

Table 2.2: List of distances of the detectors at the focal plane of VAMOS along the central trajectory. These distances are defined with respect to the position of the target.

The cathode plane is separated 2.2 mm from both anodes planes. The cathode is polarized at -450 V and both anodes are grounded. The wires are placed every 500 μm in the cathode and every 1 mm in the anodes. A schematic view of the detector is shown in Fig. 2.7. The MWPPAC is filled with isobutane gas (iC_4H_{10}) at 7 mbar of pressure. A window of 0.9 μm of Mylar isolates the beam line vacuum from the MWPPAC gas. This window is supported by vertical nylon wires of 100 μm diameter, placed every 50 mm.

When a fission fragment passes through the MWPPAC, it produces ionization in the gas. The electrons released in the ionization are accelerated by the field gradient towards the anodes, generating an avalanche, while the corresponding ions are collected on the central cathode. This cathode is segmented into 20 sections that provide 20 independent time signals in order to reduce the capacitance, and thus the rise time of the signals, improving the time resolution. The time resolution achieved with this configuration is 500 ps.

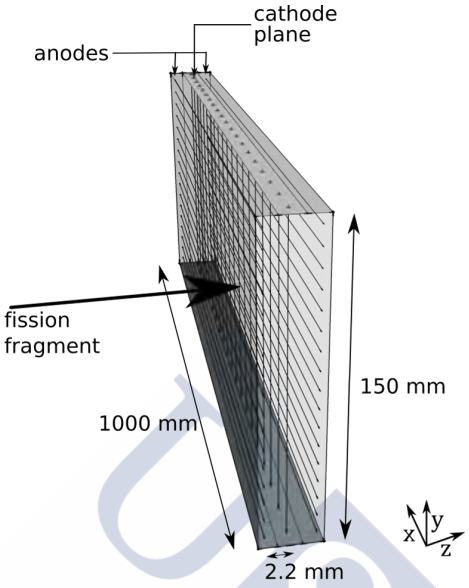

Figure 2.7: MWPPAC detector scheme. The size of the ionization region between the cathode and one anode is specified . Only few wires are shown for a clear view of the detector.

2.4.2.2 Drift Chamber

The drift chamber detector provides a measurement of both positions x and y, perpendicular to the VAMOS axis, as well as both angles θ and ϕ. The drift chamber [36, 42] (DC) is a gaseous detector where two different regions can be identified: the drift volume and the amplification region. The drift region defines an active volume of 1000 x 150 x 100 mm^3 where the primary ionization occurs and the released electrons drift towards the amplification stage. This region is limited by a cathode, placed on the upper ending, polarized at -500V, and a grounded Frisch grid [43], placed on the lower ending.

The Frisch grid is a plane made of conductive wires with a pitch of 2.54 mm. The Frisch grid has two main effects: the height of the pulse becomes

insensitive to the location of the primary ionization and the time resolution improves because only the movement of the electrons is registered, producing a signal with a short rise time.

The amplification region, below the drift region, provides a proportional multiplication of the number of drifted electrons and the readout of the signal they induce. The amplification is produced by a plane of 8 wires, placed 15 mm below the Frisch grid and separated 10 mm from each other. Aditionally, 6 guard wires, placed at the entrance and at the end of chamber, collect the electrons produced at the entrance and exit, protecting the measurements from border effects and improving the time resolution. All these wires are polarized at +475 V.

A grounded cathode plane is placed at the bottom of the amplification region. This cathode is segmented in two rows that cover the dispersive direction (x-axis). Each row is further segmented in 160 pads made of gold-plated strips. Each strip covers 6.02 x 40 mm^2 with a pitch of 6.4 mm. There is an offset of half a strip between rows to reduce the bias due to the position of the pads on the measurements. In addition, both rows are separated by a grounded wall to avoid cross-induction. The 160 pads are read out individually using GASSIPLEX chips [44].

There are six graded potential distribution electrodes along the field direction to ensure a uniform electric field within the drift region. They are regularly spaced with a distance between them of 18 mm. A schematic picture of the detector is shown in Fig. 2.8.

Both DCs and the MWPPAC are placed together without any window in between and filled with 7 mbar of isobutane. At the back face of this ensemble of detectors, a 2.5 μm Mylar window, supported by 32 vertical nylon wires, isolates this lower-pressure gas from the following detectors with higher-pressure gas.

The fast signal that comes from the amplification wires provides the drift time. The y coordinate (in the vertical plane) is determined by the drift time (t_d), referred to the MWPPAC signal (t_0), and the velocity of the electrons in the gas ($v_d = 5.528$ cm/μs) by the relation $y = v_d \cdot (t_d - t_0)$.

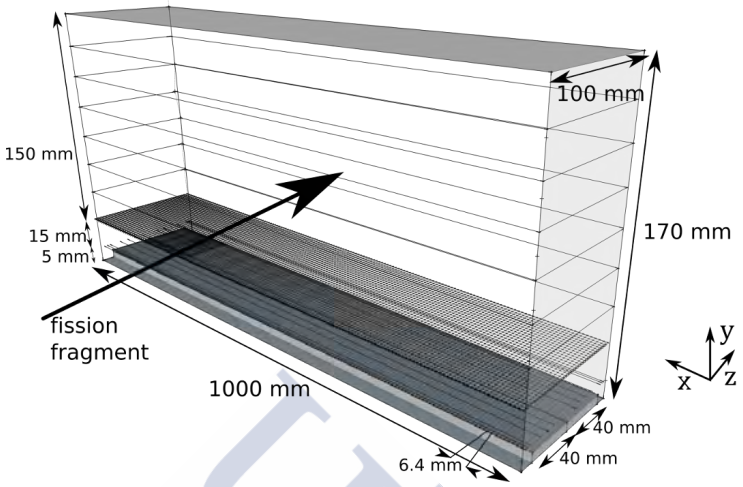

Figure 2.8: Design of the drift chamber detector. The arrow indicates a typical direction of a fission fragment.

The electron avalanche in the amplification region induces a signal on the pads. The charge accumulated in each pad depends on the distance between the pad and the center of the avalanche. The x coordinate (in the dispersive plane) is calculated by a center-of-gravity algorithm that takes into account the relative amplitudes of the induced charge in neighboring pads. This algorithm is detailed in Section 3.2.2.

The DC provides a position resolution of ~ 270 μm in the dispersive plane (x) and ~ 350 μm in the drift plane (y).

2.4.2.3 Ionization Chamber

The purpose of the ionization chamber is to measure the energy loss of the fission fragments in order to determine their atomic number.

The ionization chamber [36, 42] (IC) is based on the standard design consisting on a cathode on the upper part of the chamber, an active volume of 1000 x 150 x 360 mm^3, a Frisch grid that separates this active region

from the amplification region, an amplification grid, placed 10 mm below the Frisch grid, and a segmented anode 20 mm below the Frisch grid.

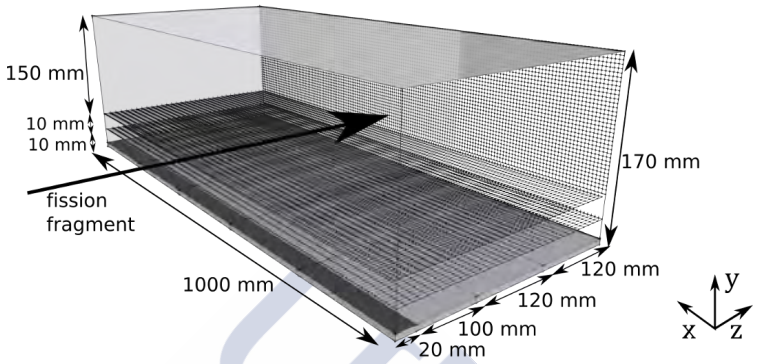

Figure 2.9: IC detector scheme. The vertical grid that ensures a good field homogeneity at the entrance of the detector is hidden to show a clear view of the full detector. The black arrow shows a typical direction of the fission fragments.

Figure 2.9 ilustrates the IC design. The anode is segmented into 3 rows along the flight path of the fragments, with each row further segmented into 5 pads. One additional row is placed at the entrance of the chamber with a length of 20 mm that acts as a guard circuit to collect δ-electrons created in the Mylar window placed between the IC and the DC. The area of the first row is 1000 x 100 mm^2 while the second and third rows are 1000 x 120 mm^2. At the entrance of the first row and at the exit of the last row, a grid of 2.54 mm pitch wires is placed between the cathode and the Frisch grid to ensure a good field homogeneity in the drift volume.

The IC is filled with isobutane gas (iC_4H_{10}) with a pressure of 40 mbar. The optimal configuration in order to have high signal keeping the proportionality under such pressure was found to be with the cathode polarized at -900 V, the Frisch grid grounded, the amplification grid polarized at +120 V, and the anode at +360 V.

The energy loss of a heavy charged particle passing through matter

with moderate energies ($0.05 \leq \beta\gamma \leq 1$) is well described by the *Bethe-Bloch equation* [45]:

$$-\frac{\mathrm{d}E}{\mathrm{d}x} = K\, z^2\, \frac{Z}{A}\, \frac{1}{\beta^2} \left[\ln \frac{2m_e c^2 \beta^2 \gamma^2}{I} - \beta^2 \right] , \tag{2.4}$$

where z and β are the charge and the velocity of the charged particle, Z and A are the atomic and mass numbers of the matter, I is the *mean excitation energy* of the matter, and $K = 4\pi N_A r_e^2 m_e c^2$, being $N_A = 6.022{\cdot}10^{23}$ mol^{-1} the Avogadro's number, $r_e = 2.8179$ fm the classical electron radius, and $m_e = 0.511$ MeV/c^2 the electron mass. In the case of compound elements, such as iC_4H_{10}, effective values are defined as

$$\begin{aligned} \left(\frac{Z}{A}\right)_{eff} &= \sum_j \omega_j \frac{Z_j}{A_j} , \\ \ln I_{eff} &= \frac{\sum_j \omega_j (Z_j/A_j) \ln I_j}{\sum_j \omega_j (Z_j/A_j)} , \end{aligned} \tag{2.5}$$

where $\omega_j = \frac{n_j A_j}{\sum_k n_k A_k}$, being n_j the number of the j^{th} kind of atom in the compound. For the case of isobutane $\left(\frac{Z}{A}\right)_{eff} = 0.586$ and $I_{eff} = 48.3$ eV.

For a small range of interaction, where the variation in the charged particle velocity is small, the component of the Bethe-Bloch equation within the square brackets remains mainly constant. In such a range, there is a simple relation between the energy loss and both the charge and the mass of the fragment

$$-\frac{\mathrm{d}E}{\mathrm{d}x} \propto \frac{z^2}{\beta^2} = \frac{M z^2}{2E} \longrightarrow \left|\Delta(E^2)\right| \lesssim z^2 M \Delta x \, . \tag{2.6}$$

Furthermore, there is a relation between the mean charge of a particle traveling a layer of matter with a certain velocity and its atomic number.

The proportionality between $\Delta(E^2)$ and $z^2 M \Delta x$ changes inside the ionization chamber as the particles are slowing down, but the relation

between both quantities remains valid, except in the region close to the *Bragg Peak*, a region of low energy where the energy loss is maximum. In this region, the velocity and effective charge of the particle varies very fast and the relation between energy loss and z becomes more complex.

As previously discussed, a fragment passing through the gas of the IC loses energy mainly by releasing electrons from the atoms of the gas. The number of released electrons is roughly proportional to the energy loss of the fragment. These electrons induce charge in the pads when they pass through the acceleration region. The voltages of the IC are chosen as a compromise between a large amplification, increasing the intrinsic resolution, and a proportional amplification between the energy loss in the primary ionization and the induced charge in the pads, preventing discharges inside the gas. In this way, the signal collected in the pads is proportional to the energy loss of the fragment.

The pressure of the ionization chamber defines the resolution of the nuclear charge. Figure 2.10 presents a *MonteCarlo* simulation of the energy loss, based on the *TRansport of Ions in Matter (TRIM)* code [46], as a function of the total energy of ^{111}Rh and ^{108}Ru, for two gas pressures in the ionization chamber. Higher pressure provides larger separation between ion species, but the *Bragg Peak*, where the separation disappears, is manifested at higher energies. The pressure of the ionization chamber was chosen as a compromise between having a large ionization, increasing the nuclear charge resolution, but not too large to shift the *Bragg Peak* to high energy or to stop fragments inside the IC.

2.4.2.4 Wall of Silicon detectors

An array of 20 x 2 silicon detectors completes the setup at the focal plane of VAMOS. They are in charge of the measurement of the remaining energy of the fragments. Each detector has a thickness of 500 μm and an area of 50 x 80 mm^2 [36, 42], with 2 mm of dead gap at the edge. This array provides an active area of 1000 x 160 mm^2. The silicon array is placed after the IC without any window in between. Figure 2.11 shows the silicon

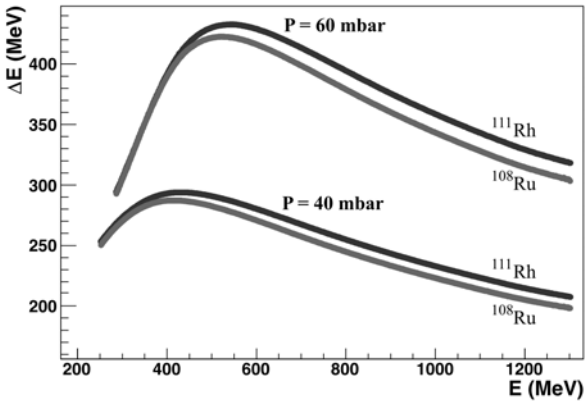

Figure 2.10: Simulated IC energy loss, as a function of the total energy, of ^{111}Rh and ^{108}Ru, for two gas pressures, 40 and 60 mbar.

array scheme.

In a silicon-lattice material, electrons are promoted from the valence to the conduction band when a charge particle passes through. This process releases electron-hole (*e-h*) pairs along the track of the particle. The *ionization energy* needed to produce one *e-h* pair is observed to be largely independent of both the energy and type of the incident radiation. This property relates the number of *e-h* pairs produced with the incident energy of the charged particle, provided the particle is fully stopped within the active volume of the detector.

A silicon detector is based on the junction between two types of doped silicons: a *n-type* silicon with a larger number of *donor impurities*, and a *p-type* silicon with a larger number of *acceptor impurities*. The charge equilibrium in the n-p junction is achieved after charge migration from one to the other size of the junction creating a electric field in the surrounding region (*depletion region*) [47].

When a charged particle passes through the silicon detector, the *e-h* pairs produced in the *depletion region* move under the effect of the electric

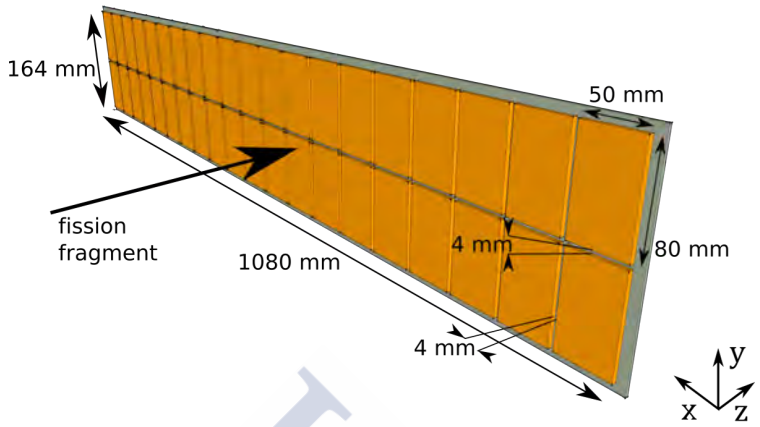

Figure 2.11: Scheme of the wall of silicon detectors.

field producing a signal proportional to this number of pairs. In order to make the signal proportional to the total number of *e-h* pairs produced in the full active volume, and therefore proportional to the energy released in the detector, a reverse bias voltage is applied to the detector, making the *depletion region* cover the full active volume. The bias voltage applied in this case is 25 V.

The range R of a particle is defined as the distance that the particle travels in matter until it is fully stopped, releasing its total energy in the matter. In this detector, a fission fragment will be fully stopped when its range is smaller than the thickness of the *depletion region*. Lighter fragments at higher energy present larger ranges, as it is extracted from Eq. 2.6,

$$R \propto \frac{E^2}{z^2 M} \ . \tag{2.7}$$

The maximum kinetic energy achieved by any fragment in this experiment is lower than 1500 MeV and the lightest fragment produced is Z∼30 and A∼80. A simulation based on the TRIM code shows a range of R=280 μm for this fast-light fragment, therefore all the fragments are fully stopped in the array of 500μm-thickness silicon detectors.

Each silicon detector is read out individually through a charge preamplifier with 2 mV/MeV sensitivity. The energy resolution for the detectors was found to be ∼60 keV (FWHM) with an alpha source.

2.4.3 Reconstruction Algorithm

The effect of the magnetic field inside the spectrometer on the trajectory of the ions defines a relation between the characteristics of the ions before passing through the spectrometer and the final transversal position and angles at the focal plane, (x_{fp},θ_{fp},y_{fp},ϕ_{fp}).

In an ideal spectrometer the position at the focal plane is given by a simple function of the characteristics of the incoming ion, such as its momentum and charge. However, the large size of VAMOS produces inhomogeneities on the magnetic field that acts on the incoming particles, making this relation more difficult to describe. In order to map the relationship between the characteristics of the ion before and after the action of the magnetic field, the VAMOS reconstruction method uses a numerical procedure with a polynomial relation between the measured positions and angles and the focal plane, and the reconstructed observables: the magnetic rigidity ($B\rho$), both angles before the spectrometer (θ and ϕ), and the path length of the ion ($Path$). The reconstruction algorithm used in VAMOS [39] is built in two steps: trajectory simulation and back-tracing reconstruction. The trajectory simulation is performed using *Zgoubi* [48], a multi-particle tracking code that simulates the trajectories of the particles inside VAMOS following measured maps of the magnetic fields of VAMOS. *Zgoubi* simulates, by ray-tracing, a set of 2000 trajectories covering the full acceptance, and provides a multi-dimensional matrix with the values of the initial $(\delta, x, \theta, y, \phi)$ and final parameters $(x_{fp}, \theta_{fp}, y_{fp}, \phi_{fp}, l)$. The parameter $\delta = (B\rho - B\rho_0)/B\rho_0$ is the fraction of deviation of magnetic rigidity from the reference one, x and y correspond to the transversal distances from the reference trajectory at the target position, $(x_{fp}, \theta_{fp}, y_{fp}, \phi_{fp})$ are horizontal and vertical positions and angles at the focal plane, and l is the difference in path length between the given and the reference path.

The back-tracing reconstruction is defined with a polynomial relation between the focal plane positions and angles, and the observables to be reconstructed:

$$\begin{aligned}
\delta &= \sum_{i,j,k,t=0}^{i+j+k+t=7} C^{(\delta)}_{ijkt} \cdot x^i_{fp} \cdot \theta^j_{fp} \cdot y^k_{fp} \cdot \phi^t_{fp} \ , \\
\theta &= \sum_{i,j,k,t=0}^{i+j+k+t=7} C^{(\theta)}_{ijkt} \cdot x^i_{fp} \cdot \theta^j_{fp} \cdot y^k_{fp} \cdot \phi^t_{fp} \ , \\
\phi &= \sum_{i,j,k,t=0}^{i+j+k+t=7} C^{(\phi)}_{ijkt} \cdot x^i_{fp} \cdot \theta^j_{fp} \cdot y^k_{fp} \cdot \phi^t_{fp} \ , \\
l &= \sum_{i,j,k,t=0}^{i+j+k+t=7} C^{(l)}_{ijkt} \cdot x^i_{fp} \cdot \theta^j_{fp} \cdot y^k_{fp} \cdot \phi^t_{fp} \ .
\end{aligned} \tag{2.8}$$

The coefficients of the polynomial functions, $C^{(\delta)}$, $C^{(\theta)}$, $C^{(\phi)}$, $C^{(l)}$, are determined from a fitting to the set of the trajectories computed by *Zgoubi*.

In order to improve the method accuracy, the full VAMOS acceptance is decomposed into small regions where the set of coefficients of Eq. 2.8 are calculated locally, by means of a third-order polynomial interpolation of the nearest simulated trajectories. The reconstruction method is applied, event by event, once the values of the set of coefficients are defined off-line.

2.5 Electronics

This section describes the electronic layout of the experiment in two components: the analogical electronic circuit in charge of collecting and processing the analogical signals that come from the detectors, and the logical electronic circuit that defines the logical trigger signals.

Three types of reactions are produced and studied in this experiment: elastic scattering between the ^{238}U beam and the ^{12}C target, fusion-induced fission of the compound nucleus ^{250}Cf, and transfer-induced fission. The trigger system is designed to distinguish these three types of events.

Elastic scattering reactions produce a target-like recoil emitted at large angle and a beam-like scattered forward emitted; the recoil is detected in SPIDER while the beam-like scattered is not measured. The *trigger SPIDER*, defined as the signal of the sectors of the second detector of SPIDER in anti-coincidence with signal from the MWFP of VAMOS, registers this type of reactions, as well as transfer reactions and transfer-induced fission were both fragments are not detected.

Fusion-induced fission reactions yield two fission fragments and no target-like recoil. One of the fragments, if within the VAMOS acceptance, is detected in the focal plane of VAMOS. The *trigger VAMOS*, designed as the coincidence between the signals from both MW, and no signal in SPIDER, identify this type of reactions, but also includes transfer-induced fission where the recoil is not detected.

Transfer- and scattering-induced fission reactions result in one target-like recoil and two fission fragments. When the recoil is detected in SPIDER and one of the fragments is detected in VAMOS, the coincidence between the signal of sectors of SPIDER and the coincidence between both MW of VAMOS defines the *SPIDER-VAMOS trigger* tagging the transfer- and scattering-induced fission events.

The signals that conform the different triggers need to be synchronized in order to perform the coincidence and anti-coincidence events. The synchronization is achieved by means of time delays applied to the primary signals. A detailed discussion of the three trigger signals is presented later in this section.

The logic trigger signals are controlled by the *Ganil Master Trigger (GMT)* module [49]. When this module receives a trigger signal, it generates a *Fast Analysis Gate (FAG)* signal that starts the data readout. The processing and storage of the data is handled by the *GANIL Data*

Acquisition System (DAS).

The analogic circuit is further split in two parts based on the investigated reaction: the first part describes the analogic electronics of the SPIDER detector, dedicated to measure the target-like recoil nucleus that comes from scattering and transfer reactions; the second part describes the analogic electronics of the detectors placed at the focal plane of the VAMOS spectrometer, focussed on the fission-fragment identification.

The SPIDER detector is divided into four sources of signal: the rings (dE_r) and sectors (dE_s) of the first silicon detector that provide the energy loss in the detector, and the rings (E_r) and sectors (E_s) of the second silicon detector that provide the remaining energy of the nucleus. Every signal is primary amplified by a *Pre-amplifier (PA)* module and further amplified by a *Spectroscopic Amplifier (AMP)* module. Each individual analogic signal from the AMP is sent to a *Analogical to digital Converter (ADC)* module, where the signal is digitized and sent to the acquisition. Each AMP module also provides a common fast logical signal that is accepted in a *Discriminator (DISCRI)* and sent to a *Gate & Delay Generator* module that introduces 1.2 μs of delay. This delayed signal, in coincidence with a *validated FAG*, starts the readout of the ADC.

The *SPIDER trigger* comes from the sectors of the second detector (E_s). The logic output of the AMP module is sent to a *FAN-IN FAN-OUT (FIFO)* module that produces a 200 ns-width NIM signal that defines the trigger signal (OR SPIDER). This signal is also used to validate the FAG by means of the coincidence between this signal, with 450 ns of delay, and the 200 ns-width FAG signal. Figure 2.12 shows a diagram of the electronic setup of the SPIDER detector.

The *ToF* of the fragments comes from the measurement in both multiwires (MWT & MWFP). The 20 signals from the MWFP are amplified in a pre-amplifier and further amplified in a *Timing Filter Amplifier (TFA)* module. Every signals is accepted in a *Constant Fraction Discriminator (CFD)* module and sent to a *Time to Digital Converter (TDC)* module. The individual signal from the MWT produces a logic signal in a CFD that is then delayed in 650 ns. This signal is transformed into a 40 ns-width

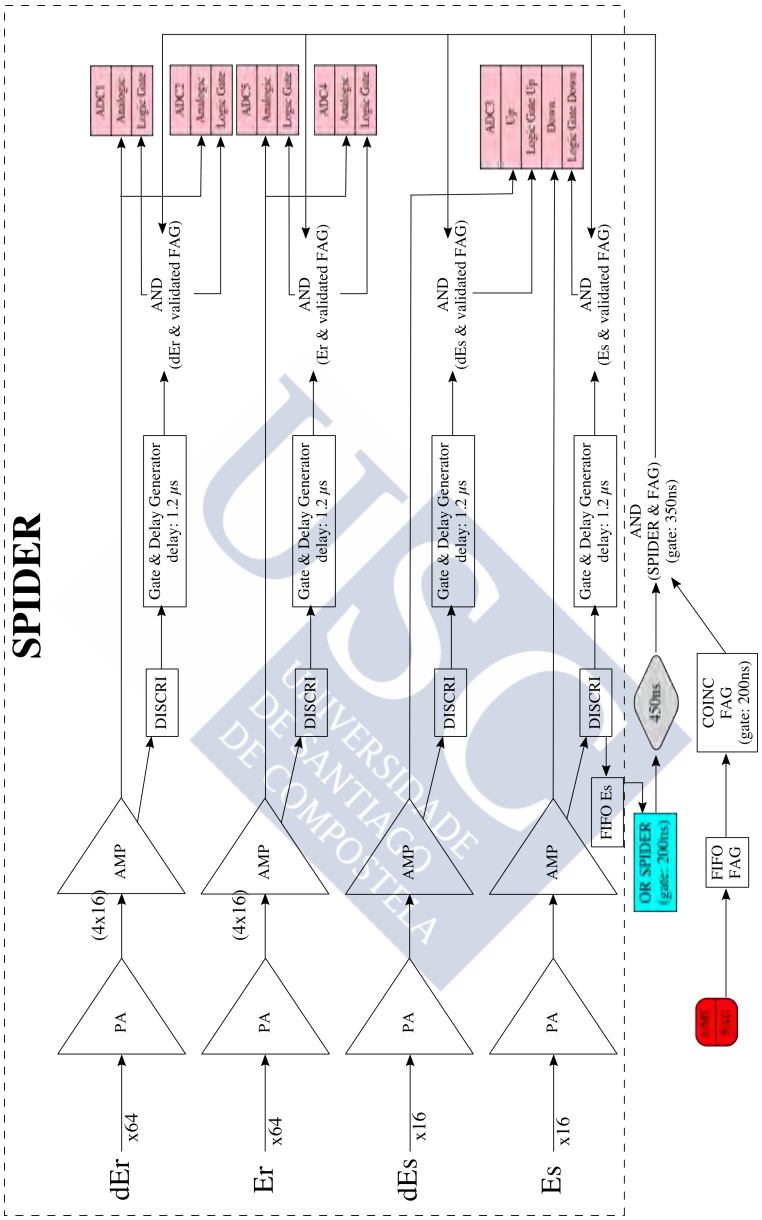

Figure 2.12: Electronic scheme of the SPIDER detector.

signal and sent to the TDC as the gate of the module. The signal from the TDC is sent to the acquisition.

The Drift Chambers provide two main observables: X and Y positions. The position of the fragments in the vertical plane (Y) comes from the signals of the wires and the position in the dispersive plane (X) comes from the charge induced in the pads. The wires provide also a measurement of the energy loss inside the chamber.

The signal from the wires is amplified in a PA and divided into two signals. One of the signals is amplified in an AMP and digitized in an ADC, where the FAG signal triggers the readout. This signal provides the energy loss in the chamber. The other signal is amplified in a TFA, accepted in a CFD and delayed in 564 ns. This signal makes a coincidence with a 10 μs-width FAG signal that inhibits the arrival of any other trigger during the readout process. Three signals come out of the coincidence module: one signal defines a *Dead Time* during which the acquisition is stopped (TGV); the second signal starts the pads-readout process; the last signal, delayed in 550 ns, stops a *Time to Amplitude Converter (TAC)* module (TWIRE), which is started by the MWFP signal validated by the FAG signal. This module provides the drift time of the electrons in the chamber, which is proportional to the position of fragment in the vertical plane.

The charge induced in the pads is measured by the Gassiplex chips in a *Track & Hold* procedure. The signal of the wires, through the *CAEN Readout for Analog Multiplexed Signals (C-RAMS)* sequencer, triggers a *Track* signal that makes the chips to record the maximum charge induced in each pad in a sequential way. During the *Hold* time, these chips store these values and send them to the acquisition. Once this process finishes, the sequencer commands a cleaning process and the chips recover their original values, being ready for a new event. The read out of the DC pads is the largest contribution to the *Dead time*, which is processed by the *Ganil Acquisition Module for Electronics Resources (GAMER).*

The IC and the wall of silicons measure the energy loss and the remaining energy, respectively. The electronic setups in both cases are similar.

The signals from the detectors are amplified in a PA, further amplified in an AMP, digitized in an ADC module, and sent to the acquisition. In the case of the wall of silicons, the AMP provides a fast signal that is accepted in a CFD and starts the ADC readout. In the case of the ionization chamber, the AMP does not provide a fast signal; the trigger of the ADC module comes from the PA, is amplified in a different AMP, and accepted in a discriminator. A gate generator and a translator NIM-ECL are used to convert the output of the discriminator in the type of signal (ECL) accepted by the ADC module.

Figure 2.13 shows a diagram of the electronic setup of the detectors related with the measurement of fission fragments. The components filled in blue indicate the nodes where signals are sent to the GMT module and form the logical trigger signals.

The electronic setup of the trigger signals is presented in Figure 2.14. The signals from the detectors are sent to the GMT module, which handles the definition of the trigger, the *Dead time*, and the FAG signal.

The *SPIDER trigger* comes from the common output of the sectors in the second detector. Due to the large cross section of the elastic scattering (417 mb measured in the angular range covered by SPIDER detector [31]), the signal is sent to a *Divider module* that admits only one event every 300, preventing a long *Dead time* in the acquisition system. The output of the *Divider module* is delayed in 200 ns and sent to the GMT module.

The *VAMOS trigger* is defined as the coincidence between the 300 ns-delayed signal from the MWT and the signal from the MWFP. The output of the coincidence is further delayed in 250 ns and sent to the GMT module.

A third trigger is defined as the coincidence between the *SPIDER trigger* and the *VAMOS trigger*. The output of the coincidence between the 100 ns-delayed signal from SPIDER and the 300 ns-delayed signal from the MWT is further delayed in 150 ns. This signal makes a new coincidence with the signal from the MWFP that is sent to the GMT module and defines the *SPIDER-VAMOS trigger*. The different delays are applied in

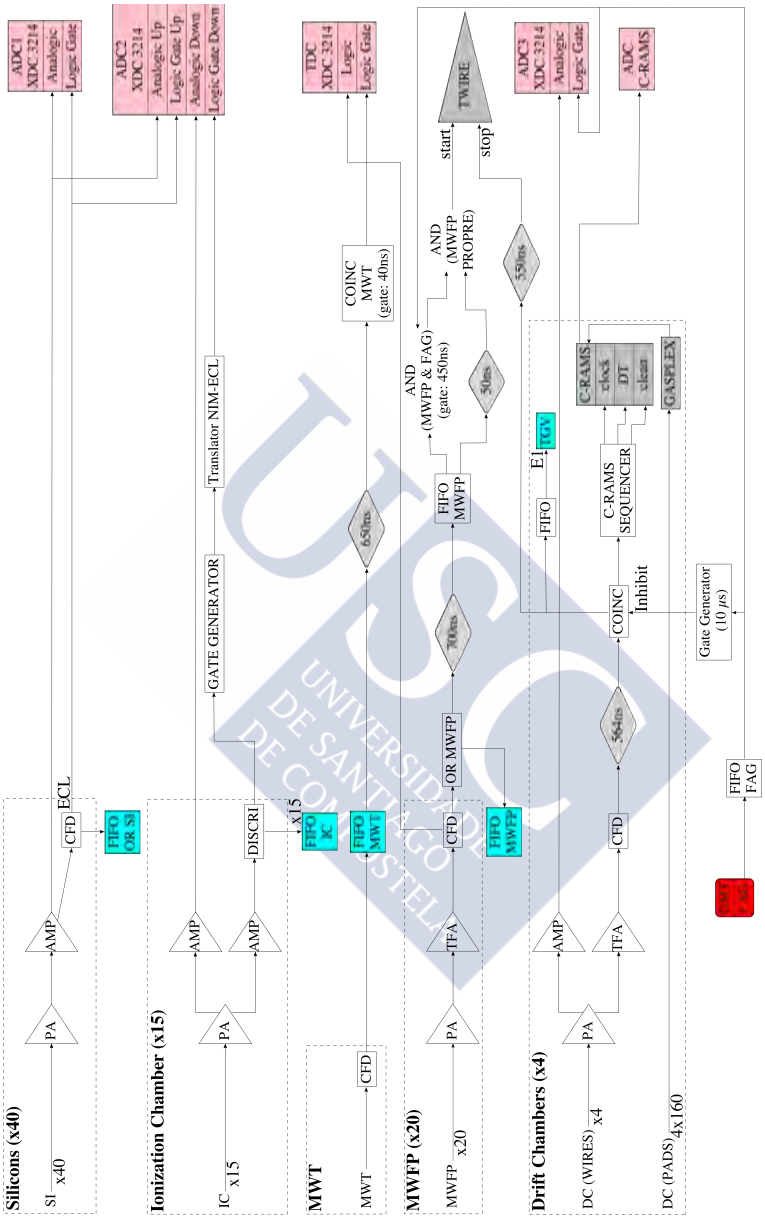

Figure 2.13: Electronic scheme of the VAMOS detectors.

order to synchronize all the signals.

Signals from the wall of silicons, the IC, and the EXOGAM detector are also sent to the GMT module. These trigger signals are redundant with the previous or not needed for the experiment purposes. They are software-disabled during the real experiment and only enabled for calibration runs.

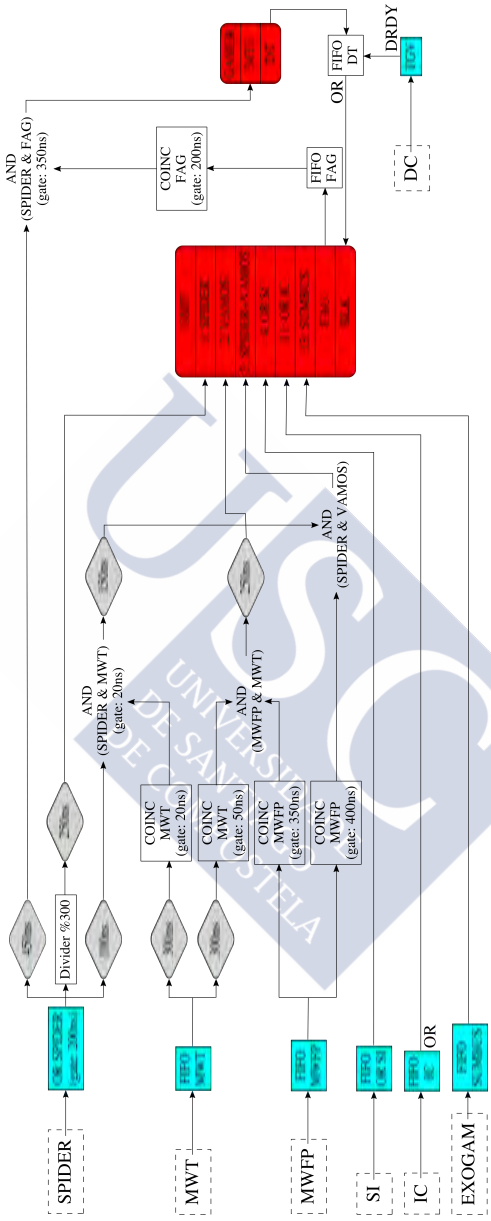

Figure 2.14: Scheme of the logical electronic setup.

USC
UNIVERSIDADE
DE SANTIAGO
DE COMPOSTELA

Chapter 3

Detectors Calibration

This chapter explains the treatment of the signals taken from the detectors involved in the fission fragment identification. It begins with a general description of the calibration methods applied to the data and continues with the explanation of the specific calibration of each detector in the VAMOS focal plane setup.

3.1 General Procedure

The general procedure of the calibration consists in a first alignment of the electronic treatment of the detectors. A physical calibration is applied afterwards using elastic scattering of ^{238}U in ^{197}Au. The last step consists in applying corrections to take into account the different behavior of the fission fragments compared with the products of elastic scattering.

The alignment of the electronics is done by means of a pulse generator. The pulse generator sends signals to every detector channel simulating a physical event with different amplitudes. The alignment procedure makes the output signal of every channel to be equal each other for the same amplitude.

The elastic scattering reaction is used to convert the output signal of the detectors into physical observables. A ^{238}U beam at 6.14 MeV/u impinging on a gold target produces the elastic scattering channel (^{238}U

+ ^{197}Au $\rightarrow$ ^{238}U + ^{197}Au). This reaction covers a large angular range in the laboratory framework, as it is shown in Fig. 3.1. The VAMOS spectrometer is centered at 20 deg with respect to the beam axis, where the energy of the scattered particles ($E_U = 1246$ MeV, $E_{Au} = 1270$ MeV) is large enough to be measured by the detection system at the focal plane.

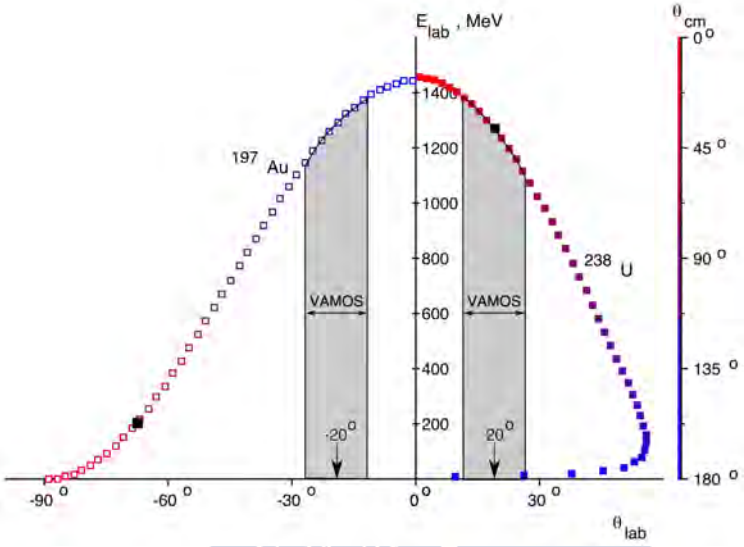

Figure 3.1: Kinematics of the elastic scattering of ^{238}U + ^{197}Au. Grey regions indicate the angular coverage of VAMOS.

Figure 3.2 shows the differential cross section of elastic scattering as a function of the angle on the laboratory framework. ^{238}U is more produced than ^{197}Au in two orders of magnitude for angles around 20°. Therefore, the calibration procedure is based on ^{238}U data.

3.2 Drift-Chamber Pads Calibration

The Drift Chamber, as it was explained in Section 2.4.2.2, is a gaseous detector that provides a measurement of the position of the ions passing through the chamber in both, horizontal and vertical axis, as well as the

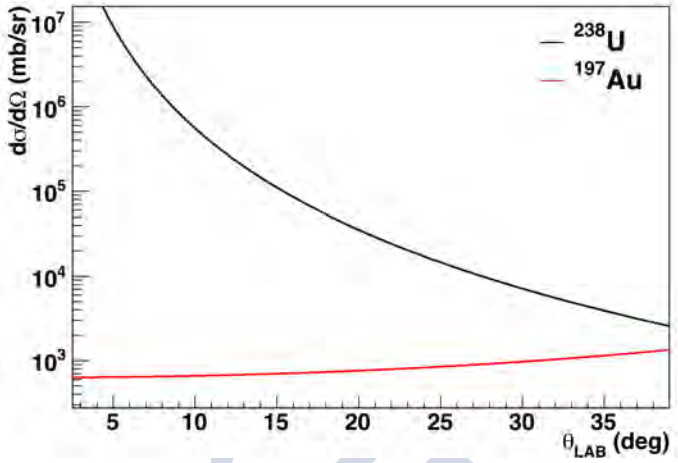

Figure 3.2: Differential cross section for the elastic scattering of ^{238}U + ^{197}Au as a function of the angle on the laboratory framework. Calculated following the Rutherford approach [50].

corresponding angles. The horizontal position is determined by the center of the charge distribution induced in two horizontal rows of pads, while the vertical position is determined by the drift time of the electrons inside the chamber. As explained in section 2.4.3, both positions, and the corresponding angles, are used by the reconstruction algorithm to obtain the magnetic rigidity ($B\rho$) and both polar and azimuthal angles of the ions before the spectrometer.

The induced charge distribution is calculated in terms of charge ratios between neighboring pads, therefore, a good calibration between them is required. An external reference is also needed to ensure an absolute measurement of the vertical drift, independent of the position of the chamber. This reference is provided by the silicon wall.

3.2.1 Induced Charge Calibration

A pulse generator sends signals to the electronics of every pad simultaneously. Six signals with different amplitudes are used in this case. The alignment procedure takes the pad number 67 of the first row as an arbitrary reference and defines a function that aligns the signal amplitude of the others pads: $Q_i^{align} = A_i + B_i \cdot Q_i + C_i \cdot Q_i^2$, where Q_i is the signal amplitude of the pad number i, (A_i, B_i, C_i) are the alignment parameters, and Q_i^{align} is the amplitude signal once it is aligned.

Figure 3.3 shows the output signals of each pad. The left and right columns show the output signal before and after the alignment, respectively. The two first rows correspond to the first drift chamber, the two last rows correspond to the second drift chamber. Most of the pads show a seventh line at very low amplitude corresponding to the pedestal, which is the response of the detection system when no input signal is present. This pedestal defines the zero detection and needs to be subtracted. After the alignment, the pedestal is unique for all the pads.

Each Gassiplex chip provides a gain in amplitude to the output signals. Each chip handles 16 channels at the same time providing the same gain to all of them. However, this gain may change from one chip to the other due to a different response of the chip itself or due to a slight difference in the bias potential applied to each chip. Therefore, once the alignment is done, a gain matching procedure is required.

The gain matching is a two-steps procedure. The first step consists in a matching in charge of each two consecutive pads when each of these pads is handled by a different chip. Figure 3.4 shows the largest induced charge per elastic scattering event of ^{238}U in ^{197}Au in four consecutive pads of the second row of the first drift chamber. There is a large difference between the pad 96 and 97, which are read by different chips.

The gain matching also applies one single scaling factor (A^{chip_j}) to the output of the pads handled by one Gassiplex chip making that the last pad of one chip shows the same maximum induced charge than the first pad of

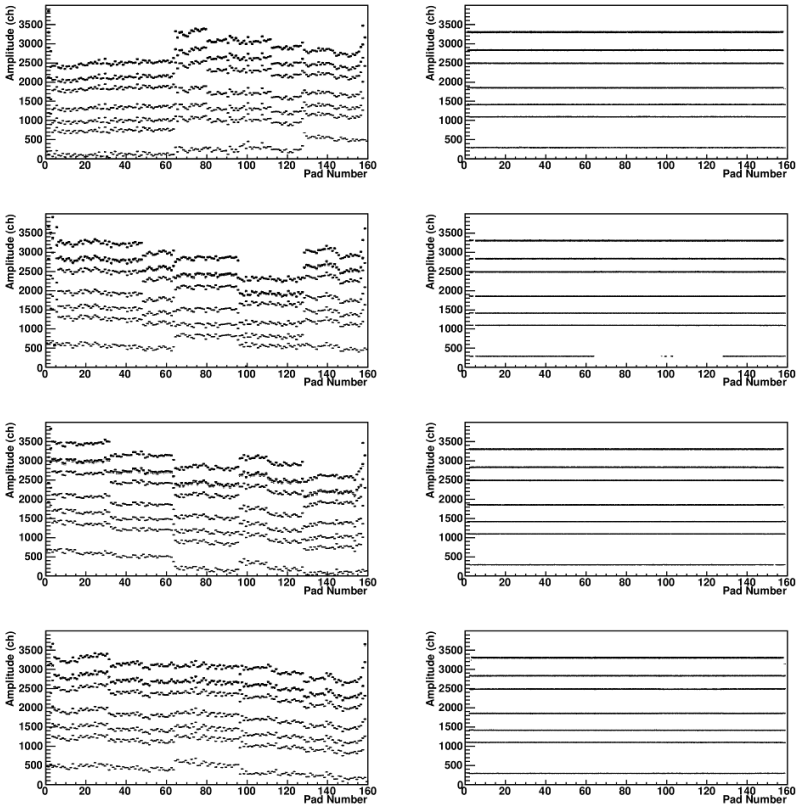

Figure 3.3: Alignment of the pads of the Drift Chamber. Left and right columns show the output signals before and after the alignment. The lower signal corresponds to pedestal, which is not present in some of the pads of the second row due to a too high threshold. The rest of the signals come from a pulse generator with different attenuation factors.

the next chip, $A^{chip_j} = \overline{Q}^{chip_{j+1}}_{MAX}(FirstPad)/\overline{Q}^{chip_j}_{MAX}(LastPad)$. This way, the gain-matched induced charge follows next equation $Q_i^{gain\ match}|_{chip_j} = A^{chip_j} \cdot Q_i^{align}|_{chip_j}$.

The second step consists in a local smoothing method that removes small fluctuations produced by field inhomogeneities. Such fluctuations

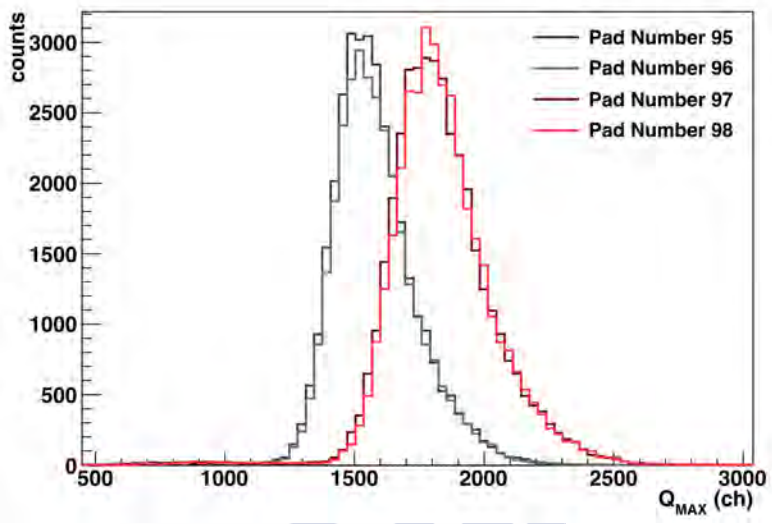

Figure 3.4: Distribution of the maximum induced charge per event of elastic scattering of ^{238}U in ^{197}Au in four consecutive pads of the second row of the first drift chamber. A further gain matching procedure is required between pad 96 and 97.

are more prominent in the second drift chamber. This method is applied over elastic scattering events. It scales the maximum induced charged of one pad by using the neighboring pads as a reference, by means of a binomial smoothing filter [51]:

$$\overline{Q}_{MAX}^{smooth}(i) = \sum_{k=-1}^{1} b_k \cdot \overline{Q}_{MAX}^{gain\ match}(i-k)\ ,$$
$$b_k = \binom{2}{1+k}/4\ , \tag{3.1}$$

$\overline{Q}_{MAX}^{gain\ match}(i-k)$ is the mean value of the maximum induced charge in the pad number $(i-k)$, after the gain matching procedure; and $\overline{Q}_{MAX}^{smooth}(i)$ is the mean value of the maximum induced charge in the pad number i, once the smoothing method is applied.

Therefore, the scaling factors that remove the fluctuations are defined as $A_i^{smooth} = \overline{Q}_{MAX}^{smooth}(i)/\overline{Q}_{MAX}^{gain\ match}(i)$

Figure 3.5 shows the maximum induced charge per event as a function of the pad number for elastic scattering events. the left and right column present the situation before and after the gain matching procedure, respectively. A deep valley is observed in channels around 80 for the second drift chamber. This valley is the shadow of a vertical bar that supports the structure, placed in between both drift chambers and must not be corrected.

The total calibration of the induced charge [1] on the drift chamber pads is summarized as follows:

$$Q_i^{cal} = A_i^{smooth} \cdot A^{chip_j} \cdot (A_i - Offset + B_i \cdot Q_i + C_i \cdot Q_i^2)\ , \qquad (3.2)$$

where Q_i and Q_i^{cal} are the raw and the calibrated induced charge in the pad number i, (A_i, B_i, C_i) are the alignment parameters, $Offset = 292$ is the pedestal, and $(A_i^{smooth}, A^{chip_j})$ are the scaling factors of the gain matching procedure.

The gain matching factors are not unique all along the experiment. The power supply system of the Gassiplex chips was rebooted several times along the experiment and every time it happened, the gain applied to the chips might have slightly changed and, therefore, also the gain matching factors (A^{chip_j}). This fluctuation ranges from -2.7% to $+8\%$. A new gain matching procedure is required every time the power supply is rebooted. In these cases, no elastic scattering data is available, so the gain matching is done directly using fission events.

The calibration parameters on the induced charge in the pads of the drift chambers are now dependent on the experimental run number. Figure 3.6 shows the induced charge per pad, produced by fission-fragment

[1] Notice that this calibration process is, in fact, an alignment procedure, where the correspondence between ADC channels and energy is not needed. The nomenclature reflects only the difference respect to the electronic alignment.

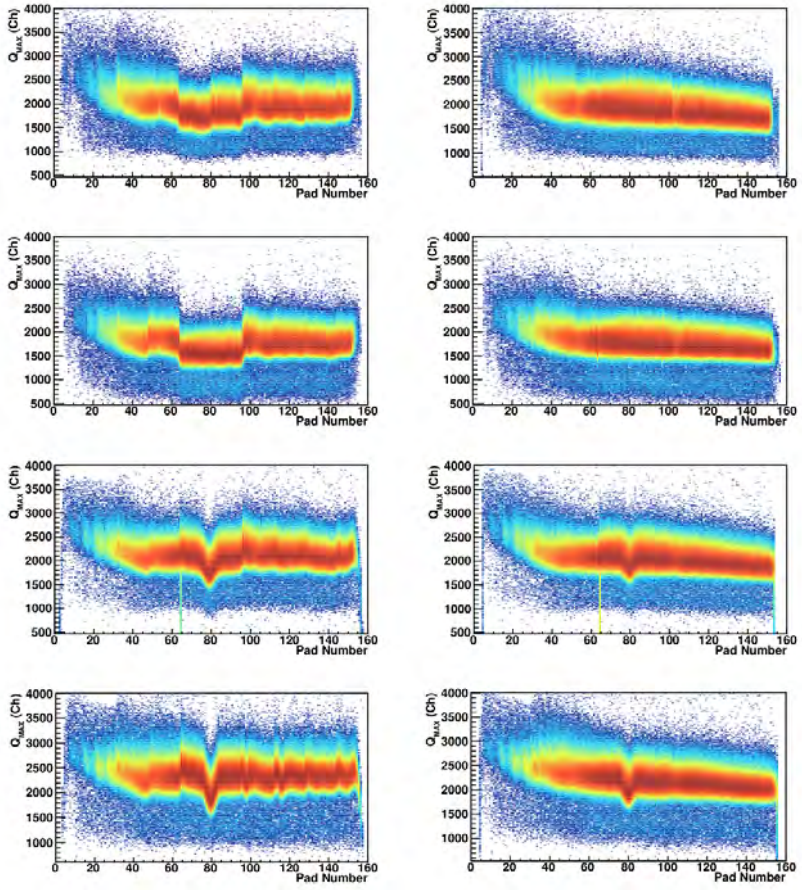

Figure 3.5: Gain matching of the Drift Chamber pads. Left and right columns show the maximum induced charge per pad before and after the gain matching procedure for elastic scattering events of ^{238}U in ^{197}Au.

events of ^{250}Cf, for one specific experimental run. The left and right column represent the situation before and after applying the corresponding calibration parameters.

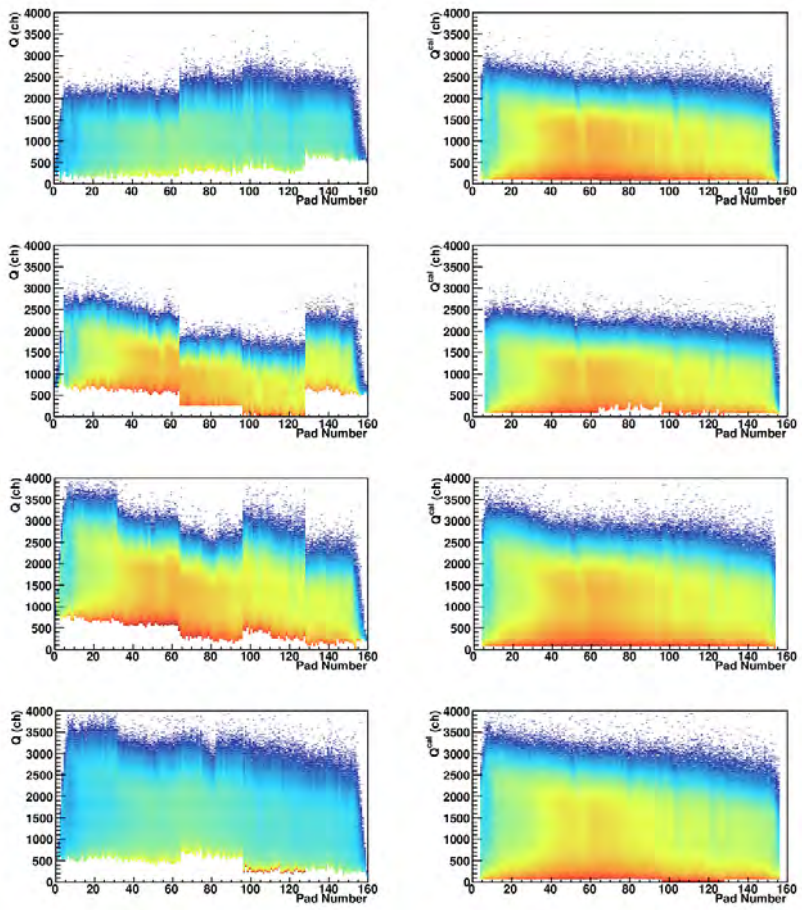

Figure 3.6: Calibration of the induced charge in the Drift Chamber pads. Left and right columns show the induced charge per pad, produced by ^{250}Cf-fission fragments, before and after the calibration procedure.

3.2.2 Determination of the Horizontal Position (x_{fp})

An ion passing through the chamber ionizes the atoms of the gas and the released electrons are accelerated towards the anodes (wires). In this process, the transversal section of the electronic cloud increases.

Assuming that this transversal diffusion is small, the charge induced on one pad depends on the distance in the horizontal axis between the position of the pad and the position where the ion passed through. In the electrostatic approximation, the induced charge density in the plane of the pads by a punctual charge, assuming infinitely long pads, is calculated as follows [52]:

$$\sigma(x) = \frac{-Q}{4L}\mathrm{sech}\frac{\pi(x - x^0)}{2L} \ , \tag{3.3}$$

where Q denotes the charge sitting on an anode wire, L is the gap distance between the anode wires and the cathode plane, x is the position in the cathode plane, perpendicular to the pads, and x^0 is the centroid of the induced charge distribution in the cathode plane.

Figure 3.7 shows the induced charge distribution in the cathode plane for a single fission-fragment event. The dots correspond to the induced charge in each pad measured from an actual event, and the black curve is a fit using the previous equation where Q, L, and x^0 are considered as free parameters. The centroid of the distribution provides a measurement of the fission-fragment position projected on the cathode plane along the dispersive axis, perpendicular to the trajectory of the ion.

The *Hyperbolic secant squared (SECHS)* is a relatively simple 3-parameter function that was proved to be a very good approximation to the charge distribution induced from a punctual charge [53]. This function possesses the advantage of having an analytic and fast computing solution for its centroid, which is defined as the center of the pad with the largest induction plus a deviation from this center based on ratio of charges of the two neighboring pads. This method provides a position reconstruction (x^0) with a resolution smaller than the size of the pad. The function can be expressed as:

$$x^0 = n_{max} + \frac{\frac{1}{2}\ln\frac{1+A}{1-A}}{\ln(\mu + \sqrt{\mu^2 - 1})} \ ,$$

$$\mu = \frac{1}{2}\left(\sqrt{\frac{Q_{n_{max}}}{Q_{n_{max}-1}}} + \sqrt{\frac{Q_{n_{max}}}{Q_{n_{max}+1}}}\right) \ , \quad A = \frac{\sqrt{\frac{Q_{n_{max}}}{Q_{n_{max}-1}}} - \sqrt{\frac{Q_{n_{max}}}{Q_{n_{max}+1}}}}{2\sinh(\mu)} \ , \tag{3.4}$$

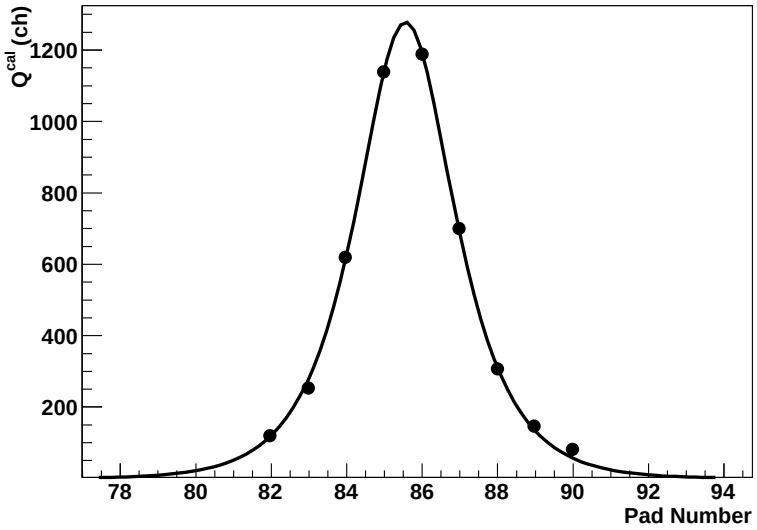

Figure 3.7: Induced charge in the Drift chamber cathode for a single fission-fragment event. The dots correspond to experimental data, and the line is a fit using the definition of the charge distribution for the electrostatic case.

where x^0 is the position of the centroid, n_{max} is the number of the pad with the largest induced charge ($Q_{n_{max}}$), and $Q_{n_{max}-1}$ and $Q_{n_{max}+1}$ are the induced charge on the left and right neighbor pad to n_{max}, respectively.

The position of the centroid, x^0, is defined in units of pad and with respect to the edge of the drift chamber, so the reconstructed position in a common external reference frame is defined as:

$$x = Cx^0 + Off \ , \tag{3.5}$$

where $C = 6.40$ mm is the distance between the pads and Off is an offset that need to be determined to fix a common external reference frame.

Four independent measurements of position are available. Figure 3.8 shows the distribution of the rows of pads in the two drift chambers; x_1

and x_2 correspond to the first drift chamber, and x_3 and x_4 correspond to the second one. Both rows of each drift chamber are fixed and, hence, their offsets are related: $Off_2 = Off_1 - 0.5PadSize$ and $Off_4 = Off_3 - 0.5PadSize$.

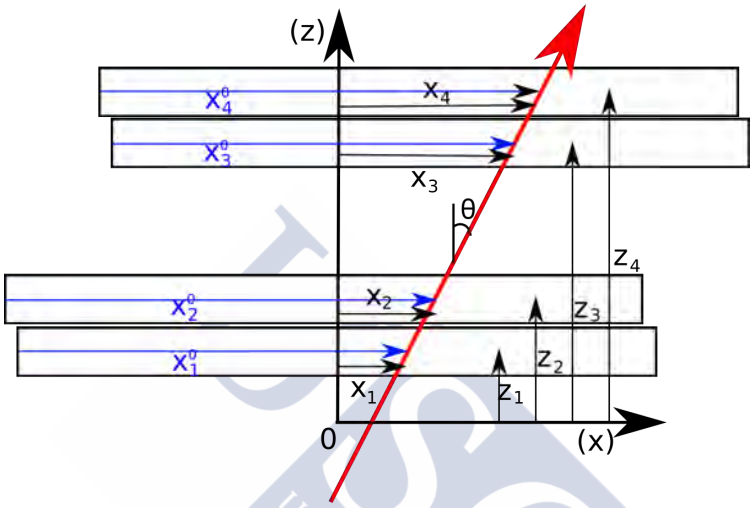

Figure 3.8: Schematic distribution of the row of pads in the drift chambers. The red arrow represents an ion passing through the detectors with an angle θ.

The offsets Off_1 and Off_3 are also related. The trajectory that an ion describes after the VAMOS spectrometer is a straight line, therefore it is possible to obtain an equation that relates both offsets as:

$$\frac{x_4 - x_1}{D_{41}} = \frac{x_3 - x_2}{D_{32}} \Rightarrow$$

$$C\left(x_4^0 - x_1^0\right) = \frac{D_{41}}{D_{32}} C\left(x_3^0 - x_2^0\right) + \frac{D_{41}}{D_{32}}\left(Off_3 - Off_2\right) - \left(Off_4 - Off_1\right) \ . \tag{3.6}$$

This equation requires the distances between the rows of pads in perpendicular axis to the drift chamber planes, ($D_{41} = z_4 - z_1$ and $D_{32} = z_3 - z_2$).

The four individual offsets are now reduced to one single offset that defines the global reference frame. This global offset is determined by

the reconstruction of the magnetic rigidity ($B\rho$) of the ions, explained in section 3.2.4.

The four measurements of the position (x_i) permit to extract, by means of a linear regression, the horizontal position at the focal plane (x_{fp}), with a resolution twice better than any individual value, and the angle of the trajectory in the horizontal plane that the ions describe once they leave the spectrometer (θ_{fp}):

$$x_{fp} = C_0 + C_1 z_{fp} \,, \qquad \theta_{fp} = tan^{-1}(C_1) \,, \tag{3.7}$$

$$\begin{aligned} C_0 &= \frac{\sum {z_i}^2 \sum x_i - \sum z_i \sum z_i x_i}{n \sum {z_i}^2 - (\sum z_i)^2} \,, \\ C_1 &= \frac{n \sum z_i x_i - \sum z_i \sum x_i}{n \sum {z_i}^2 - (\sum z_i)^2} \,, \end{aligned} \tag{3.8}$$

where $z_{fp} = 7600$ mm.

3.2.3 Determination of the Distances Between Drift Chamber Rows

As it was shown in equations 3.6 and 3.8, the position of the rows of pads are needed to determine x_{fp} and θ_{fp}. However, a discrepancy is observed when we compare the nominal values of the distances ($D_{41}^{nomial} = 158$ mm and $D_{32}^{nominal} = 79$ mm) and the slope of the distribution $\left(x_3^0 - x_2^0, x_4^0 - x_1^0\right)$. This discrepancy is shown in Fig. 3.9. The experimental distribution exhibits a slope $D_{41}/D_{32} = 1.756 \pm 4 \cdot 10^{-5}$, while the black line, that represents the nominal values, shows a slope $D_{41}/D_{32}|^{nominal} = 2$.

This discrepancy may come, either from a wrong assignment of the nominal values, or from a non homogeneous induction on the pads. As shown in Fig. 3.10, an inhomogeneous induction of charge along the track of the ion may produce that the effective position of the pad does not correspond with the center of the pad. A deeper study the position reconstruction is performed in order to obtain the correct distance between rows.

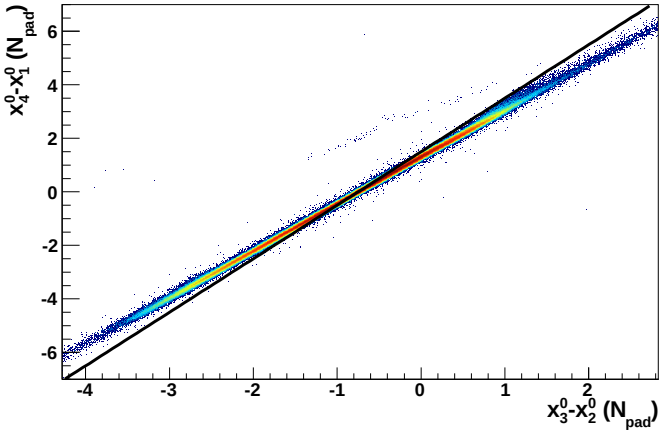

Figure 3.9: Correlation of positions (x_i^0). The slope of the distribution, following the equation 3.6, corresponds to $\frac{D_{41}}{D_{32}} = 1.756$, that differs from the nominal one $\frac{D_{41}}{D_{32}} = 2$, represented by the black line.

The reconstruction of the x-position using the *SECHS method* provides the deviation of the position respect to the center of the pad with largest induced charge, $Dev_i = x_i^0 - n_{maxi}$. This deviation has some properties respect to the tangent of the angle of the particle, $tan(\theta_{fp})$:

- The difference of deviations between two consecutive rows, $\Delta Dev_{21} = Dev_2 - Dev_1$, for a fixed angle depicts two single values and the separation between them corresponds to the size of the pad (Figure 3.11 a)).

$$\Delta Dev_{21} - \Delta Dev'_{21}|_{\tan(\theta_{fp})=const} = PadSize. \tag{3.9}$$

- The difference of tangent values for a fixed difference of deviations between two consecutive rows correspond to the size of pad divided by the effective distance between rows (Figure 3.11 b)).

$$\Delta \tan(\theta_{fp})|_{\Delta Dev_{21}=const} = \frac{PadSize}{D_{21}}. \tag{3.10}$$

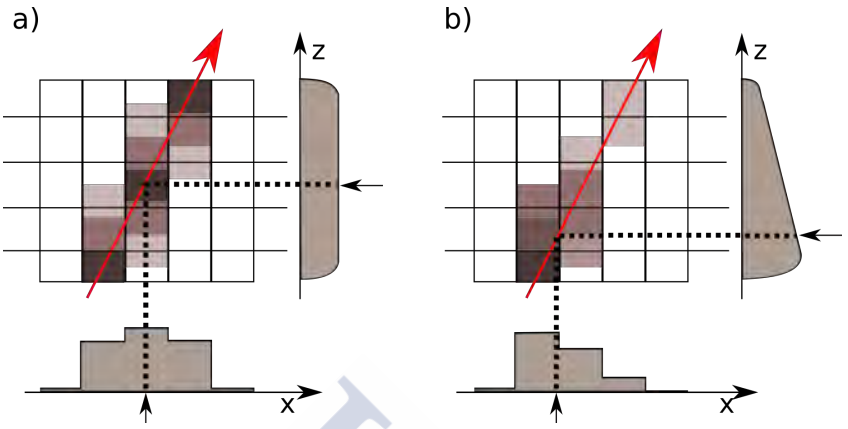

Figure 3.10: Schematic view of the inhomogeneous induction effect on the determination of the distance between pad rows. Red lines represent the track of a ion in one row of the drift chamber. Picture (a) shows the standard situation where the homogeneous induction produce a charge distribution in the x-axis which mean value correspond with the center of the row in the z-axis. Picture (b) shows how an inhomogeneous induction disturbs the charge distribution making that the effective position in the z-axis appears shifted.

Figure 3.12 presents the tangent of θ_{fp} versus the difference of Dev between the two rows of pads for the first (a) and second (b) drift chamber. The value of the $PadSize$ is deduced from the ΔDev difference in $\tan(\theta_{fp}) \approx 0$, this value is equal to 1.001 ± 0.001 in both cases, indicating that the *SECHS method* for the position reconstruction works properly and the x^0 distribution covers the full size of the pad, as expected.

The differences of tangent for $\Delta Dev \approx 0$ are $\Delta\tan(\theta_{fp}) = \frac{SizePad}{D_{21}} = 0.1950 \pm 0.0007$, and $\Delta\tan(\theta_{fp}) = \frac{SizePad}{D_{43}} = 0.1790 \pm 0.0003$ for the first and second drift chamber, respectively. Using the size of the pad $PadSize = 6.4$ mm, the correct distances between the first and second row of pads (D_{21}), and between the third and fourth row of pads (D_{43}) are obtained, $D_{21} = 32.82 \pm 0.11$ mm and $D_{43} = 35.75 \pm 0.06$ mm.

Using the value of $\frac{D_{41}}{D_{32}} = 1.756 \pm 4 \cdot 10^{-5}$ from Fig. 3.9, with $D_{41} =$

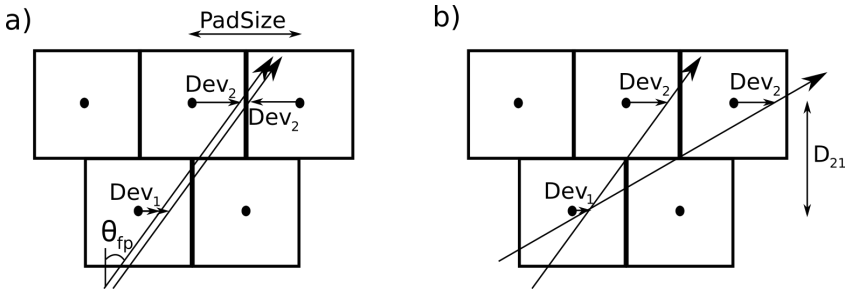

Figure 3.11: Relation between the x^0 reconstruction and pad geometry. Dev represents the deviation of x^0 respect to the central position of the pad. Figure (a) represents two events with the same angle, the values of $\Delta Dev = Dev_2 - Dev_1$ of both events are shifted by the size of the pad. Figure (b) represents two events with the same ΔDev, in this case, the difference of $tan(\theta)$ between both events is the size of the pad, divided by the distance between both pad rows (D_{21}).

$D_{43} + D_{32} + D_{21}$, the last distance, D_{32}, is 90.70 ± 0.16 mm.

The absolute values of the position of the drift chamber rows (z_i) are calculated with respect to the position of the silicon wall by using a projection of the x_i positions over the plane of the wall of silicon detectors ($z_{si} = 8441$ mm) using the equation $x_{si} = C_0 + C_1 z_{si}$ with the parameters defined in Eq. 3.8.

Every silicon detector is separated by one layer of material that is not sensitive to radiation. When an ion reaches this region there is no signal in the silicons. The position (x_{si}) shows an image of the silicon wall spacing when only events with signal in the silicon are considered. The spacing of silicon detectors observed through (x_{si}) depends of the distance between the silicon wall and the drift chambers. Once the position of the silicon wall (z_{si}) is fixed, the correct position of the drift chamber would give the correct spacing of silicons.

Figure 3.13 show the mean value of the spacing of silicons, calculated with x_{si}, as a function of the position of the first row of the first drift

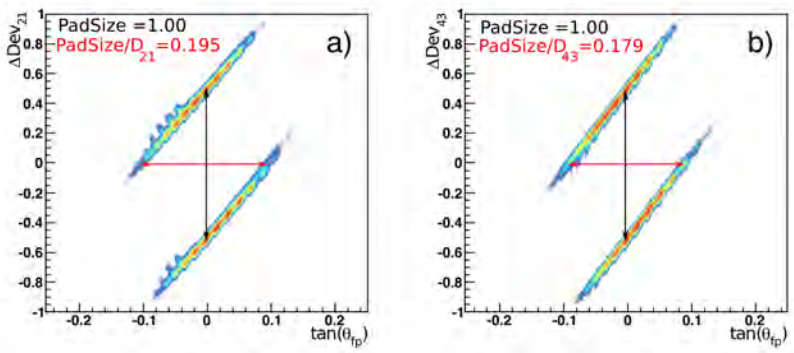

Figure 3.12: Determination of distances between pad rows using data from the elastic scattering of ^{238}U in ^{197}Au. The horizontal axis is the tangent of the angle θ_{fp}, and the vertical axis is the difference of the deviation of x^0 from the center of the pad between to consecutive rows of pads, and the horizontal pad. Vertical gaps define the size of the pads, in units of pad, and horizontal gaps define de parameter $\frac{PadSize}{D_{i(i+1)}}$. Figure (a) correspond to the first drift chamber and figure (b) correspond to the second drift chamber. In both cases, the measured size of the pad is 1, and the values of the distances between pad rows are $D_{21} = 32.8$ mm and $D_{43} = 35.7$mm, with $PadSize = 6.4$ mm by construction.

chamber. Silicon detectors are separated 54.0 mm; the position z_1 that reproduces this spacing, using a linear fit, is $z_1 = 7814.4 \pm 1.1$ mm.

Table 3.1 summarizes the absolute effective positions of the drift chamber rows.

The new positions z_i permit to calculate the relationship between offsets defined in Eq. 3.6. From a linear fit in Fig. 3.9, the value of the intercept point is $\frac{1}{C}\left(\frac{D_{41}}{D_{32}}\left(Off_3 - Off_2\right) - \left(Off_4 - Off_1\right)\right) = 1.325 \pm 4 \cdot 10^{-5}$. Using $\frac{D_{41}}{D_{32}} = 1.756 \pm 4 \cdot 10^{-5}$, $Off_2 = Off_1 - 0.5C$, $Off_4 = Off_3 - 0.5C$, and C = 6.40 mm, the relation results $Off_3 - Off_1 = -0.4 \pm 4 \cdot 10^{-4}$ mm.

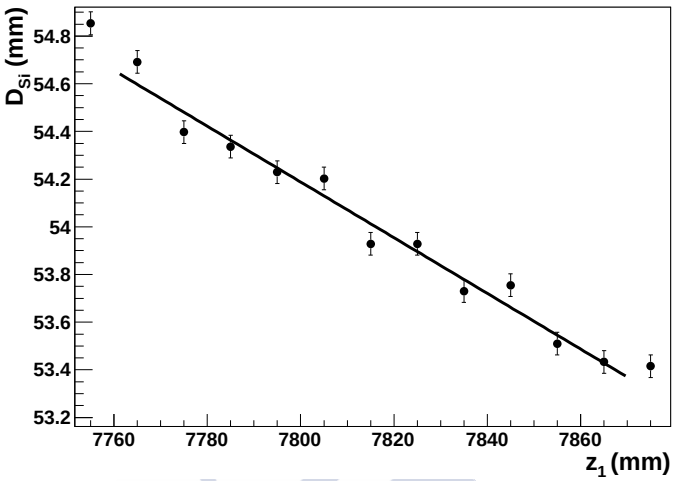

Figure 3.13: Mean value of the silicon detector spacing, calculated through the image x_{si}, as a function of the absolute position of the first row of the drift chamber. The black line correspond a linear fit of the data $D_{si} = 145.35 - 0.01169 z_1$. The position $z_1 = 7814.4$ mm reproduces the correct spacing of silicons, $D_{si} = 54.0$ mm.

Effective positions of the Drift Chamber rows		
Object		**Distance (mm)**
Drift Chamber I	Row 1	7814.4 ± 1.1
	Row 2	7847.2 ± 1.1
Drift Chamber II	Row 1	7937.9 ± 1.1
	Row 2	7973.7 ± 1.1

Table 3.1: Effective position of the drift chamber rows with respect to the target position.

3.2.4 Determination of the Global Offset

The global offset of x_{fp} is fixed by recovering the correlation between the $B\rho$ and the angle of the products of the elastic scattering channel. The energy and the $B\rho$ of the products are related through the charge states:

$B\rho = C\,(M/q)\,\beta\gamma = C\sqrt{E_k^2 + 2ME_k}/q$, where C is a conversion factor, E_k and M are the kinetic energy and mass of the product, and q is the charge state. Therefore, for each charge state, the $B\rho$ and the angle θ of the products are related.

The elastic scattering of ^{238}U in ^{197}Au, including the energy loss in the target, is simulated with the program LISE [50]. The relationship between the $B\rho$ and the angle of ^{238}U that the simulation provides for several charge states is compared with the experimental data. The experimental charge states are unknown, but the relation between $B\rho$ and θ is unique for each charge state. This feature permits to perform an iterative process that begins with the offset value that centers the axis in the middle of the drift chamber ($Off_{global} = -500$ mm) with a reasonable value of the lowest charge state, and converges to the correct offset with the correct charge state assignment, minimizing the difference between the reconstructed and the calculated $B\rho$ for each θ value.

Figure 3.14 shows the relationship between $B\rho$ and θ (in the laboratory reference system) for elastic scattering of ^{238}U in ^{197}Au, each line corresponds to a single charge state. In Fig. 3.14 (a), the reconstruction algorithm uses the position x_{fp} with the nominal offset $Off_{global} = -500$ mm, whereas in Fig. 3.14 (b), the offset of x_{fp} is obtained from the minimization process, $Off_{global} = -464.0 \pm 0.1$ mm. Figure 3.14 (c) shows the charge distribution that results from the projection of the data over the theoretical lines. The optimum offset, $Off_{global} = -464.0$ mm, presents charge states with the best resolution. The standard deviation of each charge state, averaged along the full distribution, results in $\sigma = 0.2298$, which is 15% lower than using the nominal offset. The final offsets of each row of pads are presented in Table 3.2.

3.3 Drift-Chamber Wires Calibration

The vertical position is determined by the drift time of the electrons between the point where the fragment ionizes the gas and the position of

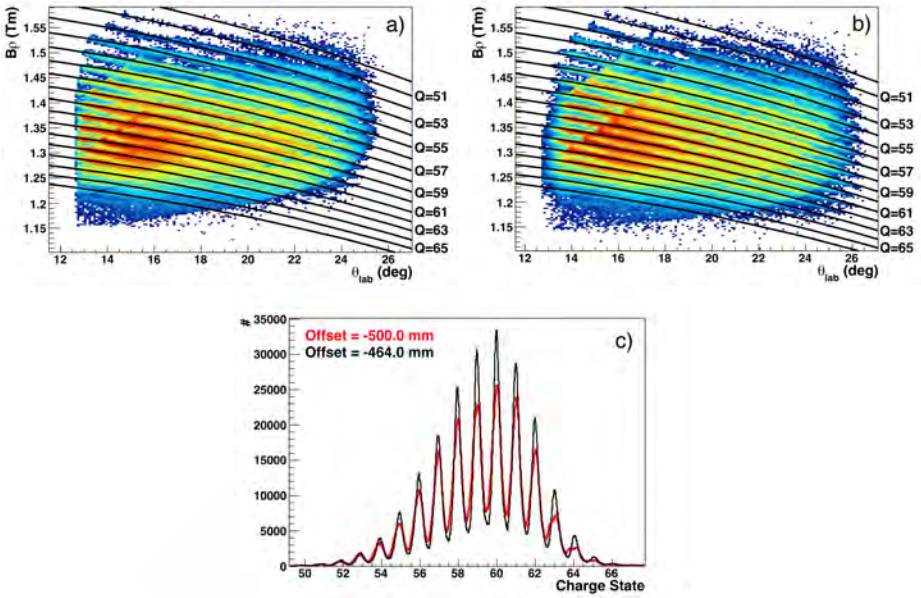

Figure 3.14: In (a), it is presented the relation between $B\rho$ and θ for elastic scattering of ^{238}U in ^{197}Au with the nominal value of the global offset, $Off_{global} = -500$ mm. In (b), instead, the calculated offset from the minimization, $Off_{global} = -464.0$ mm is applied. The black lines represent the theoretical values. Picture (c) shows the projection of the data over the theoretical lines in both cases. The average standard deviation of the charge states is reduced in 15% using the optimum offset, reaching $\sigma = 0.2298$.

Offsets of the x-position		
Object		**Offset (mm)**
Drift Chamber I	Row 1	-464.0 ± 0.1
	Row 2	-467.2 ± 0.1
Drift Chamber II	Row 1	-464.4 ± 0.1
	Row 2	-467.6 ± 0.1

Table 3.2: Final calculated offsets of the horizontal position.

the wires that collect those electrons. The drift velocity, which relates the vertical position and the drift time, is calculated in this section, along with the investigation of cross-talk effects.

3.3.1 Drift-Time Calibration

The drift time is defined as the time that the electrons created in the primary ionization need to travel from the place where the ionization takes place to the position of the wires, at the bottom of the drift region.

In order to calibrate the drift-time measurement, a time calibrator is used. The time calibrator module generates periodical signals that are sent to the four Time-to-Amplitud Converter (TAC) modules used in the drift-time measurement, with a period of $\tau_n = 320n$ ns, being n an integer value that changes randomly between 1 and 16, to cover a range of $T = 5.12\ \mu s$. The TAC modules produce signals with an amplitude that is proportional to the period τ_n.

The time calibration procedure converts the output of the TAC modules from ADC channels to time-scaled values through the equation:

$$t = A(Ch - Pedestal)\ , \tag{3.11}$$

where t is the calibrated time, A is the calibration factor, Ch are non-calibrated ADC channels, and $Pedestal$ is the value that the ADC provides when no input signal is received.

The value of the calibration factor (A) is calculated as the slope of a linear fit between the output of the ADC and the corresponding time ($t_n = t_0 + 320n$). Figure 3.15 shows the calculation of the calibration factor A of the four TAC modules.

The Pedestal values were obtained by means of a Gaussian fit to the first peak of each ADC-output distribution, where the errors correspond to the standard deviation of the Gaussians.

A list of the calibration parameters of each drift time measurement is presented in Table 3.3.

Parameters of the drift-time calibration		
Object	**A (ns/ch)**	**Pedestal (ch)**
TAC 1	$0.30502 \pm 2 \cdot 10^{-5}$	141.6 ± 1.1
TAC 2	$0.24836 \pm 2 \cdot 10^{-5}$	134.6 ± 1.4
TAC 3	$0.25447 \pm 2 \cdot 10^{-5}$	130.4 ± 1.3
TAC 4	$0.24876 \pm 2 \cdot 10^{-5}$	125.6 ± 1.3

Table 3.3: List of parameters of the drift-time calibration.

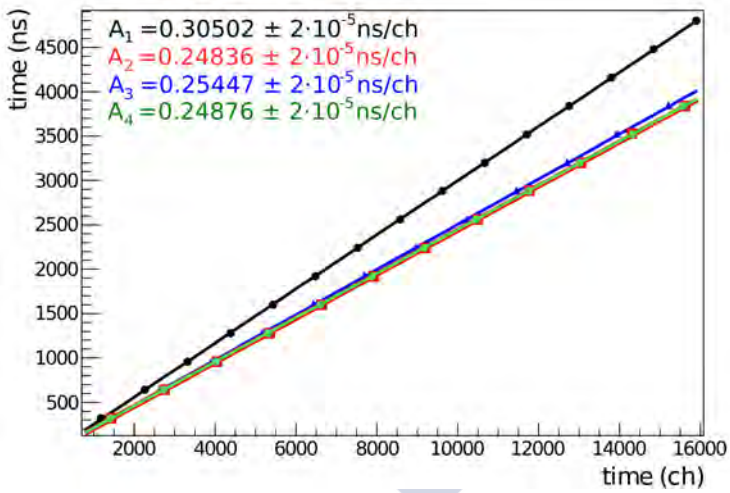

Figure 3.15: Drift-time calibration. The horizontal axis is the output of the TAC in ADC-channels, the vertical axis is the corresponding time in ns. Each point represents a signal of the time calibrator with a period of $\tau_n = 320n$ ns. The time calibration factors (A_i) are the slope of the linear fits.

3.3.2 Determination of the Vertical Position (y_{fp})

Each group of wires placed above each row of pads provides an independent measurement of the vertical position (y_i) in the drift chamber. This position is related to the drift time by means of the electron drift velocity in the gas of the chamber,

$$y_i = y_i^0 + v_{drift} t_{yi} \tag{3.12}$$

where y_i is the vertical position, y_i^0 is the vertical offset of each vertical position, t_{yi} is the drift time of the electrons in the drift region, and v_{drift} is the electron drift velocity in the gas, which roughly corresponds to $v_{drfit} \simeq 50$ mm/μs for isobutane gas at $E/P = 6$ V/(cm·Torr) [36].

A precise value of the electron drift velocity v_{drift} is obtained directly from the measurement of the drift time by using the position of the six horizontal wires at the entrance of each drift chamber, separated with a pitch of 18 mm. These wires cover the full drift region in order to homogenize the electric field and ensure a constant drift velocity. The ions that impinge the wires are stopped and do not enter the drift chamber, producing a shortage of events in the drift time measurement, as it is shown in Fig. 3.16 (a).

A value of the electron drift velocity $v_{drift} = 55.28 \pm 0.07$ mm/μs is determined as the slope of the linear relation between the drift time that correspond to the field-wires and their relative position (separated 18 mm). Figure 3.16 (b) depicts such linear relation. The position of the first field wire is arbitrarily fixed to $y_1 = 0$.

The offsets of the vertical positions, y_i^0, are determined by geometrical considerations. The beam axis, which corresponds with the center of the y axis, is placed 0.5 mm above the third field wire. Under the assumption that there is no large angles in the y axis for $y_i \approx 0$, the offsets, y_i^0 are defined to fulfill the condition $y_i^{field-wire_3} = -0.5$ mm. The resulting offsets are displayed in Table 3.4.

Following the same procedure as in the horizontal position calculation,

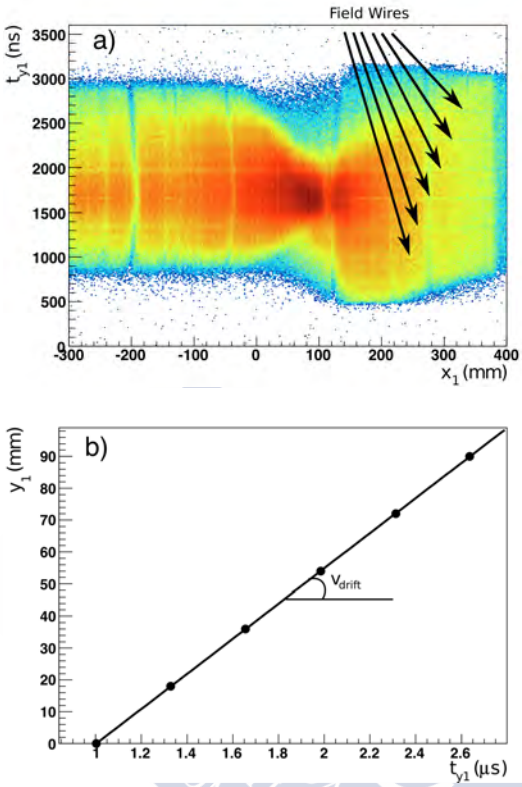

Figure 3.16: Calculation of the electron drift velocity in the drift chamber. Picture (a) is the distribution of events in the first drift chamber. The vertical axis defines the drift time of the electrons in the gas. Six horizontal wires, separated 18 mm, appear in this distribution. In (b), the drift velocity is obtained from a linear fit between the position of these wires and the corresponding drift time. The first point is fixed to y=0.

the four measurements of the position (y_i) permit to extract, by means of a linear regression, a value of the vertical position of the ions at the focal place (y_{fp}) and the angle of the trajectory (ϕ_{fp}),

$$y_{fp} = C_0 + C_1 z_{fp} \ , \qquad \phi_{fp} = \tan^{-1}(C_1) \ , \tag{3.13}$$

Offsets of vertical positions		
Object		**Offset y_i^0 (mm)**
Drift Chamber I	y_1	-109.7 ± 0.6
	y_2	-110.8 ± 0.6
Drift Chamber II	y_3	-109.7 ± 0.6
	y_4	-110.8 ± 0.6

Table 3.4: Offsets y_i^0 of the vertical position, defined as the vertical shift needed to place the third field wire (Figure 3.16) at $y_i = -0.5$ mm.

$$\begin{aligned} C_0 &= \frac{\sum {z_i}^2 \sum y_i - \sum z_i \sum z_i y_i}{n \sum {z_i}^2 - (\sum z_i)^2} \ , \\ C_1 &= \frac{n \sum z_i y_i - \sum z_i \sum y_i}{n \sum {z_i}^2 - (\sum z_i)^2} \ , \end{aligned} \tag{3.14}$$

where z_i are the positions in the beam direction (perpendicular to x_{fp} and y_{fp}) that corresponds to each measurement y_i.

3.3.3 Determination of the Distances Between the Amplification Wires of the Drift Chambers

The fact that the ions describe a straight line once they leave the dipole permits to calculate the angle of trajectory using different doublets of measurements (y_j, y_i) as follows,

$$\tan(\phi_{ji}) = \frac{y_j - y_i}{D_{ji}} \ , \tag{3.15}$$

being $D_{ji} = z_j - z_i$ the distance between the wires that measure the positions (y_j, y_i).

The value of the tangent $\tan(\phi_{ji})$ must be independent of the combination of y positions. This lets to define a set of relation between the distances (D_{ji}) that depends on the y-position measurements,

$$\frac{D_{ji}}{D_{lk}} = \frac{(y_j - y_i)}{(y_l - y_k)} \ . \tag{3.16}$$

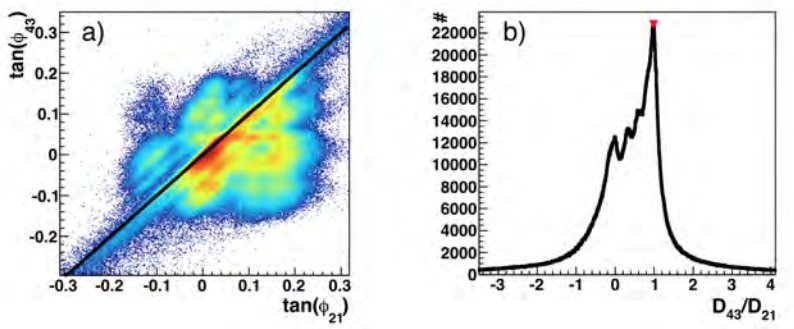

Figure 3.17: Calculation of the wires distances. Picture (a): $\tan(\phi_{ij})$ correlation between wires (y_4, y_3) and (y_2, y_1) using nominal values $D_{43}/D_{21} = 1$. The black line represent the good correlation $\tan(\phi_{43}) = \tan(\phi_{21})$. Pre-pulses events with wrong correlation are present. Picture (b): ratio of distances between wires (y_4, y_3) and (y_2, y_1). The maximum of the distribution is consistent with the nominal ratio $D_{43}/D_{21} = 1$.

Figure 3.17 (a) shows the correlation of tangents calculated with different positions, (y_4, y_3) and (y_2, y_1), using the nominal values of the distances between wires, $D_{43} = D_{21} = 40$ mm. The events that do not follow a good correlation are understood as low amplitude pre-pulses that precede the real signal and, due to low rejection-threshold levels, they are registered as good signals. The correction of these pre-pulses is explained in the next section. Figure 3.17 (b) shows the relation between the distances D_{43} and D_{21}, calculated following the equation 3.16. The pre-pulses produce a wider distribution, but the maximum still remains in $D_{43}/D_{21} = 1$, which is consistent with what is observed in the left picture.

The relations D_{32}/D_{41}, D_{32}/D_{43}, and D_{32}/D_{21} show negative correlations (Figure 3.18 (a)), which means that the assignment of z_2 and z_3 are inverted, probably due to a wrong cabling during the experiment preparation.

The low threshold levels also introduce a *cross-talk* effect between wires: the signal of one wire induces a small signal in a neighbor wire; if the

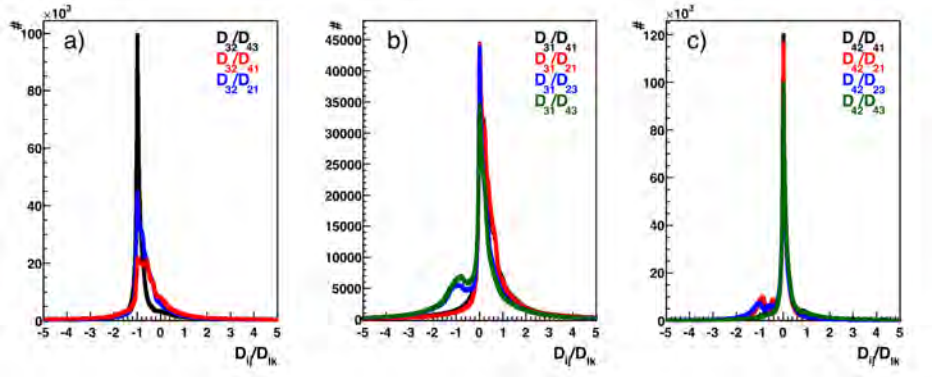

Figure 3.18: Ratio of distances between wires. Picture (a): the negative values of the distributions show that the assignment of z_2 *and*z_3 are inverted. Pictures (b) and (c): the maximum of each distribution equal to zero proves that $D_{31} = 0$ and $D_{42} = 0$ respectively.

induced signal has an amplitude higher than the threshold level, the signal is registered as a good event in the correct wire and in its neighbor at the same time.

The relations $D_{31}/D_{41} = D_{31}/D_{21} = D_{31}/D_{23} = D_{31}/D_{43} = 0$ (Figure 3.18 (b)) and $D_{42}/D_{41} = D_{42}/D_{21} = D_{42}/D_{23} = D_{42}/D_{43} = 0$ (Figure 3.18 (c)) evidence that there exist events with $z_3 = z_1$ and $z_4 = z_2$, from the *cross-talk* between y_1 and y_3, and between y_2 and y_4.

The *cross-talk* effectively reduces the number of independent measurements:

$$\begin{aligned} y'_1 &= \frac{1}{2}(y_1 + y_3) \ , \\ y'_2 &= \frac{1}{2}(y_2 + y_4) \ , \end{aligned} \tag{3.17}$$

where y'_1 and y'_2 are the only two independent measurements of the vertical position, defined as the average value of the measurements affected by *cross-talk*.

The final positions z'_1 and z'_2, which correspond to the measurements y'_1

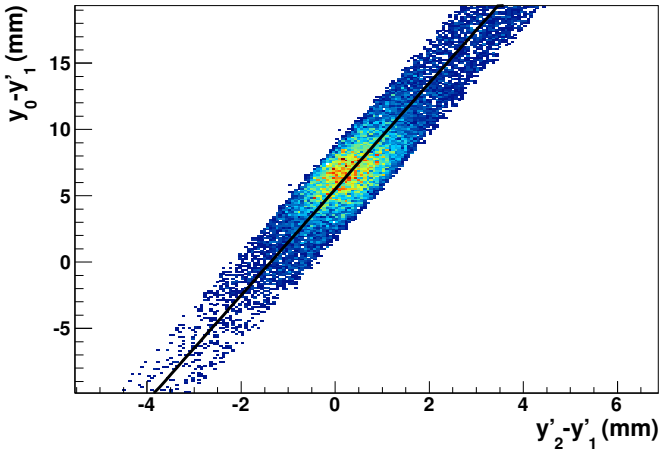

Figure 3.19: Calculation of the absolute z-position of y'_1 and y'_2. Only events without signal in the silicon detector are considered under the assumption that they reach the same y-position in the silicon wall plane, $y|_{z=z_{si}} = y_0$. A linear fit reports a value $D_{z_{si}1'}/D_{2'1'} = 4$.

and y'_2, are determined with the events that reach the interspace between the two rows of silicon detectors. These events, that do not produce any signal in the silicon detectors, are located at $y = y_0$ in the silicon-wall plane ($z = z_{si} = 8441$ mm), independently on the angle. Figure 3.19 shows the relation between $(y_0 - y'_1)$ and $(y'_2 - y'_1)$ for these events, assuming $y_0 = 0$. Following Eq. 3.16, the slope of this relation is the ratio of the distances $D_{z_{si}1'} = z_{si} - z'_1$ and $D_{2'1'} = z'_2 - z'_1$. The measured value is $D_{z_{si}1'}/D_{2'1'} = 4.0 \pm 0.1$.

With the fixed value $z_{si} = 8441$ mm, only one possible combination of z'_1 and z'_2 satisfies $D_{z_{si}1'}/D_{2'1'} = 4$ with values within the drift-chambers size. $z'_1 = 7810 \pm 1$ mm and $z'_2 = 7968 \pm 1$ mm, which are the minimum and the maximum nominal positions of the wires inside of the drift chamber.

3.3.4 Pre-pulses correction

Pre-pulses are events formed by low amplitude signals that arrive to the wire before the real signal. Therefore, the measured times of the pre-pulses are lower than the real times and, accordingly, the calculated vertical positions of the pre-pulses are lower than the real positions.

Besides being affected by *cross-talk*, each individual measurement y_i is filtered in a independent discriminator module, with an specific threshold level, hence, the pre-pulses do not appear necessarily in both cross-talked wires at the same time.

The possible combinations of pairs (y_i, y_j) are used to discriminate real events from pre-pulse events. Real events, due to the aperture of the spectrometer, present a narrow angular distribution in the vertical axis centered around zero. The pre-pulse events are shifted from the real events, showing a value of $(y_j - y_i)$ incompatible with the angle distribution.

The combined effect of two quadrupoles and the dipole of the spectrometer produces a focalization in the vertical axis that depends on the horizontal position. As shown in Fig. 3.16 (a), where the vertical position is presented as a function of the horizontal position, there is a strong vertical focalization at $x \approx 100$ mm. Furthermore, the vertical focalization in x>100 mm is inverted with respect to x<100. This makes that the shift in y the pre-pulses produce depends on the value of y itself, and that is different for the two vertical focalizations of the spectrometer, $x_{fp} < 100$ and $x_{fp} > 100$. Figure 3.20 depicts the presence of the shifted pre-pulse signals. Figure 3.20 (a) presents $(y_3 - y_1)$ as a function of y_1, the events with $(y_3 - y_1) > 1$ correspond to pre-pulses shifted in y_1, while the events with $(y_3 - y_1) < -2$ present a shift in y_3. These shifted values depends on the value of y_1. Figure 3.20 (b) shows $(y_4 - y_3)$ as a function of x_{fp}, where the shifted signals are clearly separated from the real events, placed around $(y_4 - y_3) \approx 0$. The shift is smaller for $x_{fp} < 100$ than for $x_{fp} > 100$.

Some pre-pulse events may be confused with real events when the shift occurs in both measurements (y_j, y_i) at the same time. These two shifts go

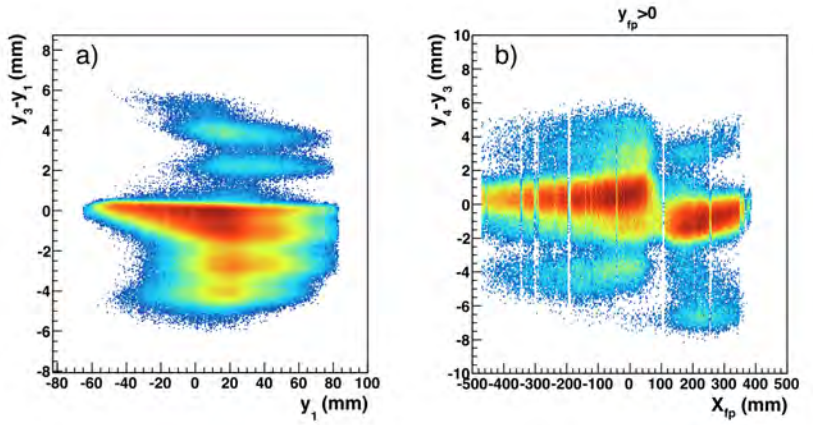

Figure 3.20: Shifted measurements of vertical positions affected by pre-pulse signals. Picture (a): evolution of the pre-pulses shifts with the vertical position. Picture (b): evolution of the pre-pulses shift with the horizontal position.

in opposite directions providing a value similar to a real one in $(y_j - y_i)$.

The correction of the shifted signals is performed over three independent regions in y_{fp}: $[-100, -30]$, $[-30, 0]$, $[0, 100]$ mm, and two independent regions in x_{fp}: $[-500, 100]$, $[100, 500]$ mm. For each of these regions, the correction method is a multi-step process that:

1. defines an offset Off_j^i, equal to the mean distance between the position of shifted and real events in the axis $(y_j - y_i)$,

2. selects the shifted events with a graphical cut in the 2-dimensional plot $(y_j - y_i, x_{fp})$,

3. applies the offset to the shifted events, $y_j^{corr} = y_j^{cut} + Off_j^i$.

This process is repeated for all the possible combinations (y_j, y_i), reducing the number of cases where pre-pulses are not corrected because the shifts appear in both positions, y_j and y_i, at the same time.

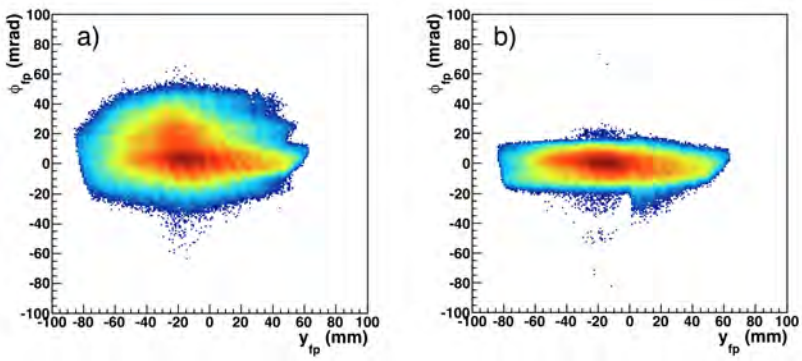

Figure 3.21: ϕ_{fp} distribution as a function of y_{fp} before (a) and after (b) the pre-pulse correction.

Figure 3.21 shows the angular distribution in the vertical axis as a function of the vertical position before (a) and after (b) the pre-pulse correction.

3.4 Ionization Chamber Calibration

The Ionization Chamber (see Sec. 2.4.2.3) is a gaseous detector that measure the energy loss of the ions inside the gas in order to determine their nuclear charge. The released electrons produced in the ionization induce a signal in the anode plane, segmented into fifteen pads, that is proportional to the energy loss in the gas volume above the pad. The electronic alignment of the pads, followed by an energy calibration, is required to obtain a nuclear charge identification with enough resolution.

3.4.1 Energy Calibration

The electronic alignment of the fifteen pads of the ionization chamber is performed using a pulse generator that sends signals through the electron-

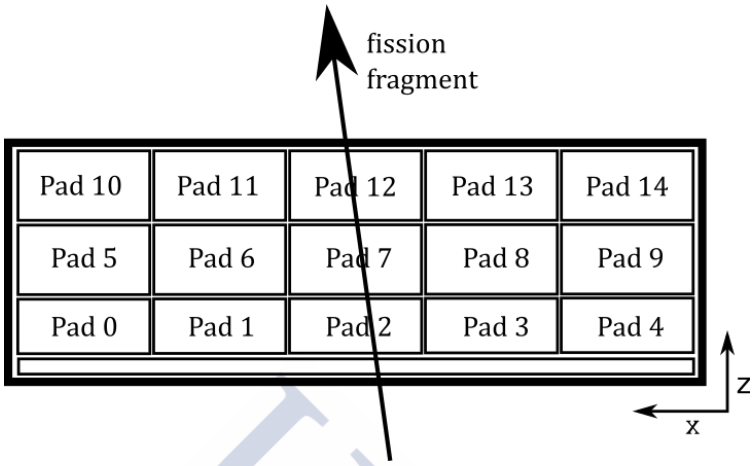

Figure 3.22: Scheme of pads in the ionization chamber.

ics of every pad at the same time. Signals with five different amplitudes are sent to the detector, covering the dynamic range of the ADC module.

The alignment procedure takes the pad number five as an arbitrary reference (see Fig.3.22), and defines a two-degree polinomial that aligns the of the rest of pads with it. The procedure also aligns the pedestal of the pads that is subtracted afterwards. In pad number six, the pedestal is not present due to a high threshold level. In this case, the pedestal is estimated by the extrapolation of the fit using the rest of the signals.

Figure 3.23 shows the output signals of each pad. Pictures (a) and (b) show the output signals before and after the alignment, respectively. The first five pads present an additional signal that is out of range in the rest of the pads; this signal is not considered in the alignment procedure.

Each pad presents a different response to the charge induced in the ionization process, that is, the amplitude of the signals that two pads produce for the same ionization may be different. This characteristic response of the detector can not be corrected by the electronic alignment; a gain correction method is required instead. This gain correction is applied based on the sharing of the total induced charge in the junction between two

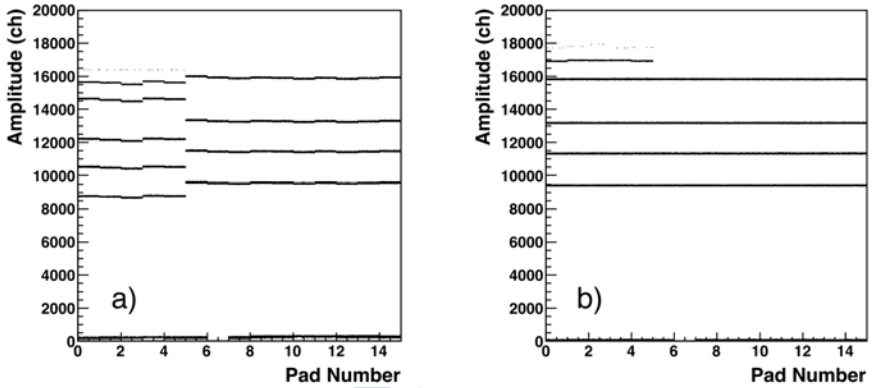

Figure 3.23: Electronic alignment of the pads of the ionization chamber. First five pads present an additional signal that is out of range in the rest of the pads.

consecutive pads.

When the trajectory of an ion crosses above the junction between two consecutive pads, the induced charge is shared between both pads. For these particular cases, whatever it is the charge fraction induced in one pad, the sum of both charges is the total induced charge. Therefore, there is a linear relation between both induced charges if there is no induction losses on the junction. This situation occurs in a small region, the sharing of charge vanishes beyond 5 mm far from the junction, therefore it is reasonable to assume, under certain considerations, that the energy loss of the ions remains constant around the junction position ($\Delta x = \pm 5$ mm). In particular, for the elastic scattering of ^{238}U in ^{197}Au, this assumption is valid because the range of the θ angle that corresponds to 5 mm at the focal plane is $\Delta\theta < 0.3$ deg, which means less than 5 MeV of difference in the total energy of the scattered ions. This variation is small compared with the total energy of ions $E_k > 1000$ MeV, which remains far from the Bragg Peak, when the energy loss varies slowly with the energy.

Assuming a constant energy loss in both sides of each junction, the elastic scattering reaction permits to obtain the gain factors that unify the

response of the pads. The mass and the nuclear charge of the ions from the elastic scattering is unique [2], producing a single relation between induced charges in neighboring pads. The ratio of the charges in both edges of each junction, where one of the pads presents null charge, defines each gain factor. These gain corrections are deduced independently for each row of pads.

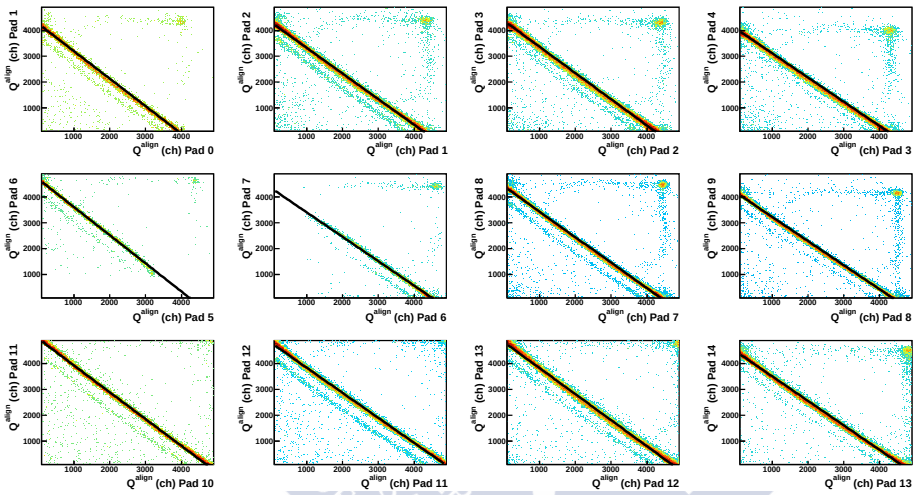

Figure 3.24: Induced charge relation on junction regions for elastic scattering. The main line correspond to ^{238}U, which is fitted with a linear relation (black lines). The lower line correspond to elastic scattered ^{197}Au. The high threshold level of the pad number 6 rejects the lower amplitude signals.

Figure 3.24 shows the induced charge relation between neighboring pads in the junction regions (the pads distribution is shown in Fig.3.22), for elastic scattering. In pad number 6, the lower-amplitude signals are rejected because the threshold level is higher, contributing to the uncertainty of the measurement because the energy loss in this region will not be recovered properly. A linear fit is applied to the ^{238}U events. The ratios between charges are calculated with the values of the linear functions at the interception points, $R = \frac{x|_{y=0}}{y|_{x=0}}$.

[2]The partner, ^{197}Au, is not taken into account in this method due to its low cross section (see Sec. 3.1).

The gain correction takes the left pad of each row as an arbitrary reference and scales the charge of the rest of the pads following the ratio of charges. The gain factor for pad i is defined as:

$$G_i = \prod_{j=j_0}^{i-1} R_{j+1}^{j} \ , \tag{3.18}$$

where j_0 is the number of the left pad of each row and R_{j+1}^{j} is the ratio of the charges of pads j and $(j+1)$:

$$R_{j+1}^{j} = \frac{Q_j|_{Q_{j+1}=0}}{Q_{j+1}|_{Q_j=0}} \ . \tag{3.19}$$

Once the induced charge is corrected by the gain factor, $Q_i^{gain} = G_i Q_i^{align}$, the total induced charge is recovered by the sum of the charges, event by event, of the pads of each row, $Q_{row}^{gain} = \sum_{i=i_0}^{i_{max}} Q_j^{gain}$, this sum involves two pads at maximum when the induction occurs at the junction of two pads.

The final energy calibration is determined row by row. The energy calibration factor, A_i^E, is defined as the average ratio between the induced charge in the row and the energy loss simulated by the LISE++ program for the elastic scattering of ^{238}U at different angles θ in the range the spectrometer covers, from 12 deg to 26 deg. The simulation creates ^{238}U events with several energies that follow the elastic scattering kinematics, takes into account the energy loss in all the previous layers of matter, and calculates the energy loss in each row of the ionization chamber as a function of the emission angle, θ.

The factors A_i^E translate the induced charge of each row to the value of energy loss in MeV, $\Delta E_i = A_i^E Q_{row_i}^{gain}$. Figure 3.25 presents the energy calibration factors obtained as a function of the emission angle in the three rows. The lines represent the average values, specified in the picture. The total energy loss in the ionization chamber is obtained by the sum of the energy loss in the three rows of pads.

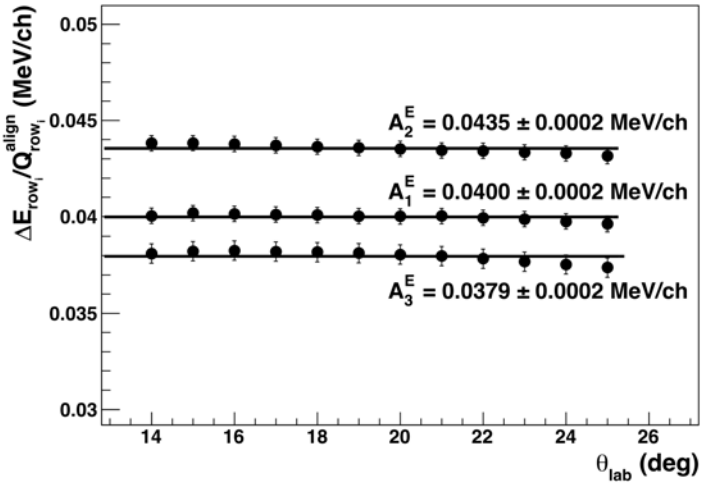

Figure 3.25: Energy calibration of the ionization chamber. In the vertical axis, the induced charge is corrected by the angle of the trajectory of the ions, $Q'^{align}_{row_i} = Q^{align}_{row_i} \cdot \cos(\theta_{fp}) \cdot \cos(\phi_{fp})$.

3.4.2 Energy Loss Corrections

Three different corrections are applied to the energy loss in the ionization chamber. The first two corrections affect to the first and last row of the chamber, both as a function of the vertical position. One last correction is performed in the pad number 6 to minimize the effect of the high threshold level.

The energy loss measured in the first row of the ionization chamber shows a dependency with the vertical position of the ions passing through the chamber. This dependence is explained as an inefficient collection of charge that affects the proportionality between the induced charge and the energy loss of the ions for high y positions. The correction scales the energy loss as a function of the vertical position using the energy loss at

$y_{row_1} = 0$ as a reference,

$$\Delta E^{corr}_{row_1} = \Delta E_{row_1} \frac{f_{\Delta E}(y_{row_1} = 0)}{f_{\Delta E}(y_{row_1})} \,, \tag{3.20}$$

where $f_{\Delta E}(y_{row_1}) = A + B \cdot \mathrm{Erf}\,(C \cdot [y_{row_1} - D])$ is a function that reproduces the mean behavior of ΔE_{row_1} with the vertical position. A, B, C, and D are free parameters that are fitted to elastic scattering data. The fission fragment data, presented in the next chapter, proves the linearity of the correction showing the same behavior in the full range of the energy loss. Figure 3.26 shows the energy loss of the scattered ^{238}U (upper line) and ^{197}Au (lower line) in the first row, corrected by the angle, $\Delta E'_{row_1} = \Delta E_{row_1} \cdot \cos(\theta_{fp}) \cdot \cos(\phi_{fp})$, as a function of the position of the ion in the first row, $y_{row_1} = y_{fp} + 543.7 \tan(\phi_{fp})$. Pictures (a) and (b) show the measured energy loss before and after the correction.

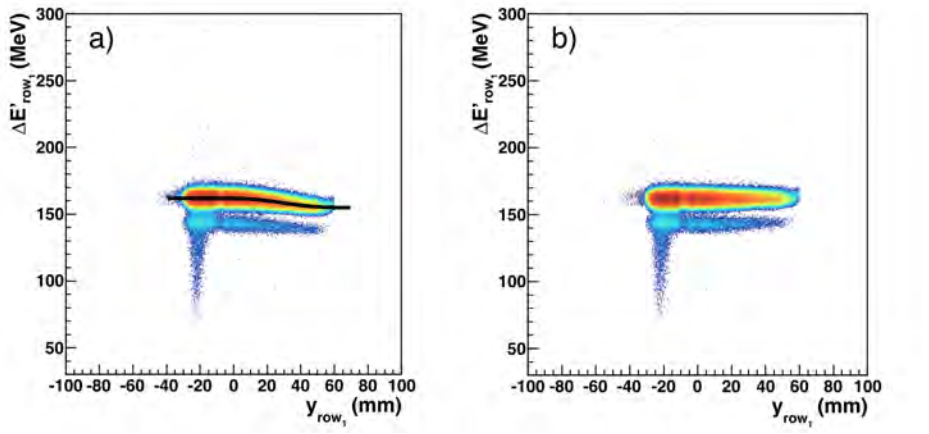

Figure 3.26: Correction of the energy loss on the first row of the ionization chamber as a function of the vertical position, using elastic scattered ^{238}U. The vertical axis is the energy loss corrected by the angle of the ion, $\Delta E'_{row_1} = \Delta E_{row_1} \cdot \cos(\theta_{fp}) \cdot \cos(\phi_{fp})$, before (a) and after (b) correction; the horizontal axis corresponds to the vertical position of the ions at the focal plane, projected in the middle of the first row of the ionization chamber, $y_{row_1} = y_{fp} + 543.7 \tan(\phi_{fp})$.

The energy loss measured in the last row of the ionization chamber is also corrected. It presents large fluctuations, produced by the influence of the electric field of the silicon detectors placed just behind the ionization chamber, which disturbs the charge collection inside the chamber.

As it is shown in Fig. 3.27, the silicon detector reached by the ions is observed to determine the behavior of the energy loss measurement. Both pictures (a) and (b) show two different sets of data. The background set corresponds to events that reach most of the silicon detectors except some specific ones. In this case, the behavior of the energy loss with respect to the vertical position is flat, as expected. The foreground set corresponds to events that reach some specific silicon detectors: silicon #1 and #38 on Fig. 3.27 (a), and silicon #13 and #26 on Fig. 3.27 (b). In these cases, the behavior of the energy loss with the vertical position needs to be corrected. This correction is similar to the one applied to the first row: the measured energy loss is scaled by a function that describes the behavior of the energy loss with the vertical position. In this case, the energy loss of reference, where no correction is needed, corresponds to $y_{row_3} = 60$ mm, where both set of data are coincident. The correction is then:

$$\Delta E^{corr}_{row_3} = \Delta E^{SiInfluence}_{row_3} \frac{f_{\Delta E}(y_{row_3} = 60)}{f_{\Delta E}(y_{row_3})} \,, \tag{3.21}$$

where $f_{\Delta E}(y_{row_3}) = A + B \cdot \mathrm{Erf}\,(C \cdot [y_{row_3} - D])$ is a function that reproduces the behavior of $\Delta E^{SiInfluence}_{row_3}$ with the vertical position, $y_{row_3} = y_{fp} + 773.7 \tan(\phi_{fp})$, for cases where the ionization chamber is influenced by the silicon detectors. Again, A, B, C, and D are free parameters that are fitted to elastic scattering data.

The high threshold level of the pad number 6 prevents a linear behavior at low energy loss because its pedestal is not present in the alignment process. It also prevents the recovery of the total induced charge on the junction with its neighboring pads. These two effects need to be corrected as well.

As mentioned in the previous chapter (Section 2.4.2.3), the energy loss of heavy ions is proportional to their mass and nuclear charge. The evolution of this energy loss is approximately linear with the depth for energies

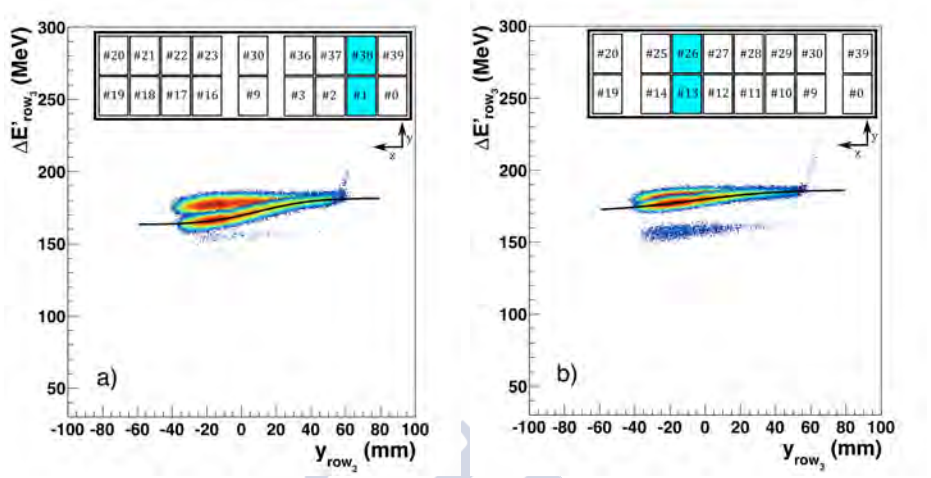

Figure 3.27: Correction of the energy loss on the last row of the ionization chamber as a function of the vertical position, using elastic scattered ^{238}U. The vertical axis is the energy loss corrected by the angle of the ion, $\Delta E'_{row_3} = \Delta E_{row_3} \cdot \cos(\theta_{fp}) \cdot \cos(\phi_{fp})$; the horizontal axis is the projection of the vertical position in the middle of the last row, $y_{row_3} = y_{fp} + 773.7 \tan(\phi_{fp})$. Both pictures (a) and (b) show two sets of data: the background set corresponds to events where the ions reach silicons that do not influence the ionization chamber, the foreground set corresponds to events where ions reach silicons number #1 and #38 (a), and #13 and #26 (b), indicated in the insets, where a wrong behavior is observed.

far from the *Bragg Peak*. In this energy region, the ratio of energy losses in two consecutive slices of matter remains almost independent on the nature of the ions, as it is shown in Fig. 3.28, being a function of the ratio of the sizes of the slices of matter:

$$\frac{\Delta E_1}{\Delta E_2} \propto \frac{\Delta s_1}{\Delta s_2} \,. \tag{3.22}$$

The first and second row of the ionization chamber satisfy the previous condition. All the ions that reach the silicon wall, which is a requirement for the identification process, remain far from the *Bragg Peak* when they

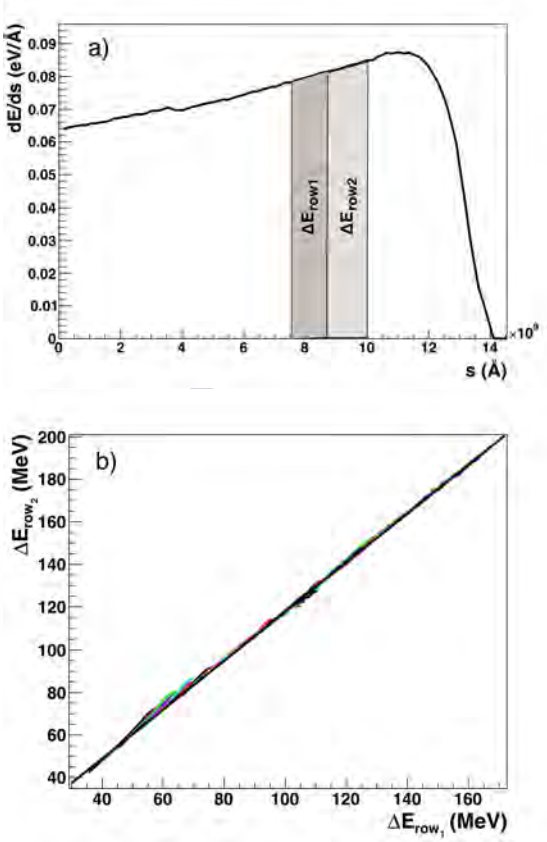

Figure 3.28: (a): simulation of the energy loss profile of ^{108}Ru as a function of the depth in C_4H_{10} at 40 mbar. ΔE_1 and ΔE_2 represents the energy loss in the first and second row of the ionization chamber. (b): linear relation between the simulated energy loss in the first and second row, for energies far from the *Bragg Peak*, $\Delta E_{row_2} = 2.9 + 1.15\Delta E_{row_1}$. Elements from Z=30 up to Z=90 are represented with different colors. This simulation is calculated using a Monte Carlo algorithm based on *TRansport of Ions in Matter (TRIM)* code [46].

pass through the first and second row of the ionization chamber. The linear relationship makes it possible to correct the energy loss in pad 6, placed in the second row, using the energy loss of the first row. The behavior of the

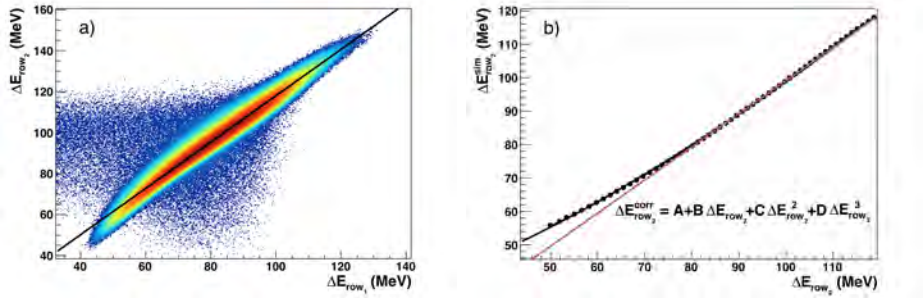

Figure 3.29: Energy loss correction in pad 6. Picture (a): relation between energy loss in the first and second chamber for pad 6. Black line represents the simulated relation. Picture (b): relation between the simulated and measured energy loss in the second row, for each value of energy loss in the first row. Red line represent a good correlation between both, it is observed that the linear relation vanishes for energies below 70 MeV. A third order polynomial function is use to correct this behavior.

energy loss in the pad 6, $\Delta E^{pad6}_{row_2}$, as a function of the energy loss in the first row, ΔE_{row1}, is extracted from fission fragment data, shown in Fig. 3.29 (a). For each value of ΔE_{row1}, $\Delta E^{pad6}_{row_2}$ is compared with the simulated energy loss, calculated by the linear relation. A third order polynomial function describes the relation between the measured and simulated energy loss in pad 6, shown in Fig. 3.29 (b). This linear relation between first and second row permits also to recover the total energy loss in the junction between pad 6 and the neighbor pads. However, when taking individual pads in the second row, the ratio of energies decreases around the junction, because of the missing charge. This behavior can be described with an *error function*.

$$\frac{\Delta E^{pad_i}_{row_2}}{\Delta E_{row_1}} = A + B \cdot \mathrm{Erf}\left(C \cdot [x_{row_2} - D]\right) \ . \tag{3.23}$$

Figure 3.30 shows the ratio of energies in the pad 7, $x_{row_2} < 60$ mm, and pad 6, $x_{row_2} > 60$ mm. The previous error function is fitted to the ratio of energies in pad 7. The function that describes this ratio in pad 6 is, by definition, complementary to the ratio in pad 7, $C' = -C$.

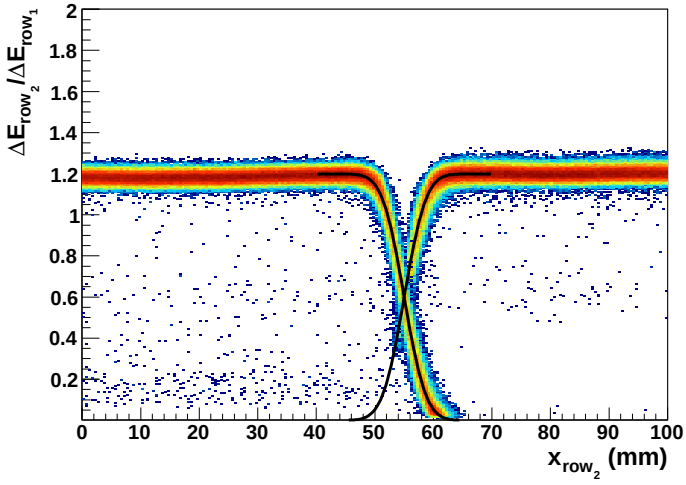

Figure 3.30: Ratio of energy losses between the first and second row on the junction between pad 7, $x_{row_2} < 60$ mm, and pad 6, $x_{row_2} > 60$ mm. The lines describe the behavior of the ratios for each pad individually.

The total energy loss in the junction place between pad 6 and 7, when the energy of pad 6 is below the threshold, can be calculated as:

$$\Delta E_{row_2} = \Delta E_{row_2}^{pad_7} + [A + B \cdot \mathrm{Erf}\,(-C \cdot [x_{row_2} - D])]\,\Delta E_{row_1}\ . \qquad (3.24)$$

Figure 3.31 shows the energy loss in the second row, around the junction place between pad 6 and 7, before (a) and after (b) correction. The total energy loss in the junction between pad 5 and 6 follows the same procedure.

3.4.3 Estimation of the Energy Loss Not Measured

The linear relation between energy losses in two consecutive slices of matter for energies far from the *Bragg Peak* shown in the previous section permits

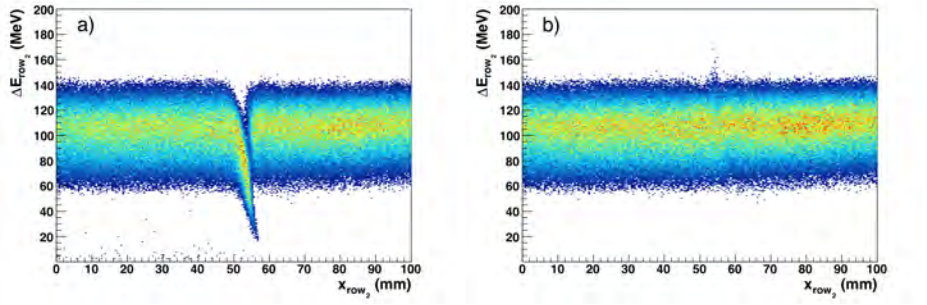

Figure 3.31: Total energy loss of fission fragments between pad 6 and pad 7, before (a) and after (b) the correction by the missing energy in pad 6.

to estimate the energy that fragments lose along the experimental setup on passive layers of matter before the ionization chamber. Using a TRIM

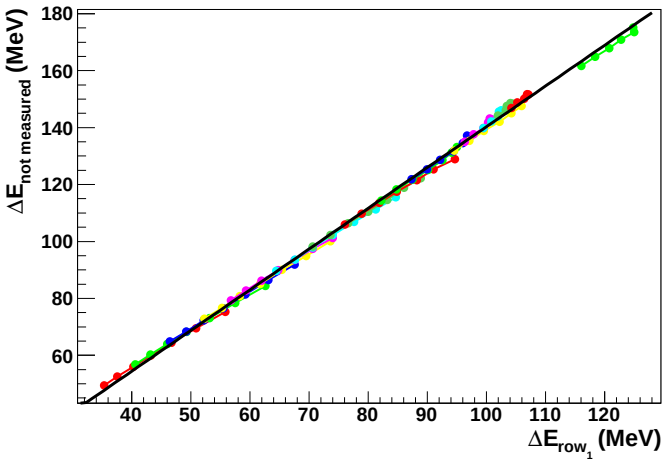

Figure 3.32: Linear relation between the simulated energy loss in the first row of the ionization chamber and the energy loss not measured in previous stages of the setup. Odd-Z fission fragments are represented with different colors from Z=33 up to Z=63. The relation $\Delta E_{not\ measured} = -2.87 + 1.431 \Delta E_{row_1}$ is obtained from a linear fit.

simulation that takes into account every layer of matter present in the experiment, the energy loss in the first row of the ionization chamber can be related with the energy loss in the previous stage of the experimental setup, independent on the fission fragment. This linear relation is shown in Fig. 3.32. The energy loss not measured is calculated as a function of ΔE_{row_1}, applying a linear fit to the simulation:

$$\Delta E_{not\ measured} = -2.87 + 1.431 \Delta E_{row_1} \ , \tag{3.25}$$

with $\Delta E_{not\ measured}$ and ΔE_{row_1} in MeV.

3.5 Silicon Wall Calibration

The Silicon wall is composed of forty silicon detectors distributed in two horizontal rows. These detectors measure the remaining energy of the fission fragments. The electrons promoted from the valence band to the conduction band in the crystal lattice of the silicon produces a signal with an amplitude proportional to the energy of the ion stopped inside the detector. The electronics of the detectors need to be aligned and the amplitude of the signals need to be calibrated in order to obtain the remaining energy of the fragments.

3.5.1 Energy Calibration

The electronic alignment of the forty detectors of the silicon wall is performed using a pulse generator that sends signals through the electronics of every detector at the same time. The pedestal value of each detector is calculated extrapolating the output of the ADC modules to a null amplitude in the input signal, assuming a linear behavior between ADC output and signal amplitude. Figure 3.33 shows the linear fit of the first silicon detector of the upper row. The labeling of the silicon detectors is depicted in Fig. 3.34.

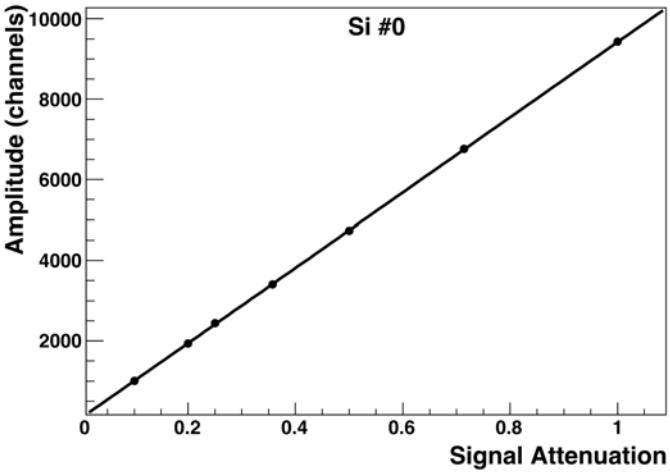

Figure 3.33: Pedestal extrapolation of silicon detector number #0. Vertical axis shows the ADC output, and horizontal axis represents the imput signal amplitude for seven attenuation factors. The pedestal corresponds to value of the ADC output for null signal amplitude.

Figure 3.34: Scheme of the silicon detectors labeling.

The alignment procedure subtracts the pedestal of each detector and defines a function, without intercept parameter, that aligns the output of rest of detectors to the first one, taken this as an arbitrary reference:

$$Q_i^{align} = A_i \cdot Q_i + B_i \cdot Q_i^2 \ , \tag{3.26}$$

where Q_i is the signal amplitude of the detector number i, (A_i, B_i) are the

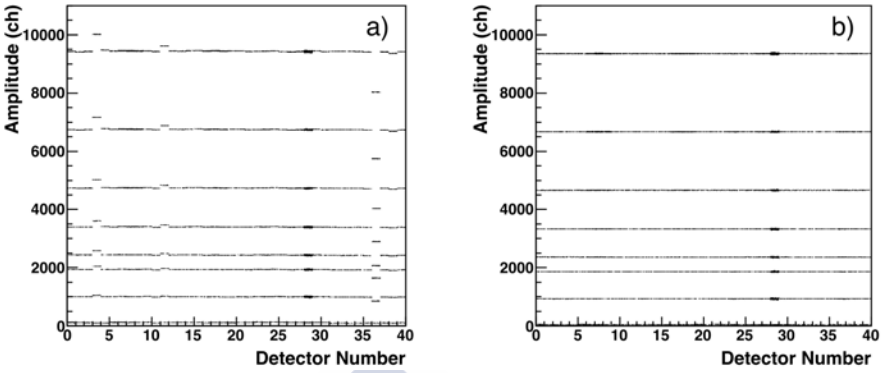

Figure 3.35: Electronic alignment of the silicon detectors.The lower signal corresponds to pedestal, the other signals are sent from a pulse generator with different attenuation factors.

alignment parameters, and Q_i^{align} is the amplitude of the aligned signal.

Figure 3.35 shows the output signals of each detector. Pictures (a) and (b) show the output signals before and after the alignment, respectively. The channel #28 shows large fluctuations that come from the interference of the leakage current of the corresponding silicon, damaged during the experiment.

The energy calibration follows the same procedure as in the ionization chamber. The energy calibration factor, A_i^E, is defined as the average ratio between the signal amplitude and the simulated energy released in the detector, using the elastic scattering of ^{238}U. The simulated energy is compared with the amplitude of the measured signal as a function of the emission angle, θ.

The factors A_i^E translate the signal amplitude of each detector to the value of the remaining energy released on the silicon wall, in MeV, $E_{res_i} = A_i^E Q_i^{align}$. Figure 3.36 presents ^{238}U data from elastic scattering in two different silicon detectors, Si #35 and Si #36, before (a) and after (b) the energy calibration.

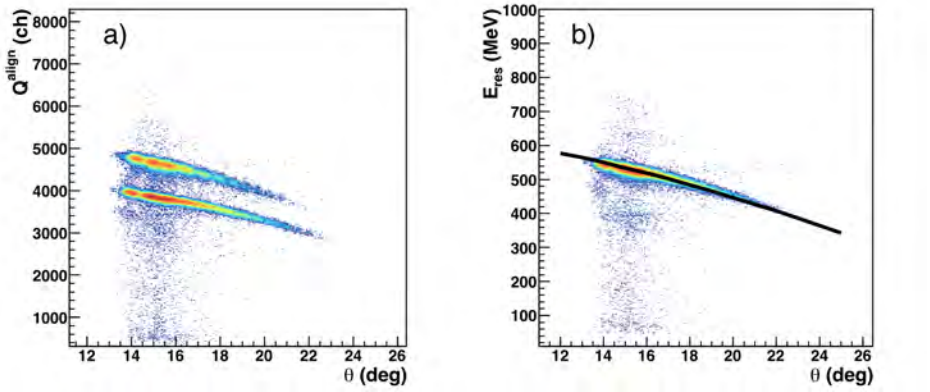

Figure 3.36: ^{238}U events from elastic scattering in Si detectors #35 and #36. Picture (a) shows the output of the alignment process as a function of the emission angle. Picture (b) shows the calibrated amplitude of both detectors matched to the simulated data, represented with a line, also as a function of the emission angle. The events that are uncorrelated to the emission angle come from ions that reach the interspace between two silicon detectors, where only a part of the residual energy is recover by the detector.

3.5.2 Energy Corrections

As shown in Fig. 3.36, many events present a residual energy that is uncorrelated to the emission angle, obtained from the elastic scattering kinematics. Most of these events, except random coincidences and inelastic events, are located at the edges of the silicon detectors. In these regions, ions may escape from the silicon lattice after few interactions, and the energy released in the detector does not correspond to the total residual energy of the ion. These events contribute to the background of the measurement and need to be subtracted.

Figure 3.37 shows the residual energy of ^{238}U from elastic scattering as a function of the horizontal position of the ions in the silicon wall. Pictures (a) and (b) present the residual energy distribution before and after subtracting the events placed at the silicon edges. The subtraction

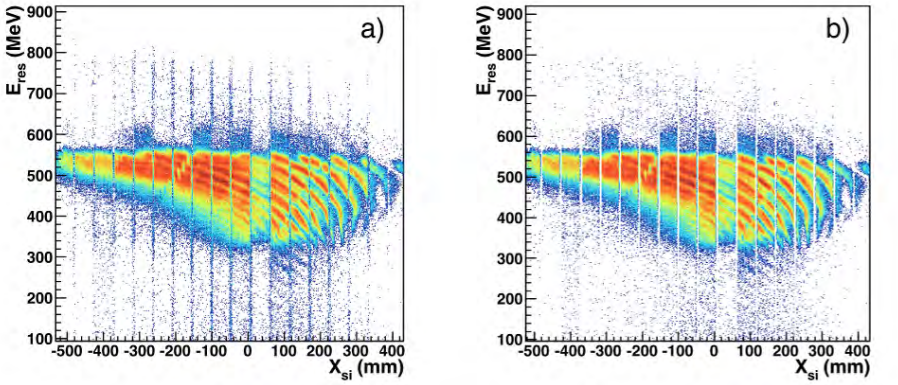

Figure 3.37: Residual energy distribution from elastic scattering as a function of the horizontal position, $x_{si} = x_{fp} + 841.4\tan(\theta_{fp})$, before (a) and after (b) subtracting events affected by edge effects. Events from Si #28 are missing in the region $0 \leq x_{si} \leq 50$ mm.

method removes all the events placed at $x_{si} \in [x_{si}^{inter} - 3$ mm, $x_{si}^{inter} + 3$ mm] being x_{si}^{inter} the position of the center of each interspace between two consecutive detectors.

Anomalous high-energy events are also present in Fig. 3.37. These events are placed at the edges of the silicons as well. Such high energies, produced by border effects on the Si inner held, are also removed by the subtraction method.

Some silicon detectors suffer from another mechanism that produces higher energies than expected. In order to investigate its origin, the detectors are scanned as a function of the angle at the focal plane, where the energy distribution is distributed between charge states. The detector Si #32 is shown as an example in Fig. 3.38 where a second bump at higher energy is present at $\theta_{fp} \approx 0$. This dependence with the orientation of the incoming ions indicates the presence of the *Channeling Effect*. The angle between the cubic lattice structure of the silicon detector and the direction of the incoming particle influences the signal amplitude: when ions impinge perpendicular to any lattice axis, the signal amplitude increases

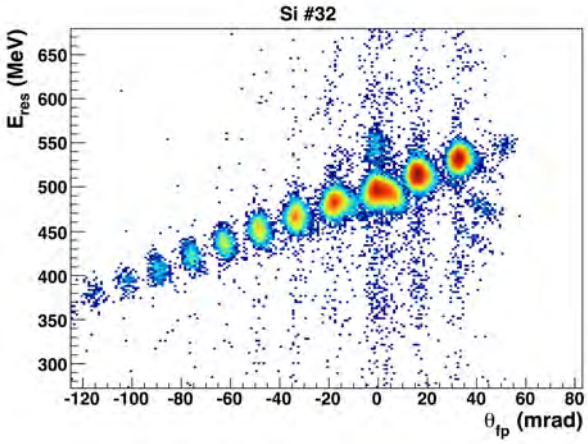

Figure 3.38: Residual energy distribution from elastic scattering as a function of θ_{fp}. The energy distribution is split in charge states for Si #32.

significantly in events where ions face a lattice node [54]. This effect reflects the behavior of the energy loss inside the lattice structure, with cells of 0.5 nm long. The resolution in angle and position is not enough to correct this effect.

Further corrections in the residual energy are applied once the nuclear charge and mass are identified for the ensemble of fission fragments in Sections 4.1 and 4.2.

3.6 Multiwire Chamber Calibration

The *Time of Flight (ToF)* of the ions is measured as time differences between the Start detector and the Multiwire Chamber. The Multiwire Chamber is divided into 20 sections. When an ion passes through one section, it produces a signal that is sent to a TDC module. These signals trigger the TDC module measurement that is stopped by the delayed

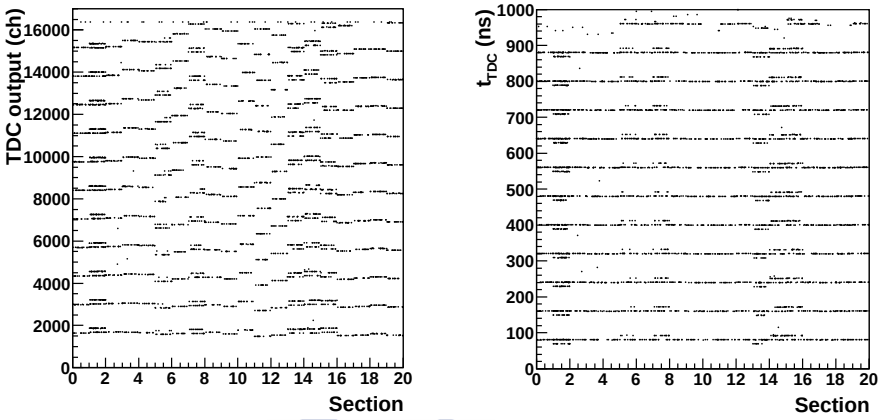

Figure 3.39: TDC time calibration. Fluctuation within the CFD module of 10 ns are present in channels #1, #5, #7, #13, #14, and #15.

signal from the Start detector.

The calibration of the TDC channels is performed with a time calibrator that sends signals to the TDC channels with a period of $\tau_n = 80n$ ns, being n integer values between 1 and 16. The TDC calibration converts the output signals into time scaled values through the equation $t_{TDC} = A + B \cdot Ch_{TDC}$, where t_{TDC} are calibrated time values, (A, B) are the calibration parameters, and Ch_{TDC} are non-calibrated TDC output.

Figure 3.39 shows the calibration of the 20 TDC-channels. The channels that correspond to sections #1, #5, #7, #13, #14, and #15 show a secondary peak with a constant shift of 10 ns with respect to the primary peak. This is an effect of fluctuations within the CFD module that will be partially removed by using the mass and nuclear charge identification.

The time measurement is inverted because the Start detector, with a fixed delay, defines the stop of the TDC. Therefore, the ToF must be calculated as:

$$ToF = Off_{ToF} - t_{TDC} \ , \tag{3.27}$$

with Off_{ToF} as the addition delay of the Start detector. The offset

Off_{ToF} is calculated from the elastic scattering, where the velocity of the scattered ion depends on the emission angle:

$$Off_{ToF} = \frac{D}{v(\theta)} + t_{TDC} \ , \tag{3.28}$$

being $v(\theta)$ the velocity of the scattered ion and D the distance between the Start detector and the multiwire chamber, derived from the reconstructed path:

$$D = \frac{Path}{\cos(\phi_{fp})} - \frac{D_{Target}^{Start}}{\cos(\theta)\cos(\phi)} + \frac{D_{FP}^{MW}}{\cos(\theta_{fp})\cos(\phi_{fp})} \ , \tag{3.29}$$

where $Path$ is the length of the trajectory followed by the ion between the target and the focal plane, projected into the horizontal axis, $D_{Target}^{Start} = 17.0$ cm is the distance between the target and the Start detector, and $D_{FP}^{MW} = 4.5$ cm is the distance between the focal plane and the multiwire chamber plane.

The offset Off_{ToF} is calculated for each section independently (see Fig. 3.40) with the velocity of ^{238}U from elastic scattering calculated as a function of the emission angle, using a LISE++ simulation where the energy loss in the target and in the start detector is taken into account.

Figure 3.41 shows the velocity of the ions from elastic scattering as a function of the emission angle in the laboratory frame. The main line corresponds to the elastic scattering of ^{238}U, the upper line corresponds to the elastic scattering of ^{197}Au, and the intermediate line corresponds to the 10-ns shift of ^{238}U events. The black line shows the theoretical velocity calculated with LISE++.

Apart from the 10-ns fluctuation of the CFD, another contribution to the background of the ToF measurement comes from missing correlations between the Start detector and the Multiwire chamber: when the chamber at the focal plane detects an ion that was not previously detected in the Start detector, the stop of the TDC provided by the delay signal of the Start detector corresponds to a later ion, therefore the measured ToF corresponds to the time difference between two different particles. This defect

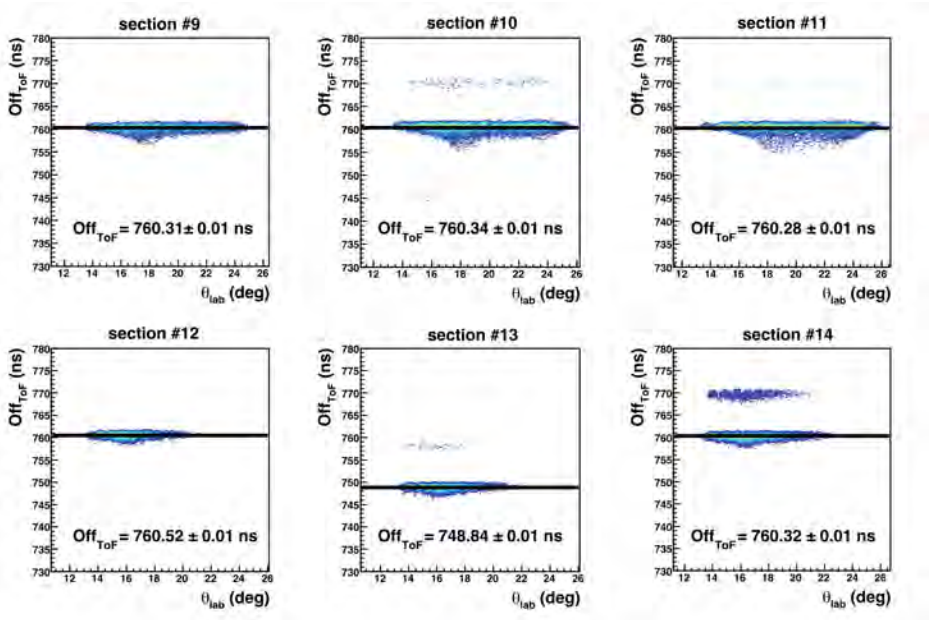

Figure 3.40: Offset calculation for ToF using ^{238}U from elastic scattering. Some sections of the multiwire chamber show a significantly different offset, such as section #13. One offset Off_{ToF_i} for each section $\#i$ is applied to the ToF calculation.

produces ∼100-ns-shifted replicas of the original distribution, following the cyclotron frequency. The relationship between the *ToF* and the residual energy permits to isolate the real distribution for the full range of fission fragments (see Fig. 3.42).

Further corrections of the evolution of the *ToF* measurement with the time will be applied from the fission fragment mass identification. Such corrections are explained in Section 4.1.

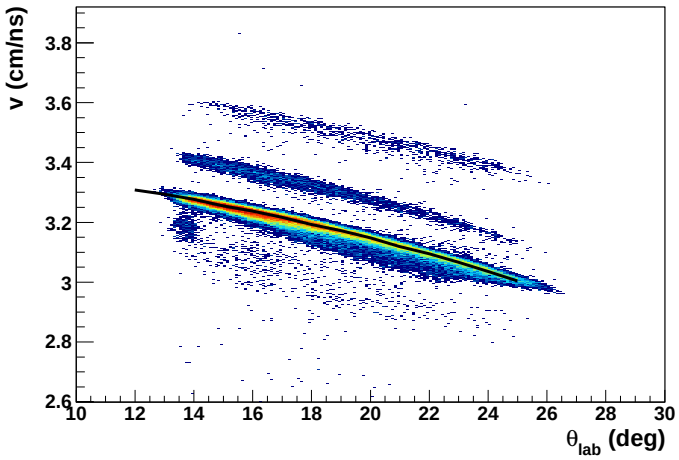

Figure 3.41: Velocity of the elastic scattering products as a function of the emission angle. ^{238}U and ^{197}Au are shown in the main and upper line, respectively. Intermediate line corresponds to 10-ns-shifted events of ^{238}U due to fluctuations in the CFD.

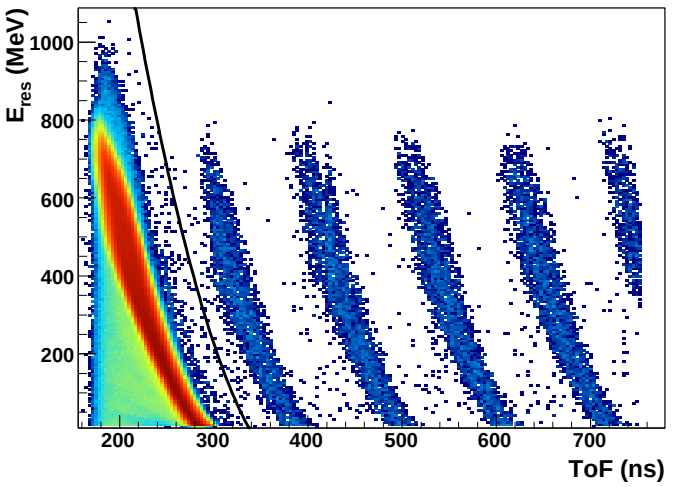

Figure 3.42: Events beyond the black line missed the correlation between the Start and the Stop of the *ToF* measurement.

USC
UNIVERSIDADE
DE SANTIAGO
DE COMPOSTELA

Chapter 4

Fission Fragment Identification

This chapter describes the methods applied to the data in order to obtain the isotopic identification of fragments produced in fission reactions induced by multi-nucleon transfer and fusion reactions, between a ^{238}U beam at 6.14 MeV/u and a ^{12}C target. The identification is done in terms of mass (A), nuclear charge (Z), and charge state (q). The mass and charge state are obtained from the magnetic rigidity reconstructed in the spectrometer with the measurement of the velocity and the total energy of the fragments. The nuclear charge is identified from the relationship between the energy loss in the ionization chamber and the remaining energy released in the silicon wall. Additionally, some corrections are applied to the direct measurements in order to improve the identification resolution. This chapter ends with a crosscheck of the fission fragment identification with the measurement of gamma emission from excited states in the fragments.

4.1 Mass and Charge State Identification

The mass (A) and charge state (q) of an ion are included in the definition of magnetic rigidity ($B\rho$), together with its velocity ($\beta\gamma$):

$$B\rho = 3.105 \left(\frac{A}{q}\right) \beta\gamma \ . \tag{4.1}$$

The previous equation permits to extract the A/q value from the velocity and the reconstructed $B\rho$ of the fragments. The velocity of the fragments is obtained from the measured *Time of Flight (ToF)* and the distance (D) that the fragments travel within the *ToF*.

$$\beta = \frac{D}{c \cdot ToF} , \qquad \gamma = \frac{1}{\sqrt{1-\beta^2}} . \tag{4.2}$$

D derives from the reconstructed $Path$, calculated in equation 3.29.

Independently, the mass of the fragments is obtained from the measurement of the total energy.

$$A^E = \frac{E}{u \cdot (\gamma - 1)} \tag{4.3}$$

where $E = E_{nm} + \Delta E + E_{res}$ is the total energy of the fragment, being E_{nm} the estimation of the energy loss released in the layers of matter previous to the ionization chamber (see Sec. 3.4.3); ΔE is the energy loss in the ionization chamber; E_{res} is the remaining energy, measured in the silicon wall. $u = 931.494\ MeV/c^2$ is the unified atomic mass unit. The combination of both observables, A^E and A/q, permits to extract the charge state value, and provides a measurement of mass with higher resolution than the one obtained directly from the energy.

Figure 4.1 (a) shows the mass and charge state identification of fragments from fusion-fission reactions of ^{238}U and ^{12}C. Each diagonal line corresponds to the group of masses with the same charge state value. The charge state distribution presented in Fig. 4.1 (b) is calculated as the ratio of A^E and A/q:

$$q^{cal} = A^E/(A/q) . \tag{4.4}$$

Fig. 4.1 (c) shows the fission-fragment mass distribution. The red line corresponds to the mass distribution calculated directly from the total energy and velocity (A^E), while the black line shows the mass distribution calculated as:

$$A^{cal} = q^{cal}_{int} \cdot (A/q) , \tag{4.5}$$

where $q^{cal}_{int} = \lfloor q^{cal} + 0.5 \rfloor$ is the closest integer value of q^{cal}.

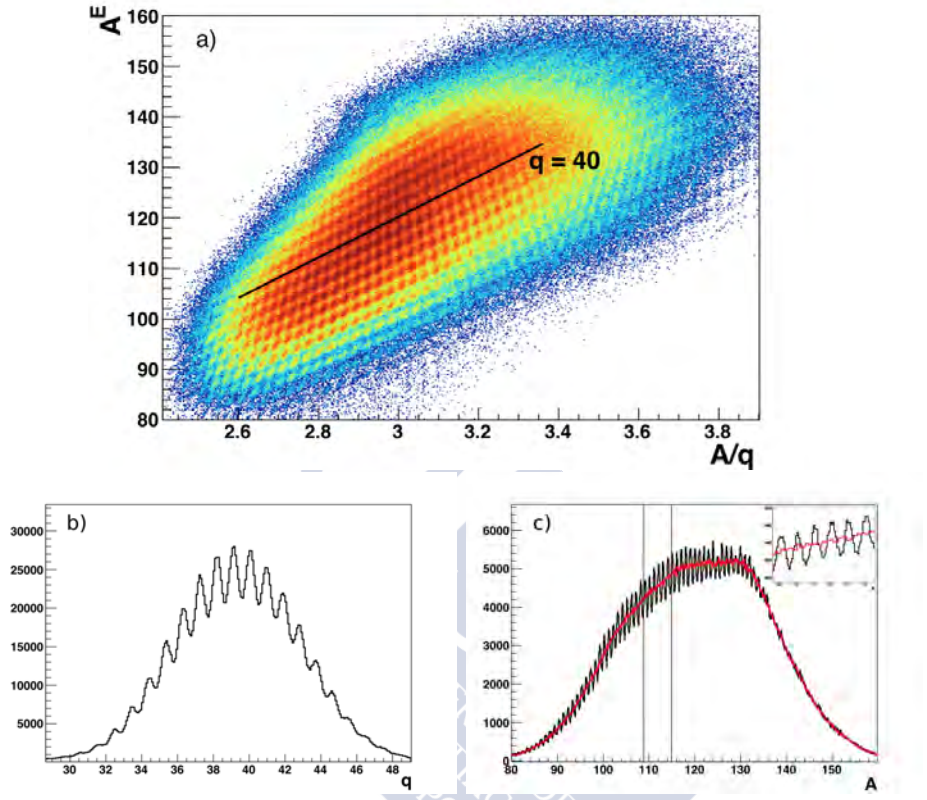

Figure 4.1: Mass and charge-state identification of fragments from fusion-fission reactions of ^{238}U and ^{12}C. In picture (a), the mass versus A/q is shown, the black line indicates one charge state $q = 40$. Picture (b) shows the charge state distribution. Picture (c) shows the mass distributions; in red, the distribution of mass obtained with the energy and the velocity of the fragments; in black, distribution of mass calculated with the measurement of A/q. The inset shows a zoom of the region within the lines.

The improvement in mass resolution is appreciable. However, the poor resolution for higher masses indicates that disalignments are present in some fundamental measurements. Corrections to the ToF, energy, and $B\rho$ of the fragments are applied in order to improve the mass resolution. More

sophisticated corrections to the charge states are included as well.

4.1.1 *ToF* Correction in A/q

The masses and the charge states are integer values; this feature defines a pattern in the relation between A^E and A/q that can be used to cross-check the ToF calibration.

The spacing of A/q for different masses evolves with the charge state, producing a smooth distribution of A/q. However, when A and q are such that A/q is also an integer value, this pattern describes a vertical line, and the A/q distribution produces a peak.

Figure 4.2 shows this effect. The simulated pattern of A versus A/q is presented in Fig. 4.2 (a); the blue lines indicate two different charge states, 40 and 50; the vertical red line indicates the combinations of A and q that produce $A/q = 3$. Experimental values of A^E versus A/q are shown in Fig. 4.2 (b) for one section of the multiwire chamber. The read line indicates the group of elements that forms a vertical line, clearly shifted from $A/q = 3$; the black lines reproduce the tilted neighboring lines of reference. The corresponding A/q distribution is shown in Fig. 4.2 (c). Several peaks are present, produced by the finite resolution of the measurement and the limited number of produced masses. The peak with lower standard deviation is placed at $A/q = 2.9172 \pm 0.0001$.

The shift in A/q is the effect of the optimization of the TDC gates that was carried out during the experiment between the elastic scattering measurements that are used for ToF calibrations and the current fission measurements. The redefinition of the TDC gates produces an additional offset in ToF that needs to be corrected:

$$ToF' = ToF + Off_T \ , \tag{4.6}$$

where ToF' is the corrected *Time of Flight* of fission fragments.

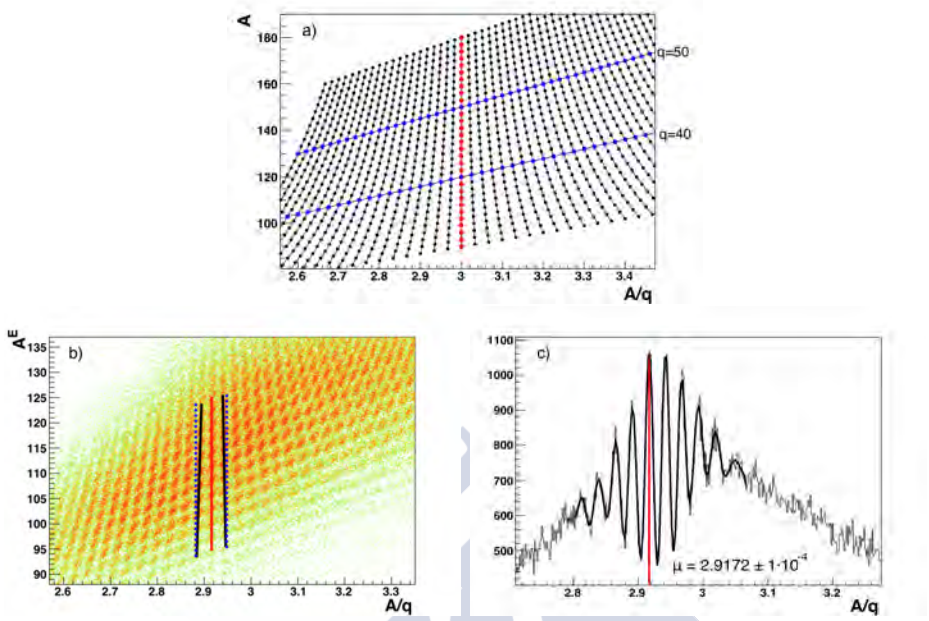

Figure 4.2: Pattern of A versus A/q. Pictures (a) and (b) show the relation between A and A/q for theoretical and experimental data, respectively. Picture (c) presents the projection of picture (b) over A/q. Red lines indicates the position of $A/q = 3$, in the experimental measurement this position appears shifted at $A/q = 2.9172 \pm 0.0001$.

Using equations 4.1 and 4.2, it is possible to infer an analytic relationship between Off_T with the difference of A/q, before and after correction,

$$\begin{aligned} Off_T &= -ToF + \sqrt{ToF^2 + K^2 \cdot \Delta\left(\frac{A}{q}\right)^2}, \\ \Delta\left(\frac{A}{q}\right)^2 &= \left(\frac{A}{q}\right)'^2 - \left(\frac{A}{q}\right)^2, \end{aligned} \tag{4.7}$$

where $K = \frac{3.105D}{cB\rho}$ and $\left(\frac{A}{q}\right)' = 3$.

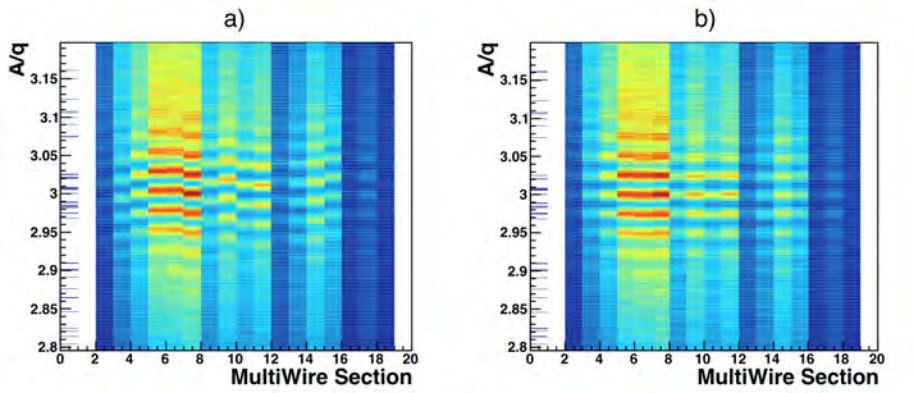

Figure 4.3: Refined alignment of the multiwire chamber using the definition of A/q. Pictures (a) and (b) show A/q as a function of the sections of the multiwire chamber, before and after correction, respectively. Differences from ± 0.3 ns to ± 1.5 ns were corrected.

For $A/q = 2.9172$, the offset results $Off_T = 5.763 \pm 0.002$ ns.

As it is shown in Fig. 4.3, the measurement of A/q permits to refine the Off_T calculation for different sections of the multiwire chamber, each section is corrected independently. The A/q method permits to correct differences of ± 0.3 ns between diverse sections of the multiwire chamber. Furthermore, A/q allows to correct the shift of the ToF measurement with the time during the experiment. Figure 4.4 shows the evolution of A/q over time, where each point corresponds to one experimental run. The observed evolution is understood as a drift of the multiwire chamber measurement with time. An additional offset, as a function of the run number, is applied to the ToF to correct this dependence.

4.1.2 Fission-Fragment Energy Corrections

The fission-fragment charge state (q) is derived from A^E and A/q values. q is affected by the energy measurement, since A^E is extract from the energy and velocity of the fragments. The combination of A^E and the

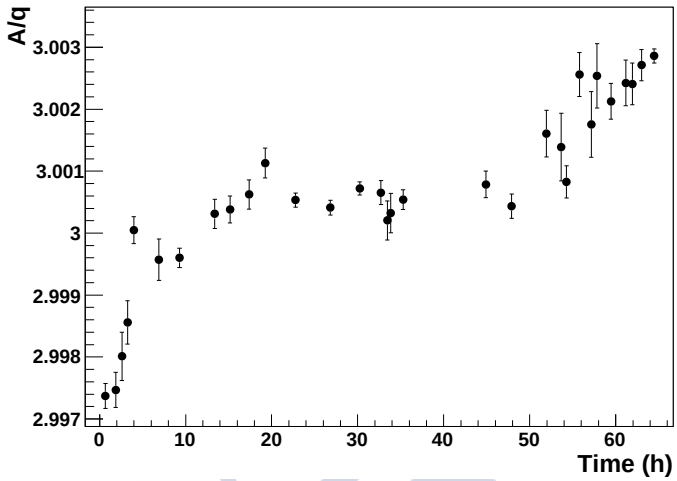

Figure 4.4: Evolution of the central peak ($A/q \approx 3$) over time. Each point correspond to one run, Off_T is defined as a function of the run number to correct this evolution.

A/q, once ToF is corrected, permits to balance deviations on the energy measurement using charge states as a reference.

4.1.2.1 Low E_{res} Correction

ADC modules usually present a non linear response to signals of very low amplitude. The residual energy of a fission fragment, measured on the silicon detectors, occasionally reaches very low values and this effect needs to be considered.

Figure 4.5 (a) shows the charge states of fission fragments as a function of the residual energy. It is observed that charge states present a behavior guided by non linear effects below 100 MeV. The solid line reproduces the shape of the charge state, $q = 36$, while the dashed line indicates the ideal behavior, extrapolated from higher energies, where the response of the

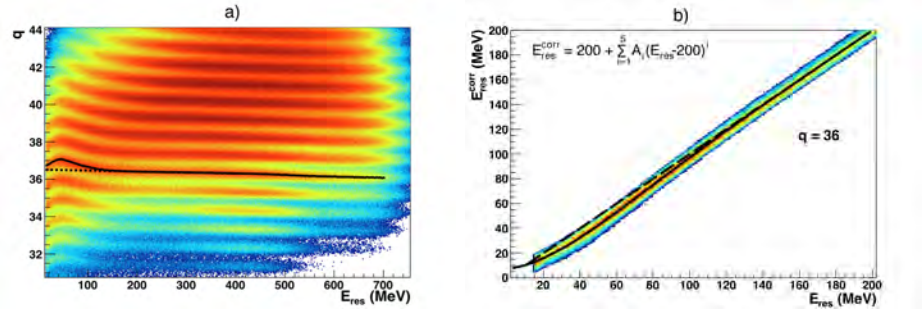

Figure 4.5: Figure (a): charge state distribution of fission fragments as a function of the residual energy in the silicon detectors. A non-linear response of the ADC modules is reflected at low energy. Figure (b): correction of the E_{res} below 200 MeV using a fifth-order polynomial function. Dashed lines represent the ideal behavior.

ADC is linear [1].

The residual energy is corrected below 200 MeV in order to make the charge states follow the ideal behavior. The correction applies a fifth-order polynomial function to the residual energy as it follows:

$$E_{res}^{corr} = 200 + \sum_{i=1}^{5} A_i \left(E_{res} - 200\right)^i \text{ (MeV)} , \tag{4.8}$$

where E_{res}^{corr} is the corrected residual energy and A_i are the parameters of the function. The function is defined with a fix point, $E_{res} = 200$ MeV, where the correction is null. The parameters A_i are calculated using the charge state $q = 36$. Figure 4.5 (b) shows the corrected residual energy of $q = 36$ that reproduces the ideal behavior as a function of the measured residual energy. The parameters, shown in Table 4.1, are such that the correction function reproduces the relation between both energies. Solid and dashed black lines represent the correction function and the identity relation, respectively.

[1] Notice that the charge state is shifted from the correct value. This shift, that affects to the full range of E_{res}, is not related with non-linear effects, and is corrected afterwards.

Parameters of E_{res}^{corr} function	
Parameter	**Value**
A_1	0.9927 ± 0.0003
A_2	$(-6.85 \pm 0.04) \cdot 10^{-4}$
A_3	$(-1.647 \pm 0.003) \cdot 10^{-5}$
A_4	$(-2.009 \pm 0.002) \cdot 10^{-7}$
A_5	$(-6.970 \pm 0.008) \cdot 10^{-10}$

Table 4.1: Parameters of low E_{res} correction.

4.1.2.2 *Bragg-Peak* correction in E_{nm}

The energy loss that the fission fragments release in the layers of matter before the ionization chamber was estimated in Section 3.4.3 as a linear function of the energy loss in the first row of the ionization chamber. This estimation assumes that the energy of the fission fragments remains far from the *Bragg Peak*, where the relationship between both is no longer linear. However, heavier fragments with higher stopping power reach quickly the *Bragg Peak* region at the energies of this experiment and deviate from the linear relation.

Figure 4.6 (a) shows the charge-state distribution of fission fragments as a function of the estimated energy loss not measured. The charge states deviate from a flat behavior at higher E_{nm}, indicating a wrong estimation of the energy not measured for heavier fragments. In order to recover a flat charge state distribution at higher E_{nm}, the energy loss not measured is redefined as a parabolic function of the energy loss in the first row of the ionization chamber as it follows:

$$E_{nm}^{corr} = A + B\Delta E_{row_1} + C\left(\Delta E_{row_1}\right)^2 \ , \tag{4.9}$$

where E_{nm}^{corr} is the new definition of the energy loss not measured, ΔE_{row_1} is the energy loss measured in the first row of the ionization chamber, and (A, B, C) are the function parameters.

Despite being close to the *Bragg Peak* region, ΔE_{row_1} remains far enough from the *Bragg Peak* to consider no nuclear-charge dependence

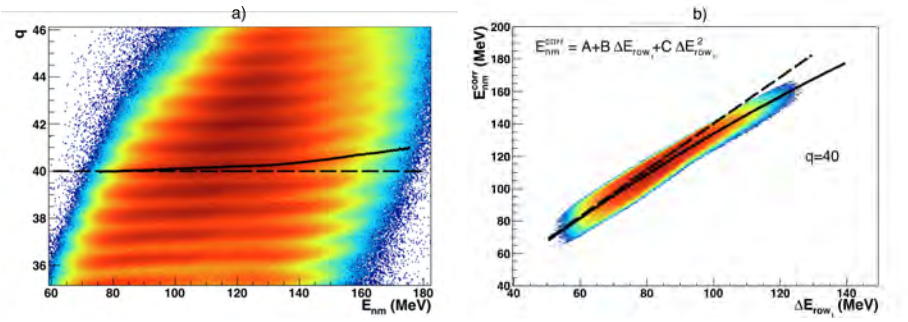

Figure 4.6: Figure (a): charge state distribution of fission fragments as a function of the energy loss not measured in layers of matter previous to the ionization chamber. The linear definition of E_{nm} as a function of the energy loss in the first row of the ionization chamber (ΔE_{row_1}) is not valid for higher E_{nm}, where heavy fragments reach the *Bragg Peak* region. Figure (b): calculation of the E_{nm} distribution needed to recover a flat behavior of $q = 40$ as a function of ΔE_{row_1}. Solid line represents a two-order polynomial function of ΔE_{row_1} that reproduces the E_{nm} distribution. Dashed lines represent the previous linear definition of E_{nm}.

in the relation between E_{nm} and ΔE_{row_1}. This assumption is verified with the experimental data: a dependence in the nuclear charge must reflect a dependence in the charge state (higher nuclear charges populate higher average charge states), however, the previous correction of the E_{nm}, independent of the charge state, fixes the full range of charge states.

Figure 4.6 (b) shows the energy loss not measured for charge state $q = 40$ as a function of the energy loss of the first row of the ionization chamber. The solid line represents the new definition of the energy not measured (E_{nm}^{corr}), while the dashed line reproduces the uncorrected E_{nm}. The parameters of Eq. 4.9 are extracted from this distribution and are shown in Table 4.2.

Parameters of E_{nm}^{corr} function	
Parameter	**Value**
A	-11.65 ± 0.13
B	1.709 ± 0.003
C	$(-2.53 \pm 0.02) \cdot 10^{-3}$

Table 4.2: Parameters of E_{nm} correction.

4.1.2.3 *Pulse Height Defect* (PHD) on Silicon detectors

Solid detectors such as silicon crystals suffer from a number of effects that reduces the amplitude of the output signal with respect to the energy released inside the detector. The combination of these effects are known as *Pulse Height Defect* (PHD) and it depends on the mass of the ion. For the same incident energy, the heavier the ions, the smaller the amplitude of the signal [55]. The PHD involves three main separated phenomena [56]: The first contribution is the energy that the ion loses in the entrance window and dead layers of the detector. This contribution increases with the stopping power of the ion, which is higher for heavier ions. A second contribution is the non-ionizing collisions that heavy ions suffer inside the detector. Finally, the third factor involves the high rate of electron-hole recombination expected in the dense plasma created along the ion track.

The calibration procedure was perform using the elastic scattering of ^{238}U, with a mass twice higher than the average of the fission fragments. With such large mass difference, the *Pulse Height Defect* plays an important role: being tens of MeV higher in ^{238}U than in the fission fragments [57]. The residual energy of fission fragments measured in the silicon detectors is, therefore, overestimated tens of MeV above the real value. This overestimation of the E_{res} produces a wrong mass identification, which is reflected in a wrong assignment of the charge states. The A/q distribution of one charge state produces a spacing of peaks that is incompatible with the spacing of masses of one unit.

Figure 4.7 shows the arbitrary case $q = 40$ selected in Fig. 4.7 (a)

with a A/q distribution shown in Fig. 4.7 (b). The A/q distribution is transformed into mass distribution, $A^{corr} = A/q \cdot q^{corr}$, with different values of charge state in Fig. 4.7 (c). The vertical axis is the difference between calculated masses and closest integer values, $A_0 = \lfloor A^{corr} + 0.5 \rfloor$. The charge state $q^{corr} = 39$ satisfies the separation of one unit between masses with the calculated mass remaining always close to the integer value. In the region of $q \approx 40$, the correct charge state is, therefore, $q^{corr} = q - 1$. The corrected charge state, q^{corr} is used to define a new E_{res} correction that takes into account the *Pulse Height Defect*. This correction provides a value of the excess of energy produced by the *Pulse Height Defect*, ΔE^{PHD}, as a function of the corrected mass of the fragments, $A^{corr} = A/q \cdot q^{corr}$.

Schmitt et al. developed, in Ref. [55], an energy calibration method for silicon detectors that depends on the mass of the incoming ion:

$$E = (a + a'A)P + b + b'A \,, \tag{4.10}$$

being E the calibrated energy, P the pulse of the signal, A the mass of the ion, and (a, a', b, b') the calibration parameters. Following this equation, the excess of energy produced by the *Pulse Height Defect* between ^{238}U and a fission fragment is

$$\begin{aligned} \Delta E^{PHD} =& (a + a'A_U)P + b + b'A_U - \left[(a + a'A_{ff})P + b + b'A_{ff}\right] \\ =& (A_U - A_{ff})a'P + (A_U - A_{ff})b' \,, \end{aligned} \tag{4.11}$$

where $A_U = 238$ is the mass of ^{238}U, and A_{ff} is the mass of the fission fragment. Considering that the measured residual energy, E_{res}, is a linear function of the pulse of the signal ,P, the excess of energy can be expressed as:

$$\frac{\Delta E^{PHD}}{238 - A_{ff}} = a''E_{res} + b'' \,. \tag{4.12}$$

The parameters a'' and b'' are obtained from the relation between the excess of energy, divided by the difference of masses respect to Uranium, and the residual energy, for the charge state $q = 40$, which covers the largest range of E_{res}. The excess of energy, $\Delta E^{PHD}\big|_{q=40}$, is defined as

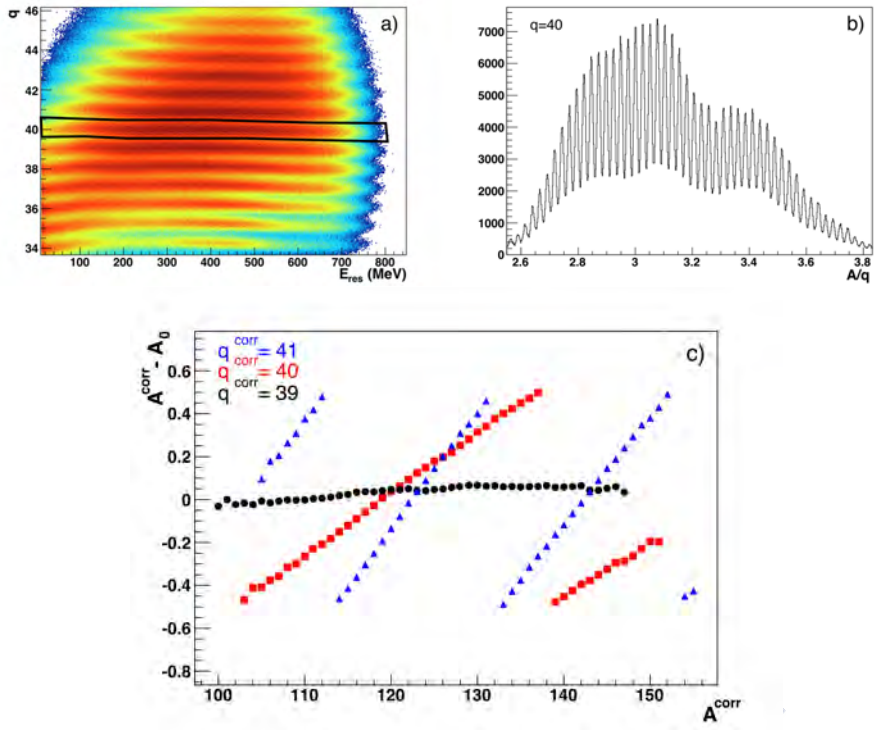

Figure 4.7: Charge-state identification. Figures (a) and (b) show the selection and the A/q distribution of $q = 40$, respectively. Figure (c) shows the assignment of the correct charge state $q^{corr} = 39$ based on the difference between the reconstructed mass, $A^{corr} = (A/q) \cdot q^{corr}$, and the corresponding integer value, A_0.

the difference of energy needed to shift the charge state $q = 40$ to the correct position $q^{corr} = 39$:

$$\Delta E^{PHD}\big|_{q=40} = (\gamma - 1) \cdot u \cdot (A/q)|_{q=40} \ , \tag{4.13}$$

and the mass of the fragments A_{ff} is extracted from A/q:

$$A_{ff}\big|_{q=40} = 39 \cdot (A/q)|_{q=40} \ . \tag{4.14}$$

Figure 4.8 shows the relation between $\frac{\Delta E^{PHD}}{238-A_{ff}}\Big|_{q=40}$ and E_{res} where

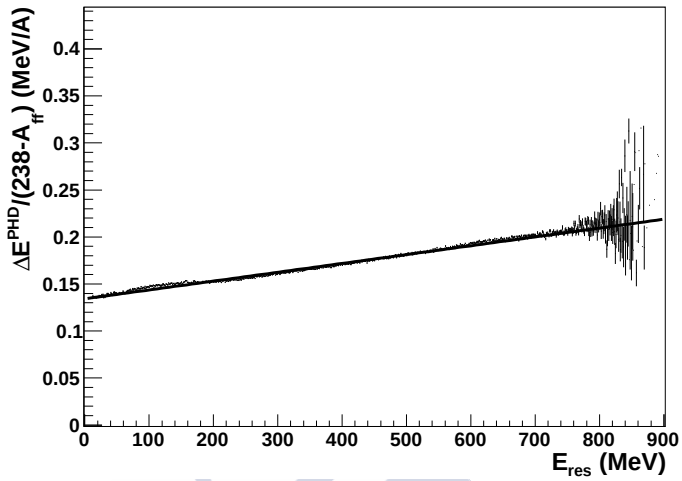

Figure 4.8: Calculation of the Excess of energy ($\Delta E^{PHD}/(238 - A_{ff})$) for q=40, as a function of the measured residual energy (E_{res}).

parameters a'' and b'' are extracted from a linear fit. The values of the parameters are shown in Table 4.3. These parameters fit, as well, the rest of the charge state distribution.

Parameters of $\frac{\Delta E^{PHD}}{238-A_{ff}}$	
Parameter	**Value**
a''	$0.13423 \pm 6 \cdot 10^{-5}$
b''	$(9.40 \pm 0.02) \cdot 10^{-5}$

Table 4.3: Parameters of $\frac{\Delta E^{PHD}}{238-A_{ff}}$ as a function of E_{res}.

The excess of energy, ΔE^{PHD}, is calculated, in the full range of fission fragments, as a function of the residual energy (E_{res}), the A/q parameter, and the corrected charge state (q^{corr}):

$$\Delta E^{PHD} = (238 - (A/q) \cdot q^{corr}) \cdot (a'' E_{res} + b'') \; . \tag{4.15}$$

q^{corr} is defined in the full range of the fission fragments using a second-

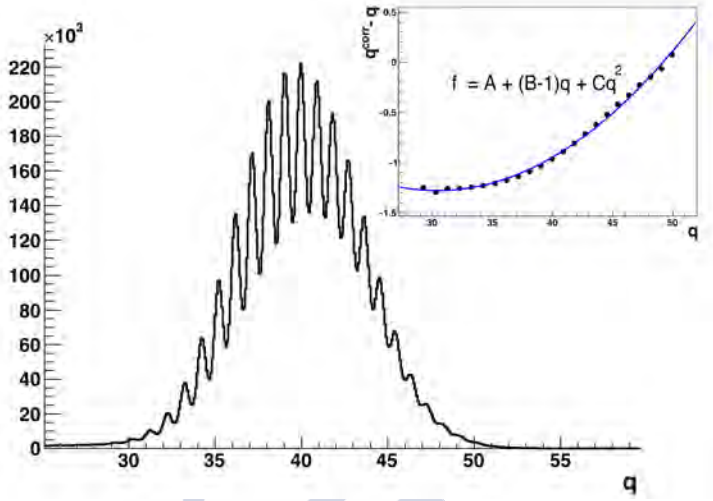

Figure 4.9: Charge-states distribution before *PHD* correction. The inset shows the quadratic relationship between the uncorrected and the corrected charge states distribution, q and q^{corr}.

order polynomial function that relates the charge state distribution, q, with its correct value, q^{corr}, that satisfies two conditions: every peak of the q^{corr} distribution is centered in the corresponding integer value, and $q^{corr}|_{q=40} = 39$.

Figure 4.9 shows the q distribution of fission fragments before *PHD* corection. The inset presents the quadratic relation between the q distribution and the correct distribution, q^{corr}. The values of the q^{corr} parameters are shown in Table 4.4.

Parameters of q^{corr} function	
Parameter	**Value**
A	2.09 ± 0.23
B	0.779 ± 0.012
C	$(3.63 \pm 0.15) \cdot 10^{-3}$

Table 4.4: Parameters of the corrected charge state distribution, q^{corr}.

The total energy is now defined as sum of the energy loss in the ionization chamber, the corrected energy loss not measured, and the corrected residual energy released in the silicon detectors, subtracting the excess of energy produced by the *Pulse Height Defect*.

$$E = \Delta E + E_{nm}^{corr} + E_{res}^{corr} - \Delta E^{PHD} \tag{4.16}$$

4.1.3 $B\rho$ Correction

The reconstruction of the fission fragments magnetic rigidity is performed, as explained in Sec. 2.4.3, based on the ionic optics of the VAMOS spectrometer. However, the behavior of the spectrometer is not as ideal as assumed in the reconstruction, and it may present third-order aberrations for ions far from the central trajectory ($B\rho/B\rho_0 = 1$, $\theta_v = 0$). Such aberrations produce a difference between the real magnetic rigidity of the ions and the reconstructed one.

One of the origins of these aberrations is the field leak that affects the magnets at their edges, creating border effects. Another factor is the interplay between the dipole and quadrupoles fields: for outer regions, the quadrupole field is stronger and affects that of the dipole due to its proximity. Particles traversing these regions do not follow the expected trajectories.

The fission-fragment mass identification permits to correct the reconstructed magnetic rigidity, as a function of the relative $B\rho$ and the angle in the VAMOS axis, assuming that the reconstructed path and angle are not sensitive to the effects of field aberrations. A deviation of 0.2% of the total variation observed in $B\rho$ proves this assumption: the reconstructed path and angle are not sensitive to such small variation.

Each charge state defines a distribution of A/q that, as shown in Figure 4.7 (c), can be compared with nominal values A_i/q_i, being A_i and q_i integer values. The difference between the mean value of A/q for each pair (A_i, q_i), and the nominal value A_i/q_i, can be expressed as a difference of magnetic

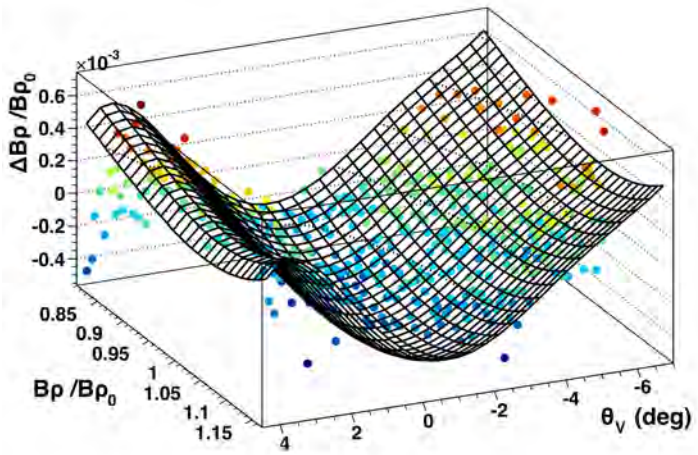

Figure 4.10: Magnetic-rigidity correction. The deviation of the reconstructed $B\rho$ respect to the real value ($\Delta(\delta)$) is reproduced as a two-dimensional function of δ and θ_V.

rigidity, once the *ToF* of the fragments is correctly defined:

$$\Delta\left(\delta\right)_i = \frac{1}{B\rho_0} \cdot 3.105 \cdot \beta\gamma \cdot \Delta\left(\frac{A}{q}\right)_i \ , \tag{4.17}$$

where $\delta = B\rho/B\rho_0$ and $\Delta(A/q)_i = A_i/q_i - < A/q >_i$.

Figure 4.10 shows $\Delta(\delta)_i$ as a function of the reconstructed δ and θ_V, for different masses and charge states, represented with colored dots. The maximum deviation, observed in the full range of $B\rho$ and θ_V, correspond to 0.2%. $\Delta(\delta)_i$ can be described with a two-dimensional fifth-polynomial function, which parameters are fitted to the distribution,

$$\Delta(\delta) = \sum_{i=0}^{5} A_i(\theta_v - x_0)^i + \sum_{j=0}^{5} B_j(\delta - y_0)^j \ . \tag{4.18}$$

The parameters of the $\Delta(\delta)$ function, A_i, B_j, x_0, and y_0 are shown in Table 4.5.

The correct magnetic rigidity is, therefore, defined as:

$$B\rho^{corr} = (\delta + \Delta(\delta)) \cdot B\rho_0 \ . \tag{4.19}$$

Parameters of δ correction.	
Parameter	**Value**
x_0	-0.79 ± 0.23
$A1$	$(-1.25 \pm 0.90) \cdot 10^{-5}$
$A2$	$(2.43 \pm 0.19) \cdot 10^{-5}$
$A3$	$(2.14 \pm 0.41) \cdot 10^{-6}$
$A4$	$(-4.42 \pm 0.75) \cdot 10^{-7}$
$A5$	$(-6.06 \pm 1.20) \cdot 10^{-8}$
y_0	0.626 ± 0.093
$B1$	$(-0.24 \pm 1.57) \cdot 10^{-4}$
$B2$	$(-3.00 \pm 0.24) \cdot 10^{-3}$
$B3$	$(4.59 \pm 0.47) \cdot 10^{-3}$
$B4$	$(-0.31 \pm 1.35) \cdot 10^{-3}$
$B5$	$(0.83 \pm 3.67) \cdot 10^{-3}$

Table 4.5: Parameters of $\Delta(\delta)$ as a function of θ_V and δ.

4.1.4 Further Charge States Corrections

The charge-state distribution is observed to evolve with the vertical position of the fission fragments. Furthermore, as shown in Fig. 4.11, the behavior depends on the silicon detector that the fragment impinges on. The charge-state calculation is corrected by the vertical position of the fragment in the plane of the silicon detectors, $y_{si} = y_{fp} + 841.8 \tan(\phi_{fp})$, in order to recover a flat distribution in y_{si}. This correction consists on a third-order polynomial function on y_{si} with parameters calculated for each silicon detector independently. This correction improves the charge state resolution in 10%, resulting in $(1.410 \pm 0.001)\%$ of $FWHM$ for q=40. The charge state distribution is shown in Fig. 4.11 (d) before (red) and after (black) correction.

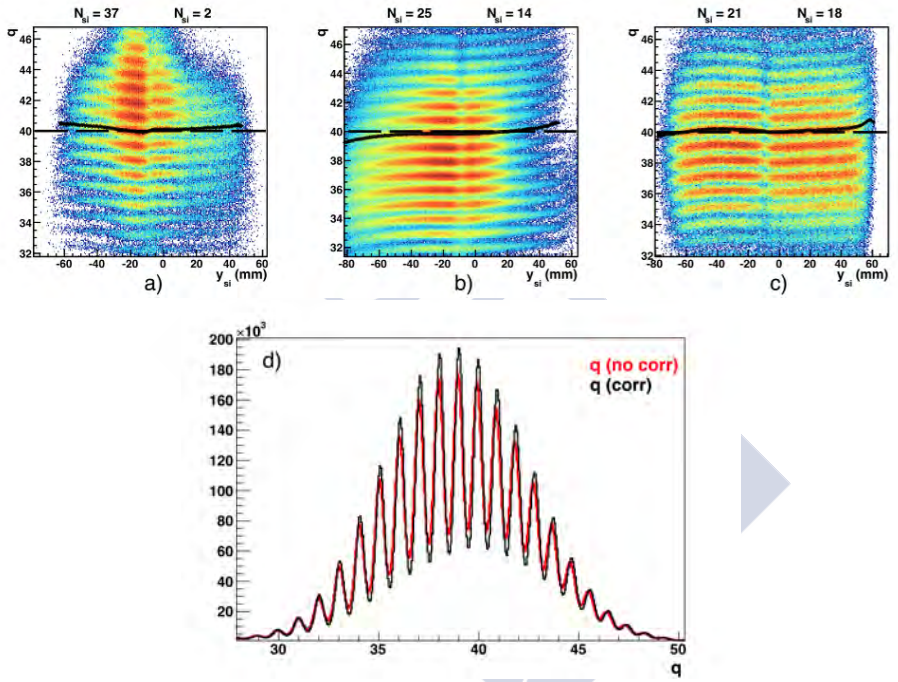

Figure 4.11: Figures (a), (b), and (c): evolution of the charge states with the vertical position of the fission fragments. The behavior is different for different silicon detectors. Figure (d): charge state distribution before (red) and after (black) correction.

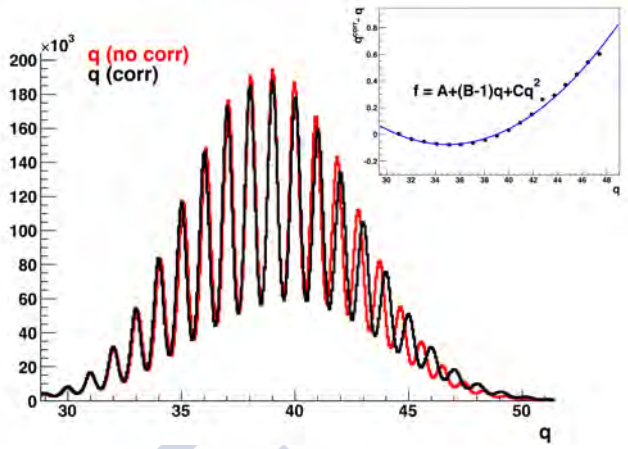

Figure 4.12: Charge-state distribution before (red) and after (black) the quadratic correction. Inset shows the quadratic function, parameters are presented in Table 4.6.

After corrections, the charge state distribution at higher values remains shifted with its mean value of each peak lower than the appropriate integer value. This shift is corrected by means of a quadratic function:

$$q^{corr} = A + Bq + Cq^2 \ , \tag{4.20}$$

with the parameters of Table 4.6.

Parameters of q correction.	
Parameter	**Value**
A	5.55 ± 0.20
B	0.678 ± 0.010
C	0.00460 ± 0.00013

Table 4.6: Parameters of q correction.

Figure 4.12 shows the charge-state distribution before and after correction, the quadratic function is shown in the inset.

The mass distribution, after corrections, is shown in Fig. 4.13. In Fig. 4.13 (b) and (c), the mass distribution is shown for both orientations

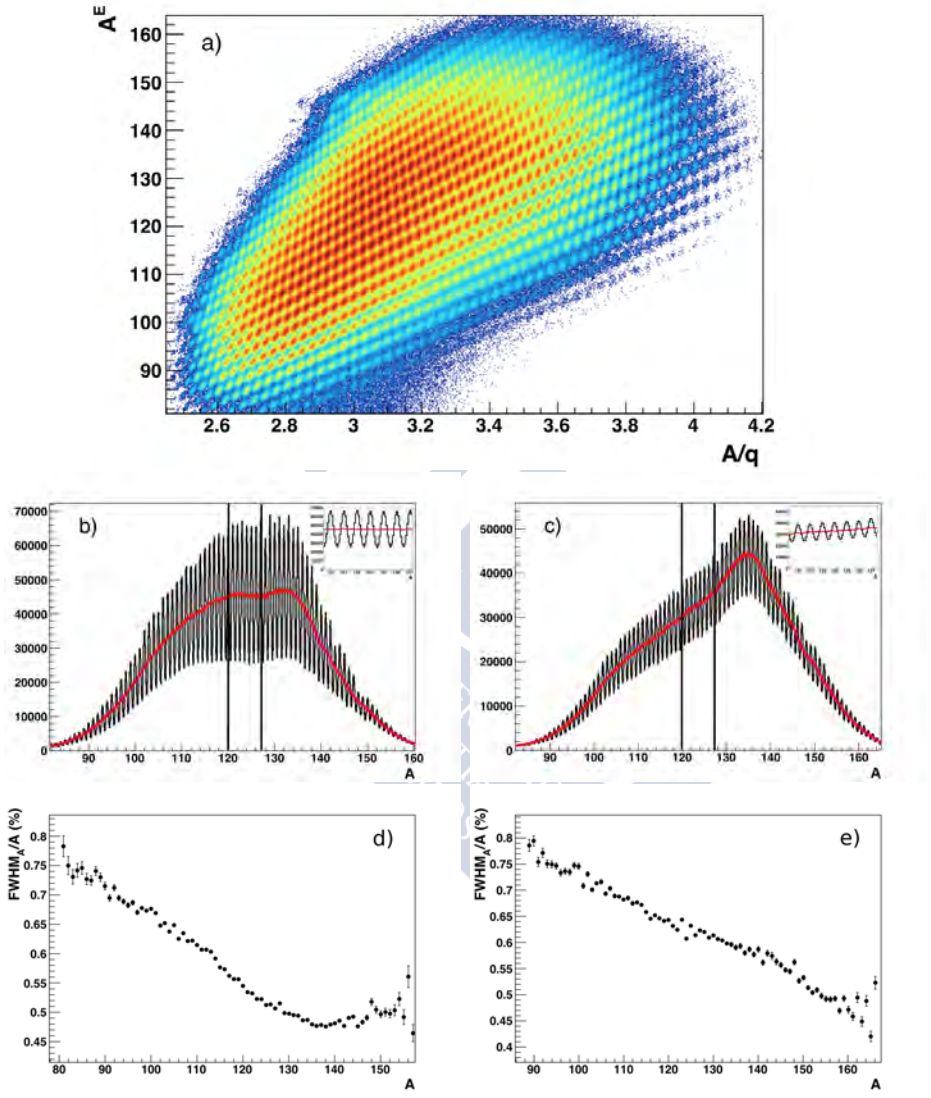

Figure 4.13: Figure (a): mass distribution of fission fragments as a function of A/q. Figures (b) and (c): mass distribution for VAMOS rotated at 20 deg and 14 deg, respectively. Red and black curves indicates the mass distribution obtained from the direct measurement of energy and velocity (A^E), and from the A/q measurement (A^{cal}). The insets show a zoom of the region within the lines. Figures (d) and (e): mass resolution, as $FWHM_A$ over A, in percentage, for VAMOS at 20 deg and 14 deg.

of VAMOS. The red curves represent the mass measurement extracted from the energy and velocity of the fragments (A^E), and the black curves represent the mass reconstruction improved with the A/q measurement, (A^{cal}).

The mass resolution ($\Delta A/A$), shown in Figs. 4.13 (d) and (e), decreases with the mass, indicating that the resolution is not limited by the energy measurement but by the *ToF* resolution. Heavier masses are slower, yielding lower value of relative *ToF* resolution. In the same way, the velocity of the fragments with VAMOS rotated at 14 deg is higher compared with VAMOS at 20 deg, hence, the relative *ToF* and mass resolution worsens. Nevertheless, Figure 4.13 (d) shows a minimum in the resolution at higher masses of $\Delta A/A \approx 0.47\%$, this limit is determined by the resolution in the magnetic rigidity reconstruction.

4.2 Nuclear Charge Identification

The identification of the nuclear charge (Z) of fission fragments is based on the relation between the energy loss that the fragments release in the ionization chamber and the residual energy, measured in the silicon wall.

The energy that an ion losses passing through matter is mostly produced by electronic interactions between the ion and the atoms of the matter (see Sec. 2.4.2.3). This interplay between the ion and the atoms produces an exchange of electrons that leaves the ion with a net charge in each interaction. The energy loss of the ion is strongly dependent of this charge, parameterized by the *Bethe-Block* equation.

The charge distribution that an ion acquires when passing through matter tends to the equilibrium charge, which is reached after a certain number of collisions, when electron capture and loss processes become balanced.

The equilibrium charge depends on the nuclear charge and the velocity

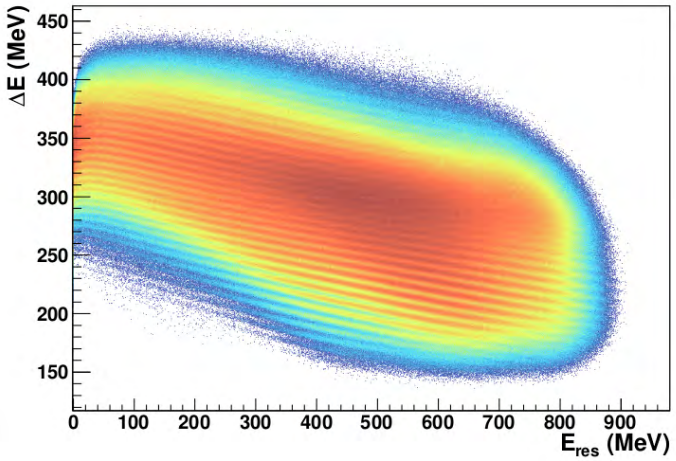

Figure 4.14: Energy loss of fission fragments, induced in $^{238}U+^{12}C$ reactions, as a function of the residual energy. Each curve defines one nuclear charge.

of the ion, as well as on the matter properties (Z, A, mean excitation energy). Therefore, there is an unequivocal relation between the energy loss and the nuclear charge of an ion, for a given velocity within a given material.

The total energy is an optimum indicator of the velocity of the ion. The combination of both, energy loss and residual energy, permits to scan the energy loss as a function of the velocity, isolating the nuclear charge contribution.

Figure 4.14 shows the energy loss of fission fragments as a function of the residual energy. Each ion defines a curve that ranges from the *Bragg Peak*, at lower residual energy, up to hundreds of MeV. The heavier ions, which correspond to the curves at higher energy loss, are affected by a low intrinsic resolution in the region of higher residual energy.

4.2.1 Energy Loss Corrections

The measurement of the energy loss suffers from defects in the ionization chamber due to pads misalignments and energy-loss evolution with the position and pressure that deteriorate the nuclear charge resolution and need to be corrected.

4.2.1.1 Fine alignment of the ionization chamber

The ionization chamber is divided into five different sections, perpendicular to the fragment trajectory. These sections were aligned using the elastic scattering of ^{238}U in ^{197}Au, which losses a large energy compared to fission fragments (see Sec. 3.4.1). The low energy loss released by fission fragments requires a refined alignment between pads. This alignment is performed using the position of the peaks that different nuclear charges produce in the energy loss distribution. Each section of the ionization chamber covers a different range of residual energy, with a region of overlapping between neighboring sections. The alignment method defines a slice of 14 MeV in E_{res}, compares the energy loss in both neighboring sections within the E_{res} slice, and scales the energy loss of one of the sections to match the peaks of both neighboring pads. The method is illustrated in Fig. 4.15.

Each picture of Fig. 4.15 shows the energy-loss distribution of two consecutive sections, for one slice in E_{res}. The peaks of each distribution are fitted with Gaussian functions in a region of good resolution. The insets show the ratios of mean values between both sections as a function of the mean values in one of the sections. The average ratio, shown as a horizontal line, defines the scaling factor that corrects the measurement. The values of the average ratios are presented in Table 4.7.

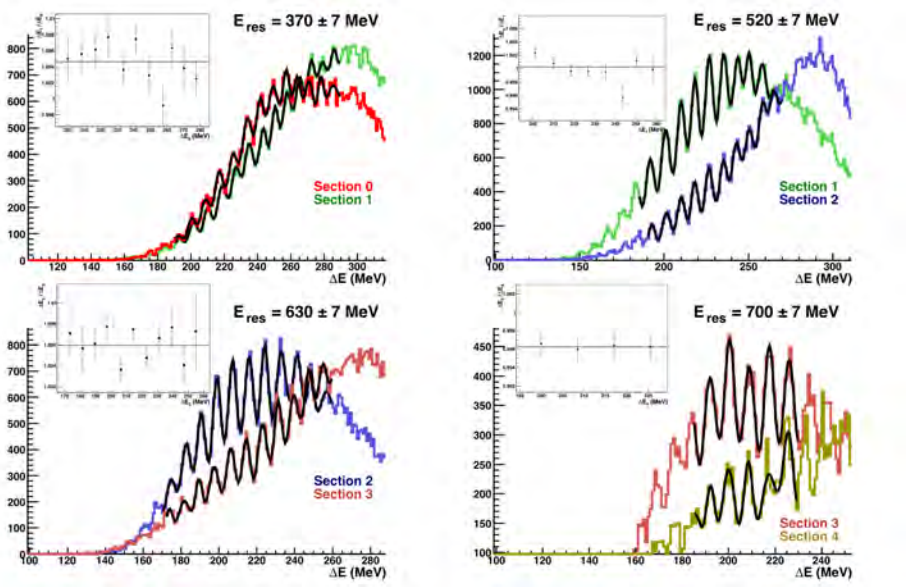

Figure 4.15: Realignment of the ionization-chamber sections with fission fragments. Each picture presents the energy-loss distribution of two consecutive sections of the ionization chamber, gated with a slice of 14 MeV in E_{res}. The peaks of the distribution, produced by different nuclear charges, are fitted with Gaussian functions. The insets show the ratio of the mean values of the Gaussians between the two sections as a function of the mean values of one of the sections. The black lines represent the average ratios.

ΔE **alignment.**	
Ratio	**Value**
$R_{10} = \Delta E_1/\Delta E_0$	1.0046 ± 0.0007
$R_{21} = \Delta E_2/\Delta E_1$	1.0011 ± 0.0003
$R_{23} = \Delta E_2/\Delta E_3$	1.0059 ± 0.0004
$R_{34} = \Delta E_3/\Delta E_4$	0.9962 ± 0.0007

Table 4.7: Nuclear charge alignment in different sections of the ionization chamber.

The aligned energy loss (ΔE^a) is corrected section by section:

$$\begin{aligned}
\Delta E_0^a &= R_{10} \cdot R_{21} \cdot \Delta E_0 \ , \\
\Delta E_1^a &= R_{21} \cdot \Delta E_1 \ , \\
\Delta E_2^a &= \Delta E_2 \ , \\
\Delta E_3^a &= R_{23} \cdot \Delta E_3 \ , \\
\Delta E_4^a &= R_{34} \cdot R_{23} \cdot \Delta E_4 \ ,
\end{aligned} \tag{4.21}$$

where section 2 is the reference and R_{ij} is the ratio between sections i and j.

4.2.1.2 Energy-loss evolution with the position at the ionization chamber

The energy loss of fission fragments in the ionization chamber presents an evolution with the vertical position. This effect was already observed and corrected with elastic scattering data. The presence of this effect in fission fragments reveals that the correction extracted from elastic scattering is not enough in the energy regime of fission fragments. A new correction is applied using, directly, the energy loss of fission fragments. The procedure consists on calculating the ratio between the nominal value of energy loss of one intermediate nuclear charge and the actual energy loss as a function of the vertical position.

Figure 4.16 shows the ratio between the nominal value of energy loss for one intermediate nuclear charge (ΔE_N), obtained by selecting one line in Fig.4.14, and the energy loss measured in the ionization chamber (ΔE), as a function of the vertical position of the fragments in the middle of the ionization chamber, $y_{IC} = y_{fp} + 653.8 \tan(\phi_{fp})$. Each section presents an evolution slightly different, hence, the correction is performed for each section independently. The black lines in Fig. 4.16 reproduce the behavior of the chosen nuclear charge, while the curves above and below each line correspond to the rest of nuclear charges.

The behavior of the ratio is parameterized by a third-order polyno-

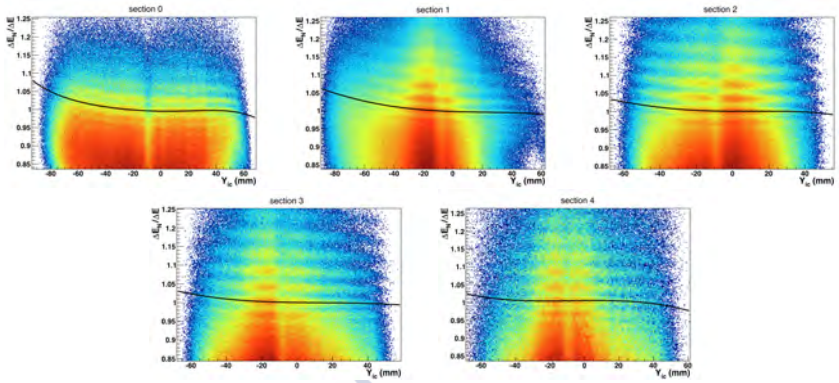

Figure 4.16: Evolution of the energy loss with the vertical position of the fragments projected in the middle of the ionization chamber. Each picture represent the ratio between the nominal energy loss of one intermediate nuclear charge and the measured energy loss in one section of the ionization chamber.

mial function of the vertical position of the fragments. The energy loss, corrected by the vertical position, is then:

$$\Delta E^{corr}|_i = \left(a_i + b_i \cdot y_{IC} + c_i \cdot (y_{IC})^2 + d_i \cdot (y_{IC})^3\right) \cdot \Delta E|_i \ , \qquad (4.22)$$

where (a_i, b_i, c_i, d_i) are the parameters for the section i.

The energy loss presents also an evolution with the horizontal position when the fragments reach some of the silicon detectors. Figure 4.17 present the ratio of the nominal energy loss of one intermediate nuclear charge and its measured energy loss, as a function of the horizontal position of the fragments projected onto the plane of the silicon wall, $x_{si} = x_{fp} + 841.4 \tan(\theta_{fp})$. The solid lines reproduces the behavior of the ratio for silicon detectors #1, #11, #15, and #18, while the dashed lines indicates the expected flat behavior.

The correction follows the same procedure of the previous case with the vertical position. The energy loss is scaled with a third-order polynomial function of the horizontal position:

$$\Delta E^{corr}|_i = \left(a_i + b_i x_{si} + c_i x_{si}^2 + d_i x_{si}^3\right) \cdot \Delta E|_i \ . \qquad (4.23)$$

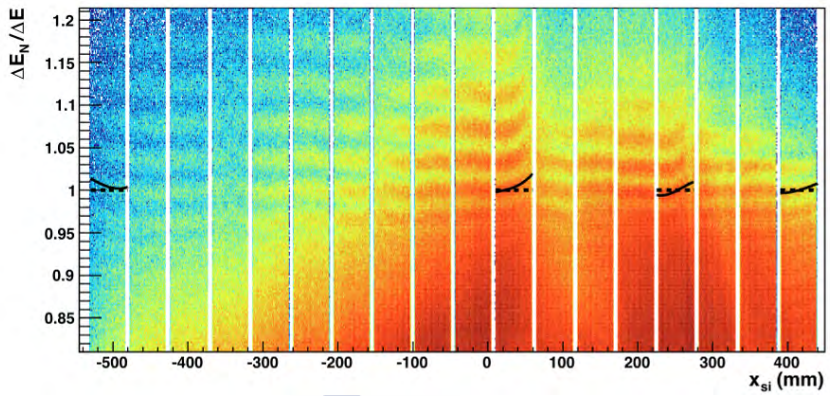

Figure 4.17: Evolution of the energy loss with the horizontal position of the fragments, projected in the plane of the silicon wall. The vertical axis presents the ratio between the nominal energy loss of one intermediate nuclear charge and the measured energy loss.

The subscript indicates, in this case, the silicon number.

4.2.1.3 Pressure variation

The gas pressure inside the ionization chamber varies over the time of the experiment, changing the effective thickness of isobutane gas from one run to the other, and thus, the energy loss of the fission fragments. In order to assure a constant nuclear charge identification over time, the pressure variation is compensated by scaling the energy loss run by run.

Figure 4.18 shows the ratio between the average energy loss (ΔE_0) that fragments release in the ionization chamber, and the energy loss (ΔE) measured on each run, as a function of time.

Both, the energy loss and residual energy are compensate by the pres-

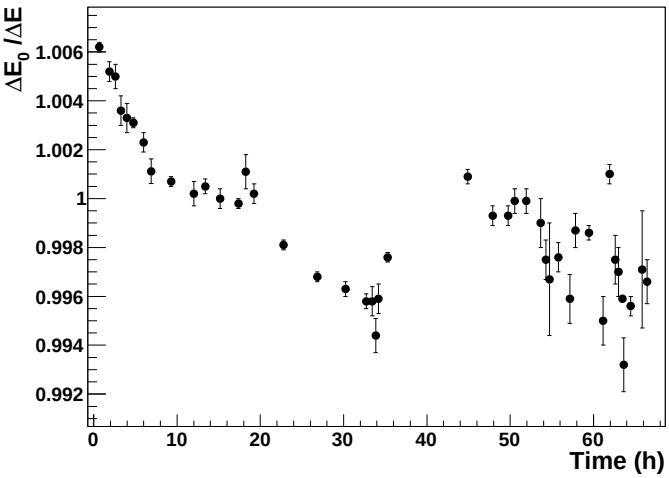

Figure 4.18: Variation of the energy loss over time. The vertical axis is the ratio between the average energy loss and the measured energy loss on each run.

sure variation.

$$\begin{aligned} \Delta E^{eff}\Big|_{run} &= R_{run} \cdot \Delta E \,, \\ E^{eff}_{res}\Big|_{run} &= E_{res} - (R_{run} - 1) \cdot \Delta E \,, \end{aligned} \tag{4.24}$$

where ΔE^{eff} and E^{eff}_{res} are the corrected energy loss and residual energy, and R_{run} is the ratio between the average and energy loss measured on each run.

4.2.2 Nuclear Charge Selection

The low energy domain that fission fragments have in this experiment prevents a trivial nuclear charge selection. A simple calculation using *TRIM (TRansport of Ions In Matter)*, which considers only the equilibrium charge, is not suitable to describe the behavior of the energy loss near

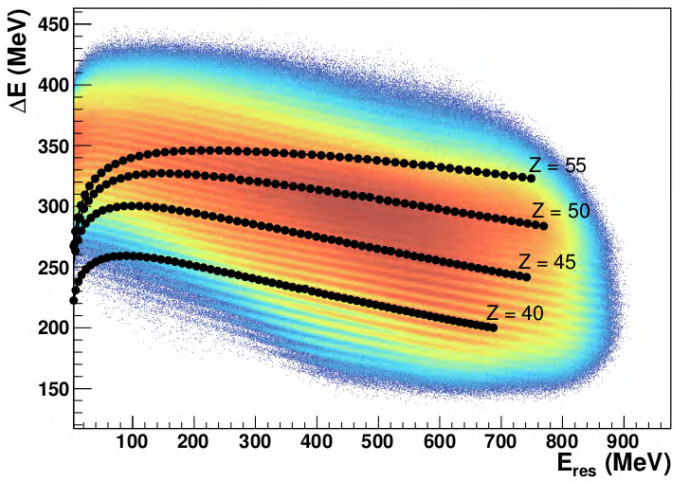

Figure 4.19: Comparison between measured fission fragment energy loss and TRIM calculations (black dots).

the *Bragg Peak*. As shown in Figure 4.19, the *TRIM* calculation, represented by black dots, agrees with the data at high energy but differs when approaching the *Bragg Peak* at low E_{res}, presenting the maximum ΔE at higher E_{res}. This discrepancy reveals the complexity of the interaction of heavy ions with matter at low energy. The assignment of the nuclear charge to each curve is performed, instead, following a empirical method that consists in a geometrical description of the curve with a continuous smooth function of ΔE and E_{res} that permits to be extrapolated to the region of high ΔE and E_{res}, where the lines are closer.

Each curve is described with a reference point and the integral of the tangent along E_{res},

$$\Delta E(E_{res}) = \Delta E_0 + \int_{E_{res_0}}^{E_{res}} \frac{\mathrm{d}(\Delta E)}{\mathrm{d}E_{res}} \mathrm{d}E_{res} \ . \tag{4.25}$$

The reference point, ΔE_0, is unique for each curve and it is an indicator of the nuclear charge that defines the curve. The tangent of the curves can

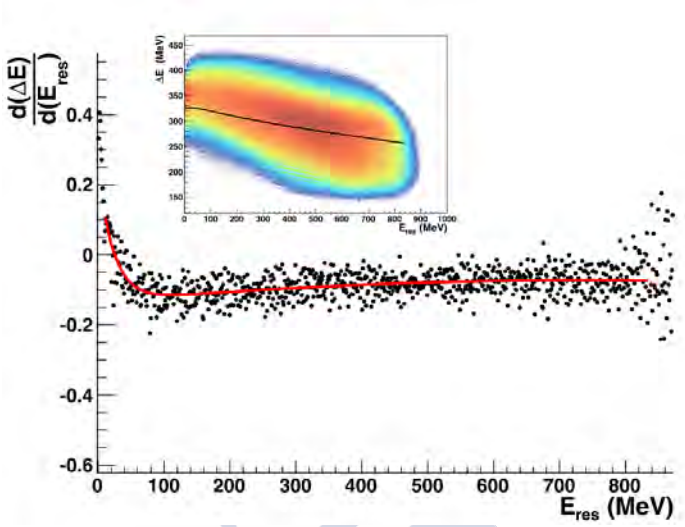

Figure 4.20: Tangent of ΔE as a function of E_{res} for a single nuclear charge. The red line represents the parameterization of the tangent.

be parametrized as a function of E_{res},

$$\frac{\mathrm{d}(\Delta E)}{\mathrm{d}E_{res}} = Ae^{BE_{res}} + C + DE_{res} + FE_{res}^2 \ . \tag{4.26}$$

The tangent is calculated as the infinitesimal difference of ΔE, as a function of E_{res} for one central curve, selected by a graphical cut in the 2D-plot ΔE vs. E_{res}. Figure 4.20 shows the tangent of this central curve, indicated in the inset by a black line. This description of the tangent can be extended to the full range of ΔE and E_{res} defining the parameters

(A, B, C, D, F) as smooth functions of E_{res} and ΔE:

$$\begin{aligned} A &= A' \cdot A_1 \cdot e^{-\ln(A_1)\cdot\frac{\Delta E}{\Delta E'}} \ , \\ B &= B' \cdot B_1 \cdot e^{-\ln(B_1)\cdot\frac{\Delta E}{\Delta E'}} \ , \\ C &= C' \cdot \left[1 + C_1 \cdot \frac{(\Delta E - \Delta E')^2}{\sqrt{(\Delta E - \Delta E')^2 + C_2^2}}\right] \ , \\ D &= D' \cdot \left[1 + D_1 \cdot e^{D_2\cdot(\Delta E - \Delta E')}\right] \ , \\ F &= F' \ , \end{aligned} \tag{4.27}$$

where $\Delta E'$ is the function that reproduces the intermediate curve shown in Fig. 4.20,

$$\Delta E' = \Delta E'_0 + \int_{E'_{res_0}}^{E_{res}} \left(A' e^{B' E_{res}} + C' + D' E_{res} + F' E_{res}^2\right) \mathrm{d}E_{res} \ , \tag{4.28}$$

with $\Delta E'_0 = 326.13$ MeV, the maximum energy loss of the curve, and $E'_{res_0} = 25.12$ MeV, the corresponding residual energy.

The reference point, ΔE_0, is defined arbitrarily as the maximum energy loss, where the tangent of each curve is null. The residual energy E_{res_0} that correspond to ΔE_o is calculated from the tangent definition, considering that the impact of higher order components (D, F) is negligible at low E_{res}:

$$E_{res_0} = \frac{1}{B} \ln\left(\frac{-C}{A}\right) . \tag{4.29}$$

The E_{res_0} definition permits to extract the value of ΔE_0 that corresponds to each pair $(E_{res}, \Delta E)$, event by event:

$$\Delta E_0 = \Delta E - \int_{\frac{1}{B}\ln\left(\frac{-C}{A}\right)}^{E_{res}} \left(A e^{B E_{res}} + C + D E_{res} + F E_{res}^2\right) \mathrm{d}E_{res} \ . \tag{4.30}$$

The value of the parameters of Eq.4.27, obtained from an iterative process, are shown in Table 4.8. The low values of D' and F' confirm the

ΔE_0 parameters.	
Parameter	**Value**
A'	0.3773
B'	-0.04194
C'	-0.1358
D'	0.0001724
F'	$-1.167 \cdot 10^{-7}$
A_1	2.0
B_1	50
C_1	0.002
C_2	40
D_1	0.0025
D_2	-0.04

Table 4.8: Parameters of the reference point, ΔE_0, as a function of E_{res} and ΔE.

validity of the approximation assumed in Eq. 4.29, the parameters D and F are negligible in the calculation of E_{res_0}, within an error of 3%.

Figure 4.21 (a) shows the distribution of the calculated ΔE_0 as a function of E_{res}, where each line corresponds to fragments with the same nuclear charge. Figure 4.21 (b) presents the nuclear charge distribution of fission fragments, calculated as a sixth-order polynomial function of ΔE_0, assuming that the central nuclear charge is Z=49 (half of the nuclear charge of the compound nucleus ^{250}Cf, produced in the fusion of ^{238}U and ^{12}C):

$$Z = \sum_{i=0}^{6} z_i \cdot \Delta E_0^i \,, \tag{4.31}$$

the parameters z_i, shown in Table 4.9, are obtained from a fit to the ΔE_0 distribution.

The assignment of the nuclear charge, as well as the mass identification, is verified with the measurement of gamma emission from excited states of different fission fragments. A detailed explanation is presented in Sec. 4.3.

Z parameters.	
Parameter	**Value**
z_0	-340.6 ± 2.5
z_1	6.081 ± 0.049
z_2	-0.03981 ± 0.00039
z_3	$(1.288 \pm 0.017) \cdot 10^{-4}$
z_4	$(-1.981 \pm 0.040) \cdot 10^{-7}$
z_5	$(1.054 \pm 0.049) \cdot 10^{-10}$
z_6	$(2.10 \pm 0.26) \cdot 10^{-15}$

Table 4.9: Parameters of the sixth-order polynomial function that converts ΔE_0 into nuclear charge.

4.2.3 Correction in Z Definition

The values of nuclear charges do not remain centered with respect to the corresponding integer value, instead, they slightly evolve with the residual energy. Figure 4.22 (a) shows such evolution, which affects strongly the regions of heaviest and lightest ions. This behavior is corrected by means of a parametrization of each Z as a function of E_{res}:

$$\begin{aligned} Z &= z_0 + z_1 E_{res} + z_2 E_{res}^2 + z_3 E_{res}^3 \ , \\ z_i &= \sum_{j=0}^{6} z_{ij} \cdot Z^j \ , \end{aligned} \tag{4.32}$$

where z_{ij} are the parameters of the function.

The correction to the nuclear charge is applied, following the previous equation, as:

$$Z^{corr} = Z \cdot \frac{z_0 + z_1 E_{res_0} + z_2 E_{res_0}^2 + z_3 E_{res_0}^3}{z_0 + z_1 E_{res} + z_2 E_{res}^2 + z_3 E_{res}^3} \ , \tag{4.33}$$

where E_{res_0} is the value of residual energy where Z is correctly centered in the integer value. Figure 4.22 (b) shows the nuclear charge distribution, as a function of E_{res}, after correction.

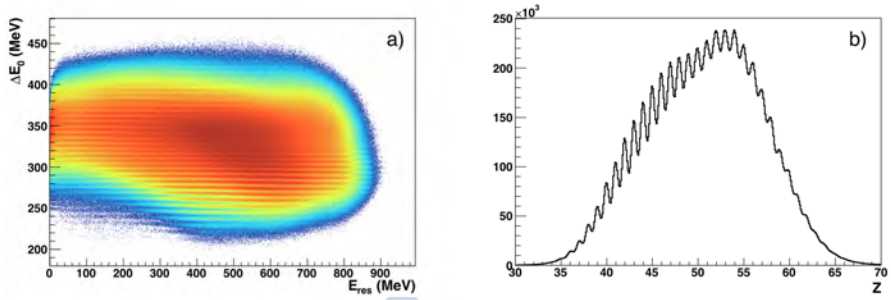

Figure 4.21: Figure (a): ΔE_0 distribution of fission fragments as a function of $Eres$, each line is produced by the fragments with the same nuclear charge. Figure (b): nuclear charge distribution of fission fragments, calculated as a sixth-order polynomial function of ΔE_0.

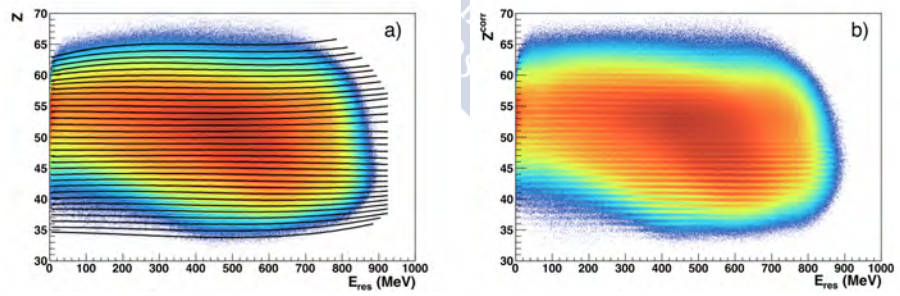

Figure 4.22: Correction of the Z definition. Figure (a): distribution of Z as a function of the residual energy. Lighter and heavier ions evolve with E_{res}. Black lines indicates the parametrization of each Z. Figure (b): distribution of Z after correction.

4.2.4 Mass Dependence Correction

The nuclear-charge identification is based on the relation between the energy loss and the residual energy. However, the energy loss is not only a function of the velocity, but is also a function of the mass of the ion. Therefore, two ions with the same nuclear charge but different mass describe slightly different curves of energy loss versus residual energy.

Figure 4.23 shows the effect of the mass dependence in the nuclear charge identification. Figure 4.23 (a) shows the nuclear charge as a function of the mass of the fragments. Each nuclear charge increases with the mass, crossing the correct integer value in a central position of its mass range. Figures 4.23 (b) and (c) show the calculation of the mean value of $Z = 41$ for two masses, $A = 98$ and $A = 103$, both mean values differ from their corresponding integer values: $\mu_Z^{A=98} = 40.813 \pm 0.002$, and $\mu_Z^{A=103} = 41.158 \pm 0.002$.

The correct nuclear charge is obtained from the former nuclear charge (Z), the mass (A), and the slope (d) that each nuclear charge describes as a function of the mass,

$$Z^{corr} = Z + (A^{central} - A) \cdot d \,, \tag{4.34}$$

where the central mass ($A^{central}$) is defined as the mass where the mean value of Z is equal to its integer value. The central mass and the slope depend on the nuclear charge.

Figure 4.24 shows the nuclear charge distribution, after the mass dependence correction, as a function of the mass.

The final nuclear charge distributions of fission fragments are shown in Fig. 4.25 (a) and (b) for both orientations of the VAMOS spectrometer. The red lines indicate the nuclear-charge distribution before any correction, while the black lines represent the final nuclear-charge distribution. Figures 4.25 (c) and (d) present the resolution achieved in both cases, the average values of the $FMWHM_Z/Z$ are shown as horizontal lines.

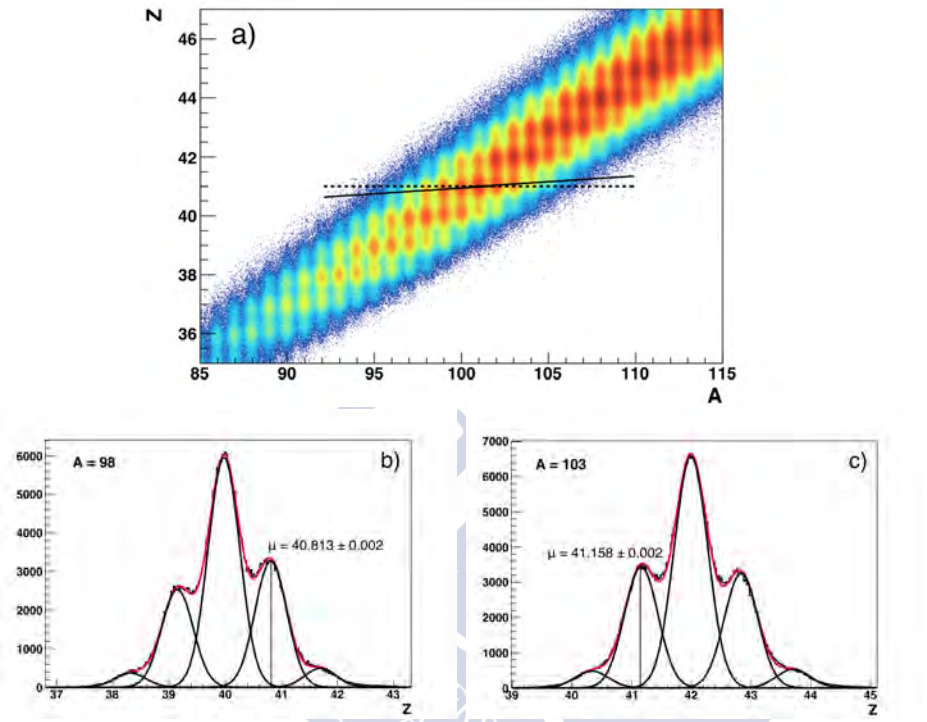

Figure 4.23: Mass-dependence correction. Figure (a): nuclear charge distribution as a function of the mass. Black line shows the evolution of $Z = 41$ with the mass. Figures (b) and (c): calculation of the mean value of $Z = 41$ for two extremal masses, $A = 98$, and $A = 103$. The mean value is higher for higher mass.

The average Z resolutions for VAMOS at 20 and 14 deg are, respectively, 1.809 ± 0.004 % and 1.869 ± 0.006 % in $FWHM_Z/Z$. The setting at 14 deg presents a worse resolution because, at this angle, the spectrometer accepts fragments at higher energy, reaching the region where the intrinsic resolution is limited.

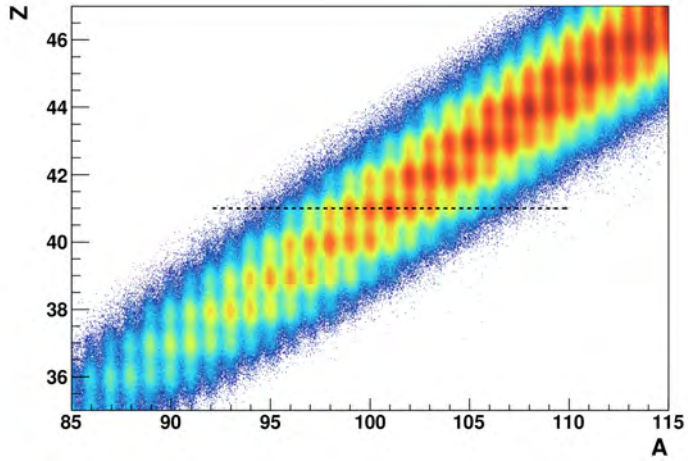

Figure 4.24: Z distribution as a function of the mass, after the mass dependence correction. Dashed line remarks Z=41.

4.3 Identification Verification

The identification of the fission fragments is verified by measuring the energy of the gamma rays emitted from the decay of excited states.

The excited states of even-even nuclei define rotational bands, states of low energy that emits gamma rays in cascade. The level scheme of the rotational bands is well know for many nuclei and the intensity of the gamma emission is high. The gamma spectrum of the rotational bands is, therefore, a good candidate to crosscheck, unequivocally, the fission fragment identification [58].

During the fission process, the fragments gain energy that is stored in the excitation of collective (deformation) and intrinsic (single particle states) degrees of freedom. After the scission point, this energy is released in the form of neutron and gamma evaporation from excited states. The energy and angle of the gamma rays emitted in the decay of these states are detected by the *EXOGAM* detector, detailed in Section 2.3.3.

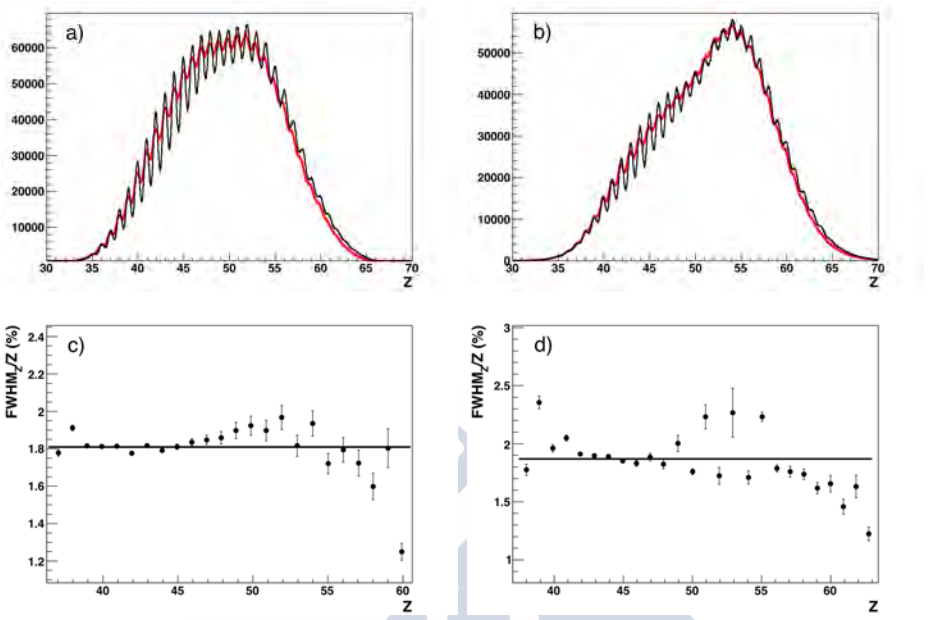

Figure 4.25: Figures (a) and (b): final Z distribution for both VAMOS orientations, 20 deg and 14 deg respect to the beam axis, respectively. Red and black curves indicates the Z distributions before and after corrections. Figures (c) and (d): final Z resolution in the same both VAMOS orientations.

Gamma rays are emitted in flight by the fission fragments, which move with an average velocity of 11% of the speed of light. The energy measured in *EXOGAM* ($E_\gamma^{measured}$) is then affected by Doppler broadening, which is corrected as:

$$E_\gamma = \gamma(1 - \beta cos(\alpha))E_\gamma^{measured} \ , \tag{4.35}$$

where $\beta = v/c$ is the velocity of the fission fragment, γ is the Lorentz factor, $\gamma = 1/\sqrt{1-\beta^2}$, and α is the angle between the fission fragment and the gamma ray.

The trajectory of the fission fragments is determined by the VAMOS reconstruction method. The trajectory of the gamma rays is defined by the position of the *EXOGAM* clovers, that rotate with the VAMOS axis. The

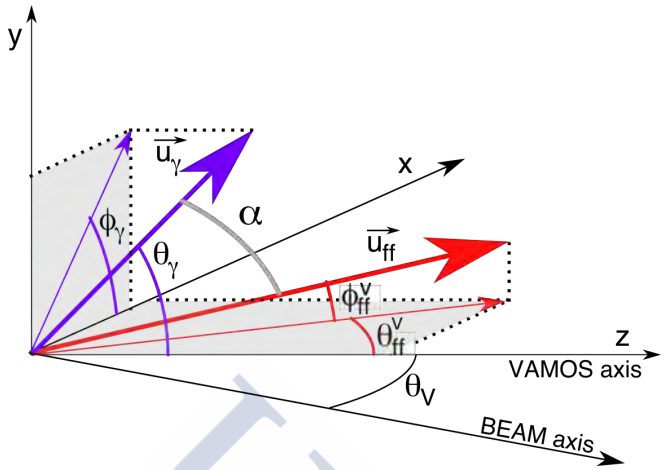

Figure 4.26: Schematic view of the fission fragment and gamma ray trajectories. The angle α between both is obtained through the angles θ^v_{ff}, ϕ^v_{ff}, θ_γ, and ϕ_γ, that both trajectories define respect to the VAMOS axis.

director vectors of both trajectories, fission fragments ($\overrightarrow{u_{ff}}$), and gamma rays ($\overrightarrow{u_\gamma}$), are described, as follows, by two orthogonal angles, (θ^v_{ff}, ϕ^v_{ff}), and (θ_γ, ϕ_γ), respectively,

$$\overrightarrow{u_{ff}} = \begin{pmatrix} sin(\theta^v_{ff})cos(\phi^v_{ff}) \\ sin(\phi^v_{ff}) \\ cos(\theta^v_{ff})cos(\phi^v_{ff}) \end{pmatrix}, \quad \overrightarrow{u_\gamma} = \begin{pmatrix} sin(\theta_\gamma)cos(\phi_\gamma) \\ sin(\theta_\gamma)sin(\phi_\gamma) \\ cos(\theta_\gamma) \end{pmatrix} . \qquad (4.36)$$

The four angles, θ^v_{ff}, ϕ^v_{ff}, θ_γ, ϕ_γ, are defined respect to the VAMOS axis, as Figure 4.26 shows. The angle between the fission fragments and the gamma rays is determined by the scalar product of the director vectors of both trajectories.

Figure 4.27 shows the gamma spectrum of ^{100}Zr, before (a) and after (b) Doppler correction.

In the light fragment region, ^{106}Ru, ^{108}Ru, and ^{110}Ru present a very characteristic level scheme of rotational bands. The selection of these

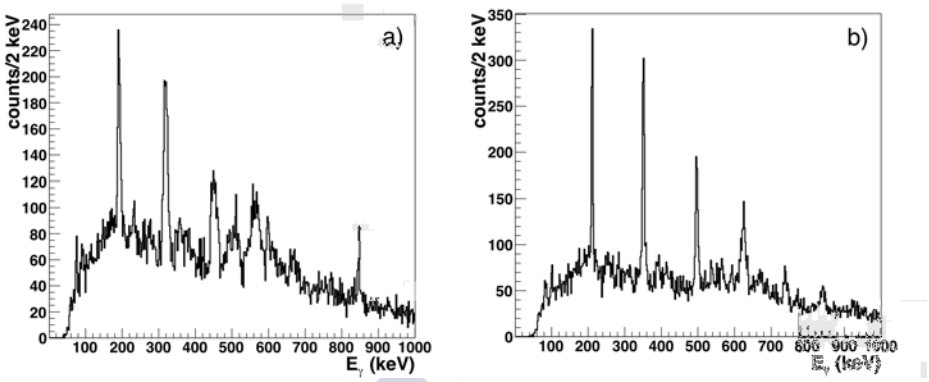

Figure 4.27: Impact of the Doppler correction in the gamma spectrum. Figures (a) and (b) show the gamma spectrum of ^{100}Zr before and after Doppler correction, respectively.

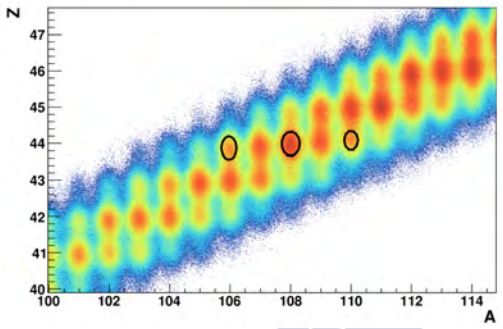

Figure 4.28: Isotopic selection of ^{106}Ru, ^{108}Ru, and ^{110}Ru from fission fragment identification.

nuclei is shown in Fig. 4.28. The comparison between the gamma spectrum of each nucleus (Fig. 4.29) with its known level scheme [59] confirms the assignment of the nuclear charge and mass of light fragments.

In the heavy fragment region, ^{148}Nd and ^{150}Nd are investigated. The selected nuclei are shown in Fig. 4.30 and the gamma spectra of both nuclei are presented in Fig. 4.31. The contamination present in the gamma

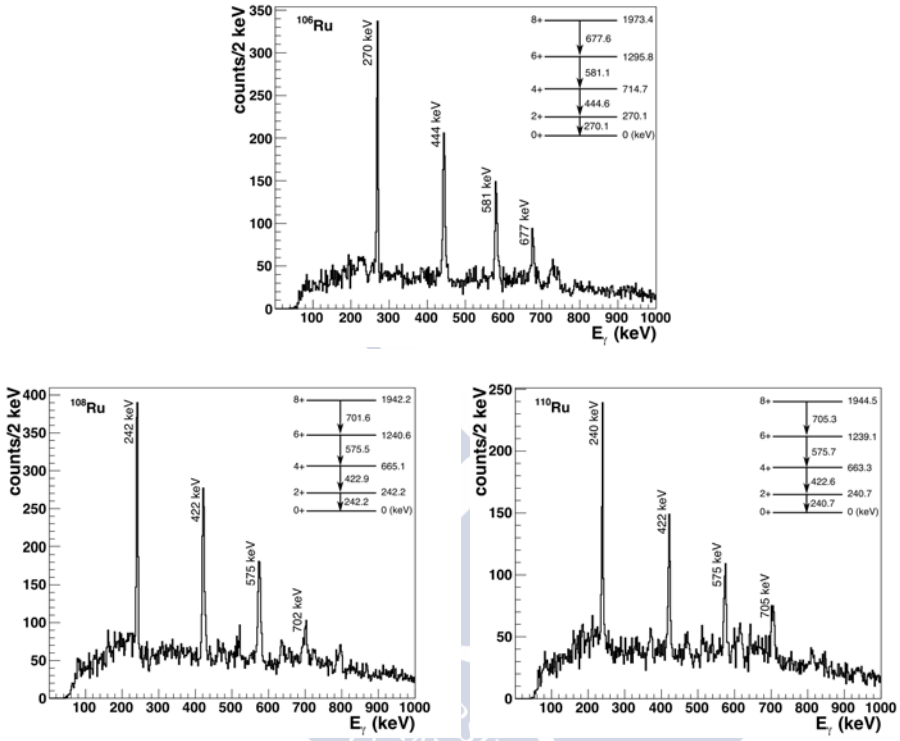

Figure 4.29: Gamma spectra of ^{106}Ru, ^{108}Ru, and ^{110}Ru. The insets show the rotational level schemes, obtained from *Evaluated Nuclear Structure Data File* [59].

spectrum of ^{148}Nd is due to the poor nuclear charge resolution for heavy fragments. Nevertheless, the rotational bands of ^{148}Nd and ^{150}Nd are observed, which confirms the fission fragment identification in the heavy fragment region.

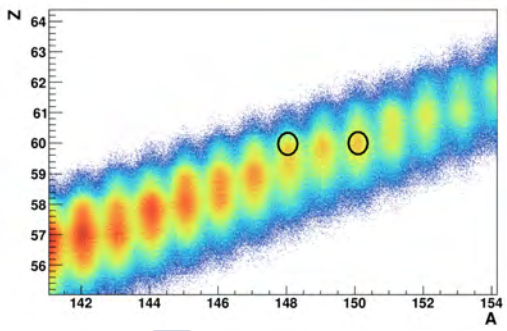

Figure 4.30: Isotopic selection of ^{148}Nd and ^{150}Nd from fission fragment identification.

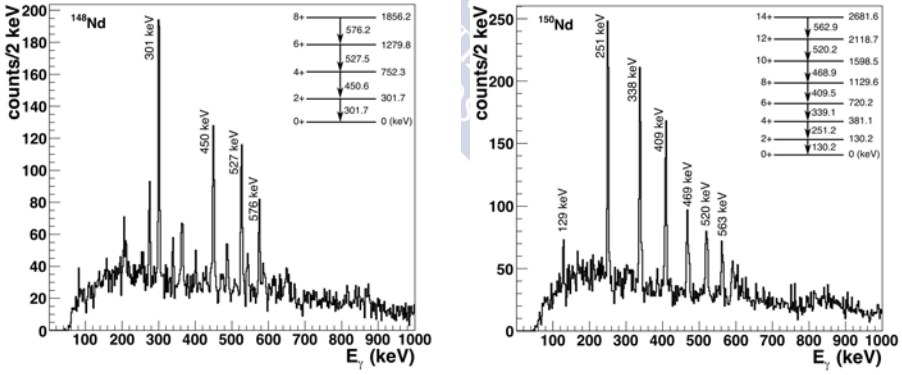

Figure 4.31: Gamma spectra of ^{148}Nd and ^{150}Nd. The insets show the rotational level schemes, obtained from *Evaluated Nuclear Structure Data File* [59].

USC
UNIVERSIDADE
DE SANTIAGO
DE COMPOSTELA

Chapter 5

Fission Yields Calculation

This chapter describes the methods used in the fission yields calculation. It begins with a discussion on the fissioning system identification, required to reconstruct the fissioning-system reference frame. The reconstruction of the fissioning-system reference frame is discussed afterwards. It continues with the description of the beam normalization and the angular acceptance of VAMOS, which defines the geometrical efficiency. Later, the intrinsic efficiency of the detectors in charge of the fission-fragment identification is described. Finally, the resulting isotopic fission yields are presented for ^{250}Cf.

5.1 Fission Yields Definition

The isotopic fission-fragment identification, presented in the previous chapter, permits to calculate the *Isotopic Fission Yields*, $Y(Z,A)$, defined as the fraction that a particular (Z,A) fragment is produced per fission. The *Isotopic Fission Yield distribution*, defined as a function of the *Isotopic Cross Section*, $\sigma(Z,A)$, is an observable independent of the experimental conditions.

$$Y(Z,A) = 200\frac{\sigma(Z,A)}{\sum_{Z,A}\sigma(Z,A)} \ . \tag{5.1}$$

The *Isotopic Cross Section* is related to the production of a particular

fragment, $N(Z,A)$:

$$N(Z,A) = \sigma(Z,A) \cdot N_{target} \cdot N_{beam} \cdot \varepsilon_g \cdot \varepsilon_i \cdot \varepsilon_\tau \ , \tag{5.2}$$

where N_{target} and N_{beam} are the number of nuclei in the target and in the beam, respectively; ε_g is the geometrical efficiency, which includes the geometrical efficiency in the detection of the fissioning system, ε_g^{fiss}, and the geometrical efficiency of the fission-fragment identification, ε_g^{ff}, as $\varepsilon_g = \varepsilon_g^{fiss} \cdot \varepsilon_g^{ff}$; ε_i corresponds to the intrinsic efficiency of the detectors, also split into two components: $\varepsilon_i = \varepsilon_i^{fiss} \cdot \varepsilon_i^{ff}$; finally, ε_τ is the dead time of the acquisition, which is negligible in this case due to the fast acquisition system, of the order of hundreds of μs, and the low rate of the experiment, of the order of 400 Hz.

The *Isotopic Fission Yields* are calculated from the number of events of each isotope measured during the experiment, corrected by the geometrical and intrinsic efficiency of the detectors in charge of the fission fragments identification.

$$Y(Z,A) = 200 \frac{\dfrac{N}{\varepsilon_g^{ff} \cdot \varepsilon_i^{ff}}(Z,A)}{\left(\displaystyle\sum_{Z,A} \dfrac{N}{\varepsilon_g^{ff} \cdot \varepsilon_i^{ff}}(Z,A) \right)} \ . \tag{5.3}$$

The *Mass Fission Yields*, $Y(A)$, and *Atomic-Number Fission Yields*, $Y(Z)$, are directly derived from the *Isotopic Fission Yields*:

$$\begin{aligned} Y(Z) &= \sum_A Y(Z,A) \ , \\ Y(A) &= \sum_Z Y(Z,A) \ . \end{aligned} \tag{5.4}$$

The fission yields of each fissioning system are deduced following a general procedure, independent of the fissioning system except in the calculation of ε_g^{ff}, which presents a dependence with the specific production of each fissioning system, detailed in Section 5.5.2.1. The identification of each fissioning system and the reconstruction of its excitation energy

is presented in Section 5.2. The reconstruction of the fissioning-system reference frame, where the fission-fragment distribution is independent of the kinematics of the reaction that induces the fission is presented in Sec. 5.3.

The different settings of VAMOS cover different ranges in angle and $B\rho$; these settings need to be normalized to the beam intensity in order to contribute with the same weight to the yields calculation. The beam normalization is described in Sec. 5.4.

ε_g^{ff} is determined by the VAMOS acceptance, presented in Sec. 5.5. The contribution of the different charge states to the total number of events of each isotope, once ε_g^{ff} is corrected, is detailed in Sec. 5.6. ε_i^{ff}, which comprises the detection efficiency at the focal plane of VAMOS and the efficiency of the Start detector, is detailed in Sec. 5.7.

5.2 Fissioning System Identification and Excitation Energy Reconstruction

As explained in Sec. 2.2, the ^{238}U beam at 6.14 MeV/u impinges on a ^{12}C target where fusion and transfer reactions produce a compound nucleus that may decay by fission.

The compound nuclei produced by transfer reactions are identified using the SPIDER detector, described in Section 2.3.2. This detector possesses the capability of identifying isotopically the light nuclei produced as a recoil of the transfer reaction by means of energy loss and total energy measurements. The segmentation of the detector provides also a measurement of the angles of the recoil nuclei (for more details, see [31]).

Figure 5.1 presents the isotopic identification of the recoil nuclei produced in transfer reactions in coincidence with the detection of one fission fragment in the VAMOS setup. Each line is assigned according to the mass and nuclear charge of the recoil nuclei and the corresponding fission-

ing system, shown in Table 5.1. Only transfer channels with recoils from ^{14}C to ^{4}He are presented. The identification of the transfer reaction channels ^{12}C(^{238}U,^{249,248}Bk)^{1,2}H are highly contaminated and the fission study is not possible in these cases.

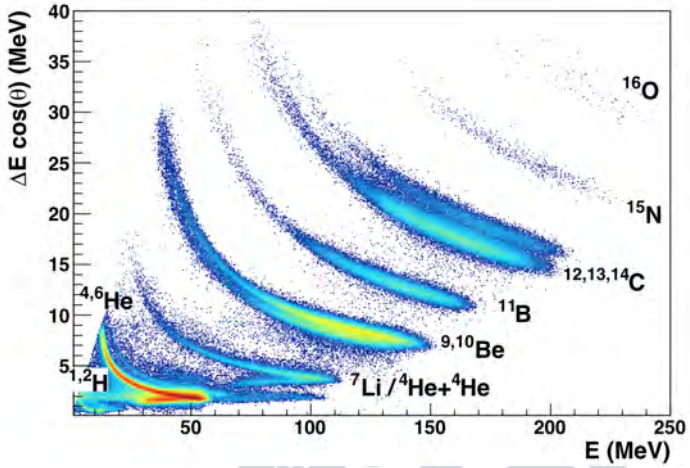

Figure 5.1: Isotopic identification of the transfer-recoil nuclei with the SPIDER detector in coincidence with the detection of fission fragments in VAMOS.

The measurement of the energy and angle of each recoil nuclei permits to reconstruct the binary reaction and extract the excitation energy, the velocity, and the angle of the fissioning system. Following the energy-momentum conservation, the excitation energy is calculated as

$$\begin{aligned} E_x &= \sqrt{(Q_{gg} + M_{fiss} + E_{beam} - E_{rec})^2 - p_{fiss}^2} - M_{fiss} \ , \\ p_{fiss}^2 &= p_{beam}^2 + p_{rec}^2 - 2 p_{beam} p_{rec} \cos(\theta_{rec}) \ , \end{aligned} \tag{5.5}$$

the velocity:

$$\beta_{fiss} = \frac{p_{fiss}}{\sqrt{p_{fiss}^2 + (M_{fiss} + E_x)^2}} \ , \tag{5.6}$$

and polar angle:

$$\cos(\theta_{fiss}) = \frac{p_{beam} - p_{rec} \cos(\theta_{rec})}{p_{fiss}} \ , \tag{5.7}$$

Transfer reactions
^{12}C(^{238}U,^{238}U)^{12}C
^{12}C(^{238}U,^{237}U)^{13}C
^{12}C(^{238}U,^{236}U)^{14}C
^{12}C(^{238}U,^{239}Np)^{11}B
^{12}C(^{238}U,^{240}Pu)^{10}Be
^{12}C(^{238}U,^{241}Pu)^{9}Be
^{12}C(^{238}U,^{242}Pu)^{8}Be
^{12}C(^{238}U,^{243}Am)^{7}Li
^{12}C(^{238}U,^{244}Cm)^{6}He
^{12}C(^{238}U,^{246}Cm)^{4}He

Table 5.1: Populated fissioning systems by transfer reactions between ^{238}U and ^{12}C.

where E_x is the total excitation energy, Q_{gg} is the ground-state to ground-state Q-value of the reaction; M, E, p, and θ represent the ground-state mass, the kinetic energy, the linear momentum, and the polar angle of the corresponding nucleus indicated by the subscript: fissioning system ($fiss$), ^{238}U beam ($beam$), or recoil nucleus (rec). β_{fiss} is the velocity of the fissioning system in units of c.

In general, the excitation energy is shared between the recoil and the scattered nuclei. However, the high level density of the heavy scattered nucleus compared to the target-like recoil, together with the relatively high energy of the first excited state of the light recoil, favor the excitation of the fissioning system. A detailed gamma-decay investigation of the recoil nucleus indicates that the probability of having an excited heavy scattered nucleus and a cold light recoil is ∼0.9 [31].

The energy of the incoming ^{238}U nuclei, assuming that the reaction takes places in the middle of the target, is 6.11 MeV/u after the slowing down in the target, where it losses 6.29 MeV.

Figure 5.2 shows the excitation-energy distribution of ^{238}U, ^{239}Np, ^{240}Pu, and ^{244}Cm for events where a fragment was detected in VAMOS

in coincidence with the measurement of a target-like recoil. ^{238}U presents a second distribution centered at null excitation energy that corresponds to random coincidences between the detection of a elastic scattered ^{12}C in SPIDER with a fission fragment, from fusion-induced fission, detected in VAMOS.

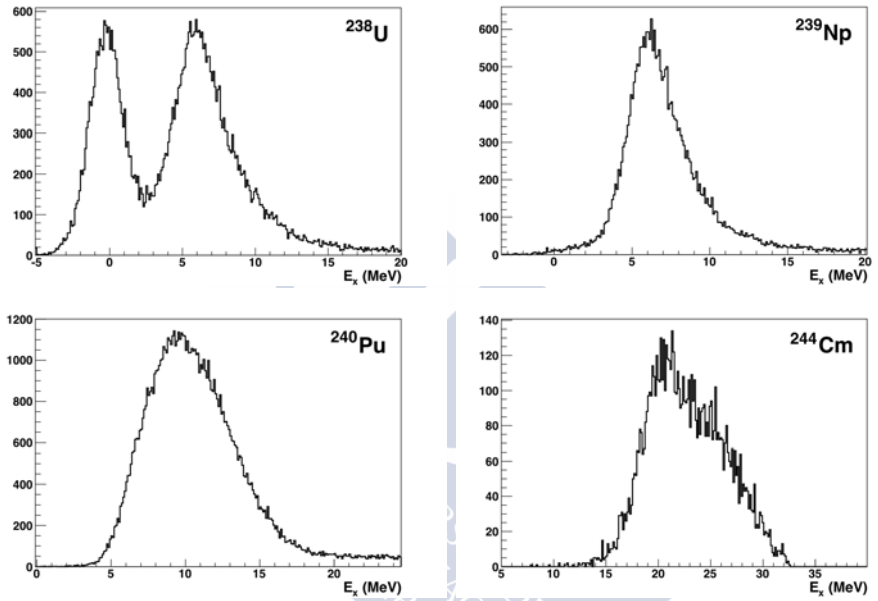

Figure 5.2: Excitation-energy distribution of the fissioning systems, ^{238}U, ^{239}Np, ^{240}Pu, and ^{244}Cm, measured in the SPIDER detector, in coincidence with a fission fragment detected in VAMOS. ^{238}U presents a second contribution at low E_x that corresponds to random coincidences between an elastic scattered ^{12}C in SPIDER and a fragment from fusion-fission, detected in VAMOS.

Figure 5.3 shows the kinematics of the four fissioning systems, ^{238}U, ^{239}Np, ^{240}Pu, and ^{244}Cm, in terms of the velocity as a function of the polar angle with respect to the beam axis. The back lines represent the kinematics corresponding to the most populated excitation energy of each system, $E_x(^{238}U)$=6.1 MeV, $E_x(^{239}Np)$=6.2 MeV, $E_x(^{240}Pu)$=9.8 MeV, and $E_x(^{244}Cm)$=21.0 MeV. The red line indicates the kinematics of the elastic scattered ^{238}U.

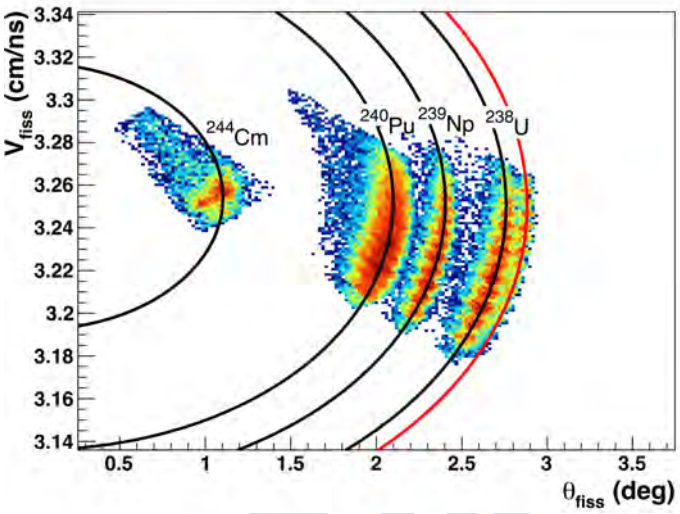

Figure 5.3: Kinematics of the fissioning systems, ^{238}U, ^{239}Np, ^{240}Pu, and ^{244}Cm, produced by transfer reaction. The black lines represent the kinematics of each system for the most populated excitation energy, $E_x(^{238}U)$=6.1 MeV,$E_x(^{239}Np)$=6.2 MeV,$E_x(^{240}Pu)$=9.8 MeV, and $E_x(^{244}Cm)$=21.0 MeV. The red line represents the kinematics of the elastic scattered ^{238}U.

Experimentally, an event is tagged as fusion-reaction when it consists on the detection of a fragment in VAMOS in coincidence with no light recoil measured in SPIDER. In this case, the compound nucleus, ^{250}Cf, does not deviate from the beam trajectory and its excitation energy and velocity are well defined: $E_x(^{250}\text{Cf})$= 45.97 MeV and $V_{fiss}(^{250}\text{Cf})$= 3.255 cm/ns.

5.2.1 Fission Fragments in SPIDER

Light fission fragments can be emitted with a polar angle large enough to hit the SPIDER detector ($\theta > 27$ deg). These fragments produce a Trigger signal in SPIDER but the energy loss that they release in the detector is

too large and the detector signal is saturated, preventing a good reconstruction. When it occurs with fragments emitted from ^{250}Cf fission, no other recoil reaches SPIDER and the event is rejected, even when the complementary fission fragment reaches the VAMOS focal plane. This effect produces a bias on the number of counts of heavy fragments emitted from ^{250}Cf fission. Figure 5.4 presents the nuclear-charge distribution of fission fragments detected in VAMOS under two conditions: the red distribution corresponds to events recorded with Trigger signal from SPIDER; the black distribution presents those events with a good reconstruction in SPIDER, scaled by a factor 4. The difference between both distributions is observed to increase for heavier fragments, indicating that the complementary light fragments reaches more often the SPIDER detector.

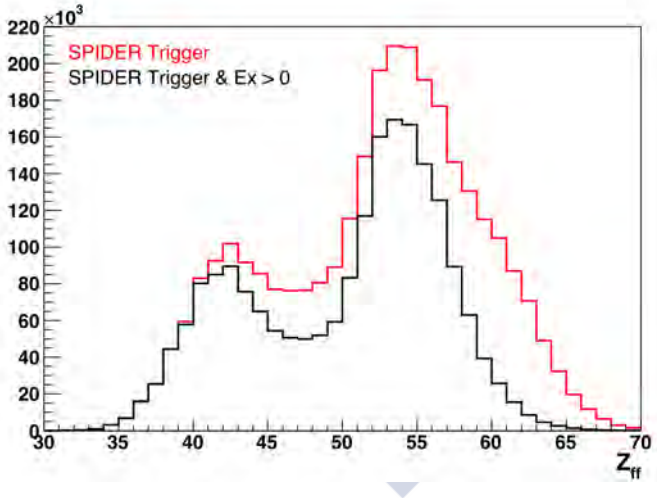

Figure 5.4: Nuclear-charge distribution of fission fragments detected in VAMOS with SPIDER Trigger. The red distribution corresponds to the total number of registered events, while the black distribution represents only the events with a good excitation energy reconstruction in SPIDER, scaled by a factor 4.

The momentum conservation permits to relate the angle of both com-

plementary fragments:

$$\sin(\theta_{ff_2}) = \sqrt{\frac{p_{ff_1}^2 \sin^2(\theta_{ff_1})}{(p_{fiss} - p_{ff_1}\cos(\theta_{ff_1}))^2 + p_{ff_1}^2 \sin^2(\theta_{ff_1})}} \,, \qquad (5.8)$$
$$p_{ff_1} = \sqrt{\gamma_{ff_1}^2 - 1}(A_{ff_1} + \nu_{ff_1})u \,,$$

where p is the linear momentum and θ is the polar angle, both in the laboratory reference system; A is the mass number after neutron evaporation and ν is the number of evaporated neutrons. The subscripts ff_1 and ff_2 refer to both fission fragments and $fiss$ refers to the fissioning system.

Once the heavy fragment (ff_1) is identified in VAMOS, the angle of the complementary light fragment (ff_2) from fusion-fission may be calculated with Eq. 5.8 under some assumptions: Figure 5.5 presents the angle obtained for the light fragment, considering that the average neutron evaporation of fragments with $Z > 60$ is $< \nu_{ff_1} >= 6$ [60] and assuming no significant pre-scission neutron evaporation. Figure 5.5 (a) shows the nuclear charge of one fragment measured in VAMOS as a function of the angle of the complementary fragment for the events with a Trigger signal in SPIDER, assuming fusion-fission. Figure 5.5 (b) shows events with excitation energy reconstruction in SPIDER. Figure 5.5 (a) presents a group of heavy fragments whose light partner fragment has an average angle of $\mu = 28.94 \pm 0.01$ deg, larger than the minimum accepted by SPIDER, as shown in Fig. 5.5 (b). These events must be considered produced in fusion-fission reactions, despite presenting a SPIDER Trigger.

Figure 5.6 presents the nuclear-charge distribution of fission fragments from fusion-fission detected in VAMOS. The red distribution corresponds to events without Trigger in SPIDER, the blue distribution corresponds to events with Trigger in SPIDER after subtracting the events with energy reconstruction in SPIDER, and the black distribution is the sum of both distributions.

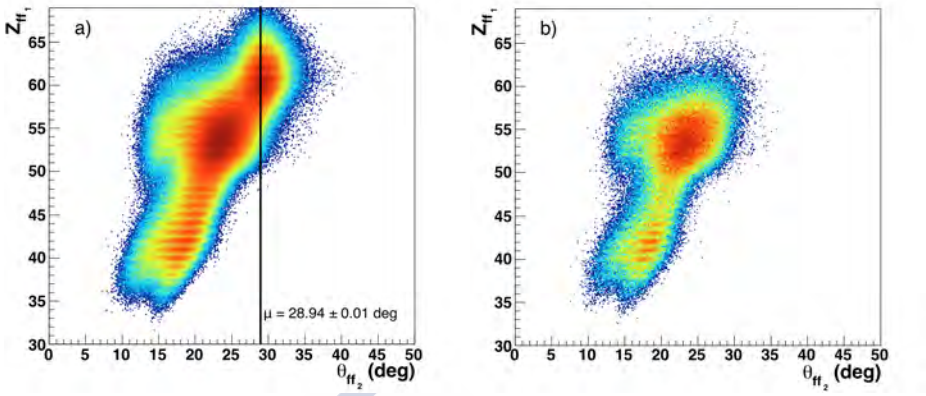

Figure 5.5: Nuclear-charge distribution of fission fragments as a function of the angle of the partner, calculated assuming fusion-fission. Figure (a) shows the events with SPIDER Trigger, while figure (b) shows the events with excitation-energy reconstruction. The partner fragments of $Z > 60$ present angles compatible with the SPIDER geometry.

5.3 Reconstruction of the Fissioning-System Reference Frame

The fissioning-system reference frame, *CM*, is defined as the reference frame where the fissioning system is at rest. The fission-fragment distribution in this reference frame is independent of the kinematics of the reaction that induces the fission. The measurement of the velocity and angle of the fissioning system permits to reconstruct the velocity and angle of the fission fragments in CM.

The transformation from *lab* to *CM* is performed following the *Lorentz Formalism*, described in the Appendix A. The velocity, β_{ff}^{CM}, and the polar angle, θ_{ff}^{CM}, of fission fragments in *CM*, are obtained as a function of the

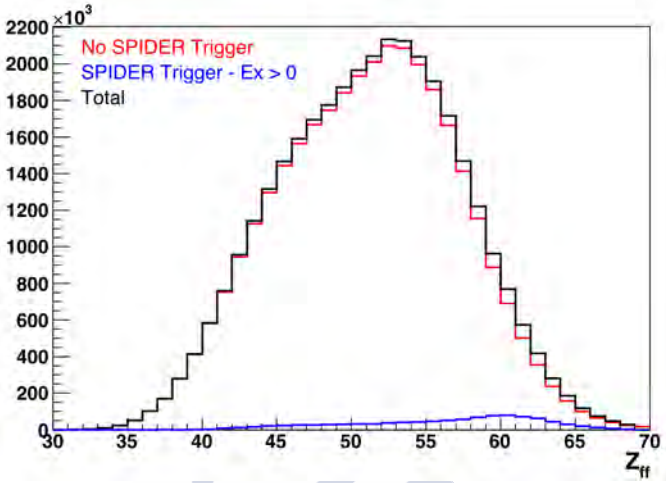

Figure 5.6: Nuclear-charge distribution of fragments from fusion-fission. The red distribution corresponds to the events without Trigger in SPIDER, the blue distribution corresponds to the events with Trigger in SPIDER after subtracting the events with energy reconstruction in SPIDER, and the black distribution is the sum of both.

observables in the *lab* reference frame,

$$\begin{aligned} \gamma_{ff}^{CM} &= \gamma_{fiss}\left(\gamma_{ff}^{lab} - \beta_{fiss}\beta_{ff}^{lab}\gamma_{ff}^{lab}\cos(\theta_{ff}^{lab})\right), \\ \cos(\theta_{ff}^{CM}) &= \frac{\gamma_{fiss}}{\beta_{ff}^{CM}\gamma_{ff}^{CM}}\left(\beta_{ff}^{lab}\gamma_{ff}^{lab}\cos(\theta_{ff}^{lab}) - \beta_{fiss}\gamma_{ff}^{lab}\right), \end{aligned} \tag{5.9}$$

where β_{ff}^{CM} and β_{ff}^{lab} are the velocity, in units of c, of the fission fragments in the *CM* and *lab* frames; β_{fiss} is the velocity of the fissioning system, presented in Sec. 5.2; γ_{ff}^{CM}, γ_{ff}^{lab}, and γ_{fiss} are the corresponding Lorentz factors, $\gamma = 1/\sqrt{1-\beta^2}$; θ_{ff}^{CM} and θ_{ff}^{lab} are the polar angles of the fission fragments with respect to the fissioning system direction in *CM* and *lab* systems, respectively.

θ_{ff}^{lab} is calculated from the reconstructed angles in VAMOS with respect to the beam axis (θ_{lab}, ϕ_{lab}) and the angle of the fissioning system (θ_{fiss},

ϕ_{fiss}),

$$\begin{aligned}\cos(\theta_{ff}^{lab}) = &\sin(\theta_{lab})\sin(\theta_{fiss})\cos(\phi_{lab})\cos(\phi_{fiss}) \\ &+\sin(\theta_{lab})\sin(\theta_{fiss})\sin(\phi_{lab})\sin(\phi_{fiss}) \\ &+\cos(\theta_{lab})\cos(\theta_{fiss})\ ,\end{aligned} \tag{5.10}$$

the definition of angles is depicted in Fig. 5.7.

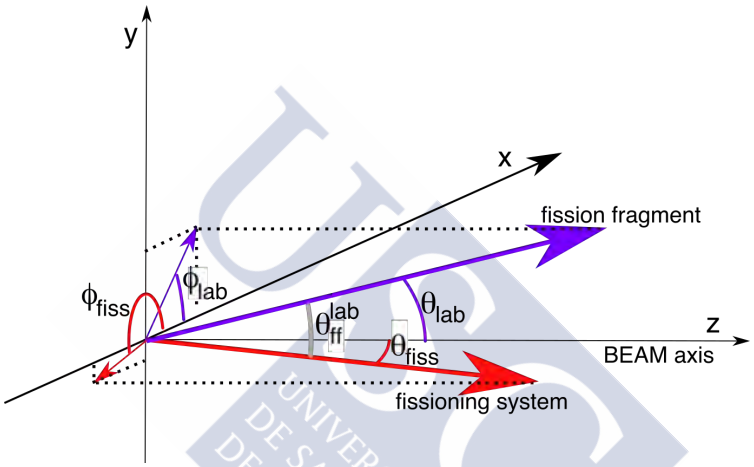

Figure 5.7: Definition of fission-fragments angles with respect to the beam axis and to the fissioning system.

The velocity of fission fragment (β_{ff}^{lab}) is calculated from the measured fission-fragment velocity (β) and corrected by the energy loss within the target and the Start detector. The calculation of β_{ff}^{lab} is detailed in the next section.

5.3.1 β_{ff}^{lab} Calculation

Considering that the fission reaction occurs in average at the middle of the target, the fission fragments are slowed down along half of the target and on the matter present in the Start detector, previous to the *ToF* measurement. Therefore, the measured velocity (β) obtained from the

ToF is lower than the actual velocity with which fragments are emitted in the fission reaction (β_{ff}^{lab}). The velocity of the fission fragments is deduced from β and the energy loss in the target and in the Start detector.

The range in a stopping material (R_i) of a heavy ion of mass A and nuclear charge Z was empirically described in [61] as:

$$R_i = k\frac{A}{Z^2}e_i^{\Gamma} + CA\ , \tag{5.11}$$

where e_i is the kinetic energy of the ion per nucleon and k, Γ, C are constants depending only on the stopping material. This equation permits to relate the velocity of the ion before and after losing energy in the target and in the Start detector.

The range of the ion, after and before the losses, are

$$\begin{aligned} R_1 &= k\frac{A}{Z^2}e_{after}^{\Gamma} + CA\ , \\ R_2 &= R_1 + t_{losses} = k\frac{A}{Z^2}e_{before}^{\Gamma} + CA\ , \end{aligned} \tag{5.12}$$

where t_{losses} is the effective thickness of the stopping material in the target and in the Start detector, that relates the energy before and after losses:

$$e_{before} = \left[e_{after}^{\Gamma} + \frac{Z^2}{A}\frac{t_{losses}}{k}\right]^{1/\Gamma}\ . \tag{5.13}$$

The effective thickness is calculated as the sum of the mass thickness of the different sopping materials in the target and in the Start detector, corrected by the angle of the fragments.

The target is made of carbon with a half thickness of $thick_{target}^{m} = 0.05$ mg/cm^2. The Start detector has two Mylar windows of 0.9 μm, with a density of $\rho_{Mylar} = 1.397$ g/cm^3, that corresponds to $thick_{Mylar}^{m} = 0.2515$ mg/cm^2. The gas inside the Start detector is isobutane at 5.5 $mbar$. The density of the gas at this pressure is $\rho_{iC_4H_{10}} = 1.31 \cdot 10^{-5}$ g/cm^3, and the thickness of the gas gap is 0.48 cm, which defines a mass thickness of $thick_{iC_4H_{10}}^{m} = 0.0063$ mg/cm^2.

The effective thickness is defined as:

$$t_{losses} = \frac{thick^{m}_{target}}{cos(\theta_{lab})} + \frac{thick^{m}_{Mylar} + thick^{m}_{iC_4H_{10}}}{cos(\theta_0 - \theta_{lab})} \ , \tag{5.14}$$

where θ_0 is the rotation angle of the Start detector with respect to the beam axis, which is $\theta_0 = 26\ deg + \theta_{VAMOS}$, being θ_{VAMOS} the rotation angle of VAMOS respect to the beam axis.

The parameters Γ and k are calculated by fitting Eq. 5.13 to the energy loss of heavy ions in the target and in the Start detector, simulated with LISE++. The simulated heavy ions range from Z=30, A=70, and $e_{before} = 3\ AMeV$ to Z=70, A=180, and $e_{before} = 12\ AMeV$. The obtained parameters are $\Gamma = 0.9649 \pm 0.032$ and $k = 45.1 \pm 4.1$.

The calculation of e_{before} with the previous parameters presents an error smaller than 1.5%; however, a dependence on the nuclear charge and on the velocity of the ions remains uncorrected. This dependence is corrected by means of a factor that depends on Z and on the velocity of the ions, $f(Z, \beta)$:

$$\begin{aligned} e^{corr}_{before} &= f(Z,\beta)\left[e^{\Gamma}_{after} + \frac{Z^2}{A}\frac{thickness_{losses}}{k}\right]^{1/\Gamma} , \\ f(Z,\beta) &= \sum_{i=0}^{3}(A_i + B_i \cdot Z + C_i \cdot Z^2)\cdot\beta^i \ , \end{aligned} \tag{5.15}$$

with $e_{after} = u\left(1/\sqrt{1-\beta^2} - 1\right)$. The parameters A_i, B_i, C_i are also obtained from a fit to the simulated data. The values of the parameters are shown in Table 5.2.

Figure 5.8 presents the relative error of the calculated e_{before} with simulated data, as a function of the velocity of the ions. Each nuclear charge show a correlation between the relative error and the velocity (red dots). The relative error of the calculated e_{before} is shown with (blue) and without (black) the $f(Z, \beta)$ function, which corrects the (Z, β) dependence and reduces the relative error to 0.1 %. β^{lab}_{ff} is calculated from β with Eq. 5.15,

$f(Z,\beta)$ **parameters**	
Parameter	**Value**
A_0	1.10099 ± 0.00013
B_0	$(4.0947 \pm 0.0027) \cdot 10^{-3}$
C_0	$(-8.1368 \pm 0.0041) \cdot 10^{-5}$
A_1	-0.4798 ± 0.0012
B_1	-0.12651 ± 0.00003
C_1	$(1.93686 \pm 0.00044) \cdot 10^{-3}$
A_2	-7.3749 ± 0.0099
B_2	1.19903 ± 0.00022
C_2	$(-1.5935 \pm 0.0004) \cdot 10^{-2}$
A_3	41.216 ± 0.065
B_3	-3.5663 ± 0.0016
C_3	$(4.3487 \pm 0.0028) \cdot 10^{-2}$

Table 5.2: Parameters of the correction function of the energy loss in the target and in the Start detector ($f(Z,\beta)$) .

event by event, as:

$$\beta_{ff}^{lab} = \sqrt{1 - \frac{1}{(e_{before}/u + 1)^2}} \, . \tag{5.16}$$

Figure 5.9 presents the resulting velocity in CM of two different fission fragments, ^{100}Nb and ^{150}Nd, as a function of $\cos(\theta_{ff}^{CM})$. The range of $\cos(\theta_{ff}^{CM})$ is limited by the angular acceptance of VAMOS.

5.4 Beam Normalization

The beam normalization is performed by computing the number of elastic-scattering events registered in SPIDER per VAMOS setting. The geometric and intrinsic efficiency of the SPIDER detector, as well as the number of nuclei in the target, are considered constant along the experiment. In

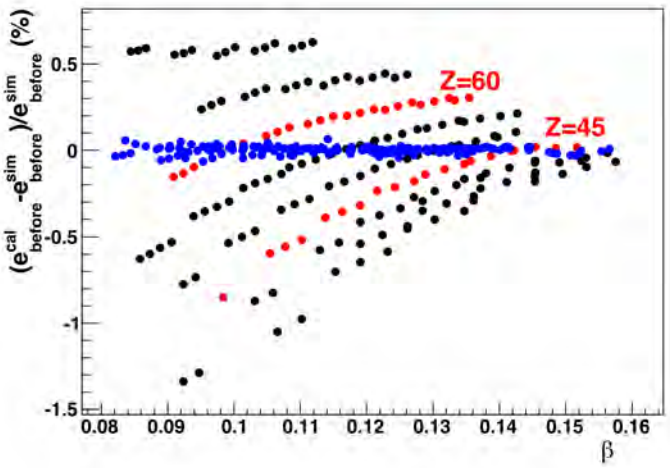

Figure 5.8: Evolution of the relative error of the calculated e_{before} with respect to the simulated values as a function of the velocity (β) before (black) and after (blue) the $f(Z,\beta)$ correction. The deviation of the calculation with respect to the simulation before the $f(Z,\beta)$ correction is observed to evolve with Z and β (red).

these conditions, the number of elastic scattering events of ^{238}U + ^{12}C is proportional to the beam intensity.

The elastic scattering reaction of a ^{238}U beam at 6.14 MeV/u and ^{12}C target emits a ^{12}C recoil with an angle covering from 0 to 90 deg with respect to the beam axis and a ^{238}U with an angle lower than 2.89 deg, preventing the VAMOS detection. From the measurement point of view, the result of a elastic scattering event is a ^{12}C recoil detected in SPIDER without any nucleus in VAMOS.

Figure 5.10 presents the SPIDER identification plot for events with a SPIDER trigger without trigger in VAMOS. The identification is performed in terms of the energy loss, corrected by the effective thickness traversed by the nuclei, as a function of the total energy. Apart from the ^{12}C from elastic scattering, the figure also shows recoils from ^{1}H to ^{16}O

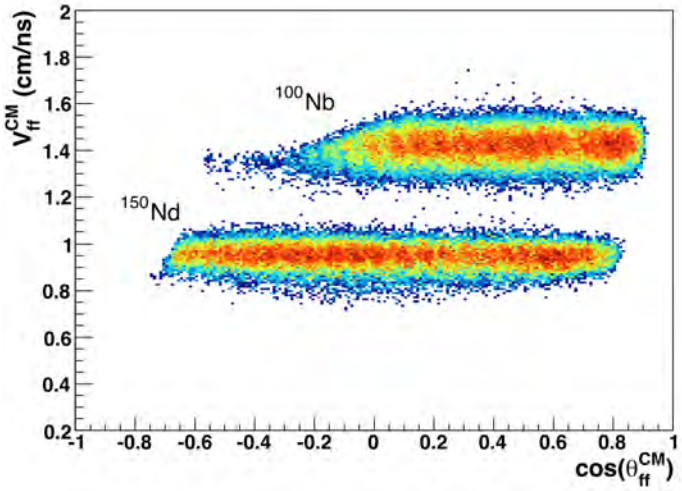

Figure 5.9: Fission-fragment velocity, in CM, as a function of $\cos(\theta_{ff}^{CM})$ for ^{100}Nb and ^{150}Nd. The diagonal cut on the velocity distribution of ^{100}Nb is due to the limitation of the VAMOS acceptance.

produced in transfer-reactions where the fission fragments are out of the VAMOS acceptance or the excitation energy of the compound nuclei is not enough to allow the fission decay.

The normalization factors are calculated as the ratio between the number of events of ^{12}C of each setting of VAMOS with respect to the first setting, taken as a reference. The values of the beam normalization factors are presented in Table 5.3.

Beam Normalization Factors		
$B\rho_0$	**VAMOS angle**	**Factor**
1.1 Tm	20 deg	1
1.2 Tm	20 deg	1.0894 ± 0.0044
1.2 Tm	14 deg	1.1684 ± 0.0047
1.3 Tm	14 deg	0.5028 ± 0.0026

Table 5.3: Normalization factors of beam intensity in the different settings.

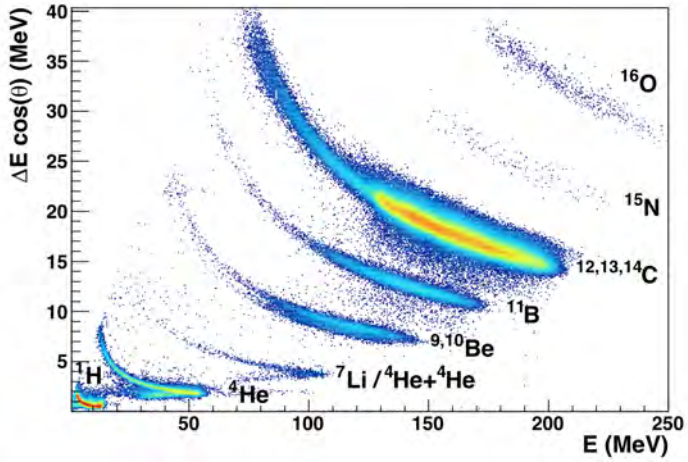

Figure 5.10: Identification of ^{12}C from elastic scattering in the SPIDER detector. Recoils from transfer channels, without detection in VAMOS, are also present.

5.5 VAMOS Acceptance

The geometrical efficiency of the fission-fragment detection, ε_g^{ff}, is determined by the VAMOS angular acceptance. This acceptance can be decomposed into two contributions: the acceptance in the azimuthal angle, f_ϕ, and the acceptance in the polar angle, $f_{\theta_{CM}}$,

$$\varepsilon_g^{ff} = f_\phi(\theta_{lab}, \delta) \cdot f_{\theta_{CM}}(A, \theta_{fiss}, \beta_{fiss}) \,, \tag{5.17}$$

where f_ϕ depends on the polar angle in the laboratory reference frame θ_{lab}, and on the relative magnetic rigidity δ of each fragment; $f_{\theta_{CM}}$ is a function of the mass of the fragments, which evolves with both polar angle and velocity of the fissioning system.

5.5.1 ϕ Acceptance (f_ϕ)

The size of the entrance window of VAMOS defines a regular acceptance in the azimuthal angle, however this acceptance is reduced by the size of the detectors at the focal plane.

The focalization that the quadrupoles produce on the trajectories of the fission fragments when they pass through the spectrometer defines a magnification factor between the incoming azimuthal angle and the outgoing vertical angle. The focalization of the quadrupoles varies with the polar angle, θ_{lab}, and the relative magnetic rigidity, $\delta = B\rho/B\rho_0$, of each fission fragment. This effect makes that the magnification factor evolves with θ_{lab} and δ. Therefore, the limitation that the size of the detectors defines at the focal plane is transformed into a limitation in the azimuthal angle at the entrance of VAMOS that evolves with θ_{lab} and δ.

Figure 5.11 (a) presents the distribution of θ_{lab} versus ϕ_{lab} for fission fragments with a relative magnetic rigidity $\delta \in (0.995, 1.005)$; Figure 5.11 (b) shows the ϕ_{lab} distribution for the central trajectory, $\delta \in (0.995, 1.005)$ and $\theta_{lab} \in (19.75, 20.25)$ deg. The limits of ϕ_{lab} are represented by double arrows.

The actual ϕ_{lab} distribution for one value of δ and θ_{lab} is flat inside the VAMOS acceptance and becomes null out of it. The measured ϕ_{lab} distribution presents, instead, an *Error function* shape in both edges due to a limited resolution in the position measurement and in the reconstruction.

The ϕ_{lab} distribution of each value of δ and θ_{lab} is fitted to a double *Error function*:

$$f(\phi_{lab}) = \frac{C_1}{\sqrt{\pi}} \left[\int_0^{A_1 \cdot (\phi_{lab} - B_1)} e^{-t^2} \mathrm{d}t + \int_0^{A_2 \cdot (\phi_{lab} - B_2)} e^{-t^2} \mathrm{d}t \right] , \quad (5.18)$$

where C_1 is the amplitude of the distribution, A_1 and A_2 are the slope of the function in both edges of the distribution, and B_1 and B_2 correspond to the values of ϕ_{lab} where the function reaches the half maximum.

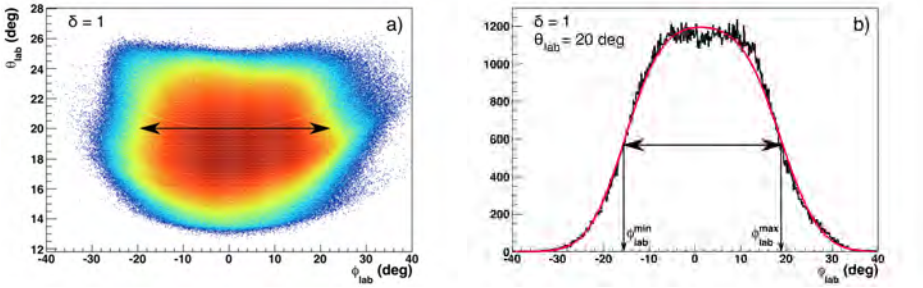

Figure 5.11: Figure (a): evolution of the azimuthal angle (ϕ_{lab}) versus the polar angle (θ_{lab}) for $\delta \in (0.995, 1.005)$. Figure (b): ϕ_{lab} distribution of the fragments that describes the central trajectory, $\delta \in (0.995, 1.005)$ and $\theta_{lab} \in (19.75, 20.25)$ deg. The red line represents a double *Error function*, fitted to the distribution, where ϕ_{lab}^{min} and ϕ_{lab}^{max}, that correspond to the limits of the distribution, are defined as the values of ϕ_{lab} where the function reach the half maximum.

The range of ϕ_{lab} is defined as the *Full Width at Half Maximum* of the function, $\Delta\phi_{lab} = \phi_{lab}^{max} - \phi_{lab}^{min} = |B2 - B1|$.

The ϕ acceptance is defined as the ratio between the range of ϕ_{lab} accepted in VAMOS and the total ϕ_{lab} range covered by fission fragments (2π):

$$f_{\phi}(\theta_{lab}, \delta) = \frac{\Delta\phi_{lab}(\theta_{lab}, \delta)}{2\pi}. \tag{5.19}$$

The ϕ acceptance is calculated for discrete points of θ_{lab} and δ. These values define a 2-D acceptance grid with a step of 0.25 deg in θ_{lab} and 0.005 in δ. The acceptance is calculated for both orientations of VAMOS, 20 and 14 deg, independently. Figure 5.12 shows f_{ϕ} as a function of θ_{lab} and δ for (a) VAMOS at 20 deg and (b) VAMOS at 14 deg. The evolution of the ϕ_{lab} distribution within the full range of θ_{lab} and δ is presented in Appendix B.

The final ϕ acceptance is calculated as a function of the θ_{lab} and δ of the fragments by means of a local multivariant interpolation of the previous

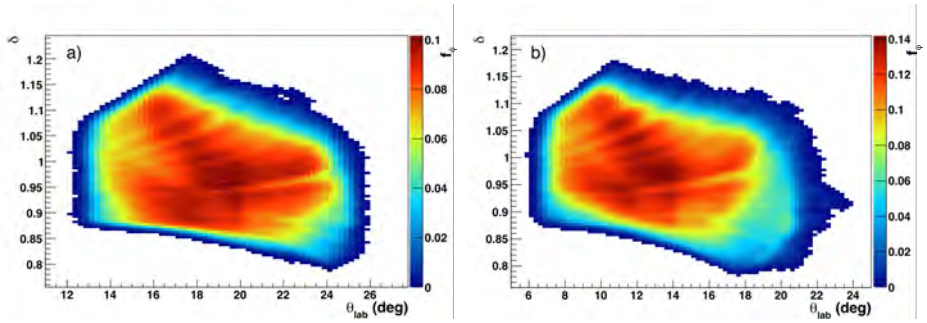

Figure 5.12: ϕ acceptance distribution (f_ϕ) as a function of the polar angle (θ_{lab}) and the relative magnetic rigidity (δ) of the fission fragments with (a) VAMOS rotated at 20 deg and (b) VAMOS rotated at 14 deg.

grid:

$$
\begin{aligned}
f_\phi(\theta_{lab},\delta) = & f_\phi(\theta_{lab}^{(0)},\delta^{(0)})\cdot\frac{\theta_{lab}-\theta_{lab}^{(1)}}{\theta_{lab}^{(0)}-\theta_{lab}^{(1)}}\cdot\frac{\delta-\delta^{(1)}}{\delta^{(0)}-\delta^{(1)}}+ \\
& f_\phi(\theta_{lab}^{(0)},\delta^{(1)})\cdot\frac{\theta_{lab}-\theta_{lab}^{(1)}}{\theta_{lab}^{(0)}-\theta_{lab}^{(1)}}\cdot\frac{\delta-\delta^{(0)}}{\delta^{(1)}-\delta^{(0)}}+ \\
& f_\phi(\theta_{lab}^{(1)},\delta^{(0)})\cdot\frac{\theta_{lab}-\theta_{lab}^{(0)}}{\theta_{lab}^{(1)}-\theta_{lab}^{(0)}}\cdot\frac{\delta-\delta^{(1)}}{\delta^{(0)}-\delta^{(1)}}+ \\
& f_\phi(\theta_{lab}^{(1)},\delta^{(1)})\cdot\frac{\theta_{lab}-\theta_{lab}^{(0)}}{\theta_{lab}^{(1)}-\theta_{lab}^{(0)}}\cdot\frac{\delta-\delta^{(0)}}{\delta^{(1)}-\delta^{(0)}}\ ,
\end{aligned}
\tag{5.20}
$$

where the points of the grid $(\theta_{lab}^{(0)},\delta^{(0)})$, $(\theta_{lab}^{(0)},\delta^{(1)})$, $(\theta_{lab}^{(1)},\delta^{(0)})$, and $(\theta_{lab}^{(1)},\delta^{(1)})$ are the closest to the interpolation point (θ_{lab},δ) satisfying $\theta_{lab}^{(0)} < \theta_{lab} < \theta_{lab}^{(1)}$ and $\delta^{(0)} < \delta < \delta^{(1)}$.

5.5.2 θ Acceptance ($f_{\theta_{CM}}$)

The VAMOS acceptance defines also a limitation in the polar angle with respect to the beam axis of the fission fragments, θ_{lab}, that depends on the $B\rho$ (see Section 2.4.1 and Fig. 2.6). The θ_{lab} distribution presents complex dependences with the velocity of the fission fragment as well as with the velocity of the fissioning system. The acceptance in polar angle is calculated, instead, in the *center-of-mass* of the fissioning system (CM), where the polar angle of the fission fragments with respect to the fissioning system, θ_{ff}^{CM}, is independent of the experimental conditions.

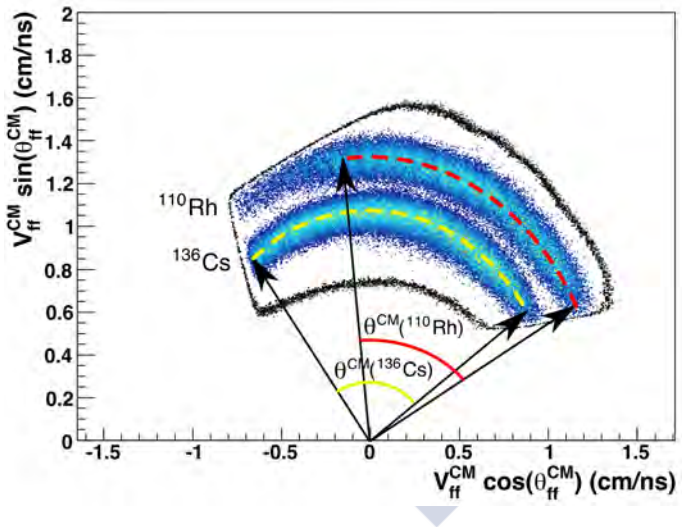

Figure 5.13: Velocity distributions of ^{110}Rh and ^{136}Cs in CM. The black curve, surrounding both distributions, represents the VAMOS aperture. The arrows indicates the limits of the angular range where the distributions are not cut by the VAMOS aperture.

Figure 5.13 presents the maximum coverage that VAMOS permits in the angular range of the fission fragments in the CM system. The velocity distributions of ^{110}Rh and ^{136}Cs are shown inside the aperture of the spectrometer represented by the black curve that cuts the distribution in different angles depending on the fission fragment. The angular range

results to be larger for heavier fragments than for lighter ones. The VAMOS aperture presented in Fig. 5.13 does not correspond to the actual VAMOS acceptance, which is reduced due to the presence of charge states. The evolution of the VAMOS acceptance with the charge states need to be taken into account as in Sec. 5.5.2.1.

$f_{\theta_{CM}}$ is calculated from the range of $\cos(\theta_{ff}^{CM})$ accepted by VAMOS

$$f_{\theta_{CM}}(A, \theta_{fiss}, \beta_{fiss}) = \frac{\Delta \cos(\theta_{ff}^{CM})}{2}(A, \theta_{fiss}, \beta_{fiss}), \tag{5.21}$$

where $\Delta \cos(\theta_{ff}^{CM}) = \cos(\theta_{ff}^{CM})|_{max} - \cos(\theta_{ff}^{CM})|_{min}$. The limits $\cos(\theta_{ff}^{CM})|_{min}$ and $\cos(\theta_{ff}^{CM})|_{max}$, shown in Figure 5.14 for $A = 110$, are defined as the limits in the transmission of the full charge state distribution of each fragment mass. The calculation of the $\cos(\theta_{ff}^{CM})$ limits and their dependence with θ_{fiss} and v_{fiss} is detailed in Section 5.5.2.1.

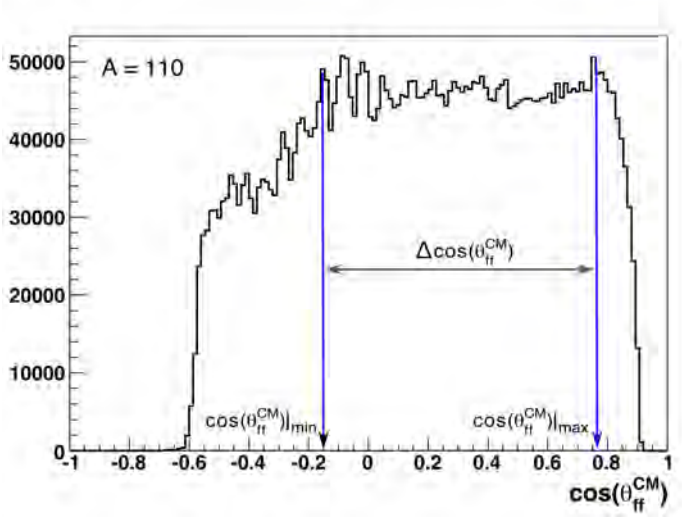

Figure 5.14: $\cos(\theta_{ff}^{CM})$ distribution of fragments with mass number $A = 110$. The arrows indicates the limits of the $\cos(\theta_{ff}^{CM})$ range, where the charge state distribution is fully transmitted.

5.5.2.1 Limits of $\cos(\theta_{ff}^{CM})$

The low beam energy, 6.14 MeV/u, prevents the emission of fully stripped fission fragments; they are emitted, instead, with different charge states. The distribution of charge states evolves with the velocity of the fragments in the *lab* system [62]. At higher velocity, less electrons remain in the fragment, and consequently, its charge state is higher. The production of each charge state is limited to a determined range of velocities which involves an angular range in θ_{ff}^{CM}.

Each individual (Z, A) yield is distributed into several charge states. The angular range of each charge state is cut by the VAMOS acceptance, diminishing the total number of detected fragments per unit of θ_{ff}^{CM}, hence, the ranges of θ_{ff}^{CM} where any charge state is cut need to be excluded from the calculation of isotopic yields.

The limits of the VAMOS acceptance in the $(B\rho, \theta_{lab})$ phase-space defines a limited range $\cos(\theta_{ff}^{CM})$ for each charge state that depends on the mass number of the fragments, for each pair $(\theta_{fiss}, \beta_{fiss})$. Assuming no energy losses on the target and the start detector, the limits of $\cos(\theta_{ff}^{CM})$ can be calculated from Eqs. 4.1 and 5.9 as:

$$\cos(\theta_{ff}^{CM})|_{limit} = \frac{\gamma_{fiss}}{\sqrt{(\gamma_{ff}^{CM}|_{limit})^2 - 1}} \cdot \left[\frac{q}{A} \frac{B\rho|_{limit}}{3.105} \cos(\theta_{ff}^{lab}|_{limit}) - \beta_{fiss} \sqrt{\left(\frac{q}{A} \frac{B\rho|_{limit}}{3.105} \right)^2 + 1} \right],$$

$$\gamma_{ff}^{CM}|_{limit} = \gamma_{fiss} \left[\sqrt{\left(\frac{q}{A} \frac{B\rho|_{limit}}{3.105} \right)^2 + 1} - \beta_{fiss} \frac{q}{A} \frac{B\rho|_{limit}}{3.105} \cos(\theta_{ff}^{lab}|_{limit}) \right], \tag{5.22}$$

with a 2% of error.

In the case of fusion-induced fission the angle of the fissioning system is zero and its velocity is the same for each event. Therefore, the limits of

$\cos(\theta_{ff}^{CM})$ are a function of the mass number, the charge state, and the limits of $B\rho$ and θ_{lab}, $\cos(\theta_{ff}^{CM})|_{limit} = f(A, q, B\rho|_{limit}, \theta_{lab}|_{limit})$. In the case of transfer-induced fission, the fissioning system is produced with a range of velocities and angles that need to be considered in the determination of the $\cos(\theta_{ff}^{CM}))|_{limit}$.

Figure 5.15 presents the angular distribution as a function of θ_{lab}, for charge states of fragments with A=120 in the CM from fusion-induced fission. The surrounding black curve represents the calculated $\cos(\theta_{ff}^{CM})|_{limit}$, from Eq. 5.22 and the $(B\rho|_{limit}, \theta_{lab}|_{limit})$ curve that the VAMOS acceptance defines. Most of the charge states are cut by the acceptance: the blue and green lines represent the minimum and maximum value of $\cos(\theta_{ff}^{CM})$ for each charge state where the distribution is not cut. The lower charge states present a cut that is not produced by the acceptance but by the minimum fragment energy needed to reach the silicon detectors in order to perform the isotopic identification. Charge states higher than $q = 42$ do not reach this lower limit. Charge states lower than $q = 37$ present a similar behavior: they are not produced close to the upper limit.

The lower limit of $\cos(\theta_{ff}^{CM})$ for each mass is defined as the lower limit of the charge state with the highest value:

$$\cos(\theta_{ff}^{CM})|_{min}(A) = \mathrm{MAX}\Big[\cos(\theta_{ff}^{CM})|_{min}(A, q)\Big]. \tag{5.23}$$

Consequently, the upper limit of $\cos(\theta_{ff}^{CM})$ for each mass is defined as the upper limit of the charge state with the lowest value:

$$\cos(\theta_{ff}^{CM})|_{max}(A) = \mathrm{MIN}\Big[\cos(\theta_{ff}^{CM})|_{max}(A, q)\Big]. \tag{5.24}$$

Figure 5.16 presents the lower and upper limits of $\cos(\theta_{ff}^{CM})$ as a function of the mass number. Blue and green curves indicate smooth functions that reproduce the limits in a restrictive way, ensuring that the full charge state distribution is transmitted in the range between both limits. The

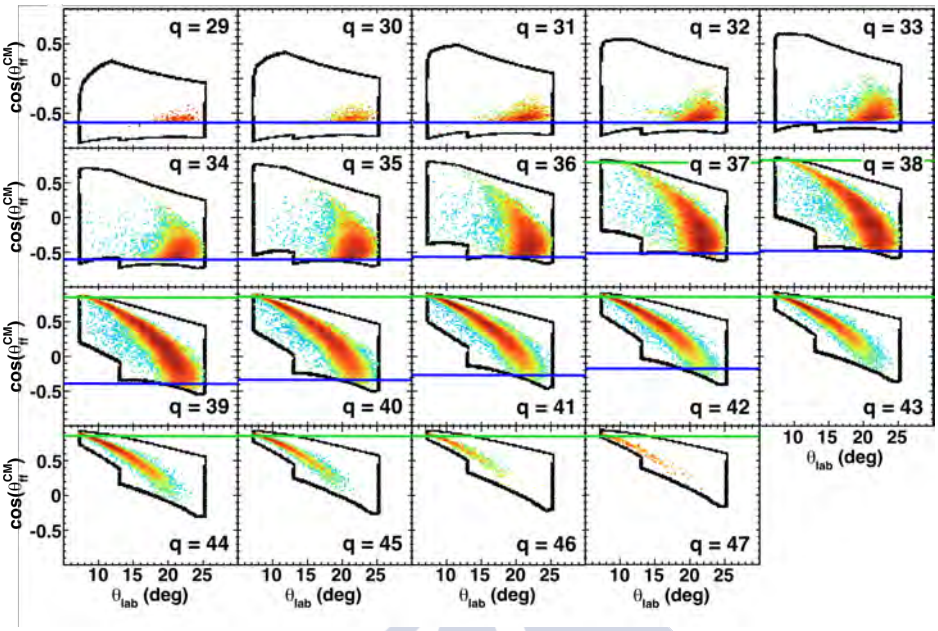

Figure 5.15: $\cos(\theta_{ff}^{CM})$ distribution, as a function of θ_{lab}, of the charge states of fission fragments with mass $A = 120$. Black curves indicates the VAMOS acceptance limits, blue and green lines indicates the limits in $\cos(\theta_{ff}^{CM})$ for each charge state.

definition of the functions is the following:

$$\begin{aligned}\cos(\theta_{ff}^{CM})|_{min}(A) = &- 0.7031 + 3.943 \cdot 10^{-2} A - 4.3090 \cdot 10^{-4} A^2 \\ &+ 1.2123 \cdot 10^{-6} A^3, \\ \cos(\theta_{ff}^{CM})|_{max}(A) = &\ 0.8957 - 1.512 \cdot 10^{-3} A.\end{aligned} \tag{5.25}$$

In the case of transfer-induced fission, the velocity and angle of the fissioning system define a $\cos(\theta_{ff}^{CM})|_{limit}$ curve that changes event by event. The maximum variation of $\cos(\theta_{ff}^{CM})|_{limit}$ curve, considering the maximum and minimum velocity and angle of the fissioning system, is observed to be lower than 0.1 respect to fusion-induced fission. Figure 5.17 presents two curves of $\cos(\theta_{ff}^{CM})|_{limits}$ surrounding the distribution of two charge states of A=120 for the maximum and minimum values of velocity and angle of

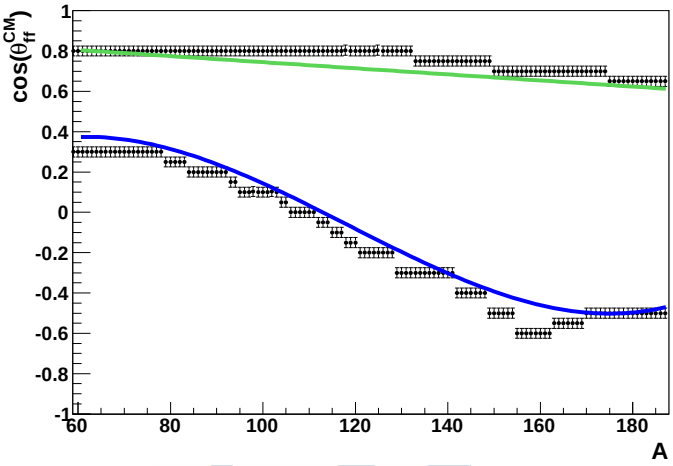

Figure 5.16: Limits of $\cos(\theta_{ff}^{CM})$. Blue and green lines reproduce, restrictively, the lower and upper limits.

the fissioning system. The limits of $\cos(\theta_{ff}^{CM})$ for transfer-induced fission are defined as

$$\begin{aligned} \cos(\theta_{ff}^{CM})|_{min}^{transfer}(A) &= \cos(\theta_{ff}^{CM})|_{min}(A) + 0.1, \\ \cos(\theta_{ff}^{CM})|_{max}^{transfer}(A) &= \cos(\theta_{ff}^{CM})|_{max}(A) - 0.05, \end{aligned} \tag{5.26}$$

where $\cos(\theta_{ff}^{CM})|_{min}(A)$ and $\cos(\theta_{ff}^{CM})|_{max}(A)$ are the limits defined in Eq. 5.25.

5.6 Charge States Addition

The limits of $\cos(\theta_{ff}^{CM})$ described in the previous section define the integration region where the total number of fission fragments ($N(Z,A)$) is computed in order to calculated the fission yields, as it was shown in Eq. 5.3,

$$N(Z,A) = \int_{\cos(\theta_{ff}^{CM})|_{min}(A)}^{\cos(\theta_{ff}^{CM})|_{max}(A)} \frac{\mathrm{d}N(Z,A)}{\mathrm{d}(\cos(\theta_{ff}^{CM}))} \mathrm{d}(\cos(\theta_{ff}^{CM})). \tag{5.27}$$

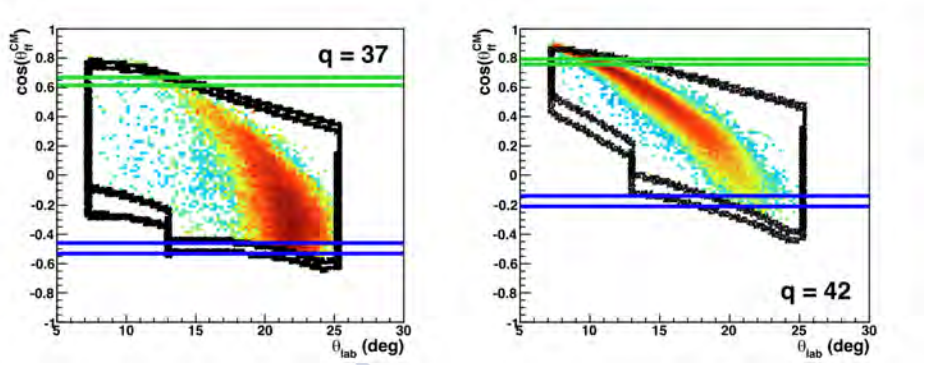

Figure 5.17: Variation of the $\cos(\theta_{ff}^{CM})$ limits in transfer-induced fission. Two charge states of fragments with $A = 120$ are presented, the limits of $\cos(\theta_{ff}^{CM})$ are indicated for the lower and higher velocity and angle of the fissioning system. A difference lower than 0.1 is achieve in $\cos(\theta_{ff}^{CM})$ compared to fusion-induced fission.

The number of fission events per unit of $\cos(\theta_{ff}^{CM})$ is calculated as the sum of the different charge states contributions produced in $\cos(\theta_{ff}^{CM})$:

$$\frac{\mathrm{d}N(Z,A)}{\mathrm{d}(\cos(\theta_{ff}^{CM}))} = \sum_{q_{min}(A)}^{q_{max}(A)} \frac{\mathrm{d}N(Z,A,q)}{\mathrm{d}(\cos(\theta_{ff}^{CM}))}. \tag{5.28}$$

Each charge-state distribution is composed of the contribution of the four different settings of VAMOS used in this experiment. The four settings present an overlap in some regions of $\cos(\theta_{ff}^{CM})$ for each charge state. The number of events per unit of $\cos(\theta_{ff}^{CM})$ in the overapping regions is chosen as the one with the largest contribution:

$$\frac{\mathrm{d}N(Z,A,q)}{\mathrm{d}(\cos(\theta_{ff}^{CM}))} = \mathrm{MAX}\left[\frac{\mathrm{d}N(Z,A,q,i)}{\mathrm{d}(\cos(\theta_{ff}^{CM}))}\right], \tag{5.29}$$

where $i = 1, 2, 3, 4$ indicates the setting in VAMOS.

Figure 5.18 (a) presents the $\cos(\theta_{ff}^{CM})$ distribution of the charge state $q = 40$ of ^{124}Sn. The contribution of each of the four settings is repre-

sented with a different color. The final distribution, represented with a black line, is the envelope of the four settings that takes the maximum number of counts for each $\cos(\theta_{ff}^{CM})$ bin. Figure 5.18 (b) shows, in black, the $\cos(\theta_{ff}^{CM})$ distribution of ^{124}Sn, obtained by adding all the charge states contributions in the range of full charge states transmission. The distributions in color represent the most produced individual charge states, from $q = 37$ to $q = 45$.

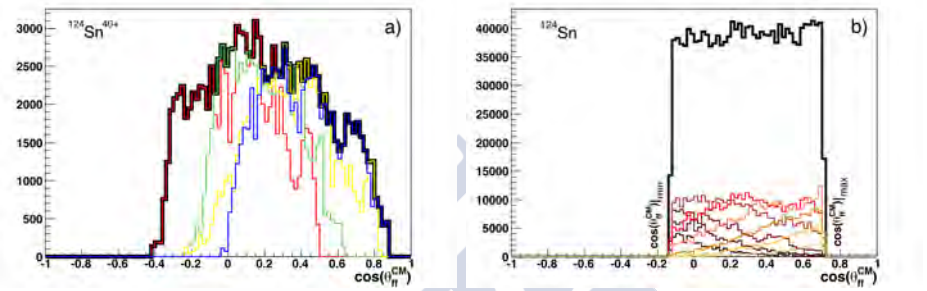

Figure 5.18: Figure (a): distribution in $\cos(\theta_{ff}^{CM})$ of the charge state $q = 40$ of ^{124}Sn. The contribution of each of the four settings are presented in colors. The envelope of the four settings is represented with a black line. Figure (b): distribution in $\cos(\theta_{ff}^{CM})$ of ^{124}Sn, in black, obtained adding the different charge states contribution. Individual charge states contributions from $q = 37$ to $q = 45$ are presented in colors.

5.7 Intrinsic Efficiency

The intrinsic efficiency of the fission fragment detection, ε_i^{ff}, is defined as the probability of having isotopic identification for each fission fragment that reaches the last detector of the VAMOS focal plane setup. The intrinsic efficiency can be factorized in several contributions, each corresponding to the involved detector:

$$\varepsilon_i^{ff} = \varepsilon_i^{DC} \cdot \varepsilon_i^{Si} \cdot \varepsilon_i^{Trigger} , \tag{5.30}$$

where ε_i^{DC} is the intrinsic efficiency of the drift chamber; ε_i^{Si} is the intrinsic efficiency of the silicon wall; and $\varepsilon_i^{Trigger}$ is the intrinsic efficiency of both the Start detector and the multiwire chamber at the focal plane, which signals in coincidence define the VAMOS trigger. The intrinsic efficiency of the ionization chamber is assumed to be $\varepsilon^{IC} = 1$.

5.7.1 Drift-Chamber Intrinsic Efficiency (ε_i^{DC})

The intrinsic efficiency of the drift chamber depends on the energy that fission fragments losses inside the chamber. Lower ionization, as explained in Section 2.4.2.3, produces less free electrons, and the amplitude of the signal induced in the chambers wires is, therefore, lower. Below a certain amplitude, these signals are rejected by the discriminators.

ε_i^{DC} is calculated as a function of the energy loss in the first row of the ionization chamber (ΔE_{row1}), which is strongly correlated with the energy loss in the drift chamber, as it was shown in Section 3.4.3. ε_i^{DC} is determined as the number of events registered in the drift chamber and in the ionization chamber at the same time, ($N_{DC\&IC}$), divided by the number of events registered in the ionization chamber individually (N_{IC}):

$$\varepsilon_i^{DC}(\Delta E_{row1}) = \frac{N_{DC\&IC}}{N_{IC}}(\Delta E_{row1}), \tag{5.31}$$

where

$$\begin{aligned} N_{IC} &= N_{tot}, \\ N_{DC\&IC} &= N_{tot} \cdot \varepsilon_i^{DC}, \end{aligned} \tag{5.32}$$

being N_{tot}, the total number of fragments within the VAMOS acceptance.

ε_i^{DC} is parametrized as a function of ΔE_{row1} as:

$$\varepsilon_i^{DC} = \left[C_1 + C_2 \Delta E_{row1} + C_3 {\Delta E_{row1}}^2\right] \mathrm{Erf}\left(A[\Delta E_{row1} - B]\right), \tag{5.33}$$

where $\mathrm{Erf}(x) = \frac{2}{\sqrt{\pi}} \int_0^x e^{-t^2} \mathrm{d}t$ is the *Error function*, and (C_1, C_2, C_3, A, B) are parameters. Their values, presented in Table 5.4, are obtained by

fitting the previous equation to the data. Each setting of VAMOS presents a different set of parameters, hence an individual fit per setting results more accurate. Figure 5.19 shows ε_i^{DC} and its parametrization as a function of the energy loss in the first row of the ionization chamber for each setting.

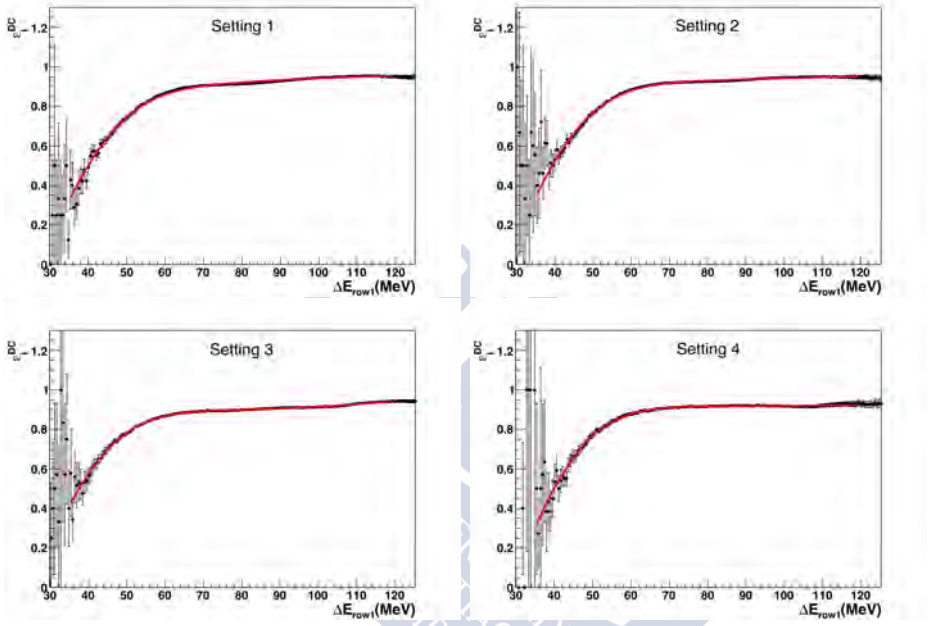

Figure 5.19: Intrinsic efficiency of the drift chamber (ε_i^{DC}), as a function of the energy loss in the first row of the ionization chamber. Each VAMOS setting is presented separately. Red curves represent the parametrization (Eq. 5.33).

5.7.2 Silicon-Wall Intrinsic Efficiency (ε_i^{Si})

The intrinsic efficiency of the silicon wall is determined by the intrinsic efficiency of each silicon detector. In the lower row, two of the detectors were inoperable during the experiment (see Fig. 5.20); the efficiency of such detectors is, therefore, null. The impact of these non-working detectors on the measured number of events is evaluated by means of the

ε_i^{DC} Function Parameters		
Parameter	**Setting 1**	**Setting 2**
C_1	0.7624 ± 0.0082	0.888 ± 0.025
C_2	$(2.820 \pm 0.023) \cdot 10^{-3}$	$(5.9 \pm 5.3) \cdot 10^{-4}$
C_3	$(-1.024 \pm 0.091) \cdot 10^{-5}$	$(-0.5 \pm 2.7) \cdot 10^{-6}$
A	0.0440 ± 0.0015	0.04254 ± 0.00080
B	26.95 ± 0.38	26.78 ± 0.18
	Setting 3	**Setting 4**
C_1	0.977 ± 0.021	0.924 ± 0.040
C_2	$(-2.30 \pm 0.45) \cdot 10^{-3}$	$(-2.5 \pm 8.5) \cdot 10^{-4}$
C_3	$(1.68 \pm 0.23) \cdot 10^{-5}$	$(2.0 \pm 4.5) \cdot 10^{-6}$
A	0.0425 ± 0.0014	0.0454 ± 0.0024
B	25.06 ± 0.62	28.28 ± 0.86

Table 5.4: Parameters of the function that reproduce the intrinsic efficiency of the drift chamber.

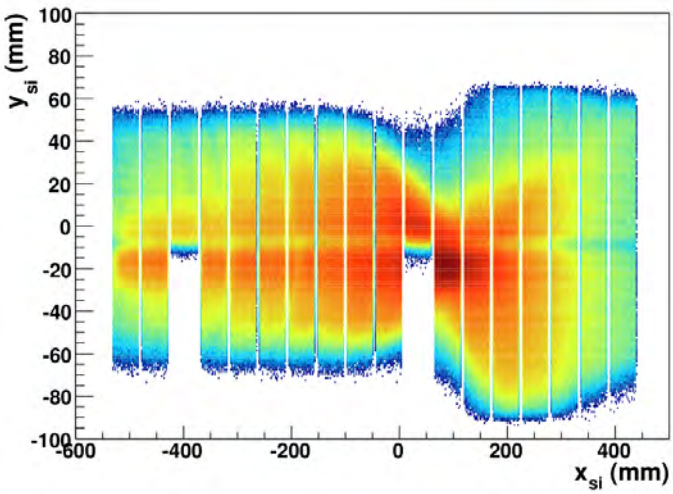

Figure 5.20: Distribution of fission events. The axes represent the horizontal and vertical position in the plane of the silicon wall. Two silicon detectors were inoperable during the experiment.

$(B\rho, \theta_{lab})$ phase-space. ε_i^{Si} is calculated as the number of events per unit of $\delta = B\rho/B\rho_0$ and θ_{lab}, detected in the drift chamber and in the silicon wall at the same time ($N_{DC\&Si}$), divided by the number of events, per unit of δ and θ_{lab}, detected in the drift chamber (N_{DC}),

$$\varepsilon_i^{Si}(\delta, \theta_{lab}) = \frac{N_{DC\&Si}}{N_{DC}}(\delta, \theta_{lab}), \tag{5.34}$$

where

$$\begin{aligned} N_{DC} &= N_{tot} \cdot \varepsilon_i^{DC}, \\ N_{DC\&Si} &= N_{tot} \cdot \varepsilon_i^{DC} \cdot \varepsilon_i^{Si}, \end{aligned} \tag{5.35}$$

being N_{tot} the total number of fragments within the VAMOS acceptance, and ε_i^{DC} and ε_i^{Si}, the intrinsic efficiency of the drift chamber and the silicon wall. In both cases, the velocity of the fragments is required to be higher than 2.8 cm/ns, in order to traverse the IC and reach the silicon detectors.

ε_i^{Si} is calculated at discrete points of δ and θ_{lab} with a step of 0.002 in δ and 0.1 deg in θ_{lab} for both orientations of VAMOS, independently. Figures 5.21 (a) and (b) present ε_i^{Si} as a function of δ and θ_{lab} for VAMOS at 20 deg and 14 deg, respectively. Figures 5.21 (c) and (d) show the evolution of ε_i^{SI} with θ_{lab} for $\delta \in (0.899, 0.901)$ (black) and $\delta \in (0.999, 1.001)$ (red).

ε_i^{Si} is computed event by event by means of a local multivariable interpolation similar to the ϕ-acceptance interpolation, presented in Eq. 5.20.

5.7.3 Trigger Intrinsic Efficiency ($\varepsilon_i^{Trigger}$)

The Start detector is composed of vertical wires, polarized at -500 V, that form the electric field that triggers the electron avalanche and creates the signals. In this experiment, some wires of the detector were affected by degradation, reducing the electric field locally and, therefore, reducing the signal amplitude from the avalanches. This effect has an impact in the detection efficiency of fission fragments: the less ionizing fragments (lighter

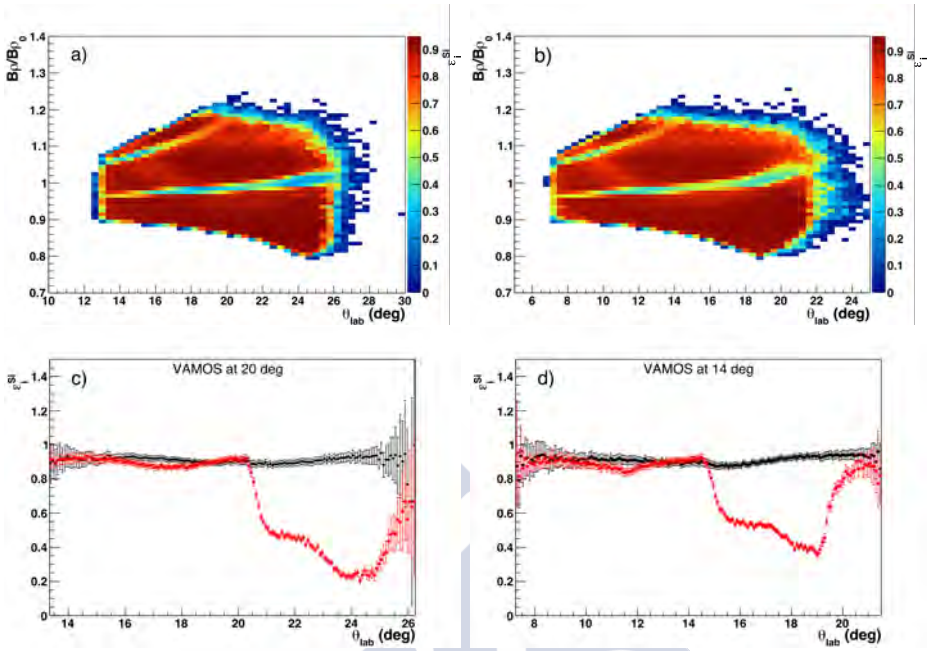

Figure 5.21: Figures (a) and (b): ε_i^{Si} distribution as a function of δ and θ_{lab} for VAMOS at 20 and 14 deg, respectively. Figures (c) and (d): evolution of ε_i^{Si} as a function of θ_{lab} for $\delta \in (0.899, 0.901)$ (black) and $\delta \in (0.999, 1.001)$ (red).

fragments) produce a lower number of electrons and the avalanche, due to the low electric-field, is not sufficient to create a signal higher than the threshold.

Figure 5.22 (a) shows the vertical angle (ϕ_{ff}^v) of fission fragments with $Z = 36$, as a function of the horizontal angle (θ_{ff}^v) with respect to the VAMOS axis. Figure 5.22 (b) shows the horizontal angular distribution for $Z = 36$ fragments from a small range of the vertical angle, $\phi_{ff}^v \in (-0.5, 0.5)$ deg. The local effect of the damaged wires is present in $\theta_{ff}^v \approx 4$ deg, and largely pronounced in $\theta_{ff}^v \approx 0$ deg, independently of ϕ_{ff}^v.

The Start detector defines the detection trigger and, therefore, an absolute efficiency correction is not feasible in this case; a relative efficiency

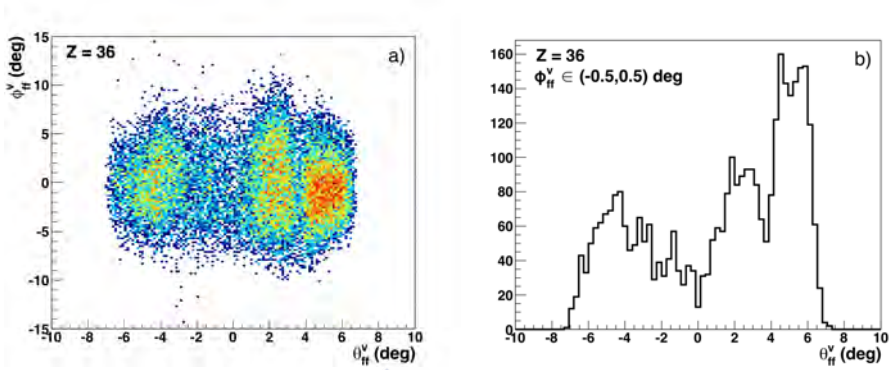

Figure 5.22: Impact of the Start detector efficiency on the fragment distribution. Figure (a): vertical angle distribution (ϕ^v_{ff}) of fragments with $Z = 36$, as a function of the horizontal angle (θ^v_{ff}). Figure (b): horizontal distribution of fragments with $Z = 36$ from a slice of the vertical angle. Events are missed in $\theta^v_{ff} \approx 4$ deg and $\theta^v_{ff} \approx 0$ deg, independently of the vertical angle.

correction is applied instead, calculated as the ratio between the number of counts of two complementary fragments.

The available excitation energy permits neutron evaporation before and after the fission process, therefore, it is not possible to relate the mass of the detected fragments with the mass of the fissioning system. However, proton evaporation is highly inhibited in this process, hence, the number of fragments emitted with a nuclear charge Z_1 must be equal to the number of fragments emitted with the complementary nuclear charge, $Z_2 = Z_{fiss} - Z_1$, being Z_{fiss} the nuclear charge of the fissioning system. This nuclear-charge conservation is reflected in the $\cos(\theta^{CM}_{ff})$ distribution: once the ϕ-acceptance and the previous efficiencies are corrected, the height of the $\cos(\theta^{CM}_{ff})$ distributions of fragments with Z_1 and Z_2 must be the same.

Figure 5.23 presents the $\cos(\theta^{CM}_{ff})$ distributions for fragments with $Z = 36$ (red) and $Z = 62$ (black), which are complementary fragments when selecting ^{250}Cf as the fissioning system. The shape of the distribution of $Z = 36$ reflects the missing events in the Start detector, while the distribution of $Z = 62$ is assumed unaffected. The shape of $Z = 62$ in the

center of the distribution differing from a flat behavior is a local effect of the ϕ reconstruction that the ϕ acceptance can not correct. This effect is included in the uncertainty of the method.

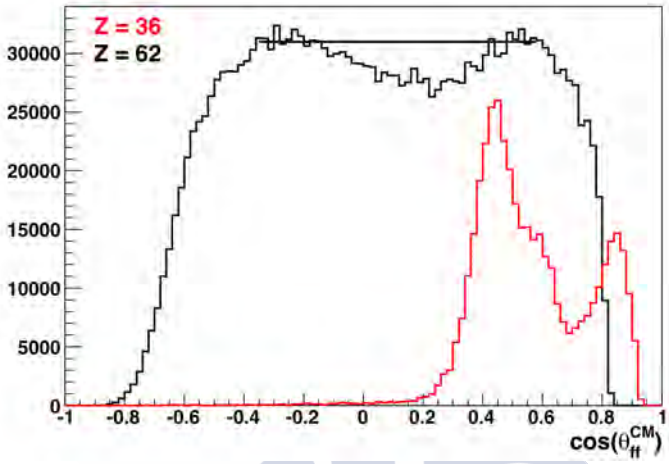

Figure 5.23: $\cos(\theta_{ff}^{CM})$ distribution of fragments with $Z = 36$ and $Z = 62$ from the fission of ^{250}Cf. The shape of the distribution of $Z = 36$ is produced by the missing events in the Start detector. The black line indicates the maximum of the distribution of the heavy fragment, that defines the reference value in the efficiency calculation for the light fragment.

The intrinsic efficiency of the Start detector ($\varepsilon_i^{Trigger}$) is calculated as the ratio between the number of events per unit of $\cos(\theta_{ff}^{CM})$ of the light fragment, Z_1, and the maximum number of events per unit of $\cos(\theta_{ff}^{CM})$ of the complementary heavy fragment, $Z_2 = 98 - Z_1$:

$$\varepsilon_i^{Trigger}\left(Z_1, \cos(\theta_{ff}^{CM})\right) = \frac{N_{Z_1}(\cos(\theta_{ff}^{CM}))}{N_{98-Z_1}^{max}}. \tag{5.36}$$

This definition assumes a negligible angular anisotropy, which in general is not satisfied. However, a previous experiment on fusion-induced fission of ^{250}Cf [24], produced in an equivalent configuration, observed no

significant anisotropy along an angular range similar to this. Therefore, $\varepsilon_i^{Trigger}$ is calculated based on ^{250}Cf data and applied to the rest of the systems.

In general, $\varepsilon_i^{Trigger}$ depends on the number of electrons released in the detector, which is proportional to the energy loss inside the filling gas. Following the *Bethe-Bloch equation* (see Eq.2.4), the $\varepsilon_i^{Trigger}$ depends on $(Z/v)^2$, where Z is the nuclear charge, and v is the velocity of the fragments in the *lab* reference frame. Figure 5.24 presents $\varepsilon_i^{Trigger}$ as a function of $(Z/v)^2$. Each color corresponds to one nuclear charge, and each point corresponds to one value of $\cos(\theta_{ff}^{CM})$ that defines, in average, one value of $(Z/v)^2$ and one value of θ_{ff}^{v} for each Z. A global tendency with $(Z/v)^2$ is evident, with the efficiency lower for lower $(Z/v)^2$. However, due to the local effect of the damaged wires in the detector, the efficiency evolves also with θ_{ff}^{v}, producing the observed behavior in each Z.

$\varepsilon_i^{Trigger}$ can be decomposed into two components:

$$\varepsilon_i^{Trigger} = \varepsilon_1^{Trigger}\left(\left(\frac{Z}{v}\right)^2\right) \cdot \varepsilon_2^{Trigger}\left(\theta_{ff}^{v}, \left(\frac{Z}{v}\right)^2\right), \tag{5.37}$$

the first component describes the global tendency, as a function of $(Z/v)^2$, while the second component takes into account also the θ_{ff}^{v} dependence.

$\varepsilon_1^{Trigger}$ is calculated from the larger $\cos(\theta_{ff}^{CM})$ values that correspond to the lower $(Z/v)^2$ values per Z, presented in Fig. 5.25 (a). This component is parametrized as :

$$\varepsilon_1^{Trigger} = C_1 + C_2 \mathrm{Erf}\left(A\left[\left(\frac{Z}{v}\right)^2 - B\right]\right), \tag{5.38}$$

where $\mathrm{Erf}(x) = \frac{2}{\sqrt{\pi}}\int_0^x e^{-t^2}\mathrm{d}t$ is the *Error function*, and (C_1, C_2, A, B) are parameters. The parameters fitted to the data are presented in Table 5.5.

$\varepsilon_2^{Trigger}$ is described by three Gaussian functions that reproduce the local effect of the missing events in θ_{ff}^{v}. Figure 5.25 (b) shows the θ_{ff}^{v}

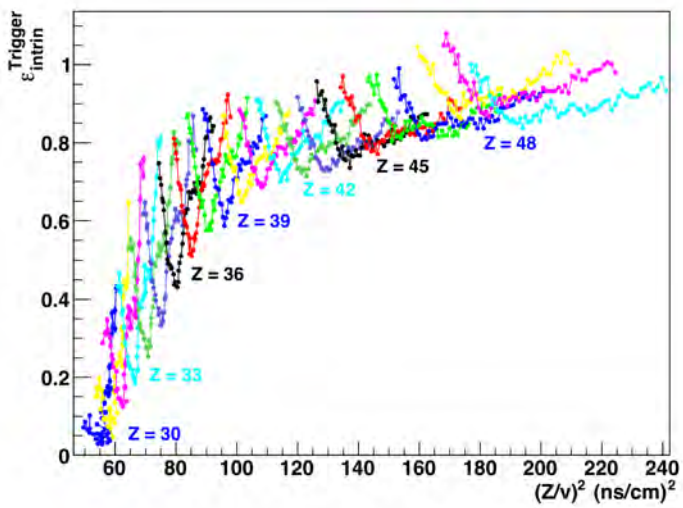

Figure 5.24: $\varepsilon_i^{Trigger}$ as a function of $(Z/v)^2$. Each color represent a single fragment Z; the points correspond to values of $\cos(\theta_{ff}^{CM})$ that are related to the average value of $(Z/v)^2$ and θ_{ff}^{v}. Two different behaviors are observed: a global tendency with $(Z/v)^2$, and a local evolution for each Z.

$\varepsilon_1^{Trigger}$ **Parameters**	
Parameter	**Value**
C_1	-131 ± 33
C_2	132 ± 33
A	0.0112 ± 0.0003
B	-122.8 ± 6.2

Table 5.5: Fitted values of the $\varepsilon_1^{Trigger}$ parametrization.

distribution of $Z = 36$, once $\varepsilon_1^{Trigger}$ is corrected. The shape of the distribution is described by the inverse of the sum of three Gaussian functions, indicated by the blue line. The three single Gaussian functions are presented in red. The positions and widths of the Gaussians functions are observed to remain constant for the different Z, while their amplitudes

increase for lower $(Z/v)^2$.

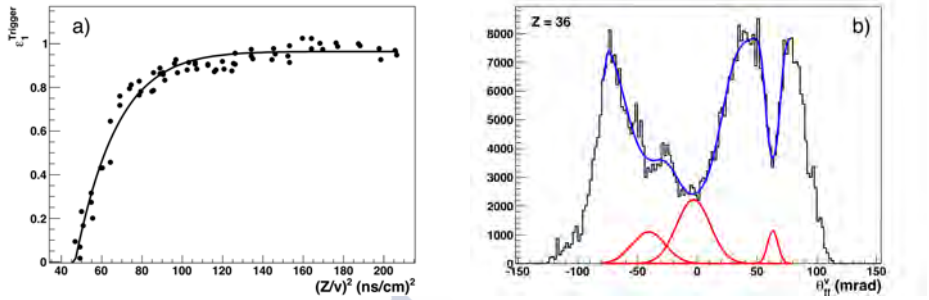

Figure 5.25: Description of the intrinsic efficiency of the Start detector. Figure (a): global component of the Start detector efficiency ($\varepsilon_1^{Trigger}$) as a function of $(Z/v)^2$. Figure (b): description of the local effect in θ_{ff}^v of the Start detector efficiency for $Z = 36$.

$\varepsilon_2^{Trigger}$ is, therefore, parametrized as:

$$\varepsilon_2^{Trigger} = \left[1 + \sum_{i=1}^{3} A_i \cdot e^{-\frac{1}{2}\left(\frac{\theta_{ff}^v - \mu_i}{\sigma_i}\right)^2}\right]^{-1}, \tag{5.39}$$

$$A_i = \left[\left(\frac{1}{2} + C'_i\right) + \left(\frac{1}{2} - C'_i\right) \mathrm{Erf}\Big(A'_i\left[(Z/v)^2 - B'_i\right]\Big)\right]^{-1} - 1,$$

where the mean and sigma values of each Gaussian function, μ_i, σ_i, presented in Table 5.6, were obtained from a fit to the data while the parameters of each amplitude, C'_i, A'_i, B'_i, were obtained from an iterative process that minimizes the deviation from a flat distribution in $\cos(\theta_{ff}^{CM})$ of each Z. Figure 5.26 shows the values of each Gaussian amplitude as a function of $(Z/v)^2$; the parametrization is indicated in blue and the values of the parameters are shown in Table 5.7.

Figure 5.27 presents the $\cos(\theta_{ff}^{CM})$ distribution of fragments with $Z = 36$ (red) and $Z = 62$ (black) from the fission of ^{250}Cf once the $\varepsilon_i^{Trigger}$ is corrected. A flatter distribution compared to that of Fig. 5.23 is obtained for the light fragment. The contribution of the four settings of VAMOS is included in this picture.

$\varepsilon_2^{Trigger}$ **Parameters**	
Parameter	**Value** $(mrad)$
μ_1	63.21 ± 0.06
μ_2	-3.17 ± 0.19
μ_3	-40.62 ± 0.34
σ_1	4.32 ± 0.06
σ_2	14.04 ± 0.13
σ_3	13.86 ± 0.23

Table 5.6: Mean and sigma values of the three Gaussians that describe the local effect of $\varepsilon_2^{Trigger}$.

A_i **Parameters**	
Parameter	**Value**
${C'}_1$	0.2297 ± 0.0001
${A'}_1$	0.02426 ± 0.00007
${B'}_1$	107.10 ± 0.01
${C'}_2$	-14.3 ± 7.4
${A'}_2$	$(5.52 \pm 0.62) \cdot 10^{-3}$
${B'}_2$	-186 ± 55
${C'}_3$	$(-3.621 \pm 0.013) \cdot 10^{5}$
${A'}_3$	$(4.047 \pm 0.003) \cdot 10^{-3}$
${B'}_3$	-920.2 ± 0.7

Table 5.7: Parameters of the Gaussian amplitudes of $\varepsilon_2^{Trigger}$.

5.8 Fission Yields

The isotopic fission yields, $Y(Z, A)$, are calculated, as mentioned in Section 5.1, following:

$$Y(Z,A) = 200 \frac{N}{\varepsilon_g^{ff} \cdot \varepsilon_i^{ff}}(Z,A) \left(\sum_{Z,A} \frac{N}{\varepsilon_g^{ff} \cdot \varepsilon_i^{ff}}(Z,A) \right)^{-1} . \tag{5.40}$$

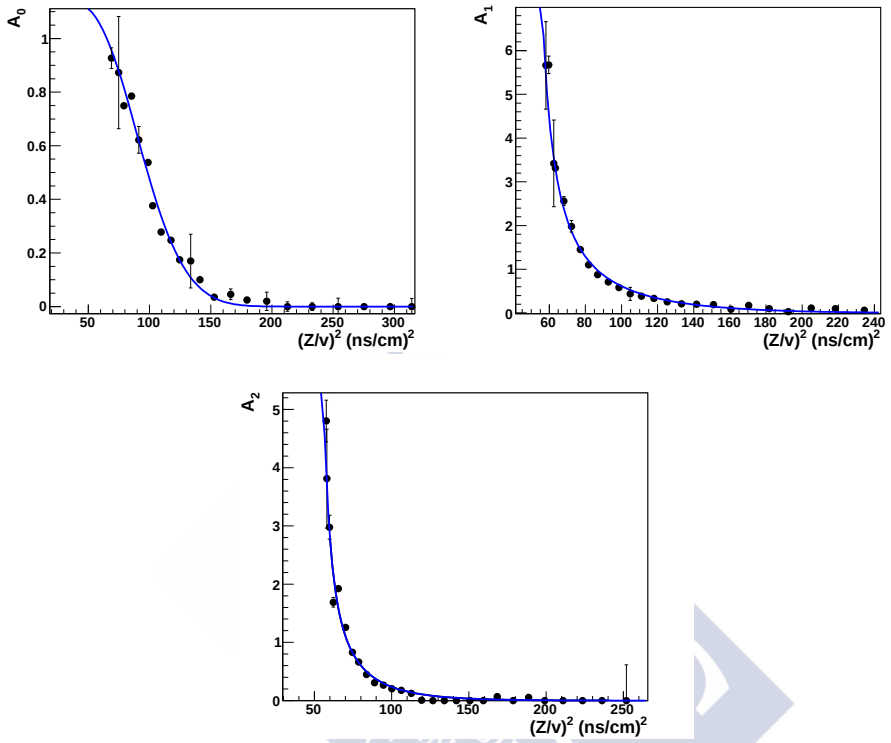

Figure 5.26: Evolution of the Gaussian amplitudes of $\varepsilon_2^{Trigger}$ as a function of $(Z/v)^2$. The blue lines reproduce the parametrization presented in Eq. 5.39.

The number of events per isotope, N, is calculated as the integral of the number of counts in the $\cos(\theta_{ff}^{CM})$ range, defined by the full transmission of charge states (Eq. 5.27). The integral includes the contribution of the different charge states (Eq. 5.28). The geometrical efficiency, ε_g^{ff} includes the ϕ and θ acceptance (Eq. 5.19 and Eq. 5.21), while the intrinsic efficiency, ε_i^{ff}, comprises the three individual intrinsic efficiencies, ε_i^{DC}, ε_i^{Si}, and $\varepsilon_i^{Trigger}$, presented in the previous section.

As an example of the result of the full process, the isotopic distribution of fission yields of ^{250}Cf is presented in Fig. 5.28. Each point corresponds

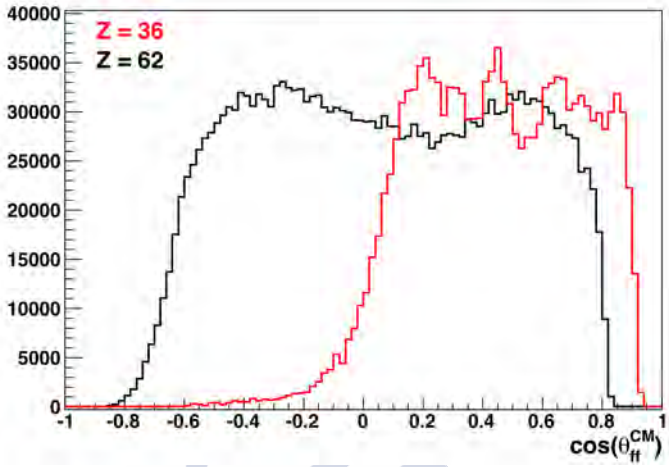

Figure 5.27: $\varepsilon_i^{Trigger}$-corrected $\cos(\theta_{ff}^{CM})$ distribution of fragments with $Z = 36$ (red) and $Z = 62$ (black) from the fission of ^{250}Cf.

to one mass and each color correspond to one nuclear charge.

5.8.1 Fission Yields Uncertainty

The uncertainty on the fission yields is calculated as the quadratic sum of the statistical and systematic uncertainty:

$$\epsilon = \sqrt{\epsilon_{stat}^2 + \epsilon_{sys}^2}. \tag{5.41}$$

The statistical uncertainty is obtained as the root square of the number of counts per isotope, previous to the normalization and the efficiency corrections, $\epsilon_{stat} = \sqrt{N}$. The systematic uncertainty takes into account the uncertainty in the determination of the ϕ acceptance and the range of $\cos(\theta_{ff}^{CM})$, as well as the uncertainty in the calculation of the intrinsic efficiency, ranging from 2% in the heavier fragments up to 10 % in the lighter fragments.

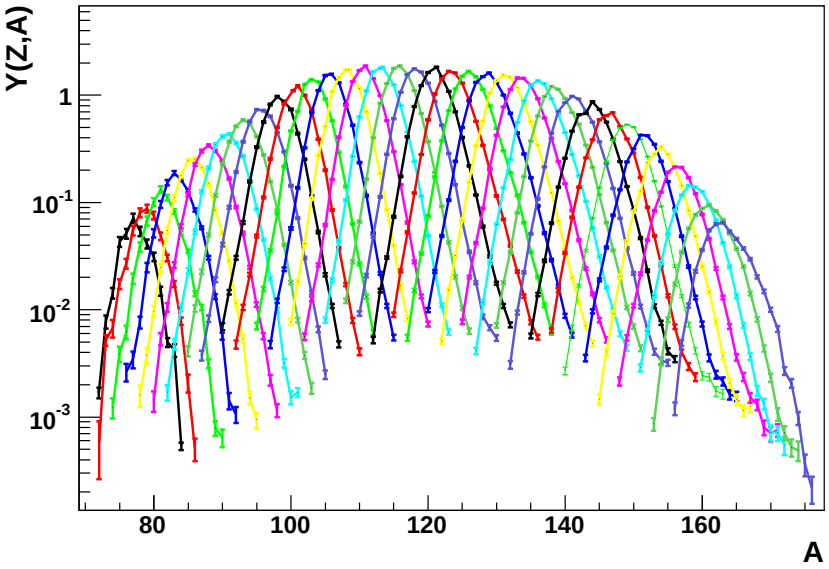

Figure 5.28: Isotopic yields of ^{250}Cf. Each line corresponds to one nuclear specie, from $_{31}$Ga up to $_{66}$Dy.

Figure 5.29 shows the ratio of yields between complementary Z fragments from ^{250}Cf. All complementary fragments present the same yields within a error lower than 5%.

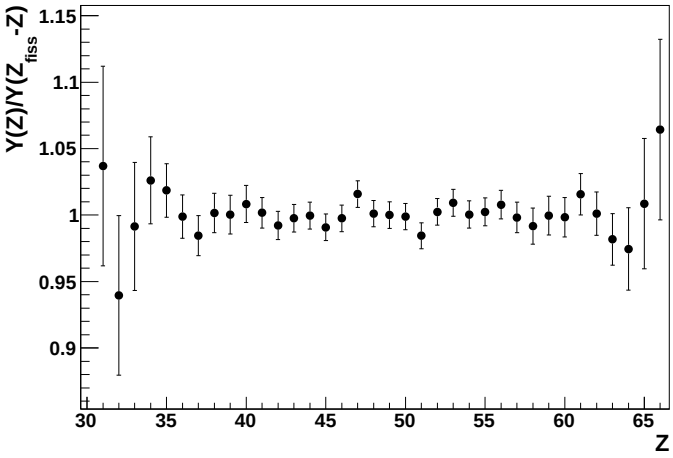

Figure 5.29: Ratio of yields of complementary Z fragments from ^{250}Cf.

Chapter 6

Results

This chapter presents several physical observables from the fragment distribution produced in fusion-induced fission of ^{250}Cf, and transfer-induced fission of ^{244}Cm, ^{240}Pu, ^{239}Np, and ^{238}U. Isotopic, isobaric, and elemental yields are presented. The neutron excess, the total neutron evaporation, and the even-odd staggering are calculated as a function of the nuclear charge of the fission fragments. Finally, the evolution of these observables is investigated as a function of the excitation energy of the fissioning system.

6.1 Fission Yields

This section presents the isotopic distributions of the relative fission yields of five fissioning systems: ^{250}Cf, ^{244}Cm, ^{240}Pu, ^{239}Np, and ^{238}U. The fission yields are also presented as a function of the nuclear charge and the post-neutron-evaporation mass of the fission fragments. The present work is compared with available previous data and with calculations from the GEF code. The fission channels are investigated in terms of the nuclear charge for the different fissioning systems.

The values of the isotopic yields of the fissioning systems addressed in this work are compiled in Appendix C.

Figure 6.1 presents the distribution of fission fragments of the five inves-

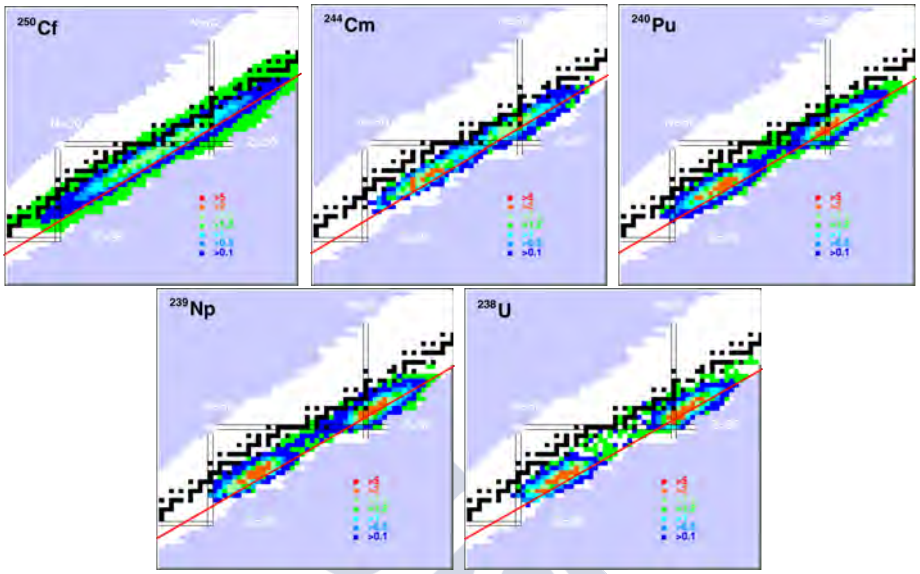

Figure 6.1: Fission-fragment distribution in terms nuclear charge versus neutron number, on top of the nuclide chart. Red lines indicates the N/Z ratio of the fissioning systems.

tigated fissioning systems in terms nuclear charge versus neutron number, on top of an schematic view of the nuclide chart. The red line correspond to the N/Z ratio of each fissioning system. Charge polarization is observed in the systems at lower excitation energy, ^{240}Pu ($\langle E_x \rangle = 10.7$ MeV), ^{239}Np ($\langle E_x \rangle = 7.5$ MeV), and ^{238}U ($\langle E_x \rangle = 7.4$ MeV), where the fragments do not show the same ratio of N/Z; instead, the heavy fragment is systematically more neutron rich than the light one. It is also observed that the neutron evaporation shifts the full distribution to less neutron-rich nuclei compared to the compound nucleus, which is more evident in the systems at higher excitation energy, ^{244}Cm ($\langle E_x \rangle = 23.0$ MeV) and ^{250}Cf ($E_x = 45.97$ MeV). These two characteristics are detailed in Sec. 6.2 and Sec. 6.3, respectively.

6.1.1 Fusion-Fission (^{250}Cf)

The fissioning system ^{250}Cf is produced in fusion reactions between the beam of ^{238}U at 6.14 MeV/u and the target of ^{12}C. This reaction introduces an excitation energy of $E_x = 45.97$ MeV into the compound system (see Sec. 5.2). This large excitation energy produces a distribution of fission fragments where the symmetric fission is favored. An angular momentum distribution (L) is also induced in the system. Following the Bass description [63], this results in $L_{RMS} = 15\hbar$.

The nuclear charge and post-neutron-evaporation mass distributions of fission yields of fusion-induced ^{250}Cf are shown in Fig. 6.2. Present data (black dots), are compared with a previous measurement (red squares) performed in the same experimental conditions with a similar setup in the first campaign of fission in inverse kinematics at GANIL [24], and with a calculation using the GEF code [19] (see Sec. 1.2.5).

No major structure effects are expected with such a large E_x and, consequently, a Gaussian shape would describe the yields distribution in nuclear charge. However, Figure 6.2(a) presents a quasi-Gaussian shaped distribution with a central plateau, which suggests that structure effects remain even at this high E_x. The yields of each asymmetric-fission component is investigated in Sec. 6.1.3.

The measured yields distribution in mass (Fig. 6.2(b)) corresponds to post-neutron evaporation, which prevents a symmetric distribution: the n-evaporation was observed to increase for heavier fragments [60] and, since the n-evaporation shifts the yields to lower mass, the heavier the fragment, the larger the shift of the yields.

An agreement with both previous data sets and GEF calculations is observed. The difference on the heavy-fragment region, Z>63 and A>150, with respect to the previous data is due to experimental limitations when measuring the heaviest fragments during the first campaign. We can observe also larger fluctuations in the symmetric region of the first campaign due to the smaller statistics. The integral of these data is normalized to

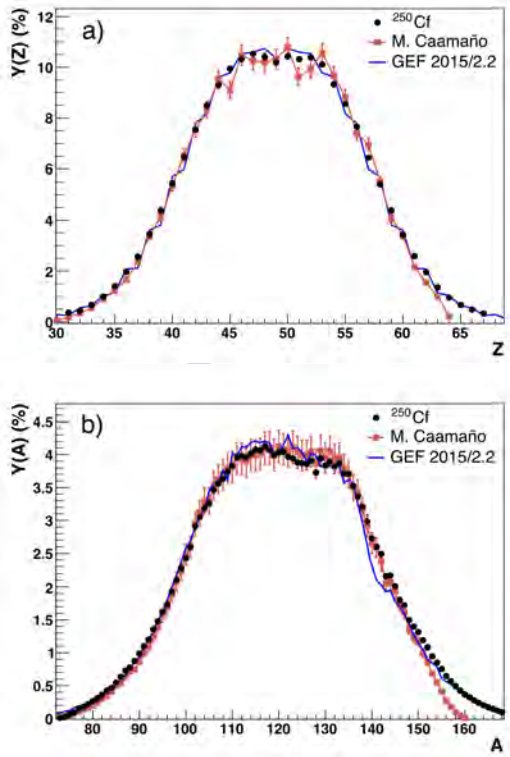

Figure 6.2: Nuclear charge (a) and post-neutron-evaporation mass (b) distributions of fission yields of ^{250}Cf, at $E_x = 45.97$ MeV. Present data (black dots) are compared with previous data measured in similar experimental conditions [24] (red squares), and with a calculation using the GEF code (blue line).

the present work excluding the region $Z > 150$ for comparison purposes.

The GEF code estimates the probability of neutron evaporation before fission in $P_1 = 0.315$, $P_2 = 0.231$, and $P_3 = 0.073$ for one, two, and three evaporated neutrons respectively. The effective mass of the fissioning system is, therefore, $A_{fiss}^{eff} = 249.0$.The fragment distributions obtained from this calculation present an excellent agreement with the present data. Concerning the mass distribution, the GEF calculation presents also a good

agreement with the data, even reproducing the asymmetric behavior in the top of the distribution, $A \in [110, 130]$. However, we can see some local differences for masses around $A \sim 140$.

Figure 6.3 presents the isotopic distributions of fission yields of ^{250}Cf, in terms of the neutron number. The present data (black dots) is compared with a previous measurement performed at VAMOS with a similar setup [24] (red squares), and with the GEF calculation (blue line). The present data shows a general asymmetric behavior, more pronounced in the range of $Z \in [49, 57]$, which suggests a not identified, systematic error that underestimates the yields at lower N. Nevertheless, these differences appear almost two order of magnitude below the largest produced yield of each Z. The GEF code, meanwhile, shows a general good agreement with the present data, although with narrower yield distributions in the region $Z \in [49, 57]$. The experimental limitation of the previous data at heavy fragments is reflected in the shift of yields for $Z > 60$, when compared to the present data, whose mean value is in a better agreement with the ones predicted by the GEF code.

6.1.2 Transfer-Fission

The fissioning systems ^{244}Cm, ^{240}Pu, ^{239}Np, and ^{238}U are produced through transfer reactions and inelastic scattering between the ^{238}U beam and the ^{12}C target. In these cases, the excitation energy depends on the kinematics of each reaction and changes event by event. This produces the distributions of excitation energy already presented in Fig.5.2.

The angular momentum induced in the fissioning systems by the transfer reactions is described in this work following a very simple model where the total angular momentum is assumed to be shared between both the heavy fissioning system and the light recoil, according to their momentum of inertia. Assuming a *Grazing Collision*, the transmitted angular momentum for each fissioning system was estimated in: $L(^{244}Cm) \sim 13\hbar$, $L(^{240}Pu) \sim 7\hbar$, $L(^{239}Np) \sim 6\hbar$, and $L(^{238}U) \sim 5\hbar$.

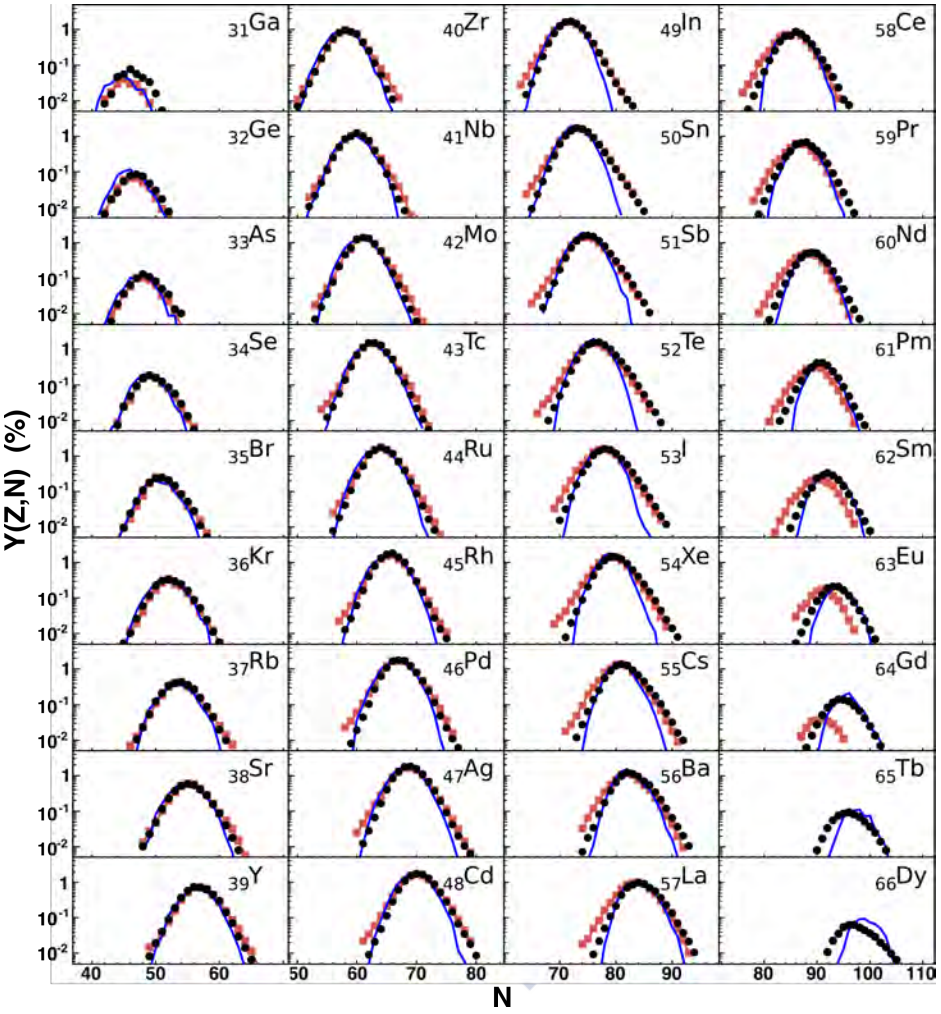

Figure 6.3: Isotopic yields of ^{250}Cf as a function of the number of neutrons. Present data (black dots) is compared with previous data [24] (red squares) and with the GEF calculation (blue line).

In this experiment, the fission-yields measurement of systems produced through transfer channels are contaminated with events from fusion reactions. With the present experimental conditions, fusion reactions are 10 times more produced than any transfer reaction. This favors random

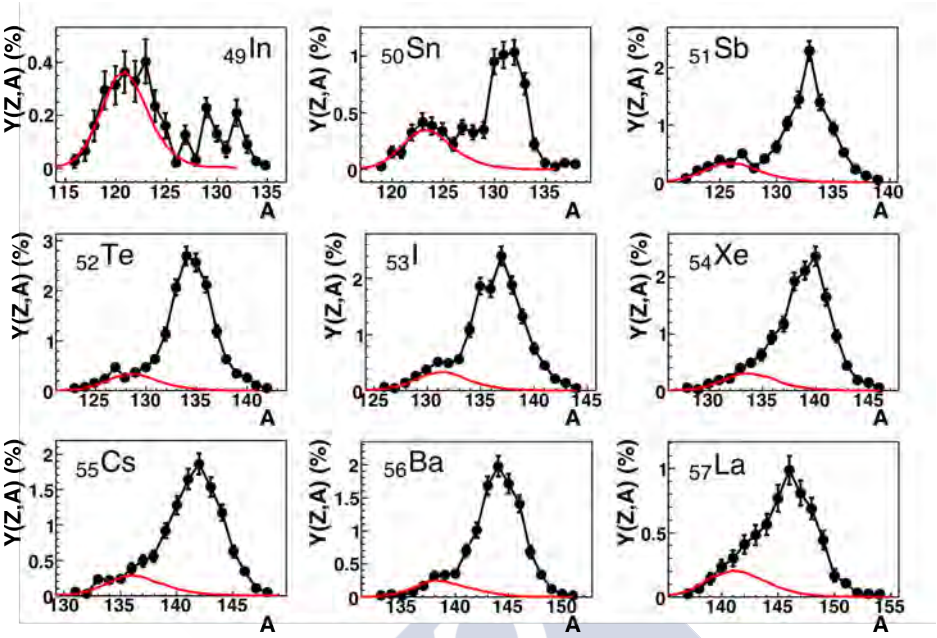

Figure 6.4: Isotopic distribution of fission yields of ^{238}U (in black), with a 21.1% of contamination from ^{250}Cf (in red).

coincidences between the identification of a transfer reaction in SPIDER with a detection of a fission fragment from fusion-fission in VAMOS. In the case of inelastic scattering, the contamination is particularly strong due to the overlap of the elastic scattering at low excitation energy. At high excitation energy there is also a strong contamination because the elastic-scattered ^{12}C, emitted with large angles, is further scattered in the aluminum collimator (see Sec. 2.3.2), producing a reconstructed angle that might mimic the inelastic scattering. Nevertheless, this effect is negligible for the rest of transfer reactions because their cross section is strongly suppressed for such large angles.

This contamination is evaluated and subtracted from the mass distribution of each fragment Z by fitting the corresponding mass distribution from fusion-fission. Figure 6.4 presents the mass distribution of fission yields of ^{238}U (in black) for fragments $Z \in [49, 57]$. These distributions

present a second contribution at low mass that fits with a $(21.1 \pm 3.0)\%$ of the ^{250}Cf yields (in red). This is particularly clear for $Z = 49$, $Z = 50$, and $Z = 51$, where the production is low for ^{238}U, but high for ^{250}Cf. Concerning the other fissioning systems, ^{239}Np and ^{240}Pu present a contamination of $(4.0 \pm 2.1)\%$ and $(2.5 \pm 1.8)\%$, respectively, while ^{244}Cm does not present a significant contamination of ^{250}Cf.

6.1.2.1 ^{244}Cm

The fissioning system ^{244}Cm is produced through the ^{12}C(^{238}U, ^{244}Cm)^{6}He $4p2n$-transfer channel. The range of excitation energy available for the present analysis comprises $E_x \in [10, 35]$ MeV, which corresponds to a mean excitation energy of $\langle E_x \rangle = 23.0$ MeV.

Figure 6.5 presents the nuclear charge (a) and the post-neutron-evaporation mass (b) yield distributions of ^{244}Cm fission. The present data (black dots) are compared with a calculation using the GEF code (blue line) and with previous measurements at different excitation energies. In the case of ^{244}Cm, our measurement suffers from a lack of statistics that produces large fluctuations; nevertheless, a predominant contribution of the asymmetric fission is observed, while the symmetric component, enhanced by the large excitation energy, strongly contributes to the distribution.

No previous measurement of the nuclear charge distribution exists for this system. The present data is only compared with a GEF calculation (Figure 6.5(a)). This comparison reveals a general agreement between both, experimental data and GEF calculation. We performed this calculation with a single value of E_x equal to the mean value of the measured distribution, and taking into account multi-chance fission, with probabilities $P_0 = 0.734$, $P_1 = 0.243$, and $P_2 = 0.023$, that leaves the fissioning system with an effective mass of $A = 243.7$.

The post-neutron-evaporation mass distribution (Fig. 6.5(b)) is compared with previous measurements: thermal-neutron-induced fission, ^{243}Cm (n_{th},f), with $E_x = 6.80$ MeV (green triangles) from I. Tsekhanovich et al.

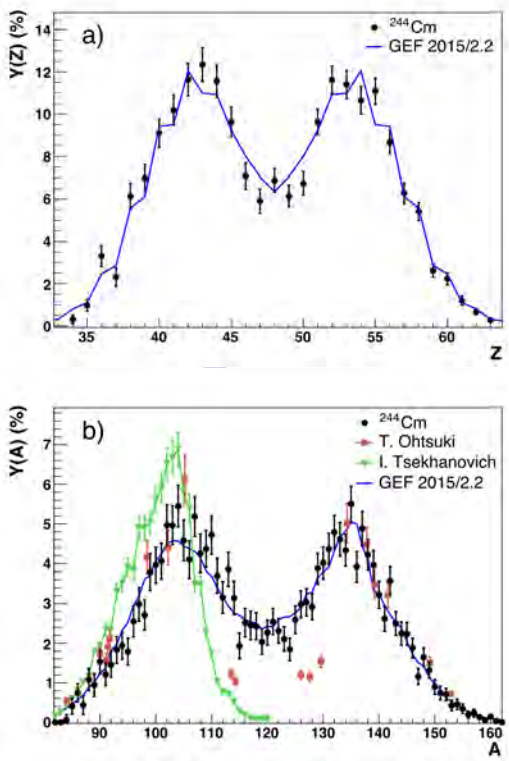

Figure 6.5: Nuclear charge (a) and post-neutron-evaporation mass (b) distributions of fission yields of ^{244}Cm, with mean excitation energy $\langle E_x \rangle$ = 23.0 MeV. The present data (black dots) are compared with previous measurement of ^{243}Cm(n_{th},f) [64] (green triangles), and ^{243}Am(p,f) [65] with E_p = 12 MeV (red squares); as well as with the GEF calculation (blue line).

[64], where only the light fragment was measured; and 12 MeV-proton-induced fission, ^{243}Am(p,f), with E_x = 18 MeV (red squares) from T. Ohtsuki et al. [65], where only the yields of fragments with a well-known level scheme are calculated. The evolution of the system with the excitation energy is evident: the system presents a strong asymmetric fission with a null symmetric component for the lowest excitation energy, while the symmetric fission becomes stronger when increasing E_x. The mass

distribution is also compared with the GEF calculation, providing a very good agreement.

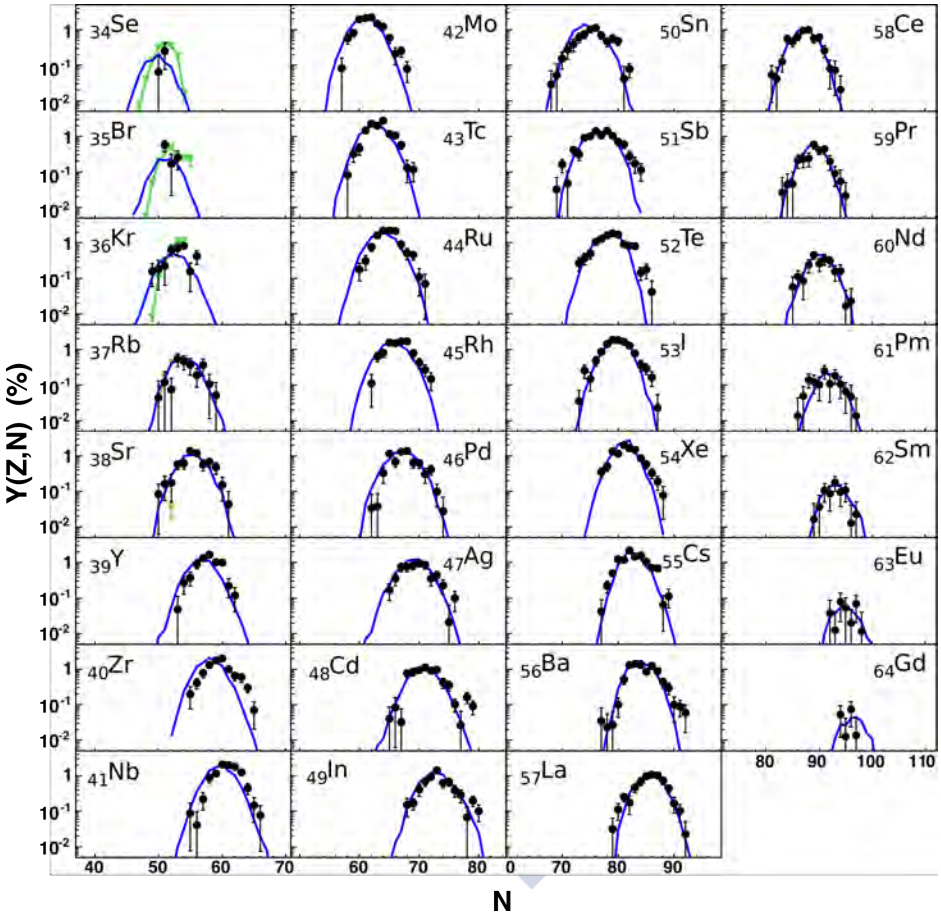

Figure 6.6: Isotopic yields of ^{244}Cm as a function of the neutron number. Present data (black dots) is compared with previous data of ^{243}Cm(n_{th},f) [64] (green triangles), and with the GEF calculation (blue line).

Figure 6.6 presents the full isotopic distribution of yields of ^{244}Cm as a function of the neutron number. Present data (black dots) are compared with the available isotopic data (green triangles) from I .Tsekhanovich et al. [64], which is reduced to the very light fragments, $Z < 39$. The data is

also compared with the GEF calculation (blue line), where it is observed a good agreement for the heavy region, $Z > 56$, with an effect similar to that observed in ^{250}Cf at $Z \in [45, 56]$, where GEF presents narrower distributions for the highest N, and slightly shifted to lower N for the lighter fragments.

6.1.2.2 ^{240}Pu

The fissioning system ^{240}Pu is produced through the ^{12}C(^{238}U, ^{240}Pu)^{10}Be $2p$-transfer channel. The range of excitation energy avaliable for this analysis comprises $E_x \in [3, 20]$ MeV, which corresponds to a mean excitation energy of $\langle E_x \rangle = 10.7$ MeV.

Figure 6.7 shows the nuclear charge distribution (a) and post-neutron evaporation mass distribution (b, c) of fission yields of ^{240}Pu, where the asymmetric fission is clearly observed to domain the distribution, with a maximum production at $Z \sim 54$, while the symmetric fission is strongly suppressed. The present data (black dots) is compared with other measurements, including data from the previous campaign of transfer-induced fission at GANIL (red squares), from M. Caamaño et al. [24], and data of thermal-neutron-induced fission from C. Schmitt et al. [66] (green triangles) and A. Bail et al. [67] (blue triangles). The measurement is also compared with a GEF calculation (blue line). In this case, the full distribution of E_x is included in the calculation, and only first-chance fission is taken into account.

Figure 6.7 (a) shows the present data in a perfect agreement with the data from M. Caamaño et al. [24] for the light-fragment region, $Z < 50$, but some diferences are observed in the heavy region for even-Z fragments, indicating some experimental limitations in this previous measurement. The comparison with the thermal-neutron-induced fission from C. Schmitt et al. [66] reveals a general agreement. At $Z > 43$ and $Z = 34$, these data present lower yields compared to the present data due to incomplete measurement, as it is shown in Fig. 6.8. The GEF calculation, meanwhile, is in excellent agreement with the present data.

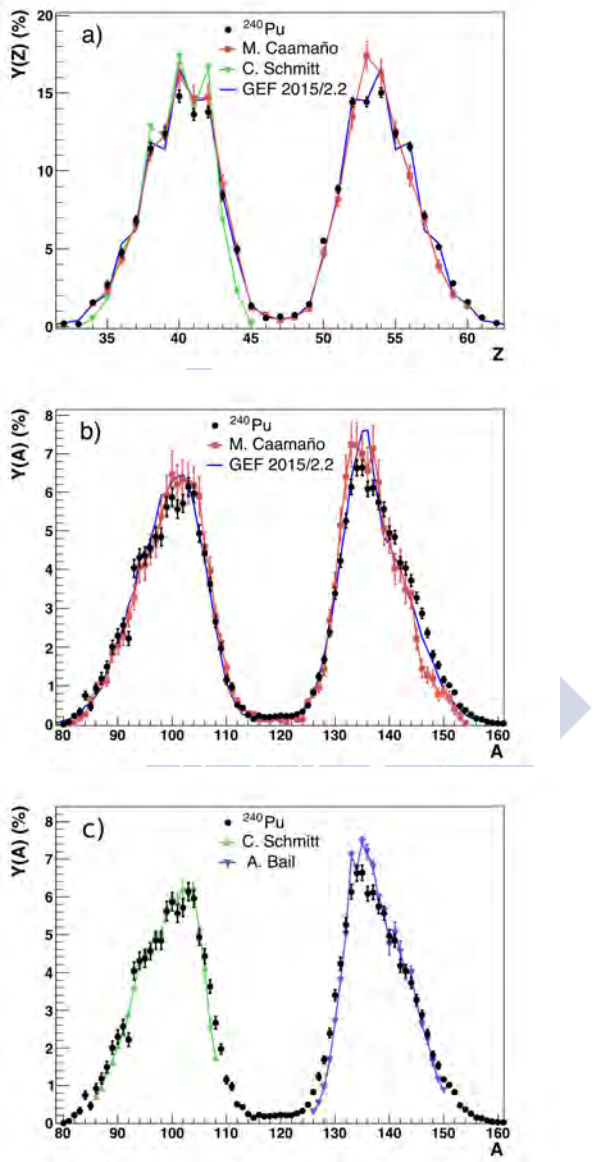

Figure 6.7: Nuclear charge (a), and post-neutron-evaporation mass (b,c) distributions of fission yields of ^{240}Pu (black dots), with mean excitation energy $\langle E_x \rangle = 10.7$ MeV, compared with previous data of ^{240}Pu, produced through ^{12}C(^{238}U,^{240}Pu)^{10}Be [24] (red squares), and ^{239}Np(n_{th},f) [66, 67] (green and blue triangles, respectively). Data is also compared with the GEF code (blue line).

The post-neutron-evaporation mass distribution is duplicated in Fig. 6.7 (b) and Fig. 6.7 (c) for comparison purposes. The mass distribution presents a higher and narrower distribution for the heavy component, which is the effect of the increasing neutron evaporation with the fragment mass. The comparison with data from M. Caamaño et al. (Fig. 6.7 (b)) reveals a general agreement, excluding the very heavy region, $A > 130$, due to the already mentioned experimental limitations. The agreement with the n_{th}-induced fission from C. Schmitt et al. and A. Bail et al. (Fig. 6.7 (c)) is also good, except at the symmetry valley, where the lower E_x of the n_{th}-induced fission produces a deeper valley, with more pronounced slopes at $A \sim 105$ and $A \sim 130$. The structure observed in $A \sim 101$, where the yield is lower than in the neighbors, is validated by C. Schmitt et al. Nevertheless, the present data show a discontinuity in $A \sim 92$ not observed in previous measurements, which is understood as an effect of the detection efficiency. The comparison with the GEF code shows a general agreement, reproducing the difference between both, the light and the heavy region, which indicates a good estimation of the evolution of the neutron evaporation with the mass.

The full isotopic distribution of fission yields of ^{240}Pu, as a function of the neutron number, is presented in Fig. 6.8, where elements from $Z = 32$ up to $Z = 63$ were measured. Present data (black dots) are compared with the data of transfer-induced fission of ^{240}Pu from the previous fission campaign at GANIL (red squares), performed under similar experimental conditions. A good agreement is achieved in the full distribution range with some discrepancies for fragments with $Z > 56$, where the previous measurement suffer from experimental limitations. Data from ^{239}Pu(n_{th},f) are also included, from C. Schmitt et al. (green triangles) and from A. Bail et al. (blue triangles). The comparison with the present data shows a general agreement. However, in $Z \in [53, 55]$, a similar behavior to the one discussed in ^{250}Cf is observed: the present data present rather asymmetric distributions that does not agree with the data from the previous fission campaign at GANIL. The comparison with the GEF code (blue line) indicates a good agreement for the light region, $Z < 48$, while, in the heavy region, the calculation predicts narrower distributions, also similar to what was observed in ^{250}Cf.

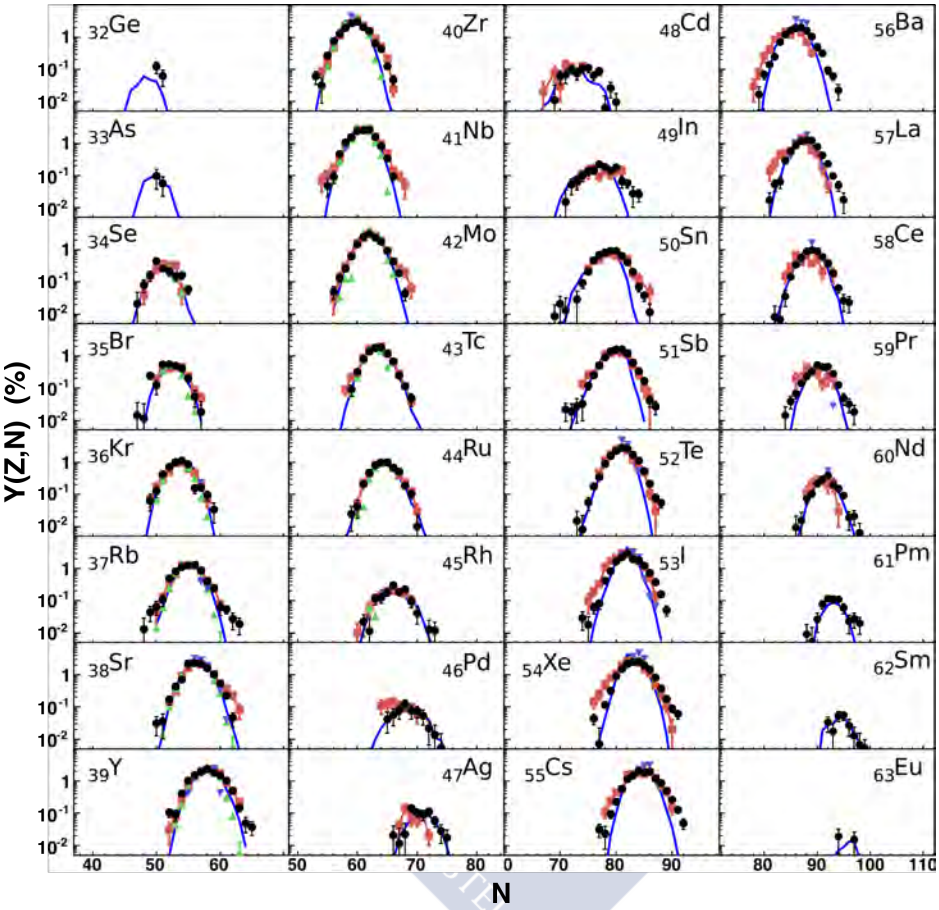

Figure 6.8: Isotopic yields of ^{240}Pu as a function of the neutron number. Present data (black dots) is compared with previous data of ^{12}C(^{238}U,^{240}Pu)^{10}Be [24], and with ^{239}Pu(n_{th},f) data [66, 67] (green and blue triangles, respectively). A GEF calculation is also included (blue line).

6.1.2.3 ^{239}Np

The fissioning system ^{239}Np is produced through the ^{12}C(^{238}U, ^{239}Np)^{11}B p-transfer channel. The range of excitation energy avaliable for this analysis comprises $E_x \in [3, 20]$ MeV, which corresponds to a mean excitation

energy of $\langle E_x \rangle = 7.5$ MeV.

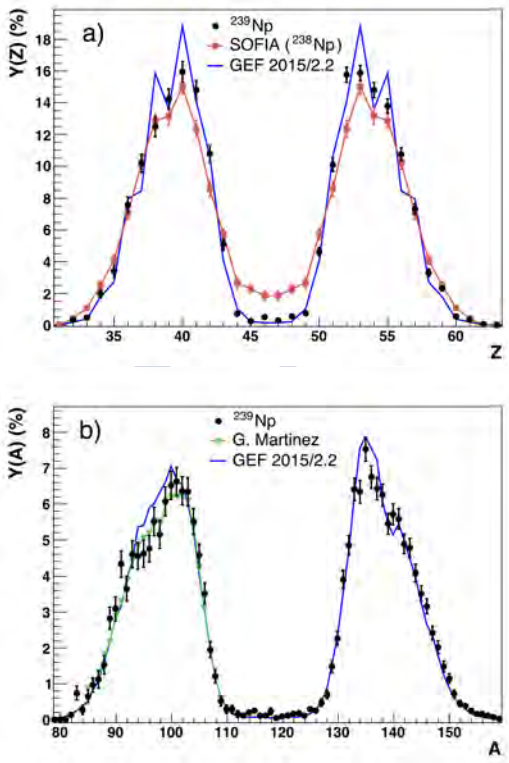

Figure 6.9: Nuclear charge (a) and post-neutron-evaporation mass (b) distributions of fission yields of ^{239}Np (black dots), with mean excitation energy $\langle E_x \rangle = 7.5$ MeV. The present data is compared with Coulomb-excitation induced fission of ^{238}Np [68] (red squares), and with ^{237}Np($2n_{th}$,f) [69] (green triangles). A calculation with the GEF code (blue line) is also presented.

Figure 6.9 presents the nuclear charge (a) and post-neutron-evaporation mass (b) distributions of fission yields of ^{239}Np. Present data (black dots) are compared with measurements of Coulomb-induced fission of ^{238}Np from the SOFIA campaign [68] (red squares) and with measurements of ^{237}Np($2n_{th}$,f) from G. Martinez et al. [69] (green triangles). A calculation from the GEF code that considers the E_x distribution and only first-chance

fission is also included (blue line).

The nuclear-charge distribution (Fig. 6.9 (a)) shows a clear asymmetric fission where fragments with $Z \sim 53$ are highly favored while fragments with $Z \sim 46, 47$ show, in comparison, a negligible production. The data of Coulomb-induced fission of ^{238}Np from the SOFIA campaign show, instead, a larger contribution of the symmetric fission, which is coherent with their higher excitation energy ($E_x \sim 12$ MeV). On the other hand, the GEF calculation present an excellent agreement with the present data, reproducing the asymmetry of the process.

The post-neutron-evaporation mass distribution (Fig. 6.9 (b)) presents an excellent agreement with the ^{237}Np($2n_{th}$,f) data from G. Martinez et al. This reaction produces an excitation energy of $E_x = 6.2$ MeV, which is closer to the present case than the SOFIA data; this is reflected in the good agreement on the steep behavior around $A \in [100, 110]$.

The isotopic distributions of ^{239}Np as a function of the neutron number are presented in Fig. 6.10. Elements from $Z = 32$ up to $Z = 62$ are displayed with back dots, together with data of ^{237}Np($2n_{th}$,f) from G. Martinez et al., indicated with green triangles. A perfect agreement is observed between both sets of measurements. The GEF calculation is also included, shown with a blue line. The agreement with the data is satisfactory overall, except for $Z \in [50, 54]$ where the calculation shows narrower distributions, as it happened in the previous fissioning systems.

6.1.2.4 ^{238}U

The fissioning system ^{238}U is produced through the inelastic scattering channel, ^{12}C(^{238}U, ^{238}U*)^{12}C. The range of excitation energy available for this analysis comprises $E_x \in [3, 20]$ MeV, which corresponds to a mean excitation energy of $\langle E_x \rangle = 7.4$ MeV.

Figure 6.11 (a) shows the nuclear charge distribution of fission yields, where the asymmetric fission is dominant with a maximum production

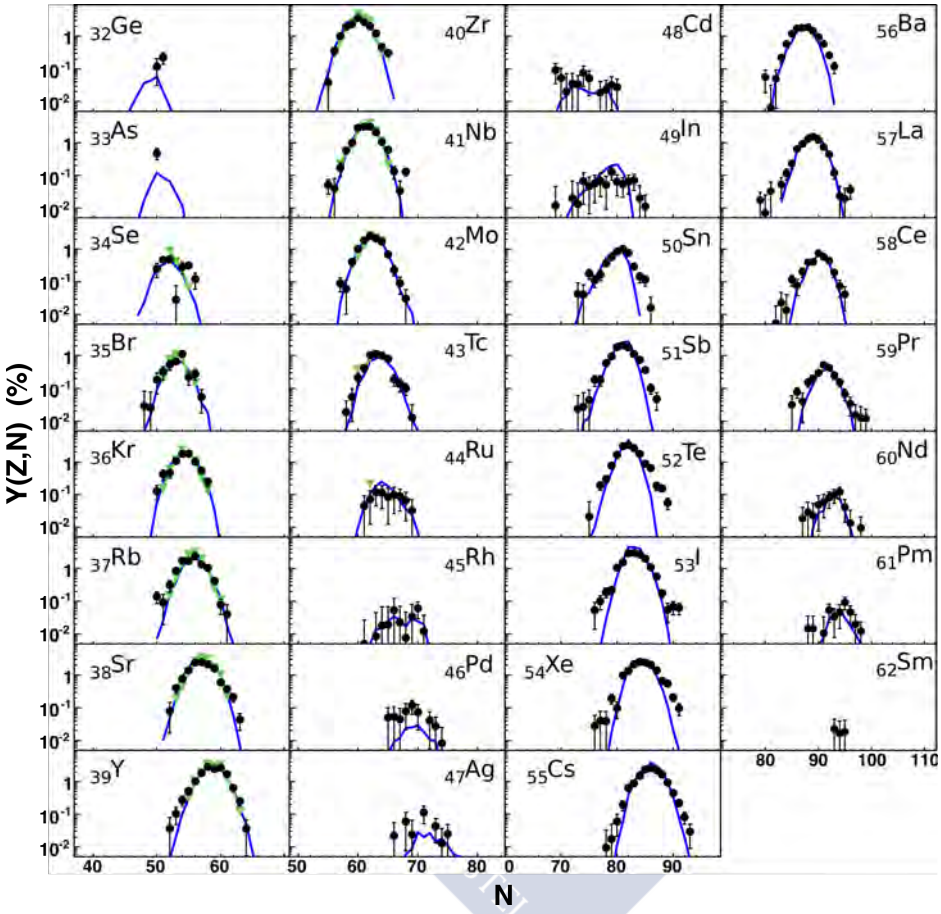

Figure 6.10: Isotopic yields of ^{239}Np as a function of the neutron number. Present data (black dots) is compared with previous data of ^{237}Np($2n_{th}$,f) [69] (green triangles), and with A GEF calculation (blue line).

at $Z \sim 52$. The present data (black dots) are compared with Coulomb-induced fission (red squares) from the SOFIA campaign [70], with a mean excitation energy estimated in $E_x = 12$ MeV. This higher excitation energy is responsible for the larger symmetric contribution, when compared to the present measurement. A calculation using the GEF code is included (blue line), where only the first-fission chance is taken into account and

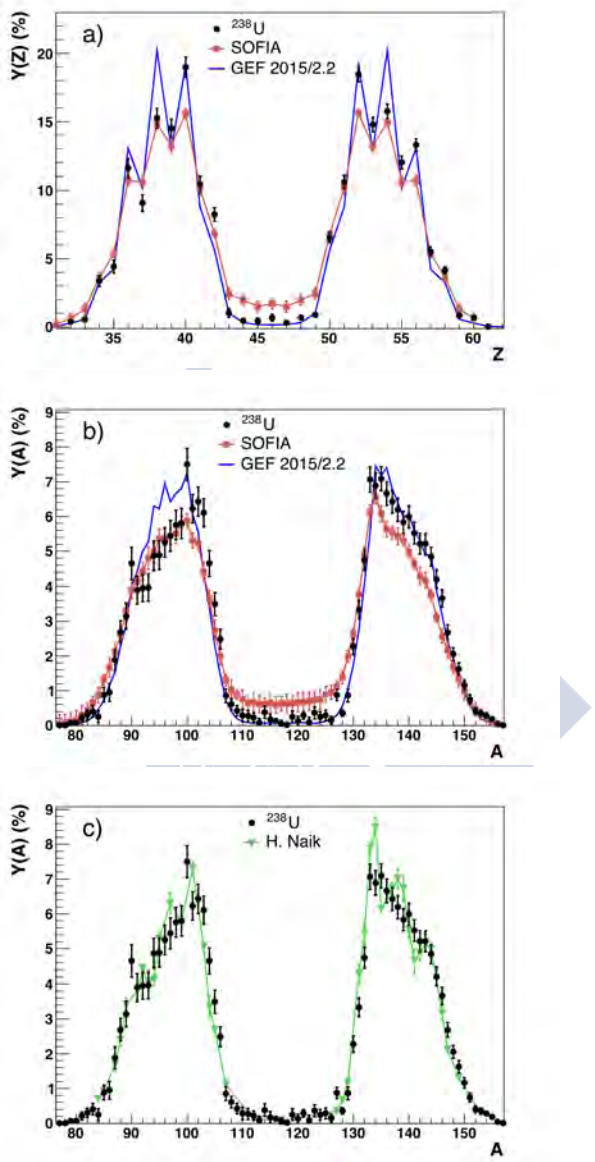

Figure 6.11: Nuclear charge (a) and post-neutron-evaporation mass (b, c) distributions of fission yields of ^{238}U, with $\langle E_x \rangle = 7.4$ MeV. Present data (black dots) is compared with Coulomb-excitation induced fission of ^{238}U [70] (red squares), and Bremsstrahlung-induced fission of ^{238}U [71] (green triangles). A GEF calculation (blue line) is included.

the E_x used in the calculation follows the experimental distribution. The agreement with the data is very good.

Figures 6.11 (b,c) show the post-neutron-evaporation mass distribution of fission yields compared with previous measurements. In Fig. 6.11 (b), the present data are compared with Coulomb-induced fission from SOFIA (red squares). The higher E_x of the Coulomb excitation produces larger neutron evaporation. This variation is stronger in the region of heavy fragments than in light fragments, where such variation is almost negligible. This effect can be explained with the energy sorting in a regime of constant temperature [20]: the excess of E_x increases the neutron evaporation primarily on the heavy fragments and, thus, the yields from SOFIA in the heavy region are shifted to lighter masses with respect to the present data while the yields in the light region are almost unaffected. The GEF calculation (blue line) presents a general good agreement with the measurement, except in the region $A \in [90, 100]$, where the calculation predicts higher fission yields. In Fig. 6.11(c), the present data (black dots) is compared with Bremsstrahlung-induced fission of ^{238}U (green triangles) from H. Naik et al. [71], with a mean excitation energy of $\langle E_x \rangle = 9$ MeV. The agreement is very good on the light-fragment region and on the symmetric region, guided by a more similar E_x, while large fluctuations are observed in H. Naik et al. data around $A \in [135, 145]$ that are not observed in the SOFIA data, and they are not predicted by the GEF code. These fluctuations might result from the measurement technique, which relies on the good determination and knowledge of the gamma-branching ratios.

Figure 6.12 presents the isotopic distribution of fission yields as a function of the neutron number. The present data (back dots) are compared with data of Coulomb-induced fission of 238U from the SOFIA campaign (red squares), and with a GEF calculation (blue line). A general agreement is observed between both set of data, except in the symmetry region, $Z \in [43, 49]$, where the difference of E_x plays a major role. The isotopic distributions of elements between $Z = 50$ and $Z = 54$ show an asymmetric behavior that favors the production of low-N isotopes in both sets of data, which suggests the influence of the spherical shell N=82. The GEF calculation shows a good agreement with data, with slightly narrower distributions in $Z \in [51, 55]$.

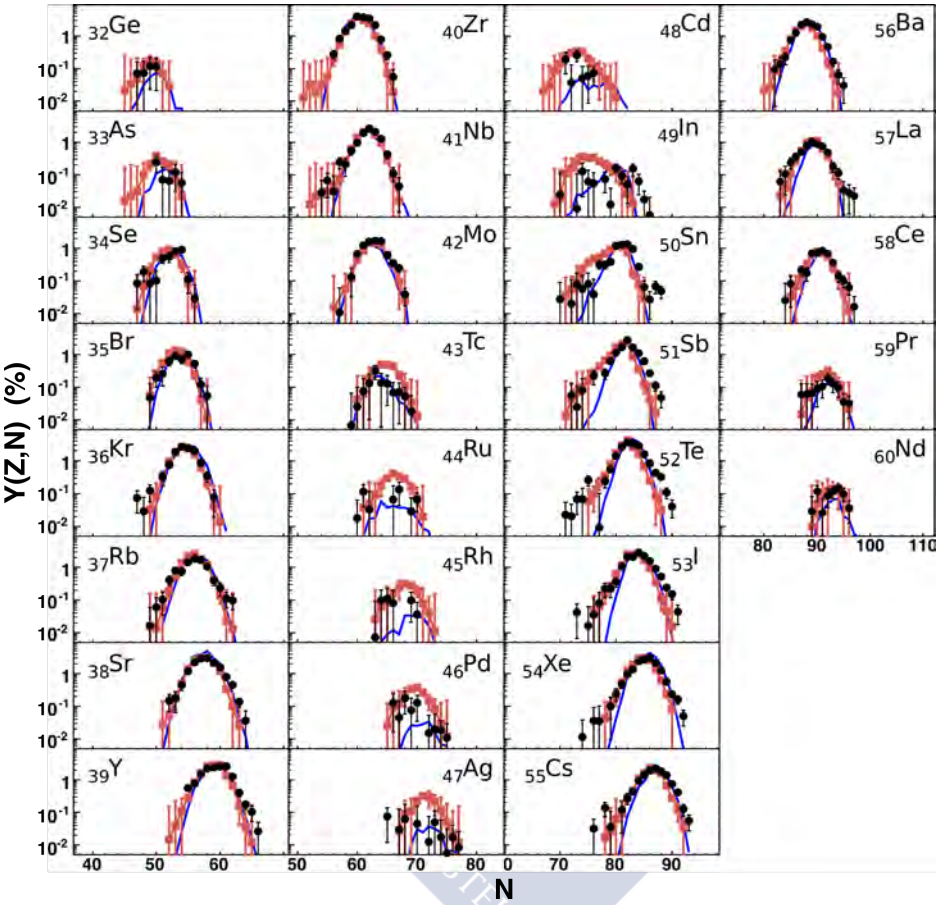

Figure 6.12: Isotopic yields of ^{238}U as a function of the neutron number. Present data (black dots) is compared with data of Coulomb-excitation induced fission of 238U [70] (red squares), and with a GEF calculation (blue line).

The five fissioning systems investigated in this work present an excellent agreement with previous measurement in terms of nuclear-charge, mass, and isotopic distributions. Some differences are observed driven by different excitation energies and particular experimental limitations. Present data show, systematically, asymmetric isotopic distributions for elements $Z \in [48, 57]$. This behavior is also observed in previous measurement of

^{238}U from Coulomb-induced fission [70], but not present in ^{250}Cf and ^{240}Pu from fusion- and transfer-induced fission [24].

The comparison with the GEF code reveals an overall agreement except for narrower isotopic distributions in the heavy-fragment region.

The previous measurements present an equivalence in neutron-induced fission. The compound nuclei investigated in this work can be produced by the reactions: ^{249}Cf(n,f), ^{243}Cm(n,f), ^{239}Pu(n,f), ^{238}Np(n,f), and ^{237}U(n,f). The neutron energies required to induce similar excitation energies to those studied here are E_n = 39.5 MeV, E_n = 16.30 MeV, E_n = 4.19 MeV, E_n = 1.28 MeV, and E_n = 1.26 MeV, respectively. The angular momentum transferred to the system by n-capture is, instead, not comparable to fusion and transfer reactions. The angular momenta calculated following the Bass description with the neutron energies above presented result: $L = 9\hbar$, $L = 7.7\hbar$, $L = 3.2\hbar$, $L = 0.3\hbar$, and $L = 0.2\hbar$, respectively. The large angular momentum induced in fusion and transfer reactions, compared with that in the equivalent n-induced system, increases the centrifugal component in the potential energy that reduces the fission barrier and, presumably, enhances the symmetric fission, making the comparison more complex.

The ^{239}Np and ^{238}U systems investigated here are particularly interesting for energy applications since the equivalent neutron-induced fission corresponds to fast neutrons. This experimental information provides, therefore, interesting hints on fast-reactor developments, although the n-induced fission at this energy introduces a much lower angular momentum, hence more asymmetric fission is expected.

6.1.3 Fission Channels

In this section, the *fission channels* of the five fissioning systems, ^{250}Cf, ^{244}Cm, ^{240}Pu, ^{239}Np, and ^{238}U, are investigated in terms of their nuclear-charge distributions. Four fission channels, following the description of Brosa et al. [18], are included in this analysis: the *Super-Long* symmet-

ric channel (SL), the *Standard-I* asymmetric channel (SI), the *Standard-II* asymmetric channel (SII), and the *Super-Asymmetric* channel (SA). According to [18], each fission channel would describe one path in the potential energy surface as a function of collective degrees of freedom, from the saddle to the scission point, with well defined characteristics in elongation and asymmetry (see Sec. 1.2.4).

Each channel contributes to the total Z distribution as a Gaussian distribution. In the present work, the sum of the four channels is fitted to the full nuclear-charge distribution of each system, bound to two conditions: the amplitude of the SL channel is fixed to the height of the distribution at the symmetry, and the width of the SL channel of the lightest systems, ^{238}U, ^{239}Np, and ^{240}Pu, is fixed to 4 units, following a general tendency observed in lighter systems [25].

The local even-odd effect of Z-distributions present in systems at low excitation energy may create mathematical artifacts that prevent for an optimum fitting. In order to avoid this effect, this even-odd effect is removed before the fitting following an inverse procedure to that described by S. Steinhäuser et al. [72]:

$$\begin{aligned} Y_G(Z) &= \frac{Y(Z)}{1+(-1)^Z \Delta_p} \,, \\ \Delta_p &= \frac{e^{2\delta_p(Z)}-1}{e^{2\delta_p(Z)}+1} \,, \end{aligned} \tag{6.1}$$

where $Y_G(Z)$ is the Z-yield once the even-odd staggering is subtracted and $\delta_p(Z)$ is the local even-odd effect, described by B. L. Tracy et al. [73], presented in Eq. 6.6.

Figure 6.13 presents the nuclear-charge distributions of the five fissioning systems. Each dashed line represents an individual fission channel and the solid line is the sum of them, fitted to the distribution. The parameters of each fission channel —position, width, and yield— are presented in Table 6.1. Notice that ^{238}U and ^{250}Cf present no contribution of the SA channel. These parameters are plotted in Fig. 6.14 as a function of the mass number of the fissioning system (A_{fiss}) with solid symbols. Previ-

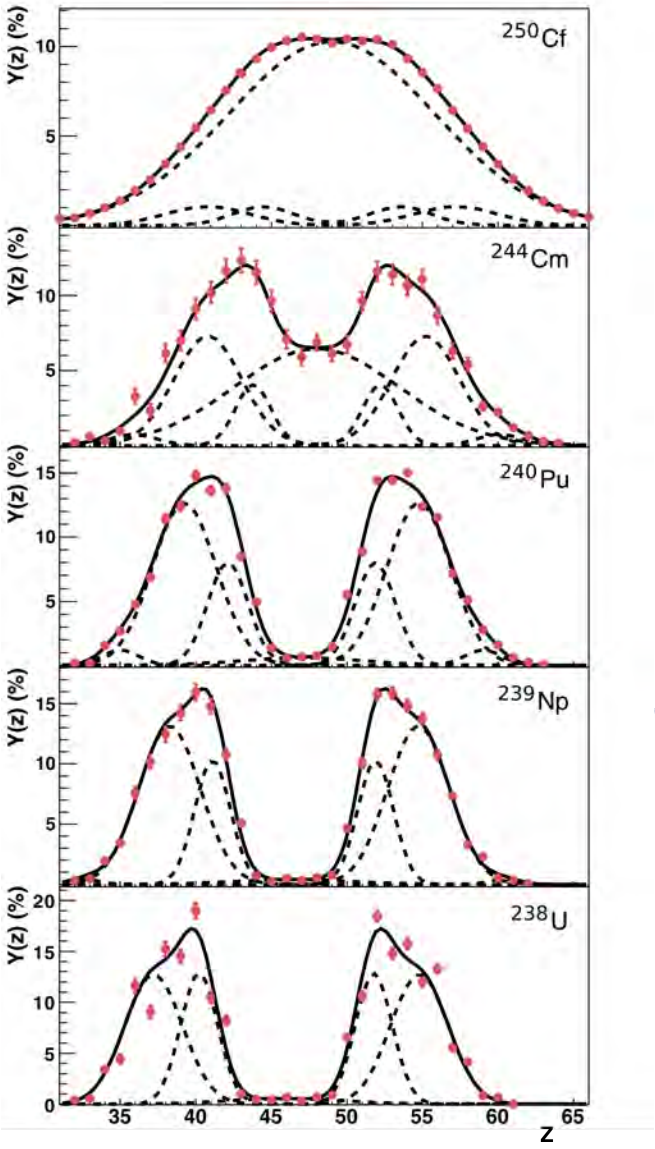

Figure 6.13: Description of the nuclear-charge distribution in terms of fission channels. The red dots represent experimental data, the dashed lines reproduce each fission channels, and the solid lines indicate the sum of the different channels.

ous measurements of lighter actinides form C. Böckstiegel et al. [74] are included with empty symbols for completeness.

Fission Channels Parameters				
System	**Channel**	**Position**	**Width**	**Yield (%)**
^{250}Cf	Standard I	53.5 ± 0.4	2.1 ± 0.2	5.3 ± 1.7
	Standard II	57.2 ± 0.8	2.8 ± 0.3	7.3 ± 1.7
	Super long	49	6.82 ± 0.01	87.78 ± 0.21
^{244}Cm	Standard I	52.2 ± 0.3	1.2 ± 0.2	11.9 ± 4.5
	Standard II	55.2 ± 0.4	2.2 ± 0.3	41.1 ± 6.3
	Super asymmetric	60.1 ± 1.0	1.50 ± 0.02	2.7 ± 1.8
	Super long	48	5.4 ± 0.5	43.9 ± 4.1
^{240}Pu	Standard I	51.9 ± 0.1	1.34 ± 0.06	26.8 ± 3.6
	Standard II	54.8 ± 0.2	2.11 ± 0.09	66.9 ± 3.7
	Super asymmetric	59.0 ± 0.1	1.22 ± 0.09	3.62 ± 0.62
	Super long	47	4	2.95 ± 0.10
^{239}Np	Standard I	51.9 ± 0.1	1.18 ± 0.06	30.3 ± 3.4
	Standard II	54.7 ± 0.2	2.04 ± 0.08	67.3 ± 3.7
	Super asymmetric	60.4 ± 0.2	1.0 ± 0.2	1.04 ± 0.30
	Super long	46.5	4	1.95 ± 0.10
^{238}U	Standard I	51.8 ± 0.1	1.23 ± 0.05	39.6 ± 4.0
	Standard II	54.8 ± 0.2	1.91 ± 0.09	60.9 ± 3.9
	Super long	46	4	2.71 ± 0.25

Table 6.1: Parameters of the fission channels, fitted to the nuclear-charge distributions.

The excitation energy changes from one system to the other and it needs to be taken into account in the comparison of fission channels between the fissioning systems since the yield of each fission channels is sensitive to such difference.

The contribution of the SL channel is observed to decrease systematically with A_{fiss} from the lightest system up to $A_{fiss} = 240$, where the large excitation energy induced in this work favors the symmetric fission and SL increases again. The contribution of SII is higher than SI for most the systems, except in $A_{fiss} \sim 225$, and it increases with A_{fiss}, up to

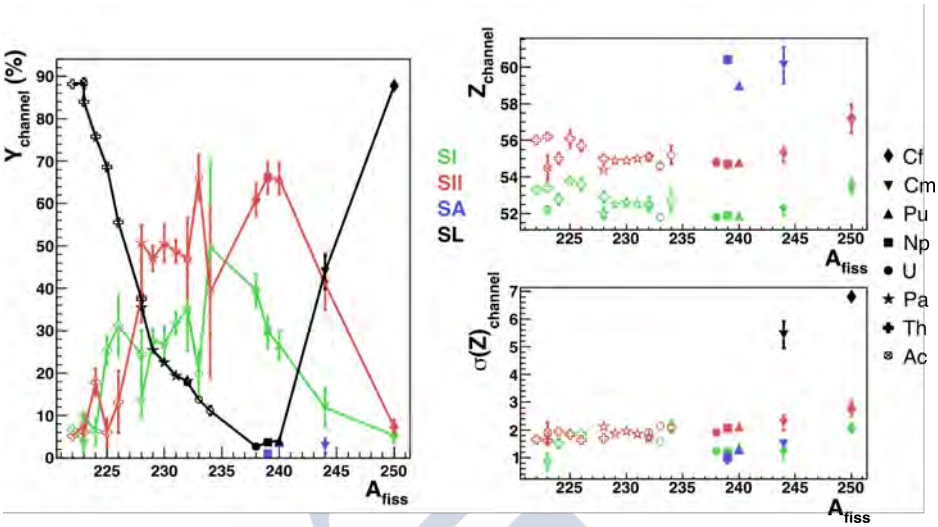

Figure 6.14: Parameters of the fission channels as a function of the mass number of the fissioning system. Solid markers indicate the present work and empty markers correspond to previous measurement [74] .

$A_{fiss} = 240$. The contribution of SI follows a similar behavior with the maximum at $A_{fiss} = 234$. These maxima on channels SI and SII are an effect of the increasing excitation energy induced on the systems displayed, particularly for $A_{fiss} > 235$. Finally, SA shows a very low contribution without significant evolution.

The positions of the asymmetric channels, remains constant with A_{fiss}, and coherent with previous data, resulting in $Z_{SI} \sim 52$, $Z_{SII} \sim 55$, and $Z_{SA} \sim 60$, for systems with $A_{fiss} \leq 244$, while slightly higher values are obtained for ^{250}Cf, $Z_{SI} \sim 53$ and $Z_{SII} \sim 57$.

A difference is observed concerning the behavior of widths of the channels between this work and Böckstiegel et al. In this work, SII presents a larger width than SI, which coincides with SA, while Böckstiegel et al. find a similar width for both SI and SII. The former observation is coherent with the description of Brosa et al., where the SII channel is understood

to be less compact than SI and, hence, the random neck rupture produces a wider distribution. The width of SL in ^{244}Cm and ^{250}Cf results larger than the general trend of $\sigma_{SL} \sim 4$, observed in lighter systems.

6.2 Neutron Excess

The isotopic measurement of fission yields achieved in this experiment permits to investigate the fission process in terms of the neutron and proton contents of fission fragments after post-scission neutron evaporation. In order to study the sharing of protons and neutrons, the neutron excess is defined as the average number of neutrons per proton in the fragments:

$$\begin{aligned} \frac{\langle N \rangle}{Z}(Z) &= \frac{1}{Z} \sum_N N \frac{Y(N,Z)}{Y(Z)} \quad , \\ Y(Z) &= \sum_N Y(N,Z) \, . \end{aligned} \tag{6.2}$$

A structure-less scission-point model (LD-SP) predicts a sharing of nucleons at scission dominated by the interplay between the Coulomb repulsion and nuclear interactions. This translates in fragments with an almost homogeneous sharing of neutrons, with a smooth increase in the number of neutrons as a function of Z, this is referred as *charge polarization*. However, this is far from the observed data at low excitation energy [60]. In this energy regime, the heavy fragment has an excess of neutrons compared with the LD-SP model prediction while the light fragment is less neutron rich. Furthermore, some particular (Z, N) configurations of the nascent fragments are favored, producing an excess or a defect of neutrons in some Z. In addition, the neutron evaporation, which also affects the measured N/Z, reflects the sharing of energy at scission, also influenced by shell effects at low energy. The neutron excess is, therefore, an observable sensitive to structure effects in the sharing of protons and neutrons between the pre-fragments at scission.

Figure 6.15 presents the neutron excess of the five fissioning system

investigated in this work, (a) ^{250}Cf, (b) ^{244}Cm, (c) ^{240}Pu, (d) ^{239}Np, and (e) ^{238}U. The present data (black dots) are compared with previous measurement (colored symbols) from [60], [66], [69], and [70]; and with GEF calculations (blue line).

The high excitation energy of ^{250}Cf, $E_x = 45.97$ MeV, reduces the effect of structure in the neutron excess, providing an overall smooth behavior, in agreement with the previous measurement of Caamaño et al. [60] in the light region, $Z < 50$. The heavy region, instead, presents a discrepancy, driven by the systematic differences already presented in the isotopic distributions (see Fig. 6.3), probably related to a limited Z resolution.

Charge polarization is observed in the neutron excess of ^{244}Cm, which presents two different behaviors: a stabilization in the heavy region with a maximum value in $Z \sim 50$, close to a spherical shell, and a lower N/Z in the light region, where a local maximum is observed around $Z \sim 40$.

The systems measured with lower E_x, ^{240}Pu, ^{239}Np, and ^{238}U, present a strong charge polarization with a clear saw-tooth shape in the neutron excess. The maximum value in $Z \sim 50$ breaks the overall increasing trend observed in the systems with higher E_x. The double magic nucleus ^{132}Sn, which corresponds to $N/Z = 1.64$, is understood to be the promoter of such large neutron excess. The low neutron excess of the complementary fragment, $Z = Z_{fiss} - 50$, compensates the excess of neutrons of the partner fragment, even after the post-scission neutron evaporation.

^{240}Pu data are compared with previous measurement from Caamaño et al. [60] and Schmitt et al. [66], showing a good agreement for the light region while a general understimation is observed in the heavy region, probably due to the same experimental issues as in ^{250}Cf. ^{239}Np data are compared with data from Martinez et al. [69], with an excellent agreement. Finally, ^{238}U is compared with data from the SOFIA campaign [70], where the effect of the different E_x populated in each experiment is observed. The present data, with $\langle E_x \rangle = 7.4$ MeV, exhibits larger values of neutron excess around $Z \sim 50$ than in the case of SOFIA data, with $\langle E_x \rangle = 12$ MeV, where shell effects are expected to be less influential. Both sets of data converge to the same value of $\langle N \rangle / Z$ for the heaviest and lightest fragments, where

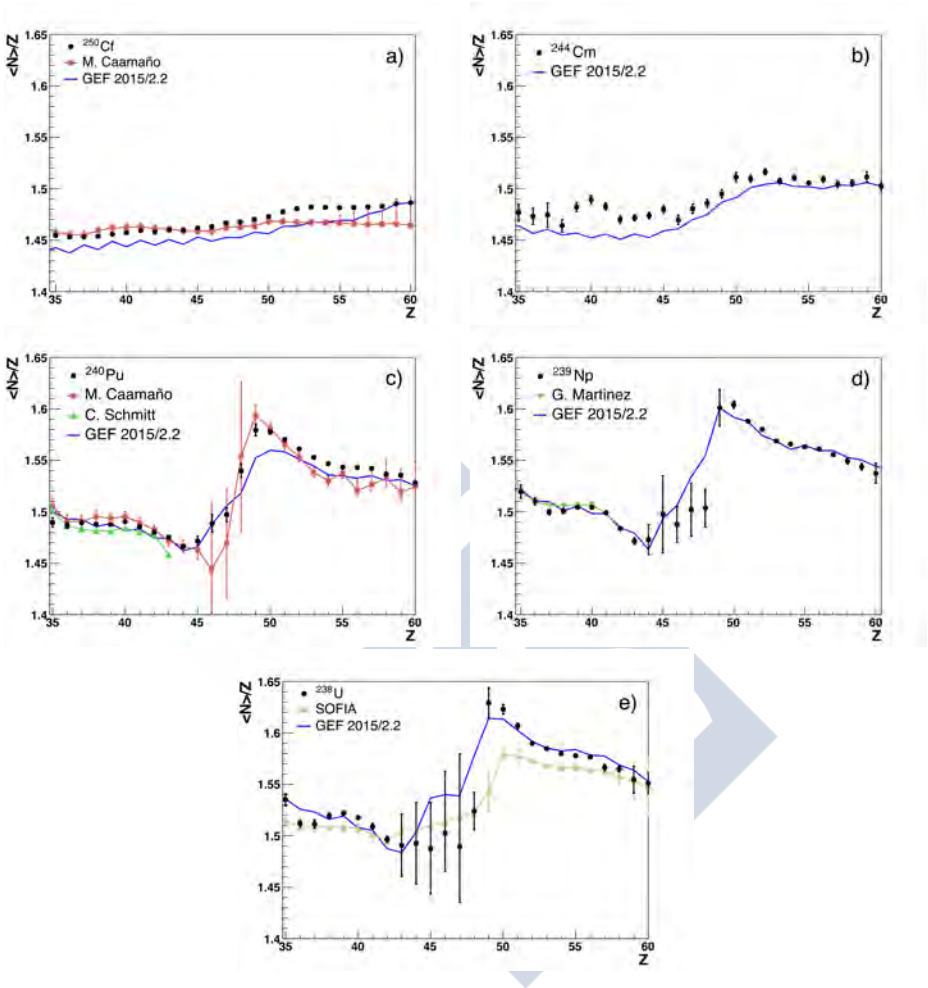

Figure 6.15: Neutron excess as a function of the nuclear charge of the fission fragments. Five fissioning systems are presented, (a) ^{250}Cf, (b) ^{244}Cm, (c) ^{240}Pu, (d) ^{239}Np, and (e) ^{238}U. Present data, indicated with black dots, are compared with previous data [60, 66, 69, 70], in color, and with GEF calculations, represented with a blue line.

no shell effect is expected. The large difference of $\langle N \rangle / Z$ observed in $Z = 50$ is not present any more in the complementary fragment, $Z = 42$.

The neutron evaporation in the light fragment was observed to be almost independent of the E_x in a range $Ex \in [6, 12]$ MeV [75, 76], which indicates that the largest contribution to the variation observed in $Z = 50$ comes from the release of the excess of E_x through neutron evaporation, since the N/Z difference at scission must be same for both, $Z = 42$ and $Z = 50$.

The GEF calculation presents a systematic discrepancy in the systems with largest E_x, ^{250}Cf and ^{244}Cm, where the model predicts lower values of neutron excess compared to the measurements, except for the heaviest fragments with $Z > 57$, where the agreement is good. In systems with lower E_x, ^{240}Pu, ^{239}Np, and ^{238}U, a general agreement between both, calculation and measurement, is achieved, except for the underestimation for $Z > 47$ in ^{240}Pu, and the large fluctuations on the symmetric regions of ^{239}Np and ^{238}U.

Figure 6.16 presents the neutron excess of the five fissioning systems together. This comparison reveals the evolution of structure effects with the excitation energy of the fissioning system. The population of high values of $\langle N \rangle / Z$ around $Z \sim 50$ decreases systematically with the fissioning systems of higher E_x. The well known spherical shell gaps in $Z = 50$ and $N = 82$, as well as the deformed shell gap in $N = 88$ [13], are indicated in the plot. The double magic nucleus ^{132}Sn is also shown.

6.3 Total Neutron Evaporation

The isotopic identification of fission fragments permits to obtain the average number of neutrons evaporated between the formation of the com-

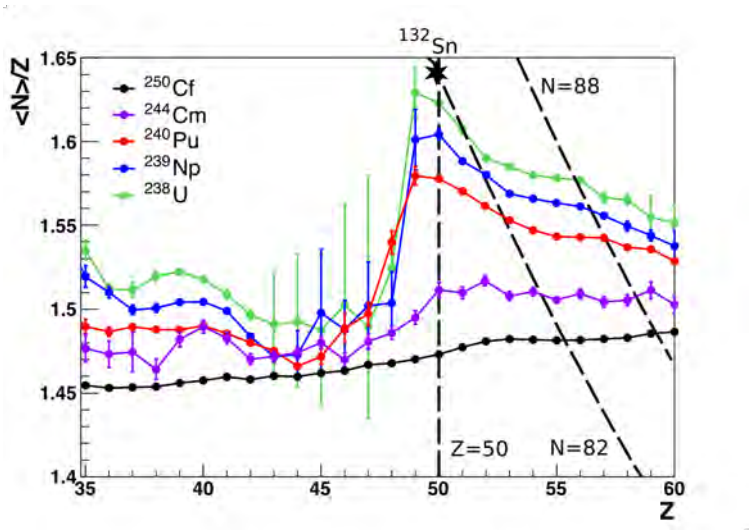

Figure 6.16: Comparison of the neutron excess of the five fissioning system studied in this work.

pound nucleus and the cooling of the fission fragments:

$$\begin{aligned} \langle \nu_{total} \rangle &= N_{fiss} - \Big(\langle N_{light} \rangle + \langle N_{heavy} \rangle \Big) \ , \\ \langle N_{light} \rangle &= \frac{1}{100} \sum_{Z=Z_{min}}^{Z_{fiss}/2} \sum_{N} N \cdot Y(N,Z) \ , \\ \langle N_{heavy} \rangle &= \frac{1}{100} \sum_{Z=Z_{fiss}/2}^{Z_{max}} \sum_{N} N \cdot Y(N,Z) \ , \end{aligned} \tag{6.3}$$

where $Y(N,Z)$ are the isotopic yields, and N_{fiss} and Z_{fiss} are the number of neutrons and protons of the compound nucleus, respectively.

The mean value of the total neutron evaporation, along the full range of the fragments distribution, is presented for each fissioning system in Table 6.2, together with their excitation energies.

Figure 6.17 presents the total neutron evaporation as a function of the excitation energy of the five fissioning systems. We observe that the

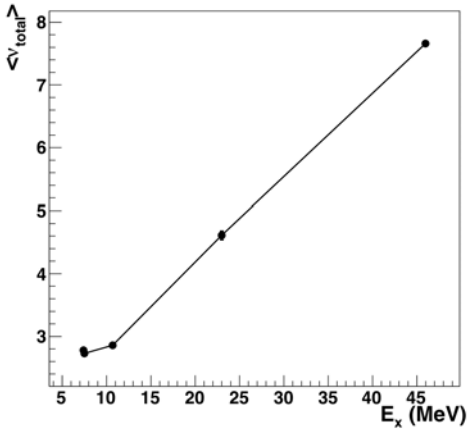

Figure 6.17: Total neutron evaporation as a function of the excitation energy of the five fissioning systems investigated.

increase of E_x is related with an increase of the neutron multiplicity, indicating that the most part of the additional E_x is released after scission in the form of neutron evaporation.

Average Total Neutron Evaporation		
System	E_x	$\langle \nu_{total} \rangle$
^{250}Cf	45.97 MeV	7.66 ± 0.02
^{244}Cm	23.0 MeV	4.61 ± 0.07
^{240}Pu	10.7 MeV	2.86 ± 0.02
^{239}Np	7.5 MeV	2.73 ± 0.03
^{238}U	7.4 MeV	2.78 ± 0.04

Table 6.2: Mean value of the total neutron evaporation along the full range of the fragment distribution.

The total neutron evaporation can be calculated as a function of the

nuclear charge of the fission fragments as:

$$\langle \nu \rangle_{total}(Z) = N_{fiss} - \left(\langle N \rangle|_Z + \langle N \rangle|_{Z_{fiss}-Z} \right) ,$$
$$\langle N \rangle|_Z = \sum_N N \frac{Y(N,Z)}{Y(Z)} , \tag{6.4}$$

where $Y(N,Z)$ and $Y(Z)$ are the isotopic and nuclear-charge yields, and N_{fiss} and Z_{fiss} are the number of neutrons and protons of the compound nucleus, respectively.

Figure 6.18 presents $\langle \nu \rangle_{total}$ as a function of the fragment Z for the five fissioning systems investigated in this work.

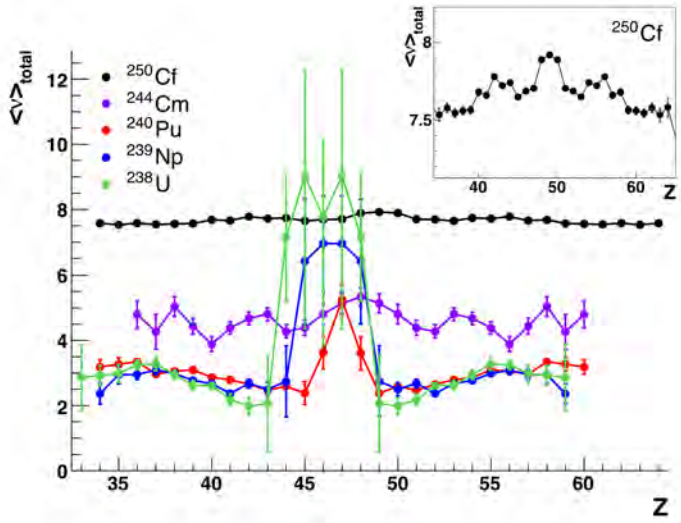

Figure 6.18: Total neutron evaporation as a function of the nuclear charge of the fragments. (Inset) Zoom of the system ^{250}Cf.

The systems with lower E_x, ^{240}Pu, ^{239}Np, and ^{238}U, show a large evaporation at the symmetry that suggests large deformations at scission, consistent with the description of the symmetric *Super Long* fission channel [18]. These systems also show a minimum of evaporation at $Z \sim 50$, where the spherical closed shells, Z=50 and N=82, affect the deformation of the

heavy fragment. The evaporation reaches a local maximum in $Z \sim 55$, suggesting the influence of a deformed shell $N \sim 88$ [13].

The systems with higher E_x, ^{250}Cf and ^{244}Cm, present larger average evaporation. They do not exhibit strong structure effects for any particular Z, although a slightly larger n-evaporation at the symmetry is observed in both cases. Furthermore, as shown in the inset of Fig. 6.18, a local maximum is observed at $Z \sim 55$, suggesting that, even at such a large E_x of 45.97 MeV, some structure effects may remain, affecting the neutron evaporation.

The total neutron evaporation of ^{250}Cf, ^{240}Pu, and ^{238}U are compared with previous measurement and GEF calculations in Fig. 6.19. The present data (black dots) show a good agreement with the measurement of the previous GANIL campaign [60] (red squares) for ^{240}Pu (b). The difference between present data and data from SOFIA [70] (green squares) for ^{238}U (c) are understood as a difference of E_x between both set of data ($\Delta E_x \sim 4.5$ MeV). In the case of ^{250}Cf (a), we observe a systematic lower evaporation of almost one neutron with respect to the previous GANIL campaign. The reason is probably related with the limits on the measurement of heavy fragments, as shown in Fig. 6.15 (a).

The GEF calculation predicts a total neutron evaporation that, in average, agrees with the present data, although does not reproduce properly the shape as a function of Z. The minimum at $Z \sim 50$, present in ^{240}Pu and ^{238}U, is not predicted by the GEF calculation, which indicates that GEF assumes a larger available excitation energy in this region.

6.4 Even-Odd Staggering

At low energy fission, experimental data shows that even fragments are systematically more produced than odd fragments. This effect is a consequence of the pairing energy: the formation of odd-odd fragments need to break nucleon pairs, which requires higher energy than the formation

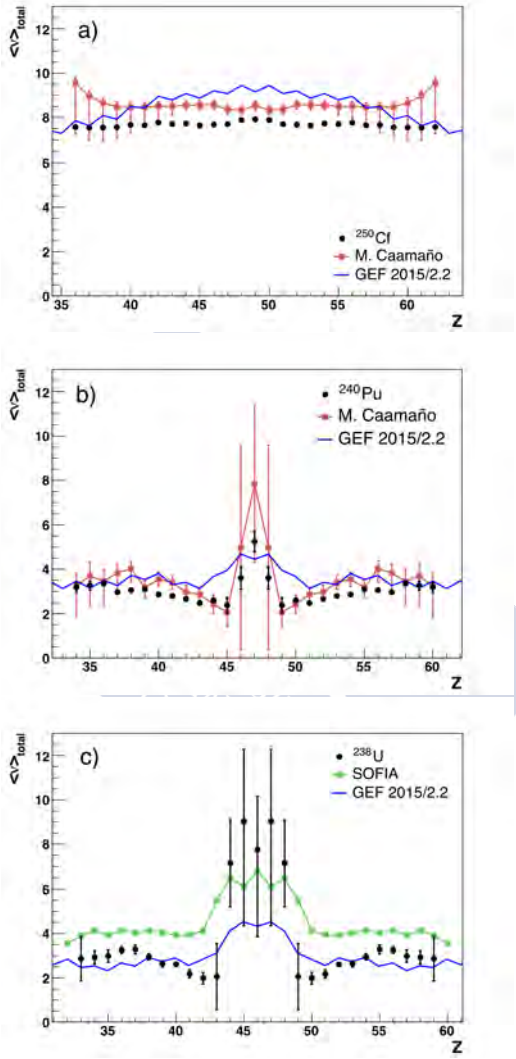

Figure 6.19: Comparison of the total neutron evaporation in ^{250}Cf (a), ^{240}Pu (b), and ^{238}U (c) with previous measurement [60, 70] (red and green squares, respectively). Calculations from the GEF code are included (blue line).

even-even fragments. The intrinsic energy, available for the rupture of pairs, comes from the energy above the barrier and the energy dissipation in the fission process along the path from the saddle to the scission point, which transforms collective energy into intrinsic energy at scission. The measurement of the even-odd staggering in nuclear charge is not affected by proton evaporation as it happens with neutrons, hence, it reflects directly the intrinsic energy at scission: the larger the intrinsic energy, the lower the even-odd effect [77].

The nuclear-charge global even-odd staggering is calculated in the five investigated fissioning systems of this work as:

$$\delta_{global} = \frac{1}{\sum_{Z} Y(Z)} \sum_{Z} (-1)^{Z} Y(Z) \ , \tag{6.5}$$

and presented in Table 6.3, where the excitation energy of each fissioning system is also indicated.

Global Even-odd Effect		
System	E_x **(MeV)**	δ_{global} (%)
^{250}Cf	45.97	0.24 ± 0.15
^{244}Cm	23.0	2.37 ± 1.53
^{240}Pu	10.7	6.32 ± 0.67
^{239}Np	7.5	1.91 ± 1.72
^{238}U	7.4	16.41 ± 1.18

Table 6.3: Global even-odd effect. The excitation energy of each fissioning system is also presented.

The global even-odd effect is investigated as a function of the fissility parameter, Z^2/A, of each fissioning system in Fig. 6.20. Black symbols correspond to this work, green symbols correspond to thermal-neutron induced fission [66, 78, 79, 80, 81, 82], red symbols, to Coulomb-excitation fission [68, 70], and blue symbols correspond to the GEF calculation. Even-Z systems present a systematic decrease as a function of Z^2/A in thermal-neutron induced fission and in present data, while no clear trend is observed in Coulomb-excitation fission. The thermal-neutron induced

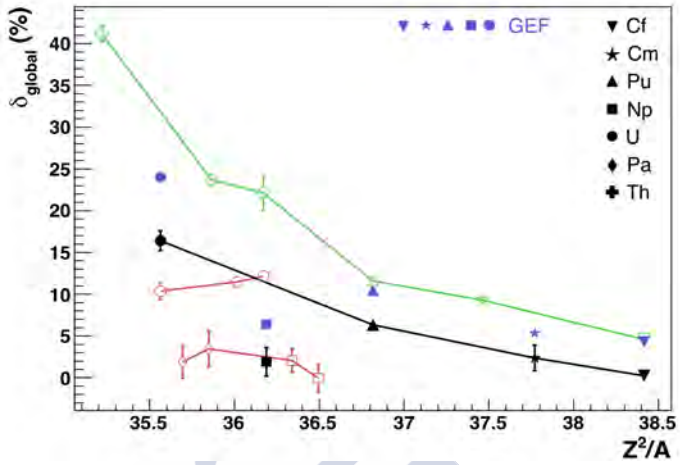

Figure 6.20: Global even-odd effect as a function of the fissility parameter. In black, the present work; in green, thermal-neutron induced fission [66, 78, 79, 80, 81, 82]; in red, Coulomb-excitation fission [68, 70]; and in blue, the GEF calculation under the conditions of the present work.

fission presents larger values of δ_{global} than transfer-induced fission, which, at the same time, present larger δ_{global} than Coulomb-excitation fission, reflecting the effect of the different excitation energy transferred in each type of reaction. A system with excitation energy E_x at the ground state, reaches the saddle point with intrinsic excitation energy $E_x - B_f$, being B_f the fission barrier. This intrinsic energy adds to the energy dissipated from saddle to scission, thus, for similar dissipation energy, the higher the excitation energy, the lower the even-odd effect.

The measured odd-Z systems (Pa and Np) present lower δ_{global} values because of the continuous presence of at least one unpaired proton. These systems also show a general decreasing tendency with the fissility parameter, and both present data and SOFIA data are in a good agreement.

The GEF calculation shows a systematically higher even-odd effect than present data, indicating an underestimation of the dissipation along the

process.

The even-odd effect is known to evolve with the asymmetry of the split [72] revealing the role of dissipation as a function of the fragment Z [83]. This local even-odd effect is obtained, following the B. L. Tracy description [73], as:

$$\delta\left(Z_i+\frac{3}{2}\right)=\left(\frac{-1}{8}\right)^{Z_i}\left[\ln Y(Z_{i+3})-\ln Y(Z_i)-3\left(\ln Y(Z_{i+2})-\ln Y(Z_{i+1})\right)\right], \tag{6.6}$$

where $Y(Z_i)$ defines the yield of the element Z_i.

The local even-odd effect is presented in Fig. 6.21 as a function of the asymmetry parameter, defined as:

$$a(Z_i)=\frac{Z_i-(Z_{fiss}-Z_i)}{Z_{fiss}}\,, \tag{6.7}$$

being Z_{fiss} the nuclear charge of the fissioning system. The symmetric region in some of the systems displayed in Fig. 6.21 is not presented due to low statistics.

The even-Z systems at low E_x, ^{238}U and ^{240}Pu, present a positive even-odd effect with a symmetric behavior for both, light ($a<0$) and heavy ($a>0$) fragment region. The odd-Z system ^{239}Np shows, instead, an anti-symmetric evolution with the fragment asymmetry, moving from positive to negative δ. The systems with higher E_x, ^{244}Cm and ^{250}Cf, present a lower even-odd effect, increasing with the asymmetry in ^{244}Cm and being almost null in the case of ^{250}Cf.

The even-odd effect in $a>0$ is systematically lower than in the negative region. Two effects may explain it: a limited Z-resolution in heavy fragments and a possible overestimation in the light fragment, due to the efficiency correction. In order to minimize these systematic differences, both regions, $a>0$ and $a<0$, are averaged:

$$\overline{\delta}=\frac{1}{2}(\delta|_{a>0}+\delta|_{a<0})\,, \tag{6.8}$$

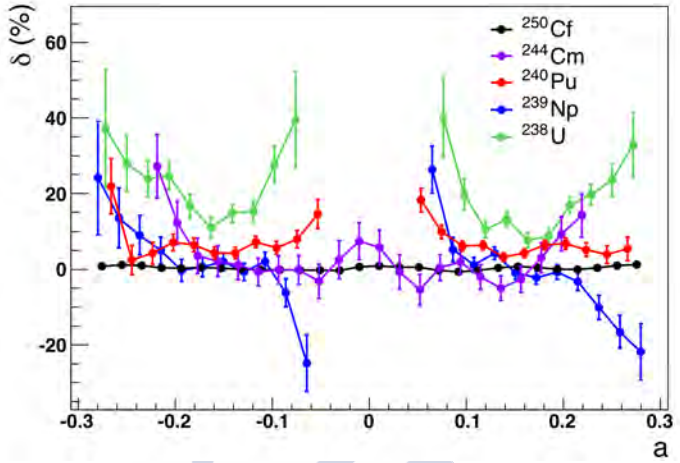

Figure 6.21: Local even-odd staggering as a function of the asymmetry parameter.

in Z-even fissioning systems, and

$$\overline{\delta} = \frac{1}{2}(\delta|_{a>0} - \delta|_{a<0}) \ , \tag{6.9}$$

in ^{239}Np.

Figure 6.22 presents $\overline{\delta}$ as a function the absolute value of the asymmetry. Figure 6.22 (a) shows ^{240}Pu (black dots) compared with measurements from Caamaño et al. [24] (red) and from Schmitt et al. [66] (green). The three sets of data present similar behavior, increasing for large values of $|a|$ and with a local maximum in $|a| \sim 0.05$ that corresponds to $Z = 49.5$. A good agreement between present data and data from Caamaño et al., both measured in similar experimental conditions, is achieved; meanwhile, the data from Schmitt et al., from thermal-neutron induced fission with a lower E_x, present, as expected, a larger even-odd staggering.

Figure 6.22 (b) shows the local $\overline{\delta}$ of ^{239}Np (black dots), compared with data of ^{238}Np from the SOFIA campaign [68] (blue) and data of ^{239}Np from I. Tsekhanovich et al. [84] (yellow). An evolution with the asymmetry

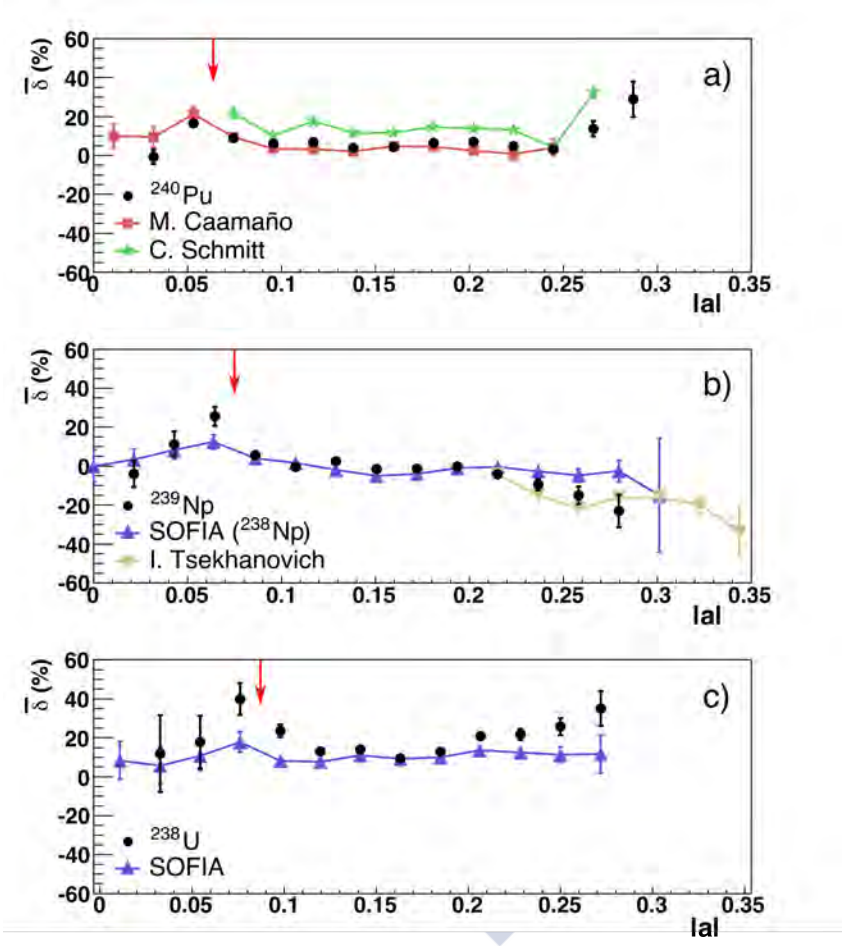

Figure 6.22: Comparison of the local even-odd effect, as a function of the asymmetry parameter, with previous measurements. (a) ^{240}Pu (black dots) is compared with data of transfer induced fission [24] (red) and data of thermal-neutron induced fission [66] (green). (b) ^{239}Np (black dots) is compared with data of Coulomb-excitation fission of ^{238}Np [68] (blue) and data of thermal-neutron induced fission [84] (yellow). (c) ^{238}U (black dots) is compared with data of Coulomb-excitation fission [70] (blue). The red arrows indicate the position $Z = 50$.

parameter is also present in this system, decreasing for higher $|a|$ and with a maximum $\overline{\delta}$ at $|a| \sim 0.06$ ($Z = 49.5$), which is also present, but less pronounced, in the SOFIA data, with higher E_x. The data from Tsekhanovich et al., from thermal-neutron induced fission, are coherent with the evolution of the present data at higher $|a|$.

^{238}U is presented in Fig. 6.22 (c). The present data (black dots) are compared with measurements from the SOFIA campaign [70] (blue), at higher excitation energy. The even-odd effect in the present data increases for higher $|a|$ while in SOFIA data it remains constant. This difference is understood as an effect of the excitation energy, which is 4.6 MeV higher than the present data. As in the other systems, both sets of data present a maximum of $\overline{\delta}$ in $|a| \sim 0.07$, corresponding to $Z = 49.5$. This common maximum can be understood as a consequence of the larger pairing gap at $Z = 50$.

6.5 Evolution With The Excitation Energy

The reconstruction of the transfer reaction that produces the fissioning system permits to study the evolution of the fission observables as a function of the excitation energy gained at saddle. In this work, the fission-fragment yield distributions, the neutron excess, the neutron evaporation, and the even-odd effect are investigated.

The E_x distributions of the systems ^{244}Cm, ^{240}Pu, ^{239}Np, and ^{238}U, presented in Fig. 5.2, are divided into several overlapping ranges that correspond to different mean values of E_x. Table 6.4 presents these ranges for each system, together with the mean value and the standard deviation of each one. ^{238}U includes the percentage of the subtracted ^{250}Cf contamination due to the effect of the ^{12}C scattering in the aluminum collimator (see Sec. 6.1.2).

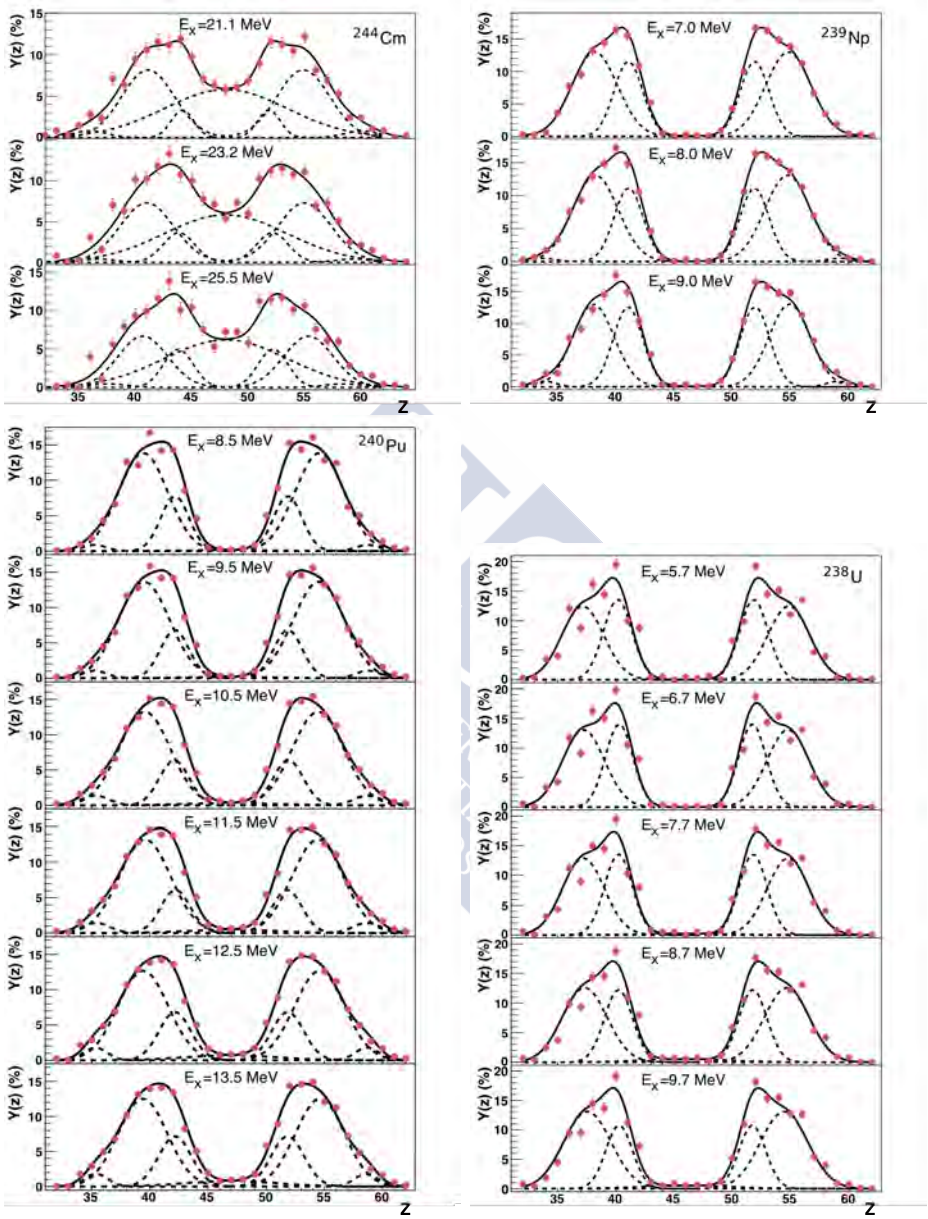

Figure 6.23: Nuclear-charge distributions of ^{244}Cm, ^{240}Pu, ^{239}Np, and ^{238}U for different excitation energies. The fitted fission channels are included.

^{244}Cm		
E_x **range**	$\langle E_x \rangle$ **(MeV)**	STD_{E_x} **(MeV)**
$[15, 25]$	21.1	2.24
$[20, 27.5]$	23.2	2.18
$[22, 32]$	25.5	2.44

^{240}Pu		
E_x **range**	$\langle E_x \rangle$ **(MeV)**	STD_{E_x} **(MeV)**
$[4, 10.7]$	8.5	1.46
$[7, 11.8]$	9.5	1.32
$[8, 13.3]$	10.5	1.46
$[9, 15.1]$	11.5	1.63
$[10, 17.3]$	12.5	1.79
$[11.2, 18.9]$	13.5	1.8

^{239}Np		
E_x **range**	$\langle E_x \rangle$ **(MeV)**	STD_{E_x} **(MeV)**
$[5, 10]$	7.0	1.30
$[5.6, 15]$	8.0	1.99
$[6.5, 20]$	9.0	2.60

^{238}U			
E_x **range**	$\langle E_x \rangle$ **(MeV)**	STD_{E_x} **(MeV)**	^{250}**Cf cont.**
$[3, 8]$	5.7	1.33	$(24.3 \pm 3.0)\%$
$[4.5, 9.5]$	6.7	1.33	$(18.5 \pm 3.0)\%$
$[5.5, 12]$	7.7	1.68	$(14.0 \pm 3.0)\%$
$[6.0, 17.5]$	8.7	2.5	$(13.5 \pm 3.0)\%$
$[6.8, 20.0]$	9.7	2.85	$(15.5 \pm 3.0)\%$

Table 6.4: Ranges, mean value, and standard deviation of E_x for each fissioning system. ^{238}U includes the percentage of ^{250}Cf contamination subtracted in each range.

6.5.1 Fission Channels

Figure 6.23 presents the nuclear-charge distributions of the four fissioning systems at different E_x. As explained in Sec.6.1.3, the fission channels *Super long*, *Standard I*, *Standard II*, and *Super Asymmetric* were fitted

to the distributions of ^{244}Cm, ^{240}Pu, and ^{239}Np. The contribution of the *Super Asymmetric* channel was observed to be negligible for ^{238}U. Figure 6.24 shows the yield (a), the mean position (b), and the width (c) of each fission channel as a function of E_x. The yield of the SL channel increases with E_x, ranging from 0 to 5% in the systems with low E_x and reaching a maximum of 40% in ^{244}Cm. This is the expected behavior for fission of actinides: the increase of E_x reduces structure effects and boosts the symmetric contribution, which reflects macroscopic components of fission. The combined yield of SI and SII channels compensates the SL evolution, decreasing with E_x. Individually, SI and SII present opposite behaviors: in ^{239}Np and ^{244}Cm, SI yield increases with E_x while SII decreases; in ^{238}U, instead, SI and SII presents an inverted trend; in ^{240}Pu, SI and SII show two different trends attending to the excitation energy, coincident with the first ($E_x < 12$ MeV) and second ($E_x > 12$ MeV) fission chance. The SA yield does not exhibit a strong evolution with E_x; it slightly increases with E_x for ^{240}Pu but remains with a low contribution in the full range of E_x.

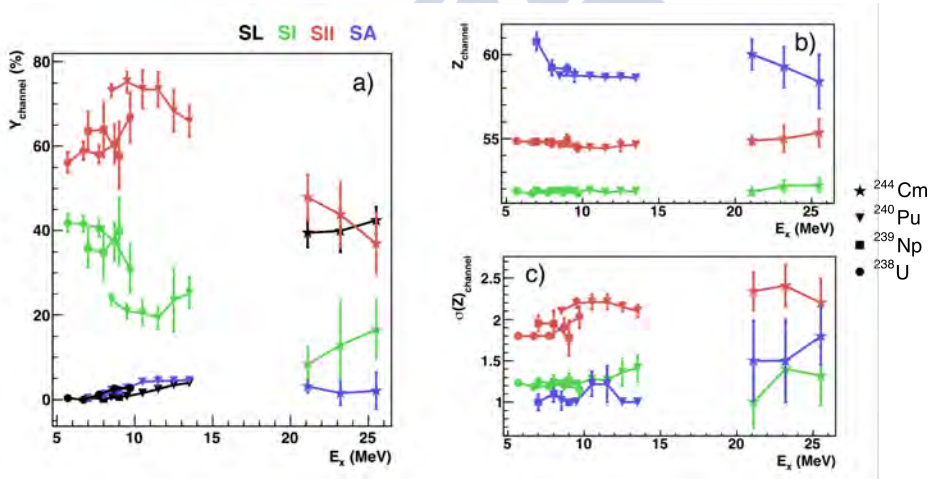

Figure 6.24: Evolution of the yields (a), the mean positions (b), and the widths (c) of the fission channels as a function of E_x.

The positions of the channels remain rather constant along the E_x range, while a clear evolution is observed in the widths. The width of SI shows a general increasing trend with E_x, which suggests that the compact

configuration at scission, characteristic of this channel, vanishes with increasing E_x. A similar general trend is appreciated in SII, although ^{239}Np presents an opposite behavior. The width of SA presents large fluctuations with no clear trend.

In general, the channel yields show that the influence of the Liquid Drop characteristics increases with increasing E_x, while shell effects, implicit in the asymmetric channels, decrease. Among them, SI decreases with E_x, guided by spherical configurations, while SII shows a slightly increasing trend, driven by the increasing nucleon mobility with E_x. The positions of the asymmetric channel remain rather constant, hence, the involved shells are rather well fixed. Finally, the channels widths show that E_x diffuses the structure configurations.

6.5.2 Neutron Excess

Figure 6.25 presents $\langle N \rangle / Z$ at different excitation energies for ^{240}Pu and ^{238}U. No significant evolution is appreciated in ^{239}Np and ^{244}Cm due to the limited range of E_x and the low statistics.

In the case of ^{240}Pu, the $\langle N \rangle / Z$ of light fragments shows no evolution with E_x. The effect of E_x is only observed on the heavy fragment, $Z > 45$, where $\langle N \rangle / Z$ decreases with increasing E_x, with the strongest impact in $Z \sim 50$, suggesting that the shell structure effect, present in this region, reduces its influence at higher E_x, as expected.

^{238}U presents large statistical fluctuations that prevent a clear observation at the symmetry. Nevertheless, an effect of E_x can be distinguished in $Z \sim 50$, where $\langle N \rangle / Z$ decreases at higher E_x. Finally, ^{238}U shows an unexpected local maximum of $\langle N \rangle / Z$ in $Z \sim 39$, which decreases with increasing E_x. This maximum was also observed in other fissioning systems present in Fig. 6.16, where its position evolves with the fissioning system, suggesting that this effect in the light fragment might be inherited from the partner heavy fragment.

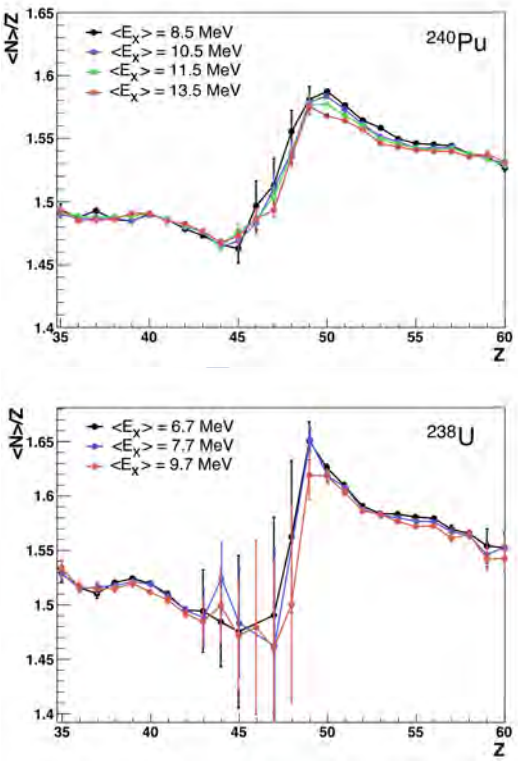

Figure 6.25: Neutron excess of ^{240}Pu and ^{238}U for different E_x.

6.5.3 Neutron Evaporation

The total neutron evaporation, averaged over the full Z-range, is presented in Fig. 6.26 as a function of E_x for the available fissioning systems, ^{244}Cm, ^{240}Pu, ^{239}Np, and ^{238}U. $\langle\nu_{total}\rangle$ shows similar trends with E_x in ^{239}Np and ^{240}Pu. ^{238}U presents, instead, a n-evaporation with higher slope, as a function of E_x, being coherent with the measurement of ^{238}U from the SOFIA campaign [70] at higher E_x (indicated with a dot).

Figure 6.27 presents the total neutron evaporation (Eq. 6.4) of ^{240}Pu and ^{238}U as a function of Z, for different E_x. The symmetric region is

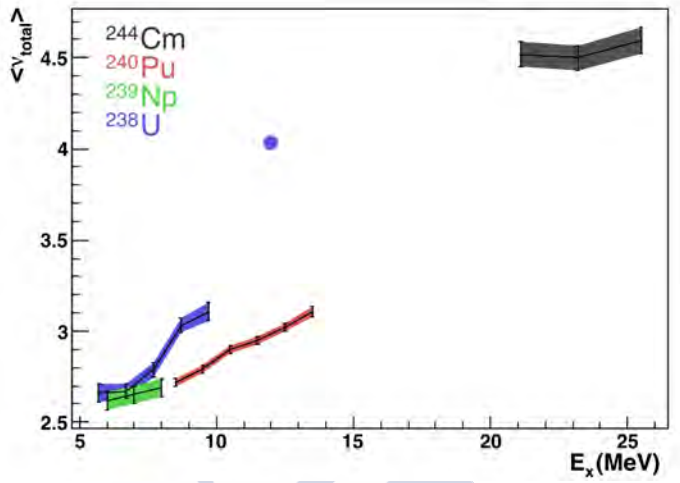

Figure 6.26: Total neutron evaporation of ^{244}Cm, ^{240}Pu, ^{239}Np, and ^{238}U as a function of E_x. Data of ^{238}U from the SOFIA campaign is included, indicated with a dot.

not presented in ^{238}U due to the large statistical fluctuations. In both cases, $\langle \nu \rangle_{total}$ increases with E_x. However, ^{240}Pu presents a stabilization at $(Z_1, Z_2) = (39, 55)$, where the evaporation does not change with E_x, suggesting a structure effect that produces a particularly stable configuration against small variations of E_x. ^{238}U presents a similar effect in $(Z_1, Z_2) = (39, 53)$. No structure effects are expected in $Z \sim 39$, but in $Z \sim 55$, typically related to the deformed shell $N \sim 88$ [13].

A particular strong evolution is observed around $Z \sim 50$: at low E_x a minimum of evaporation is present around $Z \sim 50$, with a clear increasing trend at higher Z; while at higher E_x this minimum is less pronounced, and the trend at higher Z becomes rather flat. This observation is coherent with the presence of shell effects: at low E_x, a heavy fragment around $Z \sim 50$, also affected by the spherical shell $N = 82$, presents lower neutron evaporation than its neighbors, and this difference reduces at higher E_x since the shell effect vanishes with E_x.

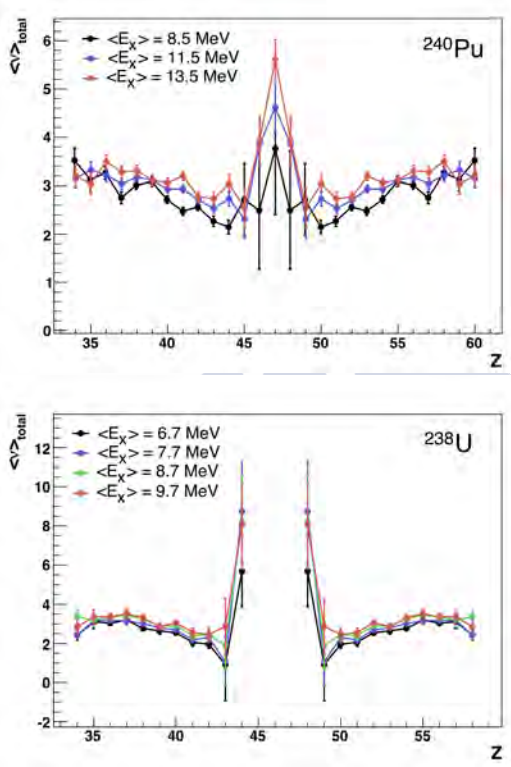

Figure 6.27: Total neutron evaporation of ^{240}Pu and ^{238}U for different E_x.

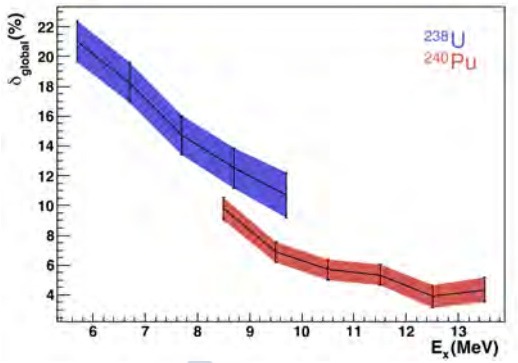

Figure 6.28: Global even-odd effect of ^{238}U and ^{240}Pu as a function of E_x.

6.5.4 Even-Odd Staggering

Figure 6.28 presents the global even-odd effect of ^{238}U and ^{240}Pu, defined in Eq. 6.5, as a function of E_x. δ_{global} is observed to decrease with increasing E_x as expected, since higher intrinsic energy is available above the barrier $(E_x - B_f)$. δ_{global} ranges from 21% to 11% in ^{238}U with a regular variation; and from 10% to 4% in ^{240}Pu, with a rather logarithm behavior, indicating that the even-odd effect saturates at high E_x where almost all the Z-pairs are already broken.

The offset between both curves might be due to a difference in the available potential energy. As discussed in Sec. 6.4, the energy dissipation along the fission path from saddle to scission transforms collective energy into intrinsic energy at scission; this intrinsic energy, together with the available energy above the barrier at scission $(E_x - B_f)$ permits the rupture of pairs, producing odd-odd fragments, which require higher energy than the formation of even-even fragments. In even-Z systems, δ_{global} permits to estimate the energy dissipated in the fission process, E_{diss}, using a simple relationship introduced by Gönnenwein in [77] :

$$E_{diss}\ \ (MeV) \simeq -4 \ln \delta_{global} - (E_x - B_f)\ \ (MeV) \qquad (6.10)$$

where E_x is the excitation energy of the fissioning system and B_f is the

height of the fission barrier.

Figure 6.29 (a) presents E_{diss} as a function of E_x, for ^{238}U and ^{240}Pu, where the values $B_f(^{238}\text{U})$=5.7 MeV and $B_f(^{240}\text{Pu})$=5.6 MeV, calculated in [85], were used. The color bands corresponds to present data and dots correspond to previous measurement of n_{th}-induced fission of ^{240}Pu [66] and Coulomb-induced fission of ^{238}U [70]. In both cases, the present data show a decreasing trend of the dissipated energy with increasing E_x, which is coherent with the previous measurements. This indicates that the decreasing behavior of the even-odd effect with E_x, shown in Fig. 6.28, is mainly governed by the energy above the barrier.

E_{diss} was observed to be proportional to the potential energy released from saddle to scission, ΔV [86], estimated as a constant proportion of 35% in Ref. [19]. Under this assumption, ΔV is calculated from the previous E_{diss} as:

$$\Delta V = E_{diss}/0.35 \tag{6.11}$$

Figure 6.29 (b) presents ΔV as a function of E_x, for ^{238}U and ^{240}Pu. Present data (color bands) show a decreasing trend with E_x, with values that ranges from $\Delta V \sim 18$ MeV to $\Delta V \sim 15$ MeV in ^{238}U, and from $\Delta E \sim 20$ MeV to $\Delta E \sim 15$ MeV in ^{240}Pu. Previous measurements of δ_{global} (color dots) [66, 70] are also included. Since the potential energy in the ground state does not change with E_x and assuming that the barrier is not affected by the possible small variation in L, this decreasing trend indicates that the scission potential energy is higher at higher E_x, and hence, assuming a potential energy surface not affected by the E_x, the fragments split would occur sooner in their descend to scission, at shorter elongations, and/or in shallower regions of the potential energy surface.

This variation of ΔV with E_x might explain in part the different slopes of ^{238}U and ^{240}Pu in Fig. 6.26. The excess of E_x would contribute to a larger evaporation but also be used in variations of the potential ΔV. Following the energy conservation:

$$\Delta V + E_x = \langle \nu_{total} \rangle \Big(\langle S_n \rangle + \langle T_n \rangle \Big) + \langle E_\gamma \rangle \ , \tag{6.12}$$

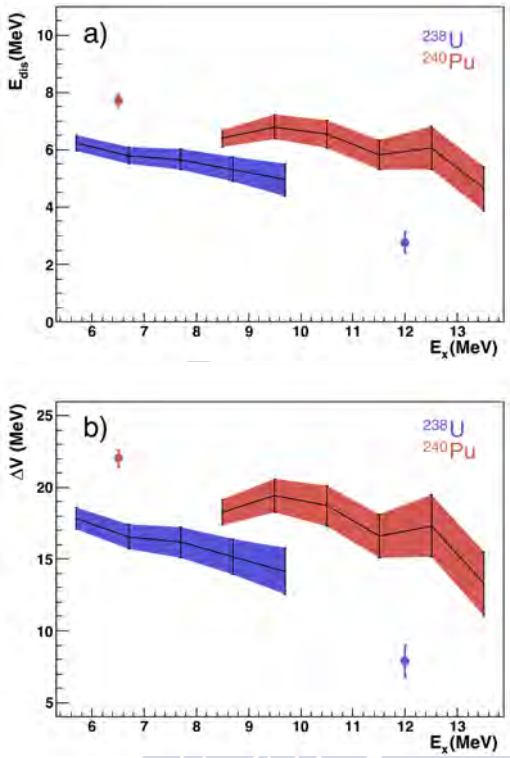

Figure 6.29: Dissipation energy from saddle to scission point (a) and potential energy from ground state to scission point (b) of ^{238}U and ^{240}Pu as a function of E_x, calculated from the even-odd effect using Eq. 6.10 and Eq. 6.11. Present data are presented in color bands and previous measurements of n_{th}-induced fission of ^{240}Pu [66] and Coulomb-induced fission of ^{238}U [70] are indicated with color dots.

where $\langle S_n \rangle$ and $\langle T_n \rangle$ are average values of the neutron separation energy and the neutron kinetic energy, and $\langle E_\gamma \rangle$ is the average energy released in gamma emission.

From Fig. 6.29 we observe an anticorrelation between ΔV and E_x, thus an increase of E_x is partly balanced by a descend in ΔV, leaving less

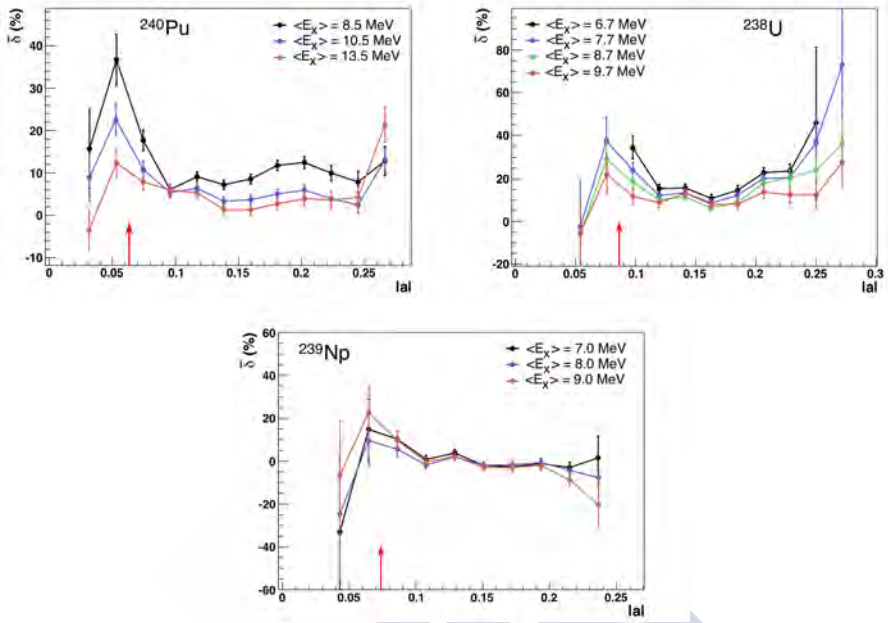

Figure 6.30: Local even-odd effect ^{240}Pu, ^{239}Np, and ^{238}U as a function of the asymmetry parameter, for different E_x. The red arrows indicate the position of $Z = 50$

energy available for post-scission evaporation.

Figure 6.30 shows the local even-odd effect (Eq. 6.6) as a function of the asymmetry parameter (Eq. 6.7), at different E_x, for ^{240}Pu, ^{239}Np, and ^{238}U. Both even-Z systems, Pu and U, present positive values of δ that decrease for increasing E_x. Such evolution is stronger at $|a| \sim 0.05$ in Pu and at $|a| \sim 0.08$ in U, which correspond to $Z \sim 50$. No evolution is observed at $|a| \sim 0.09$ ($Z \sim 52$) in ^{240}Pu, while a rather constant variation is appreciated between $|a| \sim 0.15$ and $|a| \sim 0.25$. ^{238}U presents a minimum at $|a| \sim 0.16$ ($Z \sim 54$) where δ barely changes with E_x, while, at higher $|a|$, the evolution with E_x gradually increases. Finally, the even-odd staggering of the odd-Z system ^{239}Np seems to be not affected by the E_x variation. The even-odd effect in odd-Z systems depends more on the sharing of unpaired protons between both fragments, governed by their

level densities, than on the secondary contribution of the pairs rupture.

Conclusions

Fission of neutron-rich actinides is experimentally investigated in this work. The fissioning systems —^{250}Cf, ^{244}Cm, ^{240}Pu, ^{239}Np, and ^{238}U— are produced through fusion and transfer reactions in inverse kinematics with a beam of ^{238}U at 6.14 MeV/u impinging a ^{12}C target. The SPIDER detector provides the identification of the fissioning systems while the VAMOS spectrometer permits the identification of the fission products of such systems. This experimental information made possible to study the isotopic, isobaric and elemental fission yields, the neutron excess, the total neutron evaporation, the nuclear-charge even-odd staggering, and the evolution of these observables with the initial excitation energy of the fissioning system.

The target-like recoil from transfer and inelastic reactions is detected in the SPIDER telescope where the fissioning system is identified and the excitation energy is determined by reconstructing the binary reaction. A fusion reaction is assumed when no recoil is detected. The inverse kinematics permits the forward emission of both fission fragments with a large kinetic energy in laboratory. One of the fragments is deflected in the VAMOS spectrometer and it is identified in mass, nuclear charge, and charge state with a dedicated setup at the focal plane of the spectrometer. The fission-fragment identification permits to obtain of fission yields once the geometrical and intrinsic efficiency are corrected, including the VAMOS acceptance, in order to compensate biased measurements.

The fission yields show a strong contribution of the asymmetric fission in the systems at low excitation energy: ^{238}U ($\langle E_x \rangle$ = 7.4 MeV), ^{239}Np ($\langle E_x \rangle$ = 7.5 MeV), and ^{240}Pu ($\langle E_x \rangle$ = 10.7 MeV). The position of the asymmetric component for the heavy fragment remains independent of the fissioning system, centered around $Z \sim 54$ and $A \sim 140$. The

symmetric fission increases with E_x: the systems at higher E_x —^{244}Cm ($\langle E_x \rangle = 23.0$ MeV) and ^{250}Cf ($E_x = 45.97$ MeV)— show a not negligible symmetric contribution, becoming dominant in the latter. A contribution of the asymmetric fission remains present in both cases. The study of the fission channels in nuclear charge shows the asymmetric-fission contribution described by two major channels, SI and SII, with positions fixed in $Z_{SI} \simeq 52$ and $Z_{SII} \simeq 55$. The evolution with E_x reveals a general decreasing trend of SI and a increasing trend of SII yields. Both channels become more diffuse with increasing E_x.

The neutron excess shows a clear charge polarization, with a heavy fragment more neutron rich than the light one. A saw-tooth shape is observed with a maximum of N/Z at $Z \sim 50$ for the systems at lower E_x with a clear tendency towards the double magic nucleus ^{132}Sn. This structure effect around $Z \sim 50$ reduces with increasing E_x while the light-partner fragment does not show such evolution. The light fragment show an unexpected local maximum around $Z \sim 40$ that evolves with the fissioning system.

The averaged total neutron evaporation appears to increase with E_x, being proportional to E_x after few MeV. Individually, ^{238}U presents a neutron evaporation that increases faster with E_x than the rest of the systems. A large neutron evaporation is observed at symmetry, which is consistent with a large elongation of the SL fission channel. A minimum of evaporation is present in $Z \sim 50$ at low E_x, which rapidly disappears with increasing E_x, suggesting a compact configuration at scission, driven by spherical shells.

The Z even-odd effect of even-Z systems shows a common decreasing trend with the fissility parameter that is not followed by the odd-Z system ^{239}Np, which presents an even-odd effect twice lower than the trend. A decreasing logarithmical behavior is observed in even-Z systems as a function of E_x, which reveals the saturation of the pairs rupture, while no significant evolution is observed in ^{239}Np, indicating that its even-odd effect is not governed by the pair rupture but the sharing of the unpaired proton. The local even-odd effect was observed to increase with the asymmetry at low E_x, with a local maximum at $Z \sim 50$. At higher E_x, this

behavior smoothes and the even-odd effect becomes more uniform.

The dissipation energy from saddle to scission as well as the potential energy from ground state to scission are calculated for ^{238}U and ^{240}Pu resulting, in both cases, decreasing with E_x. This behavior may be partly responsible for the different evolution of the neutron multiplicity with E_x observed in ^{238}U and ^{240}Pu. The lower ΔV at higher E_x suggests that the scission point appears sooner, at shorter elongations and/or in shallower regions of the potential energy surface.

In conclusion, this work provides new experimental information concerning the distribution of fission fragments of neutron rich actinides. Structure effects were observed to be present in different observables for low-energy fission such as the asymmetric component of the fission yields, the charge polarization of the neutron excess with maximum at $Z \sim 50$, the minimum of the neutron evaporation at $Z \sim 50$, and the local maximum of the even-odd effect at $Z \sim 50$. These effects are observed to decrease with increasing the excitation energy of the fissioning system remaining present up to tens of MeV. Finally, the comparison with previous measurements and with the GEF code calculations reveals a good overall agreement and consistence between them.

USC
UNIVERSIDADE
DE SANTIAGO
DE COMPOSTELA

Resumen

Introducción

La fisión, descubierta por Meitner y Frisch en 1939, se entiende hoy en día como un proceso largo y complejo que implica deformaciones extremas, efectos de estructura nuclear y flujos de calor que deciden las características de las distribuciones de fragmentos producidos. Sin embargo, después de casi 80 años de intenso trabajo en el estudio de la fisión, ésta sigue estando lejos de ser completamente entendida, y su descripción teórica y experimental sigue siendo incompleta.

La fisión nuclear a baja energía de excitación es uno de los fenómenos nucleares que involucra tanto el aspecto macroscópico como el aspecto microscópico de la materia nuclear: las deformaciones que los núcleos alcanzan en el punto de escisión corresponden a un movimiento colectivo de los nucleones, mientras que las distribuciones de fragmentos de fission observadas no se pueden explicar sin el efecto de la estructura de capas de sus niveles de energía.

La gran cantidad de datos experimentales en cuanto a la distribución de fragmentos muestra la fisión de actínidos como un proceso asimétrico que produce un fragmento pesado con una masa media constante en $A \sim 140$, independiente del sistema fisionante, y un fragmento ligero que completa la masa del sistema fisionante. Los modelos teóricos que tienen en cuenta la estructura nuclear relacionan la estabilización del fragmento pesado con el salto de energía de la capa esférica $N = 82$ y la capa deformada $N \sim 88$. Sin embargo, hasta esta última década, la información experimental del reparto de protones y neutrones entre los fragmentos no fue accesible.

Históricamente, el análisis experimental de los observables de la fisión sufre de dos inconvenientes principales: raramente se obtienen simultáneamente en un único experimento y las medidas del número atómico de los fragmentos son típicamente escasas, sino inexistentes. El uso de la cinemática inversa en el estudio de la fisión, iniciado por Schmidt et al. en GSI, ofrece una posibilidad de resolver estos problemas. Al contrario que en la cinemática directa, donde se acelera un haz ligero y se hace incidir sobre un blanco pesado, en cinemática inversa es el núcleo pesado el acelerado. De este modo, los fragmentos de fission adquieren mayores velocidades, facilitando la medida directa de su número atómico. En la primera aplicación experimental de esta técnica, Schmidt et al. observaron un valor medio de Z constante en el fragmento pesado para más de 20 sistemas fisionantes distintos, lo que sugiere que los protones también juegan un papel importante en el proceso de fisión.

Actualmente, dos campañas experimentales complementarias hacen uso de la cinemática inversa y de las capacidades de espectrómetros magnéticos para medir al mismo tiempo la masa y la carga nuclear de los fragmentos de fission: SOFIA en GSI, donde se estudia la fisión inducida por interacción Coulombiana de sistemas pobres en neutrones; y la campaña de fisión en VAMOS/GANIL, donde se estudian sistemas ricos en neutrones en torno al ^{238}U, producidos por reacciones de fusión y de transferencia de nucleones.

Esta tesis es parte de la campaña de fission en VAMOS/GANIL, donde las reacciones de transferencia de nucleones permiten, además, investigar la evolución de los observables de fisión con la energía de excitación del sistema fisionante.

Aparte del estudio de la fisión en sí, este proceso presenta la posibilidad de producir núcleos ricos en neutrones, lo cual es un tema actual de investigación en la física nuclear, estudiando por ejemplo la evolución de la estructura de capas en núcleos lejos de la estabilidad. La fisión de los núcleos estudiados en este trabajo producen fragmentos ricos en neutrones desde $Z = 30$ hasta $Z = 70$, lo cual abre la posibilidad de dichas investigaciones en un amplio rango de núcleos.

Además de investigación básica, este estudio es también relevante en aplicaciones industriales y en energía. Los reactores de 4^{a} generación, basados en otros combustibles distintos de ^{235}U, buscan la posibilidad de incinerar residuos radioactivos a través de un proceso continuo de fisión por encima de la barrera, inducida por la captura de neutrones rápidos. El diseño de estos reactores y la mejora de su eficiencia y su seguridad, requieren una gran cantidad de datos experimentales sobre los rendimientos de fisión de actínidos menores en un rango de energías de excitación comparable con neutrones rápidos.

Dispositivo Experimental

El experimento aquí descrito tiene lugar en GANIL, Francia, donde un haz de ^{238}U se acelera hasta 6.14 MeV/u y se envía al area experimental G1. El haz incide sobre un blanco de ^{12}C de 100 μg/cm^2 de espesor donde se producen reacciones de fusión, transferencia de nucleones y dispersión. Una vez que una de estas reacciones tiene lugar, el producto pesado puede decaer por fisión, siempre y cuando su energía de excitación lo permita.

Debido a la cinemática inversa, los dos fragmentos de fisión se emiten hacia adelante dentro de un cono de 25 deg, mientras que el núcleo ligero de retroceso de la reacción primaria (transferencia o dispersión) se emite típicamente con mayores ángulos. Este núcleo de retroceso se detecta en un doble detector de silicio (SPIDER) colocado después del blanco, compuesto de dos cristales de silicio anulares. La parte anterior de cada cristal está segmentada en 16 sectores y la parte posterior en 16 anillos, cubriendo entre 30° y 47° en ángulo polar. SPIDER mide la perdida de energía y la energía residual de los núcleos ligeros de retroceso que atraviesan el primer cristal y se detienen en el segundo. Estas dos variables permiten obtener una identificación isotópica de estos núcleos. Al mismo tiempo, la segmentación angular del detector proporciona una medida de los ángulos polar y azimutal. Estas medidas permiten reconstruir la reacción binaria primaria y obtener la energía de excitación transmitida al sistema fisionante.

Los dos productos de la fisión atraviesan SPIDER por un agujero central que evita la interacción de los fragmentos con el detector. Uno de los fragmentos dispara el detector Start, una cámara multi-hilos que proporciona la referencia de tiempo, y es desviado en el campo magnético del espectrómetro VAMOS antes de ser detectado en el dispositivo experimental colocado en su plano focal. El recorrido nominal de los fragmentos entre el blanco y el plano focal es de 7.6 m, variando ± 0.35 m en función de la rigidez magnética y el ángulo de emisión del fragmento.

El dispositivo experimental colocado en el plano focal de VAMOS permite la identificación de los fragmentos de fisión en masa, carga nuclear y estado de carga. Este conjunto de detectores está compuesto por: una cámara multi-hilos, que proporciona una medida del tiempo de vuelo de los fragmentos; dos cámara de deriva, que miden la posición y el ángulo de los fragmentos después del espectrómetro; una cámara de ionización, que mide la pérdida de energía de los fragmentos; y un muro de detectores de silicio, donde los fragmentos se paran y se mide su energía residual.

En un espectrómetro magnético las partículas cargadas se desvían en función de su rigidez magnética, que es una característica de cada fragmento que relaciona su momento con su estado de carga. Por lo tanto, la rigidez magnética, así como el ángulo de emisión y el espacio recorrido por los fragmentos entre el blanco y el plano focal, se reconstruyen evento a evento a través de la posición y ángulo de los fragmentos medidos en el plano focal, después de ser desviados. La rigidez magnética proporciona una medida conjunta, con alta resolución, de la masa y el estado de carga de cada fragmento cuyas contribuciones se separan a través de una medida de la masa alternativa, de baja resolución, obtenida de la energía y velocidad de los fragmentos. Finalmente, la identificación en carga nuclear se obtiene directamente de la pérdida de energía combinada con la energía residual.

Las reacciones de fusión y transferencia introducen energía de excitación en el sistema que promociona el núcleo compuesto y/o el núcleo de retroceso a estados excitados. Los fragmentos de fisión también adquieren energía de excitación durante el proceso de fisión. En ambos casos estos estados excitados pueden decaer a través de la emisión de gammas. Estos

rayos gamma se detectan en 6 detectores de germanio (EXOGAM) que rodean al blanco proporcionando un verificación en la identificación de los fragmentos de fisión.

La gran variedad de núcleos producidos en el proceso de fisión hace que el espacio de fases de fragmentos en rigidez magnética y ángulo no se pueda cubrir en su totalidad con la cobertura angular y en momento del espectrómetro. Con el fin de aumentar esta cobertura se han usado cuatro configuraciones distintas durante el experimento cubriendo distintas zonas de espacio de fases incluyendo dos orientaciones del espectrómetro respecto el eje del haz, 20° y 14°, y tres valores centrales de rigidez magnética, 1.1 Tm, 1.2 Tm, y 1.3 Tm.

Análisis de Datos

La identificación isotópica de los fragmentos de fisión permite calcular los rendimientos de fisión para los distintos sistemas fisionantes. Las reacciones de fusión producen el sistema ^{250}Cf con una energía de excitación bien determinada de $E_x = 45.97$ MeV, mientras que las reacciones de transferencia con estadística suficiente para este estudio resultan ser la *4p2n*-transfer, la *2p*-tranfer, la *p*-transfer y el canal inelástico, produciendo los sistemas fisionantes ^{244}Cm, ^{240}Pu, ^{239}Np y ^{238}U, con rangos en energía de excitación centrados en $\langle E_x \rangle = 23.0$ MeV, $\langle E_x \rangle = 10.7$ MeV, $\langle E_x \rangle = 7.5$ MeV y $\langle E_x \rangle = 7.4$ MeV, respectivamente.

Los rendimientos isotópicos de fisión ($Y(Z,A)$), normalizados a 200, se calculan en base al número de eventos registrados (N), corregido por la eficiencia geométrica (ε_g^{ff}) e intrínseca (ε_i^{ff}) de cada detector:

$$Y(Z,A) = 200 \frac{N}{\varepsilon_g^{ff} \cdot \varepsilon_i^{ff}}(Z,A) \left(\sum_{Z,A} \frac{N}{\varepsilon_g^{ff} \cdot \varepsilon_i^{ff}}(Z,A) \right)^{-1} . \qquad (6.13)$$

Las diferentes configuraciones de VAMOS cubren diferentes rangos en

ángulo y rigidez magnética, por tanto cada configuración necesita ser normalizada por la intensidad de haz con el fin de contribuir con el mismo peso al cálculo de los rendimientos de fisión. Esto se consigue normalizando el número de eventos registrados en SPIDER procedentes de reacciones de dispersión elástica para cada una de las configuraciones de VAMOS, asumiendo una eficiencia de SPIDER constante a lo largo del experimento.

ε_g^{ff} viene determinado por la aceptancia angular de VAMOS que se puede descomponer en dos contribuciones: la aceptancia en el ángulo azimutal ($f_\phi(\theta_{lab}, \delta)$) y la aceptancia en el ángulo polar ($f_{\theta_{CM}}(A)$):

$$\varepsilon_g^{ff} = f_\phi(\theta_{lab}, \delta) \cdot f_{\theta_{CM}}(A) \ . \tag{6.14}$$

f_ϕ depende de la focalización que los cuadrupolos producen en las trayectorias de los fragmentos cuando pasan a través del espectrómetro. Esta focalización varía con el ángulo polar (θ_{lab}) y la rigidez magnética relativa ($\delta = B\rho/B\rho_0$) de cada fragmento. De este modo f_ϕ se calcula como el rango en ϕ_{lab} cubierto por VAMOS normalizado a la emisión 2π en función de θ_{lab} y δ:

$$f_\phi(\theta_{lab}, \delta) = \frac{\Delta\phi_{lab}(\theta_{lab}, \delta)}{2\pi} \ . \tag{6.15}$$

$f_{\theta_{CM}}$ se calcula en el centro de masas del sistema fisionante, donde el ángulo polar de los fragmentos de fisión no depende de las condiciones experimentales. Este ángulo polar está también limitado por la aceptancia de VAMOS, donde, además, la distribución angular de cada estado de carga de un mismo fragmento está cortada en regiones distintas de θ_{ff}^{CM}. $f_{\theta_{CM}}$ se calcula como el rango de $\cos(\theta_{ff}^{CM})$ en el cual todos los estados de carga de cada fragmento de masa A son completamente transmitidos a través del espectrómetro, normalizado a la emisión completa:

$$f_{\theta_{CM}}(A) = \frac{\Delta\cos(\theta_{ff}^{CM})}{2}(A) \ . \tag{6.16}$$

ε_i^{ff} se define como la probabilidad de tener identificación isotópica para cada fragmento de fisión que llega al último detector del dispositivo ex-

perimental del plano focal de VAMOS. Esta eficiencia intrínseca se puede factorizar atendiendo al detector involucrado:

$$\varepsilon_i^{ff} = \varepsilon_i^{DC} \cdot \varepsilon_i^{Si} \cdot \varepsilon_i^{Trigger} \ , \tag{6.17}$$

donde ε_i^{DC} es la eficiencia intrínseca de las cámaras de deriva; ε_i^{Si} es la eficiencia intrínseca del muro de silicios; y $\varepsilon_i^{Trigger}$ es la eficiencia intrínseca del detector Start y de la cámara multi-hilos del plano focal, cuyas señales en coincidencia definen el trigger VAMOS. La eficiencia intrínseca de la cámara de ionización se asume $\varepsilon^{IC} = 1$.

ε_i^{DC} se calcula como el número de eventos registrados en coincidencia en las cámaras de deriva y en la cámara de ionización, dividido por el número de eventos registrados individualmente en la cámara de ionización, en función de la pérdida de energía en la primera fila de la cámara de ionización.

ε_i^{Si} se calcula como el número de eventos por unidad de $\delta = B\rho/B\rho_0$ y θ_{lab}, detectados en coincidencia en las cámaras de deriva y en muro de silicios, dividido por el número de eventos, por unidad de δ y θ_{lab}, detectados en las cámaras de deriva.

$\varepsilon_i^{Trigger}$ refleja el efecto de hilos no operativos en el detector Start, reduciendo el número de fragmentos ligeros registrados. $\varepsilon_i^{Trigger}$ se calcula como el ratio entre el número de eventos por unidad de $\cos(\theta_{ff}^{CM})$ del fragmento ligero y el máximo numero de eventos por unidad de $\cos(\theta_{ff}^{CM})$ del fragmento pesado complementario, para la fisión de ^{250}Cf, cuya emisión se asume isótropa en estas condiciones experimentales. $\varepsilon_i^{Trigger}$ se puede descomponer en una componente global dependiente de $(Z/v)^2$ y una componente local dependiente de $(Z/v)^2$ y θ_{ff}:

$$\varepsilon_i^{Trigger} = \varepsilon_1^{Trigger}\left(\left(\frac{Z}{v}\right)^2\right) \cdot \varepsilon_2^{Trigger}\left(\theta_{ff}, \left(\frac{Z}{v}\right)^2\right) \ . \tag{6.18}$$

$\varepsilon_1^{Trigger}$ se parametriza como:

$$\varepsilon_1^{Trigger} = C_1 + C_2 \mathrm{Erf}\left(A\left[\left(\frac{Z}{v}\right)^2 - B\right]\right) , \tag{6.19}$$

donde $\mathrm{Erf}(x) = \frac{2}{\sqrt{\pi}}\int_0^x e^{-t^2}\mathrm{d}t$ es la *Función Error*, y (C_1, C_2, A, B) son parámetros.

$\varepsilon_2^{Trigger}$ se parametriza como:

$$\begin{aligned} \varepsilon_2^{Trigger} &= \left[1 + \sum_{i=1}^{3} A_i \cdot e^{-\frac{1}{2}\left(\frac{\theta_{ff}-\mu_i}{\sigma_i}\right)^2}\right]^{-1} , \\ A_i &= \left[\left(\frac{1}{2} + C'_i\right) + \left(\frac{1}{2} - C'_i\right)\mathrm{Erf}\Big(A'_i\left[(Z/v)^2 - B'_i\right]\Big)\right]^{-1} - 1, \end{aligned} \tag{6.20}$$

donde la media y la desviación típica de cada función Gausiana, μ_i, σ_i, se obtienen de un ajuste a los datos, mientras que los parámetros de cada amplitud, C'_i, A'_i, B'_i, se obtienen a través de un proceso iterativo que minimiza la desviación, respecto de una distribución plana, de la distribución en $\cos(\theta_{ff}^{CM})$ de cada Z.

Finalmente, el número de cuentas computable para el cálculo de los rendimientos istópicos de fisión ($N(Z,A)$) se calcula como la integral de la distribución de eventos en $\cos(\theta_{CM})$ en el rango en que la distribución de estados de carga se transmite completamente:

$$N(Z,A) = \int_{\cos(\theta_{ff}^{CM})|_{min}(A)}^{\cos(\theta_{ff}^{CM})|_{max}(A)} \frac{\mathrm{d}N(Z,A)}{\mathrm{d}(\cos(\theta_{ff}^{CM}))}\mathrm{d}(\cos(\theta_{ff}^{CM})) , \tag{6.21}$$

donde el número de eventos por unidad de $\cos(\theta_{CM})$ se calcula como la suma de las contribuciones de los diferentes estados de carga:

$$\frac{\mathrm{d}N(Z,A)}{\mathrm{d}(\cos(\theta_{ff}^{CM}))} = \sum_{q_{min}(A)}^{q_{max}(A)} \frac{\mathrm{d}N(Z,A,q)}{\mathrm{d}(\cos(\theta_{ff}^{CM}))} , \tag{6.22}$$

y cada estado de carga recibe la contribución de las 4 configuraciones de VAMOS, las cuales presentan cierta superposición en algunas regiones de

$\cos(\theta_{CM})$, por lo que el número de eventos por unidad de $\cos(\theta_{CM})$ de cada estado de carga se toma como la mayor de las cuatro contribuciones:

$$\frac{\mathrm{d}N(Z,A,q)}{\mathrm{d}(\cos(\theta_{ff}^{CM}))} = \mathrm{MAX}\left[\frac{\mathrm{d}N(Z,A,q,i)}{\mathrm{d}(\cos(\theta_{ff}^{CM}))}\right], \tag{6.23}$$

donde $i = 1, 2, 3, 4$ indica cada configuración de VAMOS.

Discussión de Resultados

En este trabajo se estudia la fisión de actínidos ricos en neutrones. Los sistemas fisionantes ^{250}Cf, ^{244}Cm, ^{240}Pu, ^{239}Np y ^{238}U son producidos a través de reacciones de fusión y transferencia de nucleones, bajo cinemática inversa, con un haz de ^{238}U a 6.14 MeV/u incidiendo sobre un blanco de ^{12}C.

Los rendimientos de fisión de estos sistemas muestran una fuerte contribución de la componente asimétrica de fisión en los sistemas a baja energía de excitación: ^{238}U, ^{239}Np y ^{240}Pu. La posición de la componente asimétrica en la región de fragmentos pesados se mantiene centrada en $Z \sim 54$ y $A \sim 140$, independientemente del sistema fisionante. La fisión simétrica crece con la energía de excitación: los sistemas a mayor E_x, ^{244}Cm y ^{250}Cf, muestran una contribución simétrica no despreciable, convirtiéndose en dominante en el último caso. Ambos sistemas muestran cierta contribución de la fisión asimétrica. El estudio de los canales de fisión en términos de carga nuclear muestra la fisión asimétrica descrita mayoritariamente por dos canales, SI y SII, con posiciones fijas en $Z_{SI} \simeq 52$ y $Z_{SII} \simeq 55$. La evolución con E_x revela una tendencia decreciente en la contribución de SI y creciente en SII. Ambos canales se vuelven más anchos a mayor E_x.

El exceso de neutrones muestra una clara polarización de carga, con un fragmento pesado más rico en neutrones que el ligero. El exceso de neutrones muestra un comportamiento en diente de sierra, con un máximo en $Z \sim 50$ para sistemas a baja E_x y una clara tendencia hacia el núcleo

doblemente mágico ^{132}Sn. Este efecto de estructura en torno a $Z \sim 50$ se reduce aumentando E_x mientras que el fragmento ligero correspondiente no muestra tal evolución. El fragmento ligero muestra un inesperado máximo local alrededor de $Z \sim 40$ el cual evoluciona con el sistema fisionante.

El promedio de la evaporación total de neutrones crece con E_x, siendo proporcional a E_x después de varios MeV. Individualmente, ^{238}U presenta una evaporación de neutrones que crece con E_x más rápido que el resto de sistemas. En la simetría la evaporación es sistemáticamente mayor que en resto, siendo consistente con una gran elongación del canal de fisión SL. $Z \sim 50$ presenta un mínimo de evaporación que rápidamente desaparece aumentando E_x, lo que sugiere una configuración compacta en la escisión, guiada por capas cerradas esféricas.

El efecto par-impar en sistemas de Z par muestra una tendencia general descendiente con el parámetro de fisilidad. Esta tendencia no se cumple en el sistema de Z impar ^{239}Np, el cual presenta un efecto par-impar dos veces menor que lo esperado en el caso de Z par. El efecto par-impar muestra un comportamiento logarítmico descendiente con E_x en sistemas de Z par, lo cual revela una saturación en la ruptura de pares a alta E_x. En cambio, ^{239}Np no muestra una evolución significativa, lo que indica que en este caso el efecto par-impar no está dominado por la ruptura de pares sino por el reparto del protón desapareado. Se observa que el efecto par-impar crece con la asimetría de fragmentos a baja E_x, con un máximo local en $Z \sim 50$. A más alta E_x este comportamiento se suaviza y el efecto par-impar se vuelve más uniforme.

El efecto par-impar permite calcular la energía disipada entre la barrera de fisión y el punto de escisión, así como la energía potencial entre el estado fundamental y el punto de escisión para ^{238}U y ^{240}Pu en función de E_x, resultando en ambos casos decrecientes con E_x. Este comportamiento puede ser parcialmente responsable de la evolución en la multiplicidad de neutrones con E_x, siendo diferente para ^{238}U y ^{240}Pu.

En conclusión, este trabajo proporciona nueva información experimental en cuanto a la distribución de fragmentos de actínidos ricos en neutrones en la que distintos observables de la fisión a baja energía muestran

efectos de estructura: la componente asimétrica de los rendimientos de fisión, la polarización de carga en el exceso de neutrones, con un máximo en $Z \sim 50$, el mínimo en la evaporación de neutrones en $Z \sim 50$ y el máximo local del efecto par-impar también en $Z \sim 50$. Se observa que estos efectos decrecen con la energía de excitación del sistema fisionante permaneciendo presentes hasta varias decenas de MeV. Finalmente, parte de las observaciones se han podido verificar con medidas previas experimentales, mientras que la información nueva se ha comparado con códigos recientes, tales como GEF, ayudando a su desarrollo y a la comprensión general de la fisión.

USC
UNIVERSIDADE
DE SANTIAGO
DE COMPOSTELA

Appendix A

Lorentz Formalism

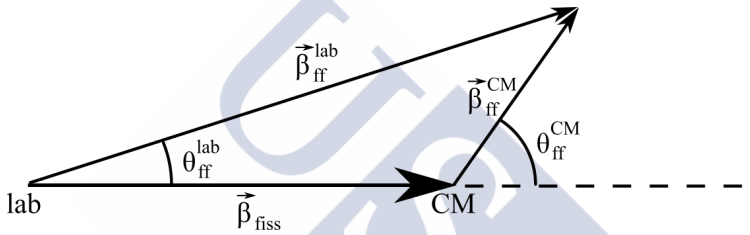

Figure A.1: Schematic view of the relationship between the center-of-mass of the fissioning system (CM) and the laboratory reference frame (lab).

The Lorentz Formalism relates the energy and momentum of a fragment calculated in the laboratory reference frame (lab) with the energy and momentum calculated in the center-of-mass of the fissioning system (CM):

$$\begin{pmatrix} E_{ff} \\ (p_{ff})_{\parallel} \\ (p_{ff})_{\perp} \end{pmatrix}^{CM} = \begin{pmatrix} \gamma_{fiss} & -\beta_{fiss}\gamma_{fiss} & 0 \\ -\beta_{fiss}\gamma_{fiss} & \gamma_{fiss} & 0 \\ 0 & 0 & 1 \end{pmatrix} \begin{pmatrix} E_{ff} \\ (p_{ff})_{\parallel} \\ (p_{ff})_{\perp} \end{pmatrix}^{lab}, \quad \text{(A.1)}$$

where E_{ff} is the total energy of the fragment, $(p_{ff})_{\parallel}$ and $(p_{ff})_{\perp}$ are the parallel and perpendicular components of the fragment momentum with respect to the fissioning system trajectory, and γ_{fiss} is the Lorentz factor of the fissioning system, $\gamma_{fiss} = 1/\sqrt{1-\beta_{fiss}^2}$, being β_{fiss} the velocity of the fissioning system in units of c.

Two independent equations are extracted from the previous tensorial definition by using the energy and the parallel component of the momentum, $(p_{ff})_{\parallel} = p_{ff}\cos(\theta_{ff})$, where θ_{ff} is the polar angle of the fragment with respect to the fissioning system velocity:

$$\begin{aligned} E_{ff}^{CM} &= \gamma_{fiss}\left(E_{ff}^{lab} - \beta_{fiss}p_{ff}^{lab}\cos(\theta_{ff}^{lab})\right), \\ p_{ff}^{CM}\cos(\theta_{ff}^{CM}) &= \gamma_{fiss}\left(p_{ff}^{lab}\cos(\theta_{ff}^{lab}) - \beta_{fiss}E_{ff}^{lab}\right). \end{aligned} \tag{A.2}$$

These equations, together with the relationships between the energy and the momentum with the mass at rest of the fission fragment ($M_{ff}^{(0)}$):

$$\begin{aligned} E_{ff}^{CM} &= \gamma_{ff}^{CM}M_{ff}^{(0)}\,, & p_{ff}^{CM} &= \beta_{ff}^{CM}\gamma_{ff}^{CM}M_{ff}^{(0)}, \\ E_{ff}^{lab} &= \gamma_{ff}^{lab}M_{ff}^{(0)}\,, & p_{ff}^{lab} &= \beta_{ff}^{lab}\gamma_{ff}^{lab}M_{ff}^{(0)}, \end{aligned} \tag{A.3}$$

permit to obtain the velocity of the fragment in CM as a function of the the velocity and the angle of the fragment in *lab* and the velocity of the fissioning system:

$$\gamma_{ff}^{CM} = \gamma_{fiss}\left(\gamma_{ff}^{lab} - \beta_{fiss}\beta_{ff}^{lab}\gamma_{ff}^{lab}\cos(\theta_{ff}^{lab})\right), \tag{A.4}$$

and the angle of the fragment in CM, once γ_{ff}^{CM} is known:

$$\cos\theta_{ff}^{CM} = \frac{\gamma_{fiss}}{\beta_{ff}^{CM}\gamma_{ff}^{CM}}\left(\beta_{ff}^{lab}\gamma_{ff}^{lab}\cos(\theta_{ff}^{lab}) - \beta_{fiss}\gamma_{ff}^{lab}\right), \tag{A.5}$$

Appendix B

Acceptance

The limits of the azimuthal angle (ϕ_{lab}) of fission fragments are presented as a function of the polar angle (θ_{lab}) for different values of the relative magnetic rigidity ($\delta = B\rho/B\rho_0$). Both orientations of VAMOS, 20 and 14 deg respect to the beam axis, are shown.

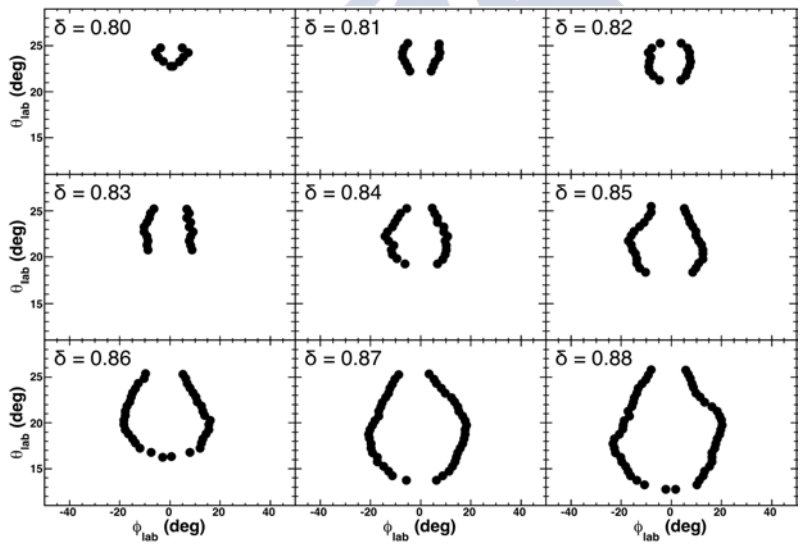

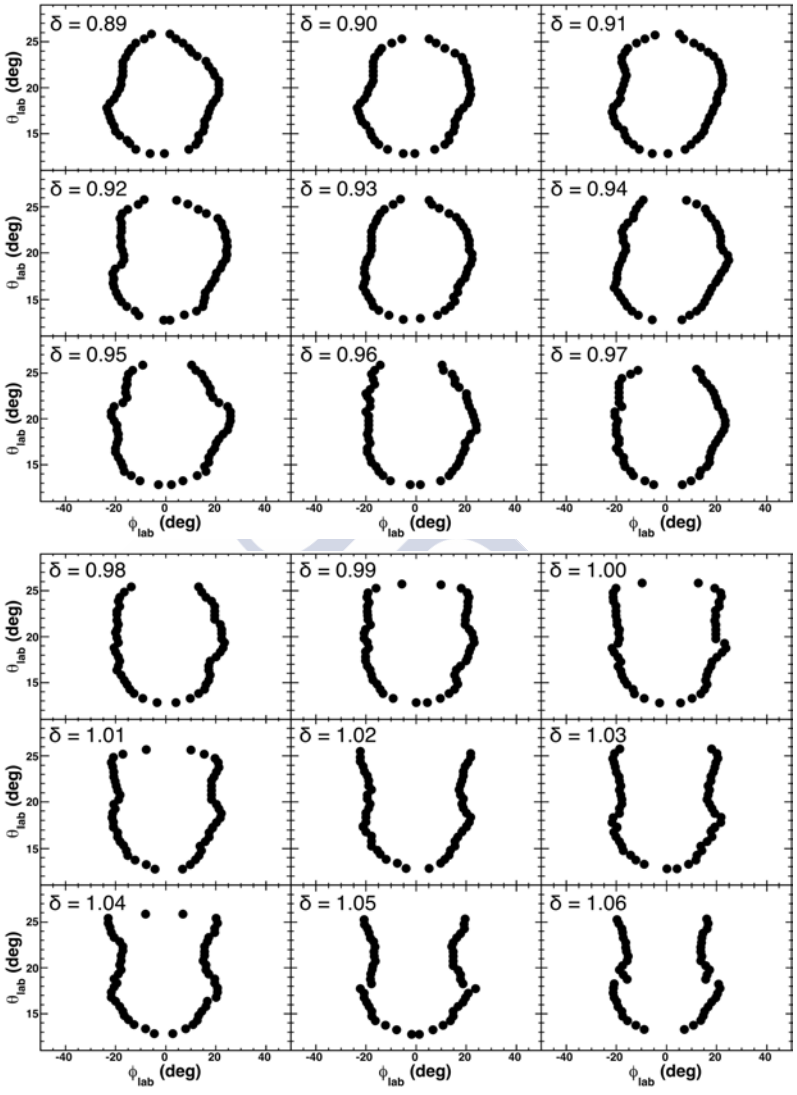
δ = 0.89
δ = 0.90
δ = 0.91
δ = 0.92
δ = 0.93
δ = 0.94
δ = 0.95
δ = 0.96
δ = 0.97
δ = 0.98
δ = 0.99
δ = 1.00
δ = 1.01
δ = 1.02
δ = 1.03
δ = 1.04
δ = 1.05
δ = 1.06
θlab (deg)
ϕlab (deg)

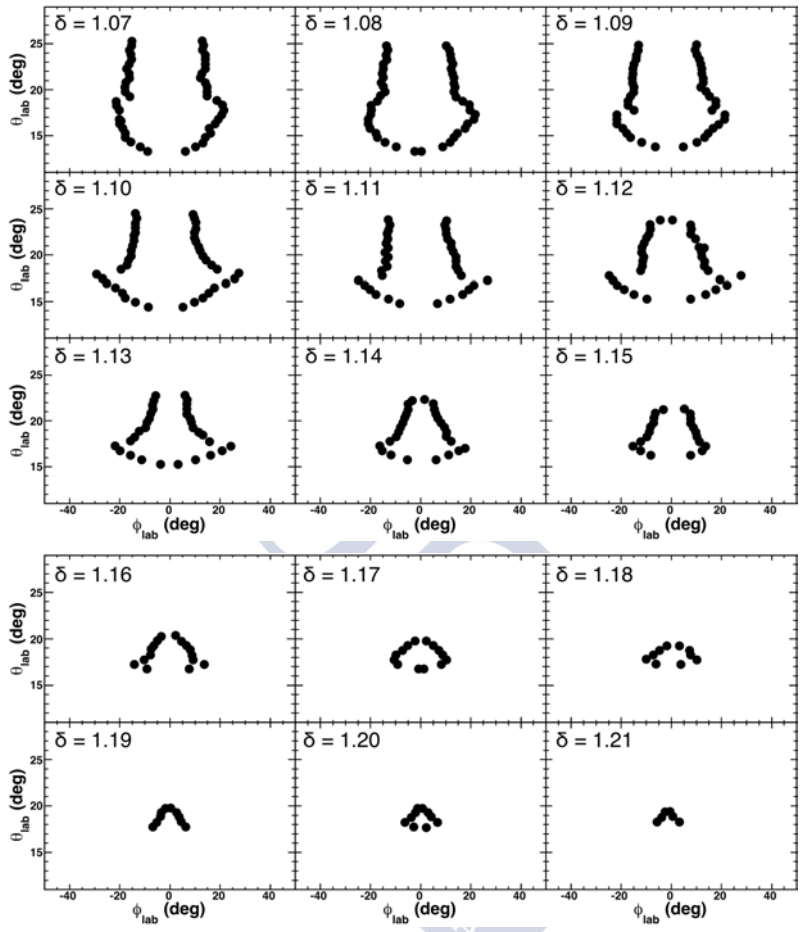

Figure B.1: Limits of ϕ_{lab} as a function of θ_{lab} and δ, with VAMOS at 20 deg.

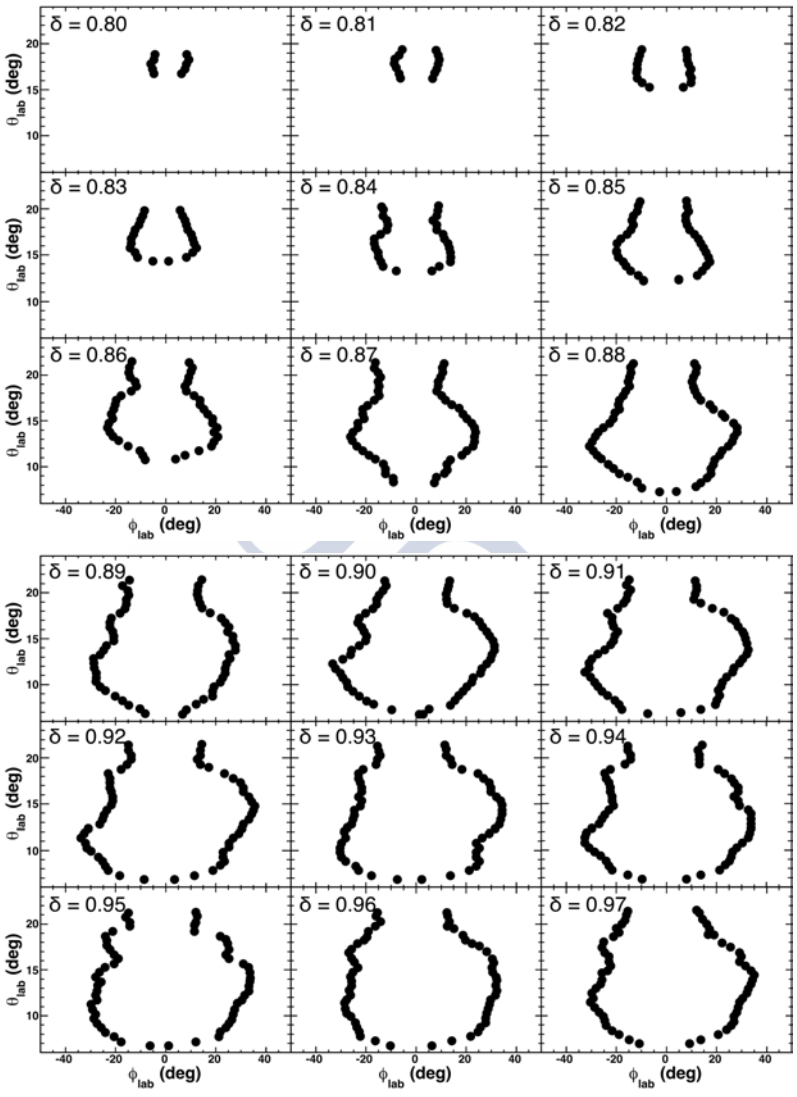
δ = 0.80
δ = 0.81
δ = 0.82
δ = 0.83
δ = 0.84
δ = 0.85
δ = 0.86
δ = 0.87
δ = 0.88
δ = 0.89
δ = 0.90
δ = 0.91
δ = 0.92
δ = 0.93
δ = 0.94
δ = 0.95
δ = 0.96
δ = 0.97
θlab (deg)
φlab (deg)

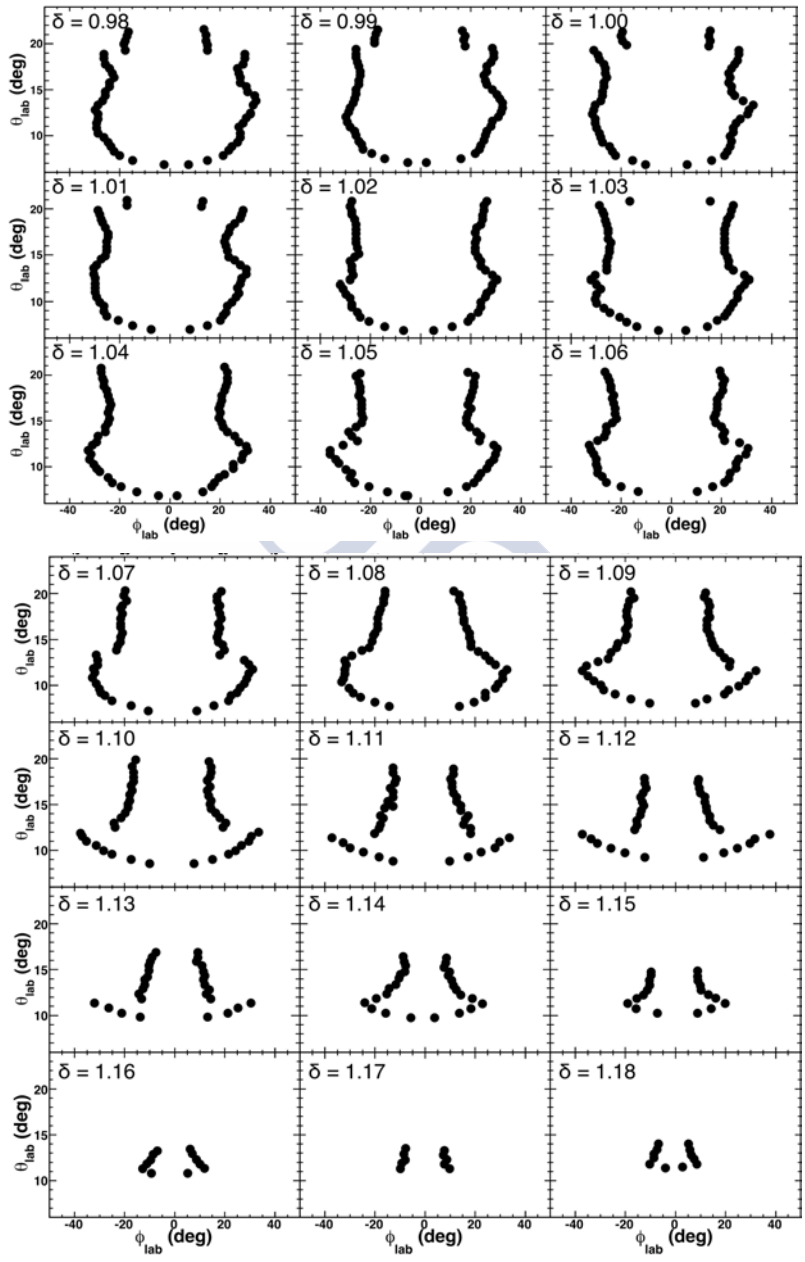

Figure B.2: Limits of ϕ_{lab} as a function of θ_{lab} and δ, with VAMOS at 14 deg.

USC
UNIVERSIDADE
DE SANTIAGO
DE COMPOSTELA

Appendix C

Isotopic Fission Yields

C.1 Isotopic Fission Yields of ^{250}Cf (E_x = 46 MeV)

^{250}Cf (E_x = 46 MeV)			
Z	**A**	**Y(Z,A) (%)**	ε
31	72	0.00179	0.00036
31	73	0.0083	0.0018
31	74	0.0152	0.0031
31	75	0.0460	0.0090
31	76	0.055	0.010
31	77	0.076	0.014
31	78	0.057	0.010
31	79	0.0439	0.0074
31	80	0.0332	0.0052
31	81	0.0159	0.0023
31	82	0.00531	0.00067
31	83	0.00448	0.00063
31	84	0.000569	4.9e-05
32	72	0.00057	0.00034
32	73	0.0050	0.0011
32	74	0.0065	0.0018
32	75	0.0168	0.0036
32	76	0.0261	0.0054
32	77	0.053	0.011
32	78	0.076	0.015
32	79	0.083	0.015
32	80	0.073	0.012
32	81	0.0468	0.0069
32	82	0.0295	0.0034
32	83	0.0168	0.0017
32	84	0.00752	0.00068
32	85	0.00201	0.00040
32	86	0.00049	0.00012
33	74	0.00121	0.00035
33	75	0.00376	0.00093
33	76	0.0061	0.0014
33	77	0.0192	0.0039
33	78	0.0370	0.0072
33	79	0.066	0.012
33	80	0.100	0.016
33	81	0.128	0.018
33	82	0.108	0.012
33	83	0.0819	0.0070
33	84	0.0504	0.0029
33	85	0.0347	0.0019
33	86	0.01375	0.00086
33	87	0.01040	0.00070
33	88	0.00312	0.00031
33	89	0.00078	0.00012
33	90	0.00063	0.00012
34	76	0.00256	0.00067
34	77	0.00340	0.00085
34	78	0.0074	0.0015
34	79	0.0244	0.0045
34	80	0.0502	0.0083
34	81	0.093	0.013
34	82	0.152	0.017
34	83	0.184	0.015
34	84	0.1603	0.0086
34	85	0.1256	0.0063

Z	A	Y(Z,A) (%)	ε	Z	A	Y(Z,A) (%)	ε
34	86	0.0842	0.0039	36	86	0.221	0.010
34	87	0.0564	0.0026	36	87	0.302	0.013
34	88	0.0295	0.0015	36	88	0.331	0.013
34	89	0.01327	0.00080	36	89	0.296	0.012
34	90	0.00557	0.00047	36	90	0.2429	0.0097
34	91	0.00141	0.00025	36	91	0.1643	0.0066
34	92	0.00103	0.00018	36	92	0.0880	0.0037
35	78	0.00156	0.00044	36	93	0.0515	0.0023
35	79	0.00364	0.00085	36	94	0.0243	0.0012
35	80	0.0096	0.0017	36	95	0.01110	0.00068
35	81	0.0244	0.0036	36	96	0.00558	0.00040
35	82	0.0529	0.0060	36	97	0.00215	0.00026
35	83	0.1073	0.0092	36	98	0.00115	0.00017
35	84	0.1764	0.0096	37	82	0.00165	0.00032
35	85	0.238	0.012	37	83	0.00475	0.00062
35	86	0.250	0.011	37	84	0.01041	0.00087
35	87	0.2068	0.0090	37	85	0.0229	0.0015
35	88	0.1461	0.0060	37	86	0.0532	0.0029
35	89	0.0841	0.0037	37	87	0.1254	0.0057
35	90	0.0511	0.0024	37	88	0.2086	0.0085
35	91	0.0279	0.0014	37	89	0.346	0.014
35	92	0.01121	0.00073	37	90	0.409	0.016
35	93	0.00518	0.00043	37	91	0.431	0.017
35	94	0.00149	0.00021	37	92	0.357	0.014
35	95	0.00094	0.00016	37	93	0.269	0.011
36	80	0.00141	0.00037	37	94	0.1578	0.0063
36	81	0.00532	0.00095	37	95	0.0868	0.0036
36	82	0.0103	0.0013	37	96	0.0446	0.0019
36	83	0.0261	0.0024	37	97	0.01944	0.00098
36	84	0.0592	0.0035	37	98	0.00988	0.00060
36	85	0.1175	0.0062	37	99	0.00316	0.00031

Z	**A**	**Y(Z,A) (%)**	ε	**Z**	**A**	**Y(Z,A) (%)**	ε
37	100	0.00153	0.00022	39	98	0.448	0.017
38	85	0.00405	0.00047	39	99	0.297	0.011
38	86	0.01031	0.00083	39	100	0.1433	0.0038
38	87	0.0226	0.0013	39	101	0.0712	0.0020
38	88	0.0498	0.0024	39	102	0.0303	0.0010
38	89	0.1163	0.0051	39	103	0.01439	0.00061
38	90	0.2273	0.0091	39	104	0.00656	0.00041
38	91	0.369	0.014	39	105	0.00248	0.00024
38	92	0.514	0.020	40	90	0.00699	0.00057
38	93	0.587	0.022	40	91	0.01439	0.00088
38	94	0.547	0.021	40	92	0.0305	0.0015
38	95	0.413	0.015	40	93	0.0649	0.0029
38	96	0.278	0.011	40	94	0.1566	0.0063
38	97	0.1563	0.0060	40	95	0.328	0.012
38	98	0.0852	0.0034	40	96	0.559	0.021
38	99	0.0403	0.0017	40	97	0.820	0.030
38	100	0.01788	0.00073	40	98	0.970	0.036
38	101	0.00800	0.00044	40	99	0.874	0.032
38	102	0.00376	0.00030	40	100	0.738	0.018
38	103	0.00186	0.00022	40	101	0.439	0.010
39	87	0.00371	0.00041	40	102	0.2528	0.0062
39	88	0.00825	0.00064	40	103	0.1150	0.0031
39	89	0.0190	0.0012	40	104	0.0529	0.0016
39	90	0.0405	0.0020	40	105	0.02124	0.00083
39	91	0.0900	0.0040	40	106	0.01088	0.00053
39	92	0.1915	0.0077	40	107	0.00477	0.00034
39	93	0.367	0.014	41	92	0.00462	0.00044
39	94	0.570	0.022	41	93	0.01051	0.00068
39	95	0.733	0.027	41	94	0.0212	0.0011
39	96	0.718	0.027	41	95	0.0486	0.0022
39	97	0.634	0.024	41	96	0.1112	0.0045

Z	A	Y(Z,A) (%)	ε	Z	A	Y(Z,A) (%)	ε
41	97	0.2543	0.0097	42	112	0.00616	0.00038
41	98	0.500	0.019	43	97	0.00474	0.00042
41	99	0.827	0.030	43	98	0.01210	0.00074
41	100	1.000	0.024	43	99	0.0238	0.0012
41	101	1.216	0.028	43	100	0.0574	0.0019
41	102	0.995	0.023	43	101	0.1370	0.0037
41	103	0.729	0.017	43	102	0.3234	0.0079
41	104	0.3874	0.0091	43	103	0.687	0.016
41	105	0.2001	0.0049	43	104	1.105	0.025
41	106	0.0849	0.0023	43	105	1.525	0.034
41	107	0.0375	0.0012	43	106	1.532	0.034
41	108	0.01715	0.00069	43	107	1.307	0.029
41	109	0.00795	0.00045	43	108	0.825	0.018
41	110	0.00405	0.00032	43	109	0.524	0.012
42	95	0.00704	0.00054	43	110	0.2346	0.0055
42	96	0.01566	0.00090	43	111	0.1158	0.0029
42	97	0.0358	0.0017	43	112	0.0513	0.0015
42	98	0.0790	0.0033	43	113	0.02184	0.00083
42	99	0.2170	0.0083	43	114	0.01082	0.00053
42	100	0.464	0.011	43	115	0.00552	0.00037
42	101	0.706	0.017	44	100	0.00772	0.00051
42	102	1.260	0.029	44	101	0.01831	0.00084
42	103	1.385	0.031	44	102	0.0411	0.0014
42	104	1.330	0.030	44	103	0.1087	0.0031
42	105	0.925	0.021	44	104	0.2749	0.0066
42	106	0.578	0.013	44	105	0.511	0.012
42	107	0.2923	0.0069	44	106	1.072	0.024
42	108	0.1409	0.0035	44	107	1.467	0.032
42	109	0.0630	0.0018	44	108	1.722	0.037
42	110	0.02675	0.00094	44	109	1.507	0.033
42	111	0.01326	0.00059	44	110	1.160	0.025

Z	**A**	**Y(Z,A) (%)**	ε	**Z**	**A**	**Y(Z,A) (%)**	ε
44	111	0.696	0.015	46	110	0.627	0.014
44	112	0.3806	0.0085	46	111	1.102	0.023
44	113	0.1863	0.0044	46	112	1.657	0.035
44	114	0.0853	0.0022	46	113	1.787	0.037
44	115	0.0395	0.0012	46	114	1.738	0.036
44	116	0.01672	0.00068	46	115	1.253	0.026
44	117	0.00822	0.00046	46	116	0.800	0.017
45	102	0.00561	0.00041	46	117	0.4555	0.0098
45	103	0.01263	0.00065	46	118	0.2420	0.0055
45	104	0.0261	0.0010	46	119	0.1146	0.0028
45	105	0.0616	0.0019	46	120	0.0488	0.0014
45	106	0.1645	0.0042	46	121	0.02218	0.00081
45	107	0.4070	0.0093	46	122	0.01105	0.00053
45	108	0.807	0.018	46	123	0.00620	0.00038
45	109	1.340	0.029	47	108	0.01218	0.00062
45	110	1.704	0.036	47	109	0.0282	0.0011
45	111	1.845	0.039	47	110	0.0665	0.0019
45	112	1.431	0.030	47	111	0.1656	0.0040
45	113	0.996	0.021	47	112	0.4035	0.0089
45	114	0.582	0.013	47	113	0.840	0.018
45	115	0.2983	0.0067	47	114	1.291	0.027
45	116	0.1468	0.0035	47	115	1.792	0.037
45	117	0.0653	0.0018	47	116	1.831	0.038
45	118	0.02796	0.00096	47	117	1.576	0.032
45	119	0.01339	0.00060	47	118	1.107	0.023
45	120	0.00735	0.00042	47	119	0.677	0.014
46	105	0.00801	0.00049	47	120	0.3705	0.0080
46	106	0.01904	0.00083	47	121	0.1914	0.0044
46	107	0.0438	0.0014	47	122	0.0923	0.0023
46	108	0.1053	0.0028	47	123	0.0426	0.0013
46	109	0.2695	0.0063	47	124	0.02036	0.00075

Z	A	Y(Z,A) (%)	ε	Z	A	Y(Z,A) (%)	ε
47	125	0.01042	0.00051	49	120	1.628	0.033
47	126	0.00634	0.00039	49	121	1.722	0.035
48	110	0.00923	0.00051	49	122	1.476	0.030
48	111	0.02094	0.00083	49	123	1.085	0.022
48	112	0.0481	0.0015	49	124	0.698	0.015
48	113	0.1129	0.0029	49	125	0.4028	0.0086
48	114	0.2817	0.0063	49	126	0.2197	0.0049
48	115	0.606	0.013	49	127	0.1172	0.0028
48	116	1.073	0.022	49	128	0.0593	0.0016
48	117	1.556	0.032	49	129	0.03128	0.00098
48	118	1.769	0.036	49	130	0.01761	0.00066
48	119	1.649	0.034	49	131	0.01080	0.00049
48	120	1.297	0.027	49	132	0.00721	0.00038
48	121	0.879	0.018	50	115	0.00902	0.00048
48	122	0.527	0.011	50	116	0.02315	0.00082
48	123	0.2869	0.0063	50	117	0.0529	0.0015
48	124	0.1466	0.0034	50	118	0.1235	0.0030
48	125	0.0679	0.0018	50	119	0.2813	0.0062
48	126	0.0347	0.0011	50	120	0.592	0.012
48	127	0.01790	0.00068	50	121	1.031	0.021
48	128	0.00861	0.00044	50	122	1.432	0.029
48	129	0.00682	0.00038	50	123	1.682	0.034
48	130	0.00548	0.00034	50	124	1.594	0.032
49	112	0.00522	0.00037	50	125	1.303	0.027
49	113	0.01501	0.00065	50	126	0.904	0.019
49	114	0.0305	0.0010	50	127	0.575	0.012
49	115	0.0734	0.0020	50	128	0.3434	0.0073
49	116	0.1750	0.0041	50	129	0.2044	0.0045
49	117	0.4088	0.0089	50	130	0.1154	0.0027
49	118	0.784	0.016	50	131	0.0698	0.0018
49	119	1.223	0.025	50	132	0.0398	0.0011

Z	**A**	**Y(Z,A) (%)**	ε	**Z**	**A**	**Y(Z,A) (%)**	ε
50	133	0.02284	0.00076	52	125	0.503	0.011
50	134	0.01348	0.00053	52	126	0.892	0.018
50	135	0.00773	0.00039	52	127	1.326	0.027
50	136	0.00559	0.00033	52	128	1.505	0.031
51	117	0.00547	0.00037	52	129	1.611	0.033
51	118	0.01517	0.00064	52	130	1.321	0.027
51	119	0.0335	0.0011	52	131	1.012	0.021
51	120	0.0750	0.0020	52	132	0.682	0.014
51	121	0.1734	0.0041	52	133	0.4475	0.0094
51	122	0.3762	0.0082	52	134	0.2859	0.0061
51	123	0.718	0.015	52	135	0.1706	0.0038
51	124	1.146	0.024	52	136	0.0934	0.0023
51	125	1.504	0.031	52	137	0.0521	0.0014
51	126	1.623	0.033	52	138	0.02929	0.00091
51	127	1.488	0.030	52	139	0.01675	0.00060
51	128	1.130	0.023	52	140	0.00884	0.00044
51	129	0.795	0.016	52	141	0.00586	0.00033
51	130	0.493	0.010	53	122	0.00518	0.00033
51	131	0.3051	0.0066	53	123	0.01538	0.00061
51	132	0.1896	0.0042	53	124	0.0323	0.0010
51	133	0.1172	0.0028	53	125	0.0691	0.0018
51	134	0.0650	0.0017	53	126	0.1562	0.0036
51	135	0.0345	0.0010	53	127	0.3402	0.0073
51	136	0.02026	0.00070	53	128	0.579	0.012
51	137	0.01095	0.00048	53	129	1.058	0.022
51	138	0.00617	0.00035	53	130	1.388	0.028
52	120	0.00998	0.00049	53	131	1.563	0.032
52	121	0.02304	0.00083	53	132	1.474	0.030
52	122	0.0489	0.0014	53	133	1.187	0.024
52	123	0.1057	0.0026	53	134	0.838	0.017
52	124	0.2429	0.0054	53	135	0.576	0.012

Z	A	Y(Z,A) (%)	ε	Z	A	Y(Z,A) (%)	ε
53	136	0.3445	0.0073	55	127	0.00415	0.00029
53	137	0.2101	0.0046	55	128	0.01177	0.00052
53	138	0.1237	0.0029	55	129	0.02758	0.00091
53	139	0.0677	0.0017	55	130	0.0629	0.0017
53	140	0.0374	0.0011	55	131	0.1372	0.0032
53	141	0.02011	0.00069	55	132	0.2545	0.0056
53	142	0.01192	0.00049	55	133	0.557	0.012
53	143	0.00717	0.00037	55	134	0.892	0.018
53	144	0.00491	0.00030	55	135	1.242	0.025
54	125	0.00774	0.00041	55	136	1.368	0.028
54	126	0.02013	0.00073	55	137	1.258	0.026
54	127	0.0420	0.0012	55	138	0.931	0.019
54	128	0.0886	0.0022	55	139	0.669	0.014
54	129	0.2084	0.0047	55	140	0.4514	0.0095
54	130	0.4239	0.0090	55	141	0.2802	0.0061
54	131	0.777	0.016	55	142	0.1784	0.0040
54	132	1.131	0.023	55	143	0.1030	0.0025
54	133	1.447	0.029	55	144	0.0581	0.0015
54	134	1.421	0.029	55	145	0.03160	0.00097
54	135	1.244	0.025	55	146	0.01620	0.00062
54	136	0.927	0.019	55	147	0.00994	0.00045
54	137	0.613	0.013	55	148	0.00605	0.00034
54	138	0.3991	0.0085	55	149	0.00442	0.00028
54	139	0.2408	0.0053	56	130	0.00718	0.00038
54	140	0.1498	0.0034	56	131	0.01795	0.00065
54	141	0.0846	0.0021	56	132	0.0345	0.0011
54	142	0.0447	0.0012	56	133	0.0806	0.0020
54	143	0.02426	0.00079	56	134	0.1750	0.0040
54	144	0.01405	0.00055	56	135	0.3760	0.0080
54	145	0.00802	0.00040	56	136	0.646	0.013
54	146	0.00525	0.00031	56	137	0.979	0.020

Z	**A**	**Y(Z,A) (%)**	ε	**Z**	**A**	**Y(Z,A) (%)**	ε
56	138	1.212	0.025	57	149	0.0371	0.0011
56	139	1.133	0.023	57	150	0.02173	0.00074
56	140	0.936	0.019	57	151	0.01068	0.00048
56	141	0.694	0.014	57	152	0.00669	0.00036
56	142	0.541	0.011	57	153	0.00406	0.00027
56	143	0.3449	0.0073	57	154	0.00333	0.00025
56	144	0.2143	0.0047	57	155	0.00320	0.00023
56	145	0.1189	0.0028	58	135	0.00570	0.00033
56	146	0.0652	0.0017	58	136	0.01389	0.00055
56	147	0.0360	0.0011	58	137	0.02851	0.00090
56	148	0.02021	0.00070	58	138	0.0644	0.0017
56	149	0.01061	0.00046	58	139	0.1386	0.0032
56	150	0.00699	0.00037	58	140	0.2594	0.0057
56	151	0.00439	0.00028	58	141	0.4621	0.0097
57	132	0.00306	0.00025	58	142	0.658	0.014
57	133	0.00936	0.00045	58	143	0.675	0.014
57	134	0.02227	0.00077	58	144	0.859	0.018
57	135	0.0509	0.0014	58	145	0.737	0.015
57	136	0.1076	0.0026	58	146	0.560	0.012
57	137	0.2140	0.0048	58	147	0.3881	0.0082
57	138	0.4405	0.0094	58	148	0.2416	0.0053
57	139	0.705	0.015	58	149	0.1406	0.0033
57	140	0.849	0.018	58	150	0.0847	0.0021
57	141	0.972	0.020	58	151	0.0466	0.0013
57	142	0.903	0.019	58	152	0.02314	0.00079
57	143	0.708	0.015	58	153	0.01082	0.00048
57	144	0.560	0.012	58	154	0.00754	0.00038
57	145	0.3674	0.0079	58	155	0.00411	0.00028
57	146	0.2294	0.0051	58	156	0.00348	0.00025
57	147	0.1352	0.0032	59	138	0.00641	0.00035
57	148	0.0709	0.0018	59	139	0.01516	0.00060

Z	A	Y(Z,A) (%)	ε	Z	A	Y(Z,A) (%)	ε
59	140	0.0337	0.0010	60	151	0.3871	0.0083
59	141	0.0723	0.0019	60	152	0.2661	0.0058
59	142	0.1385	0.0032	60	153	0.1576	0.0036
59	143	0.2599	0.0057	60	154	0.0916	0.0023
59	144	0.3830	0.0082	60	155	0.0500	0.0014
59	145	0.590	0.012	60	156	0.02529	0.00084
59	146	0.644	0.013	60	157	0.01337	0.00056
59	147	0.685	0.014	60	158	0.00725	0.00040
59	148	0.511	0.011	60	159	0.00412	0.00029
59	149	0.3897	0.0083	60	160	0.00242	0.00022
59	150	0.2897	0.0063	60	161	0.00234	0.00020
59	151	0.1708	0.0039	60	162	0.00174	0.00019
59	152	0.0900	0.0022	60	163	0.00163	0.00017
59	153	0.0489	0.0014	61	143	0.00341	0.00027
59	154	0.02584	0.00085	61	144	0.00957	0.00045
59	155	0.01344	0.00055	61	145	0.01880	0.00070
59	156	0.00691	0.00037	61	146	0.0378	0.0011
59	157	0.00400	0.00027	61	147	0.0753	0.0020
59	158	0.00295	0.00024	61	148	0.1306	0.0031
59	159	0.00235	0.00020	61	149	0.2363	0.0053
60	140	0.00269	0.00023	61	150	0.3146	0.0069
60	141	0.00677	0.00038	61	151	0.4213	0.0090
60	142	0.01670	0.00065	61	152	0.4146	0.0089
60	143	0.0355	0.0011	61	153	0.3467	0.0075
60	144	0.0710	0.0019	61	154	0.2395	0.0053
60	145	0.1369	0.0032	61	155	0.1548	0.0036
60	146	0.2405	0.0053	61	156	0.0871	0.0022
60	147	0.3812	0.0082	61	157	0.0481	0.0014
60	148	0.494	0.010	61	158	0.02492	0.00094
60	149	0.532	0.011	61	159	0.01283	0.00059
60	150	0.503	0.011	61	160	0.00730	0.00041

Z	**A**	**Y(Z,A) (%)**	ε	**Z**	**A**	**Y(Z,A) (%)**	ε
61	161	0.00353	0.00027	63	152	0.0440	0.0013
61	162	0.00246	0.00022	63	153	0.0821	0.0021
61	163	0.00214	0.00020	63	154	0.1232	0.0030
61	164	0.00160	0.00017	63	155	0.1879	0.0043
61	165	0.00155	0.00016	63	156	0.2106	0.0048
62	145	0.00146	0.00017	63	157	0.2092	0.0047
62	146	0.00402	0.00029	63	158	0.1670	0.0048
62	147	0.00918	0.00046	63	159	0.1182	0.0035
62	148	0.02041	0.00075	63	160	0.0759	0.0023
62	149	0.0434	0.0013	63	161	0.0450	0.0015
62	150	0.0821	0.0021	63	162	0.02383	0.00092
62	151	0.1271	0.0030	63	163	0.01278	0.00060
62	152	0.2331	0.0052	63	164	0.00686	0.00040
62	153	0.2819	0.0062	63	165	0.00354	0.00027
62	154	0.3295	0.0071	63	166	0.00232	0.00021
62	155	0.2820	0.0062	63	167	0.00149	0.00016
62	156	0.2107	0.0047	63	168	0.00128	0.00015
62	157	0.1429	0.0033	63	169	0.00079	0.00013
62	158	0.0840	0.0025	63	170	0.00069	0.00011
62	159	0.0485	0.0016	64	150	0.00046	9.3e-05
62	160	0.02518	0.00096	64	151	0.00277	0.00022
62	161	0.01468	0.00064	64	152	0.00616	0.00036
62	162	0.00780	0.00042	64	153	0.01337	0.00057
62	163	0.00370	0.00028	64	154	0.02731	0.00092
62	164	0.00206	0.00020	64	155	0.0509	0.0015
62	165	0.00145	0.00017	64	156	0.0829	0.0021
62	166	0.00115	0.00015	64	157	0.1157	0.0028
63	148	0.00206	0.00020	64	158	0.1416	0.0041
63	149	0.00537	0.00032	64	159	0.1372	0.0040
63	150	0.01067	0.00049	64	160	0.1244	0.0037
63	151	0.02121	0.00076	64	161	0.0943	0.0028

Z	A	Y(Z,A) (%)	ε	Z	A	Y(Z,A) (%)	ε
64	162	0.0673	0.0021	66	157	0.00488	0.00032
64	163	0.0415	0.0014	66	158	0.01084	0.00054
64	164	0.02485	0.00093	66	159	0.02269	0.00091
64	165	0.01329	0.00059	66	160	0.0358	0.0013
64	166	0.00703	0.00039	66	161	0.0545	0.0018
64	167	0.00363	0.00026	66	162	0.0623	0.0020
64	168	0.00173	0.00019	66	163	0.0643	0.0021
64	169	0.00131	0.00016	66	164	0.0533	0.0017
64	170	0.00071	0.00012	66	165	0.0452	0.0015
65	153	0.00084	0.00012	66	166	0.0369	0.0013
65	154	0.00319	0.00025	66	167	0.0293	0.0011
65	155	0.00794	0.00041	66	168	0.02016	0.00099
65	156	0.01695	0.00068	66	169	0.01472	0.00082
65	157	0.0337	0.0011	66	170	0.00979	0.00060
65	158	0.0561	0.0019	66	171	0.00657	0.00053
65	159	0.0752	0.0024	66	172	0.00267	0.00027
65	160	0.0862	0.0027	66	173	0.00205	0.00026
65	161	0.0924	0.0028	66	174	0.00097	0.00019
65	162	0.0816	0.0025	66	175	0.000361	9.4e-05
65	163	0.0678	0.0021	66	176	0.000215	6.8e-05
65	164	0.0504	0.0016	67	158	0.00067	0.00012
65	165	0.0364	0.0012	67	159	0.00278	0.00025
65	166	0.02483	0.00093	67	160	0.00684	0.00042
65	167	0.01392	0.00062	67	161	0.01535	0.00070
65	168	0.00801	0.00049	67	162	0.02500	0.00098
65	169	0.00427	0.00034	67	163	0.0367	0.0013
65	170	0.00227	0.00023	67	164	0.0434	0.0015
65	171	0.00105	0.00016	67	165	0.0408	0.0014
65	172	0.00070	0.00011	67	166	0.0349	0.0013
66	155	0.000356	8.3e-05	67	167	0.0269	0.0010
66	156	0.00119	0.00017	67	168	0.0218	0.0011

Z	**A**	**Y(Z,A) (%)**	ε
67	169	0.01786	0.00099
67	170	0.01483	0.00086
67	171	0.01161	0.00087
67	172	0.00938	0.00074
67	173	0.00686	0.00074
67	174	0.00385	0.00063
67	175	0.00258	0.00041

C.2 Isotopic Fission Yields of ^{244}Cm (E_x = 23 MeV)

^{244}Cm (E_x = 23 MeV)			
Z	**A**	**Y(Z,A) (%)**	ε
34	84	0.06	0.13
34	85	0.25	0.17
35	86	0.56	0.19
35	87	0.17	0.15
35	88	0.25	0.14
36	85	0.16	0.10
36	86	0.18	0.14
36	87	0.23	0.16
36	88	0.63	0.20
36	89	0.71	0.27
36	90	0.82	0.19
36	91	0.16	0.11
36	92	0.42	0.17
37	87	0.043	0.086
37	88	0.12	0.12
37	89	0.074	0.081
37	90	0.54	0.21
37	91	0.46	0.20
37	92	0.37	0.18
37	93	0.19	0.10
37	94	0.36	0.18
37	95	0.106	0.095
37	96	0.051	0.065
38	88	0.084	0.077
38	89	0.16	0.11
38	90	0.18	0.13
38	91	0.59	0.18
38	92	0.62	0.20
38	93	1.37	0.29
38	94	1.20	0.25
38	95	0.58	0.19
38	96	0.68	0.20
38	97	0.48	0.17
38	98	0.16	0.10
38	99	0.044	0.058
39	92	0.047	0.066
39	93	0.27	0.14
39	94	0.38	0.15
39	95	0.91	0.24
39	96	1.31	0.29
39	97	1.67	0.32
39	98	1.03	0.23
39	99	1.01	0.21
39	100	0.22	0.12
39	101	0.118	0.076
40	95	0.20	0.12
40	96	0.41	0.13
40	97	0.79	0.22
40	98	1.31	0.27
40	99	1.78	0.32
40	100	2.02	0.30
40	101	0.98	0.21
40	102	0.66	0.20
40	103	0.59	0.17
40	104	0.303	0.088

Z	**A**	**Y(Z,A) (%)**	ε	**Z**	**A**	**Y(Z,A) (%)**	ε
40	105	0.070	0.050	43	108	1.15	0.25
41	97	0.040	0.057	43	109	1.05	0.22
41	98	0.22	0.11	43	110	0.58	0.15
41	99	0.87	0.24	43	111	0.13	0.081
41	100	1.15	0.26	43	112	0.116	0.065
41	101	2.07	0.32	44	104	0.177	0.091
41	102	2.04	0.33	44	105	0.31	0.14
41	103	1.80	0.28	44	106	0.77	0.21
41	104	1.24	0.23	44	107	1.65	0.28
41	105	0.45	0.15	44	108	2.23	0.34
41	106	0.147	0.098	44	109	2.22	0.32
41	107	0.076	0.068	44	110	2.15	0.32
42	99	0.082	0.078	44	111	0.91	0.23
42	100	0.57	0.18	44	112	0.51	0.18
42	101	0.82	0.21	44	113	0.46	0.13
42	102	1.95	0.31	44	114	0.111	0.078
42	103	2.11	0.32	44	115	0.070	0.063
42	104	2.26	0.36	45	107	0.112	0.089
42	105	1.50	0.30	45	108	0.63	0.19
42	106	1.21	0.22	45	109	0.81	0.23
42	107	0.59	0.18	45	110	1.58	0.29
42	108	0.21	0.11	45	111	1.50	0.29
42	109	0.248	0.082	45	112	1.67	0.27
42	110	0.079	0.047	45	113	1.70	0.28
43	101	0.082	0.076	45	114	0.80	0.22
43	102	0.32	0.13	45	115	0.42	0.14
43	103	0.46	0.17	45	116	0.271	0.099
43	104	1.47	0.28	45	117	0.145	0.076
43	105	2.26	0.36	46	109	0.039	0.050
43	106	1.97	0.34	46	110	0.33	0.16
43	107	2.76	0.36	46	111	1.17	0.23

Z	A	Y(Z,A) (%)	ε	Z	A	Y(Z,A) (%)	ε
46	112	0.69	0.21	49	117	0.151	0.083
46	113	1.31	0.26	49	118	0.167	0.058
46	114	1.39	0.28	49	119	0.41	0.15
46	115	0.65	0.19	49	120	0.69	0.18
46	116	0.63	0.18	49	121	0.92	0.20
46	117	0.31	0.14	49	122	1.42	0.23
46	118	0.41	0.13	49	123	0.64	0.18
46	119	0.098	0.060	49	124	0.69	0.18
46	120	0.028	0.042	49	125	0.39	0.14
47	112	0.167	0.083	49	126	0.29	0.12
47	113	0.36	0.13	49	127	0.068	0.063
47	114	0.75	0.20	50	118	0.029	0.040
47	115	0.76	0.21	50	119	0.052	0.056
47	116	0.85	0.23	50	120	0.154	0.078
47	117	0.99	0.24	50	121	0.27	0.13
47	118	0.88	0.21	50	122	0.40	0.15
47	119	0.36	0.14	50	123	0.61	0.18
47	120	0.43	0.13	50	124	0.75	0.19
47	121	0.23	0.10	50	125	1.01	0.23
47	122	0.021	0.041	50	126	1.12	0.21
48	115	0.032	0.045	50	127	0.71	0.18
48	116	0.77	0.19	50	128	0.46	0.14
48	117	0.85	0.21	50	129	0.57	0.14
48	118	0.94	0.21	50	130	0.48	0.13
48	119	1.11	0.23	50	131	0.042	0.048
48	120	0.93	0.19	51	122	0.048	0.053
48	121	0.96	0.18	51	123	0.42	0.11
48	122	0.42	0.13	51	124	0.31	0.10
48	123	0.35	0.11	51	125	0.90	0.19
48	124	0.102	0.039	51	126	1.00	0.20
48	125	0.027	0.039	51	127	1.41	0.22

Z	**A**	**Y(Z,A) (%)**	ε	**Z**	**A**	**Y(Z,A) (%)**	ε
51	128	1.04	0.20	53	136	0.77	0.17
51	129	1.42	0.23	53	137	0.37	0.12
51	130	1.04	0.20	53	138	0.292	0.096
51	131	0.71	0.16	53	139	0.163	0.071
51	132	0.59	0.14	53	140	0.022	0.032
51	133	0.27	0.11	54	131	0.36	0.11
51	134	0.172	0.081	54	132	0.52	0.15
51	135	0.111	0.057	54	133	1.35	0.24
52	125	0.27	0.11	54	134	1.16	0.22
52	126	0.37	0.13	54	135	2.04	0.28
52	127	0.50	0.15	54	136	1.67	0.25
52	128	1.07	0.20	54	137	1.51	0.24
52	129	1.31	0.23	54	138	0.85	0.18
52	130	1.63	0.26	54	139	0.59	0.15
52	131	1.84	0.25	54	140	0.33	0.10
52	132	1.71	0.26	54	141	0.190	0.083
52	133	0.92	0.19	54	142	0.079	0.062
52	134	0.83	0.17	55	132	0.043	0.048
52	135	0.81	0.16	55	133	0.221	0.082
52	136	0.145	0.057	55	134	0.49	0.11
52	137	0.176	0.079	55	135	1.23	0.22
53	126	0.035	0.036	55	136	1.21	0.22
53	127	0.26	0.11	55	137	2.20	0.28
53	128	0.145	0.079	55	138	1.47	0.23
53	129	0.48	0.15	55	139	1.59	0.23
53	130	0.86	0.20	55	140	1.06	0.20
53	131	1.42	0.22	55	141	0.72	0.16
53	132	1.84	0.27	55	142	0.69	0.14
53	133	1.81	0.27	55	143	0.065	0.054
53	134	1.66	0.25	56	135	0.027	0.033
53	135	1.28	0.22	56	136	0.100	0.056

Z	A	Y(Z,A) (%)	ε	Z	A	Y(Z,A) (%)	ε
56	137	0.52	0.15	58	144	0.64	0.15
56	138	1.31	0.22	58	145	0.94	0.17
56	139	1.39	0.22	58	146	0.99	0.18
56	140	1.31	0.21	58	147	0.57	0.14
56	141	0.85	0.19	58	148	0.61	0.14
56	142	1.24	0.21	58	149	0.259	0.094
56	143	0.86	0.18	58	150	0.081	0.059
56	144	0.43	0.13	58	151	0.073	0.059
56	145	0.30	0.10	58	152	0.021	0.029
56	146	0.099	0.068	59	142	0.026	0.044
56	147	0.088	0.043	59	143	0.043	0.044
56	148	0.059	0.042	59	144	0.045	0.053
56	149	0.030	0.030	59	145	0.209	0.086
57	136	0.032	0.033	59	146	0.227	0.096
57	137	0.111	0.056	59	147	0.24	0.10
57	138	0.255	0.072	59	148	0.59	0.15
57	139	0.175	0.096	59	149	0.405	0.099
57	140	0.46	0.13	59	150	0.43	0.13
57	141	0.70	0.17	59	151	0.198	0.089
57	142	0.98	0.19	59	152	0.090	0.051
57	143	1.08	0.20	59	153	0.054	0.059
57	144	1.01	0.20	59	154	0.021	0.029
57	145	0.74	0.18	60	145	0.057	0.053
57	146	0.44	0.12	60	146	0.114	0.053
57	147	0.168	0.080	60	147	0.086	0.060
57	148	0.103	0.052	60	148	0.238	0.095
57	149	0.023	0.030	60	149	0.46	0.12
58	140	0.042	0.045	60	150	0.26	0.10
58	141	0.127	0.063	60	151	0.35	0.12
58	142	0.55	0.13	60	152	0.308	0.098
58	143	0.45	0.12	60	153	0.155	0.072

Z	A	Y(Z,A) (%)	ε
60	154	0.162	0.077
60	155	0.017	0.029
60	156	0.023	0.029
61	148	0.048	0.042
61	149	0.141	0.060
61	150	0.123	0.066
61	151	0.101	0.066
61	152	0.25	0.10
61	153	0.109	0.077
61	154	0.185	0.082
61	155	0.106	0.065
61	156	0.066	0.050
61	157	0.047	0.050
61	158	0.013	0.029
62	151	0.016	0.030
62	152	0.036	0.042
62	153	0.108	0.059
62	154	0.087	0.058
62	155	0.182	0.082
62	156	0.096	0.058
62	157	0.109	0.058
62	158	0.013	0.029
63	155	0.038	0.050
63	156	0.013	0.029
63	157	0.079	0.058
63	158	0.053	0.050
63	159	0.020	0.029
63	160	0.070	0.050
63	161	0.012	0.029
64	158	0.053	0.041
64	159	0.013	0.029
64	160	0.074	0.050
64	161	0.014	0.029

C.3 Isotopic Fission Yields of ^{240}Pu (E_x = 10.7 MeV)

^{240}Pu (E_x = 10.7 MeV)			
Z	**A**	**Y(Z,A) (%)**	ε
32	82	0.123	0.048
32	83	0.061	0.032
33	83	0.097	0.060
33	84	0.058	0.035
34	81	0.021	0.026
34	82	0.081	0.035
34	83	0.158	0.054
34	84	0.438	0.081
34	85	0.259	0.065
34	86	0.212	0.058
34	87	0.153	0.051
34	88	0.162	0.041
34	89	0.059	0.018
35	83	0.011	0.021
35	84	0.249	0.065
35	85	0.121	0.059
35	86	0.54	0.10
35	87	0.55	0.11
35	88	0.488	0.087
35	89	0.406	0.074
35	90	0.204	0.053
35	91	0.055	0.030
35	92	0.018	0.020
36	85	0.065	0.035
36	86	0.126	0.048
36	87	0.417	0.087
36	88	0.70	0.11
36	89	1.00	0.13
36	90	1.11	0.13
36	91	0.86	0.11
36	92	0.158	0.052
36	93	0.168	0.043
36	94	0.095	0.032
36	95	0.033	0.021
37	85	0.013	0.016
37	86	0.044	0.022
37	87	0.065	0.030
37	88	0.108	0.043
37	89	0.501	0.089
37	90	0.81	0.11
37	91	1.12	0.13
37	92	1.24	0.14
37	93	1.28	0.13
37	94	0.855	0.096
37	95	0.395	0.070
37	96	0.246	0.043
37	97	0.062	0.028
37	98	0.054	0.015
37	99	0.027	0.014
37	100	0.019	0.010
38	89	0.036	0.026
38	90	0.169	0.053
38	91	0.432	0.075
38	92	0.721	0.097
38	93	2.12	0.17

Z	**A**	**Y(Z,A) (%)**	ε	**Z**	**A**	**Y(Z,A) (%)**	ε
38	94	2.30	0.17	40	105	0.124	0.029
38	95	2.16	0.17	40	106	0.048	0.016
38	96	1.60	0.13	41	96	0.048	0.027
38	97	1.04	0.11	41	97	0.092	0.036
38	98	0.546	0.073	41	98	0.471	0.071
38	99	0.227	0.044	41	99	1.07	0.11
38	100	0.046	0.021	41	100	1.54	0.13
39	92	0.091	0.035	41	101	2.40	0.16
39	93	0.412	0.073	41	102	2.53	0.16
39	94	1.02	0.11	41	103	2.64	0.15
39	95	1.50	0.14	41	104	1.59	0.12
39	96	1.93	0.15	41	105	0.805	0.084
39	97	2.38	0.18	41	106	0.344	0.053
39	98	1.77	0.15	41	107	0.094	0.025
39	99	1.47	0.13	42	98	0.050	0.021
39	100	1.013	0.095	42	99	0.131	0.036
39	101	0.493	0.062	42	100	0.262	0.049
39	102	0.148	0.037	42	101	0.620	0.080
39	103	0.049	0.024	42	102	1.45	0.12
39	104	0.037	0.017	42	103	2.47	0.15
40	94	0.032	0.023	42	104	3.08	0.17
40	95	0.269	0.059	42	105	2.39	0.16
40	96	0.739	0.091	42	106	1.76	0.13
40	97	1.28	0.12	42	107	0.915	0.086
40	98	1.95	0.15	42	108	0.425	0.058
40	99	2.70	0.19	42	109	0.184	0.036
40	100	2.99	0.18	42	110	0.044	0.018
40	101	2.05	0.14	43	102	0.091	0.035
40	102	1.49	0.11	43	103	0.312	0.059
40	103	0.640	0.073	43	104	0.794	0.090
40	104	0.426	0.053	43	105	1.41	0.12

Z	**A**	**Y(Z,A) (%)**	ε	**Z**	**A**	**Y(Z,A) (%)**	ε
43	106	1.78	0.13	46	111	0.042	0.026
43	107	1.83	0.13	46	112	0.056	0.030
43	108	1.17	0.11	46	113	0.078	0.036
43	109	0.667	0.081	46	114	0.123	0.043
43	110	0.243	0.049	46	115	0.077	0.036
43	111	0.116	0.028	46	116	0.074	0.029
43	112	0.048	0.021	46	117	0.053	0.026
44	103	0.025	0.017	46	118	0.022	0.015
44	104	0.042	0.024	46	119	0.014	0.014
44	105	0.210	0.050	46	120	0.0053	0.0094
44	106	0.464	0.069	46	121	0.0041	0.0065
44	107	0.791	0.092	47	111	0.0028	0.0078
44	108	0.96	0.10	47	112	0.030	0.011
44	109	0.994	0.096	47	113	0.020	0.020
44	110	0.673	0.083	47	114	0.011	0.023
44	111	0.514	0.065	47	115	0.022	0.026
44	112	0.184	0.043	47	116	0.144	0.041
44	113	0.102	0.030	47	117	0.108	0.033
44	114	0.010	0.013	47	118	0.091	0.033
45	106	0.022	0.015	47	119	0.112	0.031
45	107	0.011	0.017	47	120	0.058	0.021
45	108	0.115	0.041	47	121	0.028	0.016
45	109	0.127	0.045	47	122	0.017	0.013
45	110	0.185	0.047	47	123	0.0049	0.0063
45	111	0.300	0.062	48	117	0.011	0.022
45	112	0.187	0.046	48	118	0.061	0.029
45	113	0.225	0.050	48	119	0.068	0.032
45	114	0.096	0.034	48	120	0.104	0.032
45	115	0.042	0.023	48	121	0.076	0.030
45	116	0.003	0.010	48	122	0.110	0.035
46	110	0.005	0.018	48	123	0.110	0.032

Z	**A**	**Y(Z,A) (%)**	ε	**Z**	**A**	**Y(Z,A) (%)**	ε
48	124	0.066	0.021	50	129	0.905	0.074
48	125	0.088	0.024	50	130	0.915	0.074
48	126	0.0063	0.0084	50	131	0.633	0.062
49	117	0.0005	0.0093	50	132	0.404	0.050
49	118	0.003	0.015	50	133	0.201	0.036
49	119	0.002	0.016	50	134	0.070	0.021
49	120	0.016	0.020	50	135	0.038	0.013
49	121	0.053	0.027	50	136	0.0113	0.0089
49	122	0.066	0.030	51	120	0.020	0.012
49	123	0.097	0.034	51	121	0.035	0.015
49	124	0.139	0.039	51	122	0.021	0.012
49	125	0.146	0.037	51	123	0.019	0.014
49	126	0.224	0.042	51	124	0.027	0.019
49	127	0.187	0.041	51	125	0.033	0.024
49	128	0.145	0.034	51	126	0.120	0.034
49	129	0.180	0.035	51	127	0.252	0.045
49	130	0.066	0.026	51	128	0.510	0.060
49	131	0.060	0.019	51	129	0.911	0.081
49	132	0.027	0.017	51	130	1.397	0.093
49	133	0.026	0.011	51	131	1.53	0.10
49	134	0.0030	0.0054	51	132	1.61	0.10
50	119	0.009	0.011	51	133	1.161	0.084
50	120	0.021	0.015	51	134	0.623	0.063
50	121	0.013	0.019	51	135	0.333	0.045
50	122	0.001	0.016	51	136	0.167	0.030
50	123	0.029	0.024	51	137	0.041	0.016
50	124	0.093	0.031	51	138	0.027	0.012
50	125	0.210	0.043	52	125	0.015	0.015
50	126	0.469	0.057	52	126	0.008	0.014
50	127	0.686	0.068	52	127	0.055	0.024
50	128	0.822	0.071	52	128	0.177	0.032

Z	**A**	**Y(Z,A) (%)**	ε	**Z**	**A**	**Y(Z,A) (%)**	ε
52	129	0.341	0.048	54	135	1.50	0.10
52	130	0.895	0.076	54	136	2.20	0.12
52	131	1.57	0.10	54	137	2.48	0.12
52	132	2.24	0.12	54	138	2.57	0.13
52	133	2.78	0.13	54	139	1.94	0.11
52	134	2.67	0.13	54	140	1.421	0.090
52	135	1.680	0.095	54	141	0.820	0.069
52	136	1.105	0.078	54	142	0.375	0.045
52	137	0.528	0.053	54	143	0.174	0.032
52	138	0.213	0.035	54	144	0.090	0.023
52	139	0.080	0.021	54	145	0.061	0.019
52	140	0.054	0.016	55	133	0.023	0.016
53	128	0.018	0.015	55	134	0.096	0.028
53	129	0.061	0.022	55	135	0.227	0.037
53	130	0.082	0.028	55	136	0.568	0.060
53	131	0.423	0.056	55	137	1.156	0.087
53	132	0.826	0.071	55	138	1.47	0.10
53	133	1.63	0.10	55	139	2.04	0.11
53	134	2.27	0.12	55	140	1.82	0.11
53	135	2.85	0.14	55	141	1.94	0.11
53	136	1.96	0.12	55	142	1.231	0.087
53	137	1.77	0.10	55	143	0.858	0.074
53	138	1.197	0.084	55	144	0.498	0.052
53	139	0.732	0.066	55	145	0.259	0.037
53	140	0.372	0.045	55	146	0.126	0.026
53	141	0.156	0.030	55	147	0.048	0.017
53	142	0.050	0.017	56	135	0.017	0.011
54	131	0.007	0.015	56	136	0.070	0.022
54	132	0.117	0.028	56	137	0.138	0.029
54	133	0.316	0.050	56	138	0.244	0.041
54	134	0.898	0.072	56	139	0.715	0.065

Z	**A**	**Y(Z,A) (%)**	ε	**Z**	**A**	**Y(Z,A) (%)**	ε
56	140	1.212	0.084	58	145	0.570	0.060
56	141	1.62	0.10	58	146	0.896	0.074
56	142	1.90	0.11	58	147	0.964	0.075
56	143	1.99	0.11	58	148	0.885	0.074
56	144	1.604	0.098	58	149	0.603	0.059
56	145	1.052	0.075	58	150	0.368	0.046
56	146	0.481	0.052	58	151	0.188	0.032
56	147	0.312	0.041	58	152	0.063	0.019
56	148	0.095	0.024	58	153	0.026	0.014
56	149	0.063	0.018	58	154	0.023	0.012
56	150	0.022	0.011	59	142	0.0030	0.0068
57	138	0.017	0.012	59	143	0.014	0.012
57	139	0.053	0.021	59	144	0.039	0.016
57	140	0.064	0.024	59	145	0.068	0.022
57	141	0.289	0.046	59	146	0.139	0.029
57	142	0.584	0.064	59	147	0.230	0.039
57	143	0.857	0.074	59	148	0.328	0.048
57	144	1.155	0.085	59	149	0.521	0.057
57	145	1.271	0.089	59	150	0.456	0.054
57	146	1.226	0.084	59	151	0.460	0.052
57	147	0.801	0.068	59	152	0.282	0.042
57	148	0.423	0.050	59	153	0.127	0.028
57	149	0.232	0.035	59	154	0.048	0.019
57	150	0.097	0.023	59	155	0.032	0.015
57	151	0.050	0.017	59	156	0.018	0.011
57	152	0.018	0.011	59	157	0.0117	0.0076
58	140	0.0081	0.0098	59	158	0.0053	0.0062
58	141	0.0069	0.0097	60	146	0.009	0.011
58	142	0.035	0.018	60	147	0.015	0.012
58	143	0.144	0.033	60	148	0.074	0.021
58	144	0.344	0.044	60	149	0.107	0.028

Z	**A**	**Y(Z,A) (%)**	ε
60	150	0.211	0.037
60	151	0.292	0.045
60	152	0.385	0.047
60	153	0.203	0.037
60	154	0.153	0.029
60	155	0.093	0.022
60	156	0.019	0.011
60	157	0.0209	0.0099
60	158	0.0066	0.0062
61	149	0.0091	0.0092
61	150	0.0054	0.0091
61	151	0.026	0.016
61	152	0.079	0.025
61	153	0.115	0.029
61	154	0.112	0.029
61	155	0.108	0.026
61	156	0.060	0.020
61	157	0.023	0.013
61	158	0.028	0.014
61	159	0.020	0.011
61	160	0.0019	0.0044
62	152	0.0009	0.0078
62	153	0.003	0.010
62	154	0.033	0.016
62	155	0.017	0.013
62	156	0.054	0.019
62	157	0.055	0.018
62	158	0.027	0.015
62	159	0.013	0.011
62	160	0.0068	0.0087
62	161	0.0053	0.0044

C.4 Isotopic Fission Yields of ^{239}Np (E_x = 7.5 MeV)

^{239}Np (E_x = 7.5 MeV)			
Z	**A**	**Y(Z,A) (%)**	ε
32	82	0.116	0.086
32	83	0.221	0.083
33	83	0.48	0.17
34	84	0.25	0.12
34	85	0.46	0.14
34	86	0.50	0.13
34	87	0.028	0.049
34	88	0.29	0.12
34	89	0.319	0.047
34	90	0.121	0.061
35	83	0.029	0.054
35	84	0.025	0.052
35	85	0.18	0.11
35	86	0.32	0.14
35	87	0.53	0.18
35	88	0.67	0.16
35	89	1.10	0.17
35	90	0.221	0.099
35	91	0.28	0.10
35	92	0.054	0.037
36	86	0.130	0.061
36	87	0.42	0.15
36	88	0.47	0.15
36	89	1.09	0.23
36	90	1.79	0.25
36	91	1.84	0.23
36	92	1.02	0.18
36	93	0.56	0.12
36	94	0.254	0.083
37	88	0.092	0.073
37	89	0.31	0.12
37	90	0.86	0.20
37	91	1.77	0.23
37	92	1.71	0.25
37	93	2.37	0.28
37	94	1.34	0.19
37	95	1.05	0.16
37	96	0.414	0.094
37	97	0.078	0.038
37	98	0.040	0.038
38	90	0.080	0.064
38	91	0.40	0.12
38	92	0.75	0.17
38	93	1.39	0.21
38	94	2.44	0.28
38	95	2.51	0.29
38	96	2.10	0.25
38	97	1.59	0.20
38	98	0.59	0.12
38	99	0.373	0.090
38	100	0.214	0.063
38	101	0.043	0.023
39	91	0.037	0.042
39	92	0.104	0.057
39	93	0.266	0.089

Z	A	Y(Z,A) (%)	ε	Z	A	Y(Z,A) (%)	ε
39	94	0.52	0.13	41	107	0.133	0.053
39	95	1.02	0.18	41	108	0.033	0.034
39	96	1.83	0.23	42	100	0.062	0.051
39	97	2.78	0.30	42	101	0.41	0.10
39	98	2.39	0.27	42	102	1.00	0.16
39	99	2.69	0.26	42	103	1.83	0.21
39	100	1.67	0.18	42	104	2.50	0.25
39	101	0.63	0.11	42	105	2.13	0.23
39	102	0.253	0.074	42	106	1.72	0.20
39	103	0.036	0.031	42	107	0.69	0.13
40	95	0.038	0.045	42	108	0.230	0.077
40	96	0.359	0.098	42	109	0.090	0.048
40	97	1.00	0.16	42	110	0.031	0.027
40	98	1.96	0.25	43	101	0.019	0.023
40	99	2.33	0.26	43	102	0.055	0.045
40	100	3.56	0.31	43	103	0.210	0.086
40	101	2.71	0.26	43	104	0.42	0.11
40	102	1.99	0.22	43	105	1.04	0.15
40	103	1.23	0.15	43	106	1.12	0.17
40	104	0.467	0.098	43	107	1.00	0.16
40	105	0.302	0.070	43	108	0.80	0.15
41	97	0.040	0.042	43	109	0.185	0.072
41	98	0.169	0.076	43	110	0.134	0.059
41	99	0.58	0.14	43	111	0.100	0.039
41	100	1.00	0.17	43	112	0.013	0.019
41	101	2.81	0.26	44	105	0.046	0.049
41	102	3.05	0.27	44	106	0.073	0.060
41	103	3.03	0.28	44	107	0.119	0.073
41	104	2.11	0.21	44	108	0.115	0.077
41	105	1.06	0.16	44	109	0.086	0.073
41	106	0.60	0.12	44	110	0.098	0.072

Z	**A**	**Y(Z,A) (%)**	ε	**Z**	**A**	**Y(Z,A) (%)**	ε
44	111	0.091	0.059	47	122	0.025	0.023
44	112	0.067	0.051	48	117	0.091	0.056
44	113	0.033	0.038	48	118	0.053	0.052
45	106	0.005	0.022	48	119	0.020	0.052
45	108	0.008	0.036	48	120	0.035	0.038
45	109	0.018	0.051	48	121	0.034	0.029
45	110	0.019	0.050	48	122	0.075	0.046
45	111	0.053	0.069	48	123	0.051	0.036
45	112	0.023	0.048	48	124	0.004	0.016
45	113	0.007	0.039	48	125	0.019	0.022
45	114	0.034	0.046	48	126	0.023	0.022
45	115	0.062	0.032	48	127	0.032	0.026
45	116	0.012	0.026	48	128	0.027	0.021
46	108	0.015	0.021	49	121	0.020	0.048
46	111	0.050	0.049	49	122	0.013	0.045
46	112	0.054	0.056	49	123	0.066	0.054
46	113	0.045	0.052	49	124	0.047	0.040
46	114	0.079	0.057	49	125	0.057	0.043
46	115	0.116	0.053	49	126	0.069	0.047
46	116	0.073	0.052	49	127	0.050	0.041
46	117	0.003	0.026	49	128	0.126	0.056
46	118	0.041	0.035	49	129	0.064	0.040
46	119	0.027	0.025	49	130	0.053	0.032
46	120	0.008	0.017	49	131	0.063	0.037
47	112	0.001	0.020	49	132	0.071	0.037
47	113	0.022	0.033	49	133	0.020	0.028
47	115	0.061	0.053	49	134	0.011	0.014
47	116	0.025	0.041	50	123	0.042	0.051
47	118	0.113	0.062	50	124	0.040	0.040
47	120	0.043	0.030	50	125	0.179	0.059
47	121	0.013	0.024	50	126	0.111	0.044

Z	A	Y(Z,A) (%)	ε	Z	A	Y(Z,A) (%)	ε
50	127	0.166	0.056	52	132	1.68	0.16
50	128	0.361	0.082	52	133	3.06	0.21
50	129	0.562	0.096	52	134	3.36	0.23
50	130	0.84	0.12	52	135	2.66	0.19
50	131	1.00	0.12	52	136	1.75	0.16
50	132	0.78	0.11	52	137	0.88	0.11
50	133	0.289	0.071	52	138	0.656	0.092
50	134	0.141	0.048	52	139	0.189	0.055
50	135	0.114	0.040	52	140	0.158	0.038
50	136	0.016	0.019	52	141	0.057	0.022
51	121	0.033	0.027	53	129	0.053	0.039
51	122	0.042	0.034	53	130	0.101	0.046
51	124	0.024	0.036	53	131	0.191	0.064
51	125	0.027	0.047	53	132	0.222	0.068
51	126	0.044	0.046	53	133	1.05	0.13
51	127	0.181	0.067	53	134	1.58	0.16
51	128	0.177	0.060	53	135	2.97	0.21
51	129	0.59	0.10	53	136	3.00	0.21
51	130	0.94	0.12	53	137	2.69	0.19
51	131	1.82	0.17	53	138	2.00	0.18
51	132	2.05	0.18	53	139	1.09	0.13
51	133	1.78	0.17	53	140	0.565	0.092
51	134	1.13	0.13	53	141	0.177	0.053
51	135	0.73	0.11	53	142	0.055	0.033
51	136	0.362	0.069	53	143	0.068	0.030
51	137	0.100	0.034	53	144	0.063	0.024
51	138	0.047	0.026	54	130	0.028	0.031
52	127	0.022	0.040	54	131	0.041	0.036
52	129	0.195	0.056	54	132	0.039	0.038
52	130	0.304	0.081	54	133	0.194	0.064
52	131	0.78	0.11	54	134	0.098	0.051

Z	**A**	**Y(Z,A) (%)**	ε	**Z**	**A**	**Y(Z,A) (%)**	ε
54	135	0.99	0.12	56	141	1.16	0.13
54	136	1.34	0.15	56	142	1.71	0.16
54	137	2.11	0.19	56	143	1.77	0.17
54	138	2.56	0.19	56	144	1.86	0.17
54	139	2.45	0.19	56	145	1.43	0.14
54	140	2.02	0.17	56	146	0.95	0.12
54	141	1.41	0.14	56	147	0.569	0.090
54	142	0.664	0.097	56	148	0.260	0.062
54	143	0.548	0.087	56	149	0.115	0.044
54	144	0.209	0.053	57	136	0.018	0.013
54	145	0.096	0.038	57	137	0.007	0.018
55	133	0.009	0.023	57	138	0.033	0.029
55	134	0.018	0.032	57	139	0.001	0.025
55	135	0.061	0.039	57	140	0.053	0.033
55	136	0.190	0.065	57	141	0.115	0.043
55	137	0.63	0.10	57	142	0.231	0.068
55	138	0.90	0.12	57	143	0.64	0.10
55	139	1.50	0.15	57	144	0.90	0.11
55	140	2.33	0.18	57	145	1.25	0.14
55	141	2.62	0.20	57	146	1.53	0.14
55	142	2.21	0.18	57	147	1.18	0.13
55	143	1.61	0.16	57	148	0.73	0.11
55	144	0.93	0.11	57	149	0.438	0.083
55	145	0.446	0.073	57	150	0.118	0.042
55	146	0.226	0.056	57	151	0.023	0.023
55	147	0.081	0.032	57	152	0.019	0.020
55	148	0.030	0.020	57	153	0.035	0.016
56	137	0.006	0.026	58	140	0.005	0.013
56	138	0.050	0.044	58	141	0.022	0.025
56	139	0.220	0.069	58	142	0.013	0.028
56	140	0.57	0.10	58	143	0.115	0.041

Z	A	Y(Z,A) (%)	ε
58	144	0.078	0.040
58	145	0.202	0.067
58	146	0.396	0.078
58	147	0.404	0.088
58	148	0.75	0.11
58	149	0.578	0.095
58	150	0.438	0.085
58	151	0.193	0.058
58	152	0.073	0.040
58	153	0.041	0.028
59	144	0.031	0.027
59	145	0.077	0.027
59	146	0.040	0.032
59	147	0.155	0.048
59	148	0.205	0.058
59	149	0.301	0.069
59	150	0.522	0.082
59	151	0.424	0.078
59	152	0.251	0.062
59	153	0.154	0.043
59	154	0.068	0.026
59	155	0.034	0.020
59	156	0.015	0.016
59	157	0.012	0.016
59	158	0.012	0.011
60	146	0.003	0.012
60	147	0.019	0.024
60	148	0.029	0.031
60	149	0.023	0.031
60	150	0.050	0.042
60	151	0.060	0.040
60	152	0.080	0.042
60	153	0.099	0.045
60	154	0.122	0.050
60	155	0.042	0.028
60	156	0.014	0.020
60	157	0.003	0.011
60	158	0.010	0.011
61	149	0.015	0.020
61	150	0.015	0.020
61	152	0.011	0.023
61	153	0.053	0.030
61	154	0.033	0.026
61	155	0.047	0.032
61	156	0.093	0.038
61	157	0.046	0.025
61	158	0.020	0.020
61	159	0.012	0.011
62	154	0.003	0.016
62	155	0.023	0.023
62	156	0.016	0.023
62	157	0.019	0.023
62	158	0.004	0.016

C.5 Isotopic Fission Yields of ^{238}U (E_x = 7.4 MeV)

^{238}U (E_x = 7.4 MeV)			
Z	**A**	**Y(Z,A) (%)**	ε
32	79	0.067	0.088
32	80	0.071	0.092
32	81	0.119	0.099
32	82	0.113	0.093
33	83	0.24	0.13
33	84	0.069	0.097
33	85	0.064	0.065
33	86	0.120	0.088
33	87	0.056	0.060
34	81	0.081	0.072
34	84	0.10	0.11
34	85	0.50	0.16
34	86	0.56	0.19
34	87	0.82	0.19
34	88	0.91	0.16
34	89	0.111	0.070
34	90	0.029	0.047
35	84	0.041	0.079
35	85	0.186	0.095
35	86	0.25	0.15
35	87	0.62	0.18
35	88	0.89	0.20
35	89	0.73	0.19
35	90	0.99	0.22
35	91	0.52	0.13
35	92	0.121	0.069
35	93	0.055	0.056
36	84	0.027	0.049
36	85	0.121	0.068
36	87	0.32	0.15
36	88	0.77	0.19
36	89	1.89	0.28
36	90	2.69	0.33
36	91	2.43	0.30
36	92	1.97	0.26
36	93	0.89	0.17
36	94	0.35	0.13
36	95	0.076	0.057
37	86	0.014	0.043
37	87	0.055	0.058
37	88	0.096	0.069
37	89	0.40	0.14
37	90	0.80	0.20
37	91	0.76	0.21
37	92	1.42	0.24
37	93	1.84	0.27
37	94	1.72	0.26
37	95	1.07	0.19
37	96	0.41	0.13
37	97	0.23	0.10
37	98	0.113	0.058
37	99	0.099	0.049
38	90	0.136	0.078
38	91	0.16	0.11
38	92	0.43	0.15

Z	**A**	**Y(Z,A) (%)**	ε	**Z**	**A**	**Y(Z,A) (%)**	ε
38	93	1.17	0.22	40	105	0.261	0.075
38	94	2.23	0.29	40	106	0.055	0.038
38	95	2.94	0.32	41	97	0.021	0.065
38	96	3.01	0.32	41	98	0.223	0.087
38	97	2.15	0.28	41	99	0.17	0.12
38	98	1.57	0.21	41	100	0.52	0.16
38	99	0.78	0.14	41	101	0.92	0.19
38	100	0.451	0.094	41	102	1.86	0.24
38	101	0.139	0.044	41	103	2.55	0.27
38	102	0.036	0.035	41	104	2.05	0.23
39	94	0.54	0.14	41	105	1.28	0.18
39	95	0.75	0.18	41	106	0.41	0.10
39	96	1.47	0.23	41	107	0.110	0.053
39	97	2.19	0.29	41	108	0.043	0.037
39	98	2.42	0.28	42	99	0.002	0.051
39	99	2.54	0.28	42	101	0.10	0.10
39	100	2.59	0.24	42	102	0.62	0.15
39	101	1.25	0.18	42	103	1.16	0.19
39	102	0.40	0.10	42	104	1.58	0.23
39	103	0.175	0.053	42	105	1.65	0.22
39	104	0.105	0.052	42	106	1.65	0.20
39	105	0.027	0.023	42	107	0.60	0.13
40	96	0.259	0.092	42	108	0.353	0.089
40	97	0.79	0.16	42	109	0.250	0.064
40	98	1.39	0.22	42	110	0.037	0.021
40	99	2.14	0.28	43	103	0.004	0.076
40	100	3.91	0.34	43	104	0.04	0.11
40	101	3.75	0.31	43	105	0.07	0.12
40	102	3.43	0.29	43	106	0.23	0.15
40	103	2.14	0.22	43	107	0.08	0.13
40	104	0.78	0.13	43	108	0.09	0.10

Z	**A**	**Y(Z,A) (%)**	ε	**Z**	**A**	**Y(Z,A) (%)**	ε
43	109	0.044	0.072	48	123	0.049	0.052
43	110	0.055	0.064	48	124	0.066	0.042
43	111	0.041	0.047	49	124	0.043	0.076
43	112	0.014	0.035	49	125	0.044	0.061
44	104	0.008	0.048	49	127	0.068	0.045
44	105	0.103	0.078	49	128	0.010	0.027
44	110	0.02	0.11	49	129	0.155	0.047
44	111	0.115	0.093	49	130	0.089	0.037
44	113	0.023	0.046	49	131	0.048	0.037
44	114	0.067	0.040	49	132	0.146	0.064
45	109	0.05	0.11	49	133	0.062	0.040
45	110	0.04	0.13	49	134	0.017	0.015
45	111	0.01	0.12	49	135	0.006	0.015
45	114	0.071	0.077	50	120	0.003	0.062
45	115	0.024	0.049	50	123	0.008	0.097
46	112	0.06	0.11	50	125	0.027	0.094
46	114	0.10	0.12	50	126	0.001	0.075
46	115	0.02	0.10	50	127	0.290	0.080
46	116	0.092	0.092	50	128	0.303	0.081
46	118	0.004	0.038	50	129	0.378	0.090
46	119	0.015	0.038	50	130	1.19	0.14
46	120	0.016	0.018	50	131	1.28	0.15
46	121	0.010	0.018	50	132	1.32	0.14
47	120	0.030	0.062	50	133	0.97	0.12
47	121	0.009	0.041	50	134	0.271	0.065
47	122	0.002	0.025	50	135	0.065	0.035
47	123	0.012	0.025	50	136	0.027	0.020
47	124	0.006	0.017	50	137	0.068	0.028
48	119	0.12	0.12	50	138	0.049	0.020
48	121	0.22	0.10	51	123	0.027	0.073
48	122	0.029	0.066	51	125	0.02	0.10

Z	**A**	**Y(Z,A) (%)**	ε	**Z**	**A**	**Y(Z,A) (%)**	ε
51	127	0.16	0.10	53	131	0.16	0.10
51	129	0.241	0.097	53	132	0.16	0.10
51	130	0.60	0.12	53	133	0.32	0.11
51	131	1.14	0.15	53	134	1.05	0.15
51	132	1.69	0.18	53	135	2.08	0.19
51	133	2.75	0.22	53	136	2.09	0.19
51	134	1.66	0.17	53	137	2.84	0.21
51	135	1.11	0.14	53	138	2.26	0.20
51	136	0.62	0.10	53	139	1.57	0.16
51	137	0.267	0.064	53	140	0.91	0.12
51	138	0.112	0.037	53	141	0.523	0.091
51	139	0.047	0.024	53	142	0.245	0.057
52	123	0.018	0.032	53	143	0.151	0.050
52	124	0.010	0.028	53	144	0.044	0.026
52	125	0.046	0.045	54	128	0.008	0.026
52	126	0.030	0.079	54	130	0.018	0.056
52	127	0.209	0.090	54	131	0.002	0.068
52	130	0.190	0.096	54	133	0.039	0.091
52	131	0.53	0.12	54	134	0.184	0.099
52	132	1.34	0.16	54	135	0.42	0.12
52	133	2.69	0.21	54	136	0.92	0.14
52	134	3.61	0.24	54	137	1.36	0.16
52	135	3.37	0.23	54	138	2.41	0.20
52	136	2.87	0.20	54	139	2.72	0.20
52	137	1.61	0.15	54	140	3.07	0.21
52	138	0.84	0.11	54	141	2.13	0.18
52	139	0.446	0.086	54	142	1.25	0.14
52	140	0.329	0.060	54	143	0.570	0.095
52	141	0.110	0.038	54	144	0.237	0.057
52	142	0.042	0.023	54	145	0.164	0.051
53	130	0.027	0.092	54	146	0.050	0.026

Z	**A**	**Y(Z,A) (%)**	ε	**Z**	**A**	**Y(Z,A) (%)**	ε
55	131	0.027	0.030	56	151	0.030	0.022
55	133	0.117	0.065	57	140	0.032	0.070
55	134	0.001	0.072	57	141	0.069	0.080
55	136	0.066	0.096	57	142	0.207	0.093
55	137	0.23	0.11	57	143	0.34	0.10
55	138	0.40	0.10	57	144	0.47	0.11
55	139	0.91	0.14	57	145	0.75	0.13
55	140	1.42	0.17	57	146	1.03	0.14
55	141	1.91	0.18	57	147	0.86	0.12
55	142	2.18	0.19	57	148	0.74	0.11
55	143	1.82	0.17	57	149	0.478	0.092
55	144	1.40	0.15	57	150	0.179	0.061
55	145	0.74	0.11	57	151	0.113	0.042
55	146	0.413	0.079	57	152	0.033	0.028
55	147	0.127	0.050	57	153	0.028	0.022
55	148	0.056	0.029	57	154	0.022	0.018
56	133	0.004	0.014	58	143	0.053	0.067
56	134	0.001	0.029	58	145	0.182	0.072
56	138	0.040	0.087	58	146	0.149	0.076
56	139	0.087	0.082	58	147	0.69	0.11
56	140	0.179	0.089	58	148	0.73	0.11
56	141	0.74	0.12	58	149	0.85	0.12
56	142	1.23	0.15	58	150	0.69	0.10
56	143	2.23	0.18	58	151	0.369	0.075
56	144	2.69	0.20	58	152	0.142	0.050
56	145	2.34	0.19	58	153	0.101	0.039
56	146	1.94	0.16	58	154	0.062	0.025
56	147	0.94	0.11	58	155	0.016	0.017
56	148	0.468	0.081	59	146	0.039	0.068
56	149	0.168	0.051	59	147	0.040	0.066
56	150	0.063	0.028	59	148	0.047	0.062

Z	**A**	**Y(Z,A) (%)**	ε
59	149	0.074	0.064
59	150	0.093	0.060
59	151	0.173	0.067
59	152	0.121	0.061
59	153	0.093	0.050
59	154	0.033	0.030
59	155	0.031	0.021
60	149	0.006	0.054
60	150	0.097	0.058
60	151	0.009	0.047
60	152	0.076	0.052
60	153	0.110	0.048
60	154	0.152	0.048
60	155	0.097	0.041
60	156	0.035	0.025

USC
UNIVERSIDADE
DE SANTIAGO
DE COMPOSTELA

Bibliography

[1] J. Chadwick. "Possible existence of a neutron". *Nature*, 129:312, 1932.

[2] E. Fermi. "Possible production of elements of atomic number higher than 92". *Nature*, 133:898, 1934.

[3] O. Hahn and F. Strassmann. "Über den Nachweis und das Verhalten der bei der Bestrahlung des Urans mittels Neutronen entstehenden Erdalkalimetalle". *Die Naturwissenschaften*, 27:11, 1939.

[4] L. Meitner and O. R. Frisch. "Disintegration of Uranium by Neutrons: a New Type of Nuclear Reaction". *Nature*, 143:239, 1939.

[5] O. R. Frisch. "Physical Evidence for the Division of Heavy Nuclei under Neutron Bombardment". *Nature*, 143:276, 1939.

[6] N. Bohr and J. A. Wheeler. "The mechanism of Nuclear Fission". *Phys. Rev.*, 56:426, 1939.

[7] T. Ichikawa et al. "Contrasting fission potential-energy structure of actinides and mercury isotopes". *Phys. Rev. C*, 86:024610, 2012.

[8] C. F. v. Weizsäcker. "Zur Theorie der Kernmassen". *Zeitschrift für Physik*, 96:431, 1935.

[9] M. G. Mayer. "On Closed Shell in Nuclei". *Phys. Rev.*, 74:235, 1948.

[10] S. G. Nilsson. "Binding states of individual nucleons in strongly deformed nuclei". *Dan. Mat. Fys. Medd.*, 29:16, 1955.

[11] V. M. Strutinsky. "Shell Effects in nuclear masses and deformation energies". *Nucl. Phys. A*, 95:420, 1967.

[12] M. Bolsterli et al. "New Calculation of Fission Barriers for Heavy and Superheavy Nuclei". *Phys. Rev. C*, 5:1050, 1972.

[13] B. D. Wilkins et al. "Scission-point model of nuclear fission based on deformed-shell effects". *Phys. Rev. C*, 14:1832, 1976.

[14] J. Bardeen et al. "Theory of superconductivity". *Phys. Rev.*, 108:1175, 1957.

[15] H. J. Krappe and J. R. Nix. "Modified definition of the surface energy in the liquid drop formula". *Physics and Chemistry of Fission, Proceedings of a the third IAEA Symposium*, 1:159, 1973.

[16] E. Konecny and H. W. Schmitt. "Fission energies and neutron emission in 13-MeV Proton-induced fission of ^{226}Ra". *Phys. Rev.*, 172:1213, 1968.

[17] W. Reisdorf et al. "Fission fragment K x-ray emission and nuclear charge distribution for thermal neutron fission of ^{233}U, ^{235}U, ^{239}Pu and spontaneous fission of ^{252}Cf". *Nucl. Phys. A*, 177:337, 1971.

[18] Ulrich Brosa, Siegfried Grossmann, and Andreas Müller. "Nuclear Scission". *Physics Reports*, 197:167, 1990.

[19] K.-H. Schmidt et al. "General Description of Fission Observables: GEF Model Code". *Nuclear Data Sheets*, 131:107, 2016.

[20] K.-H. Schmidt and B. Jurado. "Entropy Driven Excitation Energy Sorting in Superfluid Fission Dynamics". *Phys. Rev. Lett.*, 104:212501, 2010.

[21] T. von Egidiy and C. Bucurescu. "Experimental energy-dependent nuclear spin distributions". *Phys. Rev. C*, 80:054310, 2009.

[22] K.-H. Schmidt et al. "Low-energy fission studies of neutron-deficient projectile fragments of ^{238}U". *Phys. Lett. B*, 325:313, 1994.

[23] J.-F. Martin et al. "Studies on fission with ALADIN. Precise and simultaneous measurement of fission yields, total kinetic energy and total prompt neutron multiplicity at GSI". *Eur. Phys. J. A*, 51:174, 2015.

[24] M. Caamaño et al. "Isotopic yield distributions of transfer- and fusion-induced fission from ^{238}U+^{12}C reactions in inverse kinematics". *Phys. Rev. C*, 88:024605, 2013.

[25] K.-H. Schmidt et al. "Relativistic radioactive beams: A new access to nuclear-fission studies". *Nucl. Phys. A*, 665:221, 2000.

[26] `http://pro.ganil-spiral2.eu/laboratory/research/scientific-production`.

[27] Dufour J. P. et al. "Projectile fragments isotopic separation: Application to the LISE spectrometer at GANIL". *Nucl. Instr. and Meth. A*, 248:267, 1986.

[28] Villari A. C. C and the SPIRAL group. "The accelerated ISOL technique and the SPIRAL project". *Nuclear Physics A: Research opportunities with accelerated beams of radioactive ions*, GANIL S 01 01, 2001.

[29] Anne R. et al. "The achromatic spectrometer LISE at GANIL". *Nucl. Instr. and Meth. A*, 257:215, 1987.

[30] F. Azaiez, D. Beaumel, B. Blank, W. Catford, F. Chautard, et al. "GANIL / SPIRAL - 2001-2007 - Achievements, Highlights and Perspectives". *in2p3-00336915*, 2008.

[31] C. Rodríguez-Tajes et al. "Transfer reactions in inverse kinematics: An experimental approach for fission investigations". *Phys. Rev. C*, 89:024614, 2014.

[32] `http://pro.ganil-spiral2.eu/laboratory/detectors/exogam/exogam-detectors`.

[33] S.L. Shepherd et al. "Measurements on a prototype segmented Clover detector". *Nucl. Instr. and Meth. A*, 434:373, 1999.

[34] Hervé Savajols et al. "VAMOS: a Variable Mode high acceptance Spectrometer". *Nucl. Phys. A*, 654:1027, 1999.

[35] Hervé Savajols et al. "VAMOS: A variable mode high acceptance spectrometer for identifying reaction products induced by SPIRAL beams". *Nucl. Instr. and Meth. B*, 204:146, 2003.

[36] S. Pullanhiotan et al. "Performance of VAMOS for reactions near the Coulomb barrier". *Nucl. Instr. and Meth. A*, 593:343, 2008.

[37] Bertrand Jacquot. "VAMOS optics". `http://pro.ganil-spiral2.eu/laboratory/experimental-areas/g1-vamos/beam-optics/vamos-optics/at_download/file`.

[38] Bertrand Jacquot. "Introduction aux spectromètres et séparateurs en physique nucléaire". `http://pro.ganil-spiral2.eu/laboratory/experimental-areas/g1-vamos/beam-optics/spectrometers-separators-joliot-curie-shool-2008/at_download/file`, 2008.

[39] S. Pullanhiotan et al. "Improvement in the reconstruction method for VAMOS spectrometer". *Nucl. Instr. and Meth. B*, 266:4148, 2008.

[40] E. D. Klema et al. "Energy resolution of silicon surface-barrier detectors for oxygen and sulphur ions". *Nucl. Instr. and Meth. Phys. Res.*, 225:72, 1984.

[41] H. Hötzl et al. "Experiences with large-area Frisch grid chambers in low-level alpha spectrometry". *Nucl. Instr. and Meth. Phys. Res.*, 223:290, 1984.

[42] M. Rejmund et al. "Performance of the improved larger acceptance spectrometer: VAMOS++". *Nucl. Instr. and Meth. A*, 646:184, 2011.

[43] O. Frisch. "Isotope analysis of uranium samples by means of their α-ray groups". *British atomic energy report*, Br-49, 1944.

[44] J.C. Santiard et al. "GASPLEX a low-noise analog signal processor for readout of gaseous detectors". *CERN-ECP*, 94:17, 1994.

[45] K. A. Olive et al. "PDG". *Chin. Phys. C*, 38:090001, 2014.

[46] J. F. Ziegler. `http://www.srim.org`.

[47] Glenn F. Knoll. *"Radiation detection and measurement"*. John Wiley & Sons, Inc., New York, second edition, 1989.

[48] François Méot. "The ray-tracing code Zgoubi". *Nucl. Instr. and Meth. A*, 427:353, 1999.

[49] A. Boujrad and F. Saillant. "The New GANIL Data Acquisition System". *2000 IEEE Nuclear Science Symposium Conference Record*, 12:192, 2001.

[50] O. Tarasov & D. Bazin. `http://lise.nscl.msu.edu/lise.html`.

[51] P. Marchand and L. Marmet. "Binomial smoothing filter: A way to avoid some pitfalls of least-squares polynomial smoothing". *Rev. Sci. Instrum.*, 54:1034, 1983.

[52] Ichita Endo et al. "Systematic shifts of evaluated charge centroid for the cathode read-out multiwire proportional chamber". *Nucl. Instr. and Meth.*, 188:51, 1981.

[53] Kwong Lau, Lörg Pyrlik. "Optimization of centroid-finding algorithms for cathode strip chambers". *Nucl. Instr. and Meth. A*, 366:298, 1995.

[54] L. Bardelli et al. "Influence of crystal-orientation effects on pulse-shape-based identification of heavy-ions stopped in silicon detectors". *Nucl. Instr. and Meth. A*, 605:353, 2009.

[55] H. W. Schmitt et al. "Precision Measurements of Correlated Energies and Velocities of ^{252}Cf Fission Fragments". *Phys. Rev.*, 137:B837, 1965.

[56] E. P. Steinberg et al. "Pulse Height Response Characteristics for Heavy Ions in Silicon Surface-Barrier Detectors". *Nucl. Instr. and Meth.*, 99:309, 1972.

[57] E. C. Finch et al. "Measurements of the pulse height defect and its mass dependence for heavy-ion silicon detectors". *Nucl. Instr. and Meth.*, 113:29, 1973.

[58] A. Shrivastava et al. "Prompt γ-ray spectroscopy of isotopically identified fission fragments". *Phys. Rev. C*, 80:051305(R), 2009.

[59] National Nuclear Data Center. "Evaluated Nuclear Structure Data File (ENSDF)". `http://www.nndc.bnl.gov/ensdf`.

[60] M. Caamaño et al. "Characterization of the scission point from fission-fragment velocities". *Phys. Rev. C*, 92:034606, 2015.

[61] J.P. Dufour et al. "Projectile fragments isotopic separation: Application to the Lise Spectrometer at Ganil". *Nucl. Instr. and Meth. A*, 248:267, 1986.

[62] E. Baron et al. "Charge exchange of very heavy ions in carbon foils and in the residual gas of GANIL cyclotrons". *Nucl. Instr. and Meth. A*, 328:177, 1993.

[63] Reiner Bass. *"Nuclear Reactions with Heavy Ions"*. Springer-Verlag, Berlin, 2010.

[64] I. Tsekhanovich et al. "Fission-products formation in the thermal-neutron-induced fission on odd Cm isotopes". *Phys. Rev. C*, 70:044610, 2004.

[65] T. Ohtsuki et al. "Systematic analysis of mass yields curves in low-energy fission of actinides". *Phys. Rev. C*, 40:2144, 1989.

[66] C. Schmitt et al. "Fission yields at different fission-products kinetic energies for thermal-neutron-induced fission of ^{239}Pu". *Nucl. Phys. A*, 430:21, 1984.

[67] A. Bail et al. "Isotopic yield measurement in the heavy mass region for ^{239}Pu thermal neutron induced fission". *Phys. Rev. C*, 84:034605, 2011.

[68] J.-F. Martin. *"Coulex fission of ^{234}U, ^{235}U, ^{237}Np, and ^{238}Np studied within the SOFIA experimental program"*. PhD thesis, Université Paris-Sud, 2015.

[69] G. Martinez et al. "Mass and nuclear charge yields of ^{237}Np($2n_{th}$,f) at different fission fragment kinetic energies". *Nucl. Phys. A*, 515:433, 1990.

[70] E. Pellerau. *"Contribution à la mise en place, à la réalisation, et à l'analyse des données de rendements de fission issues de l'expérience SOFIA au GSI"*. PhD thesis, Université Paris-Sud, 2013.

[71] H. Naik et al. "Mass yield distributions of fission products from photofission of ^{238}U induced by $11.5 - 17.3$ MeV bremsstrahlung". *Eur. Phys. J. A*, 49:94, 2013.

[72] S. Steinhäuser et al. "Odd-even effects observed in the fission of nuclei with unpaired protons". *Nucl. Phys. A*, 634:89, 1998.

[73] B. L. Tracy et al. "Rb and Cs Isotopic Cross Sections from 40-60-MeV-proton Fission of ^{238}U, ^{232}Th, and ^{235}U". *Phys. Rev. C*, 5:222, 1972.

[74] C. Böckstiegel et al. "Nuclear-fission studies with relativistic secondary beams: Analysis of fission channels". *Nucl. Phys. A*, 802:12, 2008.

[75] R. Müller et al. "Fragment velocities, energies, and masses from fast neutron induced fission of ^{235}U". *Phys. Rev. C*, 29:885, 1984.

[76] A. A. Naqvi et al. "Fission fragment properties in fast-neutron-induced fission of ^{237}Np". *Phys. Rev. C*, 34:218, 1986.

[77] Cyriel Wagemans. *"The Nuclear Fission Process"*. CRC-Press, Florida, 1991.

[78] M. Djebara et al. "Mass and nuclear-charge yields for ^{249}Cf(n_{th},f) at different fission-product kinetic energies". *Nucl. Phys. A*, 496:346, 1989.

[79] D. Rochman et al. "Isotopic yields from the reaction ^{245}Cm(n_{th},f) at the Lohengrin mass separator". *Nucl. Phys. A*, 710:3, 2002.

[80] W. Lang et al. "Nuclear charge and mass yields for ^{235}U(n_{th},f) as a function of the kinetic energy of the fission products". *Nucl. Phys. A*, 345:34, 1980.

[81] U. Quade et al. "Nuclide yields of light fission products from thermal-neutron induced fission of ^{233}U at different kinetic energies". *Nucl. Phys. A*, 487:1, 1988.

[82] J.P. Bocquet et al. "Characteristics of Mass and nuclear charge distributions of ^{229}Th(n_{th},f). Implications for fission dynamics". *Z. Phys. A*, 335:41, 1990.

[83] M. Caamaño, F. Rejmund, and K.-H. Schmidt. "Evidence for the predominant influence of the asymmetry degree of freedom on the

even-odd structure in fission-fragment yields". *J. Phys. G: Nucl. Part. Phys.*, 38:035101, 2011.

[84] I. Tsekhanovich et al. "Mass and charge distributions in the very asymmetric mass region of the neutron induced fission of ^{238}Np". *Nucl. Phys. A*, 688:633, 2001.

[85] S. Bjørnholm and J. E. Lynn. "The double-humped fission barrier". *Rev. Mod. Phys.*, 52:725, 1980.

[86] F. Rejmund et al. "Pair breaking and even-odd structure in fission-fragment yields". *Nucl. Phys. A*, 678:215, 2000.